PhD Thesis in Material Science

January 2015

SPIN-DEPENDENT TRANSPORT IN OXIDE-BASED TUNNEL JUNCTIONS

Regina Galceran Vercher

Supervisors:

Prof. Benjamín Martínez Perea

Dr. Lluís Balcells Argemí

Tutor:

Prof. Jordi Sort Viñas

Institut de Ciència de Materials de Barcelona (ICMAB-CSIC)

Universitat Autònoma de Barcelona (UAB)

Als meus pares, Anna i Josep,

i a la resta de la meva família

CONTENTS

Part II. Growth and characterization of thin films and heterostructures

PART III: Micro and nano-fabrication of tunnel junction devices

PART IV: Magnetoresistive properties of spin-dependent tunnelling devices

PART V: Conclusions

PART VI: APPENDIX

THESIS ABSTRACT:

This thesis studies the magnetotransport properties of tunnel junctions in which one of the electrodes is the ferromagnetic oxide $La_{0.7}Sr_{0.3}MnO_3$(LSMO). In particular, we focus on two different phenomena: (i) magnetoresistance (MR) in tunnel junctions with a single magnetic electrode and (ii) spin filtering in magnetic tunnel junctions. The tunneling effect is extremely sensitive to the interfaces and good quality of the heterostructures is crucial toward the optimal performance of the devices. For this reason, much of the thesis is dedicated to the growth (by sputtering) and characterization of thin films, to the study of interfaces in heterostructures and to the fabrication of junctions.

With respect to the junctions with a single magnetic electrode, we concentrate on the tunnelling transport as a function of temperature and magnetic field applied in Pt/$LaAlO_3$/LSMO junctions. In our work, we have identified the different physical mechanisms which play a relevant role on the MR of this system: tunnelling anisotropic magnetoresistance (TAMR), of the order of 4 % at low temperature, and another contribution to the MR, of the order of 17 %. Furthermore, TAMR at low magnetic field is attributed to rotation of magnetic domains.

In the case of junctions with two magnetic electrodes, we must also take into account the relative orientation between their magnetizations. The studied system is Fe/MgO/LSMO, in which a large tunnel magnetoresistance (TMR) is expected due to the combination of spin filtering from the Fe/MgO and the half-metallicity of LSMO. As a consequence of the formation of FeO_X at the Fe/MgO interface, we obtain different sign of the TMR for different junctions: a negative TMR of 4 % at low temperatures is ascribed to a magnetically disordered FeO_X and a positive TMR of 25 % at 70 K is attributed to magnetic ordering of the FeO_X at the interface with MgO, which results in spin filtering. When the MgO barrier thickness is reduced to 1.2 nm, this ordered FeO_X coupled antiferromagnetically to the LSMO layer gives rise to an interesting magnetoresistive behaviour, especially when measured with the magnetic field applied out-of-plane. We have not been able to avoid the formation of FeO_X in this heterostructure, even for *in-situ* growth or annealings, and we suggest that the MgO barrier is permeable to the oxygen from the manganites, which would be responsible for the oxidation of the Fe.

On the other hand, aiming at the fabrication of junctions with magnetic tunnel barrier which acts as spin filter, we have studied the possibility of using La_2CoMnO_6 (LCMO) thin films as barrier. This material is ferromagnetic, insulating and possesses perovskite structure, but there are only a few works on its thin film growth. What is more, such works are performed with pulsed laser deposition and thicknesses are above 100 nm, thus not suitable as insulating barriers in spin filters. We have performed a detailed study of the growth, optimization and characterization of LCMO thin films. In this regard, we have achieved epitaxial, insulating, ferromagnetic thin films (from 20 to 5 nm), with Curie temperatures around 230 K and perpendicular magnetic anisotropy. LCMO/LSMO heterostructures, whose magnetoresistive properties remain to be studied in future work, have also been grown.

RESUM DE LA TESI:

Aquesta tesi estudia les propietats de magnetotransport en unions túnel on un dels elèctrodes és l'òxid ferromagnètic $La_{0.7}Sr_{0.3}MnO_3$(LSMO). En concret, ens interessem per dos fenòmens diferents: (i) magnetoresistència (MR) en unions túnel amb un sol elèctrode magnètic i (ii) filtratge d'espí en unions túnel magnètiques. L'efecte túnel és extremadament dependent de les interfícies i una bona qualitat de les heteroestructures resulta crucial per a obtenir un bon rendiment dels dispositius. És per aquest motiu que bona part d'aquesta tesi es dedica al creixement (per polvorització catòdica) i caracterització de capes primes, a l'estudi de les interfícies de les heterostructures i a la fabricació de les unions.

Pel que fa a les unions amb un únic elèctrode magnètic, ens centrem en l'estudi del transport túnel en funció de la temperatura i del camp magnètic aplicat en unions de Pt/$LaAlO_3$/LSMO. En el nostre treball hem identificat diferents mecanismes físics que juguen un paper important en la MR d'aquest sistema: la magnetoresistència túnel anisòtropa (TAMR), de l'ordre de 4 % a baixa temperatura, i una altra contribució a la magnetoresistència, de l'ordre de 17%. A més, TAMR a baix cap magnètic s'atribueix a rotació de dominis magnètics.

En el cas d'unions amb dos elèctrodes magnètics, també cal tenir en compte l'orientació relativa entre les magnetitzacions d'aquests. El sistema que estudiem és Fe/MgO/LSMO, en el qual s'espera un valor de magnetoresistència túnel (TMR) gran degut a la combinació del filtratge d'espín per part del Fe/MgO i la semimetal·licitat del LSMO. Com a conseqüència de la formació de FeO_X en la intercara Fe/MgO, obtenim diferent signe de TMR per a diferents unions: una TMR negativa de 4% a baixes temperatures s'atribueix a un FeO_X magnèticament desordenat i una TMR positiva de 25% a 70 K s'atribueix a la ordenació magnètica del FeO_X a la intercara amb el MgO, que dóna lloc a filtratge d'espín. Quan el gruix de la barrera d'MgO es redueix a 1.2 nm, aquesta capa ordenada de FeO_X s'acobla antiferromagnèticament amb la de LSMO donant lloc a un comportament molt interessant de la MR especialment quan es mesura aplicant el camp magnètic fora del pla de la capa. La formació de FeO_X en aquesta estructura no s'ha aconseguit eliminar amb creixement *in-situ* ni amb recuits, i se suggereix que la barrera d'MgO és permeable a l'oxigen de la manganita, que seria responsable de l'oxidació del Fe.

Per altra banda, amb l'objectiu de fabricar unions amb barrera túnel magnètica que actuï com a filtre d'espín, hem estudiat la possibilitat d'utilitzar capes primes de La_2CoMnO_6 (LCMO) com a barrera. Aquest material és ferromagnètic, aïllant i amb estructura de doble perovskita, però hi ha pocs treballs sobre la seva preparació en capes primes. A més a més, en aquests les capes estan crescudes per depòsit de làser pulsat i els gruixos són superiors a 100 nm, i per tant no aptes per actuar com barreres aïllants en filtres d'espí. L'objectiu principal s'ha orientat cap a un estudi detallat del creixement, optimització i caracterització de les propietats de capes primes de LCMO. En aquest sentit, s'han aconseguit capes (de 20 a 5 nm) epitaxials, aïllants i ferromagnètiques amb temperatures de Curie prop del 230 K i anisotropia magnètica perpendicular. S'han crescut heterostructures epitaxials de LCMO/LSMO, les propietats magnetoresistives de les quals es preveuen aprofundir en futurs treballs.

ATTRIBUTIONS AND FUNDING

I would like to acknowledge the work of all the people who have contributed to the work compiled in this thesis.

- Samples were grown at the ICMAB by Lluís Balcells, José Cisneros-Fernández and Regina Galceran.
- Growth of Fe was done at IMM (Madrid) by Alfonso Cebollada.
- Magnetic measurements were done by SQUID technician, Bernat Bozzo.
- X-ray diffraction measurements were carried out by ICMAB technicians: Anna Crespi, Joan B. Esquius and Fco. Javier Campos.
- HR-XRD measurements have been performed by Jaume Roqueta, Josep Santiso and Pablo García at ICN2 (Cerdanyola del Vallès).
- Synchrotron XRD measurements were carried out by Carlos Frontera, Jaume Roqueta and Josep Santiso at the KMC2 beamline (BESSY-II at Helmholtz-Zentrum, Berlin).
- AFM images were taken by Maite Simón, Laura López and Regina Galceran.
- HAADF-STEM images have been taken by María de la Mata, César Magén and Jordi Arbiol. TEM images have been taken by Núria Bagués.
- XPS measurements were done by Lorenzo Calvo at the Serveis Cientificotècnics de la UB and by Guillaume Sauthier at the ICN2.
- Ion beam etching of Fe was done by Federico Golmar and Saül Vélez at NanoGUNE.
- Lithography was done by Regina Galceran with the help of Edgar León, Javier Tornos and Fabián Cuéllar (UV lithography) and Judit Oró (electron beam lithography).
- Measurements at the PPMS were done by Regina Galceran with the assistance of Bernat Bozzo, Lluís Balcells and José Cisneros-Fernández.
- Useful discussions on magnetic tunnel junctions were held with Carlos Boubeta, Jacobo Santamaría, Zouhair Sefrioui and Fèlix Casanova.
- I acknowledge useful discussions and guidance of Lluís Balcells, Benjamín Martínez and Carlos Frontera.

I also recognize the funding from the Ministerio de Ciencia e Innovación through the FPI grant.

PERSONAL ACKNOWLEDGEMENTS

A nivell científic, m'agradaria donar les gràcies a totes les persones que m'han ajudat a entendre una mica més el què és la ciència, que m'han ensenyat a raonar, a expressar-me amb més claredat o a ser més didàctica. Sobretot, també, als que m'han comunicat la il·lusió per la investigació o que m'han transmès, amb el seu exemple, les ganes de voler fer les coses bé –en les múltiples vessants que té la feina del qui intenta fer recerca.

A nivell personal, agraeixo a tots als qui he vist treballar amb generositat i alegria, als qui saben encoratjar, escoltar o simplement ajuden a fer el dia a dia més agradable. I les persones que m'han sabut recolzar en tot moment. És gràcies a elles que no només puc agrair allò bo de què he gaudit durant aquest temps, sinó també allò millorable, que m'ha ajudat a créixer. Són elles qui han donat sentit al meu creixement, tant personal com científic, durant aquests quatre anys.

Entre aquests, vull mencionar els meus directors de tesi, el Benja i el Lluís:

Al Benja, per la oportunitat que m'has donat de poder formar part del teu grup dins de l'ICMAB. Per compartir la teva experiència en magnetisme i per mostrar-me que la tasca d'un investigador principal també va més enllà de la ciència... Per no haver escatimat en mi, duent-me a congressos, cursos i oferint-me la possibilitat de fer dues estades en altres laboratoris.

Al Lluís, per ésser un referent clar de científic motivat, que creus i t'il·lusiones pels experiments que proposes. Per tot el teu suport al laboratori i per haver estat al meu costat dia rere dia. Perquè t'has interessat pel meu estat d'ànim i m'has deixat ser partícip del teu. Ets per a mi el meu "pare científic", de qui he començat a caminar de la mà... Gràcies per haver-te mostrat tal com ets.

També agrair a les persones que he tingut més a prop, els meus companys de despatx (o gairebé):

Al Carlos, que saps ser didàctic com ningú, i m'has donat la confiança perquè et faci les preguntes més xorres, de les quals sempre he acabat aprenent. Per haver co-escrit amb mi el meu primer article i haver-me dedicat moltíssim del teu temps. Perquè m'has sabut mimar dia rere dia i pels cafès que hem compartit.

Al Jose, que sempre has estat atent i disposat a donar-me un cop de mà, generosament oferint-me molt més del que et demanava. Per haver-me escoltat i confiat en mi, per haver-me cuidat en tot moment, per les tardes de tonteries i per totes les teves preguntes curioses que també m'han fet pensar i aprendre.

A l'Ignasi, per transmetre'm el teu entusiasme per la física i per cercar d'entendre els fenòmens des de l'arrel, i les ganes d'explicar-m'ho. Per les tardes cantant els "bububobs" al despatx. Pels teus consells sincers i el teu vot de confiança.

A la resta de membres del meu grup: la Zorica, l'Alberto, el Bernat, el Felip... i als nostres fidels col·laboradors de l'ICN2: el Roqueta i el Santiso... També els diversos becaris o

precaris del nostre grup amb qui he compartit el dia a dia en els laboratoris, les angoixes i les alegries: el Luís Peña, la Laura i la Núria. I més recentment, també el Pol i l'Adrià. Perquè ben acompanyada es treballa molt millor!

A tota la gent amb qui he col·laborat, tant si el projecte ha donat fruit com si no: el Luís Garzón amb l'AFM, el Jordi Sort amb el nanoindentador, el Sergio València al sincrotró BESSY, el Claude Monti a Odelló, el Xavi Martí –sempre optimista!-, el Patxi López amb el MOKE, el Carlos Boubeta amb la seva gran habilitat bibliogràfica i per tots els seus consells sobre unions túnel... Moltes gràcies.

Muchas gracias a la gente que conocí durante mi estancia breve en la Universidad Complutense de Madrid. A Tornos y Fu, que me iniciasteis en el fantástico mundo de la litografía óptica de uniones túnel, junto con Ana, Mariona, Gabriel, Mirko... Me hicisteis sentir como en casa y fue un placer compartir con vosotros las conversaciones filosóficas entorno a las tapitas y birras de los jueves. También gracias a Zouhair y Jacobo, por vuestra gran experiencia y acogida. Y también a Alfonso Cebollada, del Instituto de Microelectrónica de Madrid, por toda su ayuda.

Je voudrais aussi remercier les gens de UMR (CNRS-Thales), qui m'avez si bien accueilli pendant mon séjour à Paris. À Edouard, qui m'as beaucoup appris et motivée, à Manuel Bibes, pour cette magnifique opportunité, et au group entier. Ça a été pour moi un vrai plaisir travailler avec vous et découvrir les nuits "open-mike".

A tota la gent de l'ICMAB: en especial, al meu grupet de dinar i de celebracions (la Jessi, l'Ignasi, la Mariona, l'Anna, la Marixa, la Roberta, l'Aura, l'Oriol, el Joan...). També els companys de dinar dels primers anys (Luís Peña i Luís Garzón), quan anàvem al restaurant d'Educació. Als de la 3ª planta que ens posem al dia davant de la fotocopiadora (Jessica, Laura, Markos...) i a la gent de fer cafès (Cristina, Romén, Marta, Bernat,...), als habituals del ferrocarril (Blai, Nerea...), als de la coral per fer-me riure com mai... i tants altres amb qui hem compartit somriures, preocupacions, congressos, cursos, o festes de final de tesi!

Als tècnics, per les vostres explicacions, la vostra paciència, i tota la feina que feu. Especialment amb els qui he tingut el plaer de treballar: l'Anna Crespi i la Judit, sempre disposades a ajudar amb un somriure; l'Edgar, que t'involucres per tal que tot surti bé; i el Bernat, que no et deixo descansar, entre d'altres.

Finalment, a tota la gent de fora de l'ICMAB però que sento prop meu: els meus amics que m'escolteu, m'aconselleu i em mimeu quan ho necessito. I especialment als que, a més a més, deixeu que jo també us escolti o us cuidi, perquè això em fa recordar el què és vertaderament important. Entre aquests, els de Lleida, els del galliner, els d'Espai Ignasià, els físicspelmón, les físikes (Núria, Anna, Pilar, Ana, Rita)... Una menció especial a les meves companyes de pis (Ares, Neus i Anna), que hem fet família. I, com no, a la meva família, el bé més preuat que tinc, a qui ho dec tot i a qui estimo amb bogeria. Pel vostre suport incondicional i per fer-me feliç, GRÀCIES.

ABBREVIATION LIST

AF – Antiferromagnetic

AFM – Atomic force microscopy / atomic force microscope

AMR –Anisotropic magnetoresistance

AP (configuration) – Antiparallel configuration

BE – Binding energy

BSE – Backscattered electrons

CMR – Colossal magnetoresistance

CO – Charge ordering

CS-AFM – Current-sensing atomic force microscopy

DE – Double exchange

DOS – Density of states

EBL – electron beam lithography

EDAX – Energy dispersive X-ray analysis

EFTEM – Energy-filtering transmission electron microscopy

f.u. – formula unit

FIB- Focused Ion Beam

FM- ferromagnetic

FWHM- full width half maximum

GADDS- General Area Detector Diffraction System

GFMC – Grupo de Física de Materiales Complejos, Universidad Complutense

GMR- Giant magnetoresistance

H – Magnetic field

HAADF-STEM: High angle annular dark field scanning transmission electron microscope.

H_C – coercive field

HS – High spin

I – Insulator

I(V) –Current vs voltage

IBE – Ion beam etching

IP – In-plane

ICMAB –Institut de Ciència de Materials de Barcelona

ICN2 – Institut Català de Nanociència i Nanotecnologia

IMM– Instituto de Microelectrónica de Madrid

J (vector)– total angular momentum

J – current

L- orbital momentum

LAO – $LaAlO_3$

LCMO – La_2CoMnO_6

LS- Low spin

LSMO – $La_{0.7}Sr_{0.3}MnO_3$

M –Metallic

MMA – Methyl methacrylate

MPMS – Magnetic properties measurement system

MR – Magnetoresistance

MRAM – Magnetic Random Access Memory

M_{sat}- Saturation magnetization

MTJ – Magnetic tunnel junction

OP – Out-of-plane

P (configuration) – Parallel configuration

P – Spin polarization

PLD – pulsed laser deposition

PM – Paramagnetic

PMA – Perpendicular magnetic anisotropy

PMMA- Polymethyl methacrylate

p_{O2} – Partial oxygen pressure

PPMS – Physical properties measurement system

R – Resistance

RF – Radiofrequency

RIE – Reactive ion etching

R_{rms} – root mean squared roughness

RRX – X-ray reflectometry

RT – room temperature

S (vector) – Spin momentum

SAF – Synthetic antiferromagnet

SE – Superexchange

SEM –Scanning electron microscope

SQUID – Superconducting Quantum Interference Device

STO – $SrTiO_3$

STT –MRAM – Spin-transfer-torque Magnetic Random Access Memory

TAMR –Tunnelling anisotropic magnetoresistance

T_C – Curie temperature

T_g – growth temperature

TEM – transmission electron microscope

TMR- tunnelling magnetoresistance

UV – ultraviolet

XPS – X-ray photoemission spectroscopy

XRD – X-ray diffraction

ZFC-FC: zero-field cooled field cooled

PART I:

INTRODUCTION

CHAPTER 1. MOTIVATION, AIM AND OUTLOOK OF THIS THESIS

1.1 MOTIVATION

Electronic devices nowadays basically rely on the transport of charge carried by electrons: current flows in and out of the different elements in a circuit. However, another degree of freedom of the electrons is their spin, which has not yet been fully exploited. This is what spintronics, a relatively new field of study, is trying to do: take advantage of the spin degree of freedom of electrons, and not only their charge, for device functionality. Its potential applications include information storage, computing and quantum information [1–3].

In the case of information storage, the search for both the increase in surface density and the reduction of power consumption in devices considers the use of spin (or magnetic states) as an excellent potential candidate for data storage. Its main advantages are the non-volatility (no power is needed to retain the magnetic polarization, and so the information does not fade away with time), the non-destructivity during the read-out process (the state is not modified by read operation) and the absence of a wear-out mechanism (because switching the magnetic polarization does not involve movement of atoms or electrons) [4]. So, the use of spins may provide alternatives to the limitations of electronics as we know it, and opens new horizons for electronic devices.

Since 1997, reading heads of disk drives which utilize magnetic properties (collective spin phenomena) are already commercially available. They consist in stacks of alternating ferromagnetic and non-magnetic metal layers, whose resistance varies notably depending on the magnetization orientation of each layer. Thus, such a system provides a unique way of sensing magnetic states, useful for reading stored information. This is called the giant magnetoresistance effect, discovered by Albert Fert and Peter Grünberg in 1980, which earned them the Nobel Prize in Physics 2007. The tunnelling magnetoresistance (TMR) effect achieved even larger responses and allowed reduction of the memory cell area and integration in the complementary metal-oxide-semiconductor transistor read circuitry [4]. The new type of random access memory, non-volatile with high-performance read and write characteristics, which employs ferromagnetic storage devices integrated with standard semiconductor circuitry is called magnetoresistive random access memory (MRAM) [4].

The development of spintronics implies the control of different processes: production, transport and detection of the spin polarized current. To achieve these purposes different approaches can be used: improvement of already existing devices to increase spin filtering and spin detection, the search and/or development of new materials with high degree of spin polarization, the search for novel ways for generation and manipulation of spin-polarized currents…[3]

A spin-polarized current may be generated by passing the electrons through a highly spin-polarized material. The ideal material for that purpose would be a fully spin-polarized material, i.e. a half-metallic material [2]. Unfortunately half-metal materials (most of them oxides) are scarce in natures [5]. A particular example is $La_{0.7}Sr_{0.3}MnO_3$ (LSMO).

Luckily, in compensation, transition-metal oxides offer a plethora of potential functionalities due to the numerous degrees of freedom they possess and the close correlation between them. In these materials charge, orbital, spin and lattice degrees of freedom are strongly correlated (see Fig 1.1) allowing the tuning of their physical properties for strengthening a desired functionality (ferroelectricity, ferromagnetism, antiferromagnetism, metallicity, superconductivity, optical properties, etc). This large variety and tunability of the properties allows envisaging materials which perform multiple tasks or that can be manipulated by various independent stimuli [6]. Some examples are the active barriers in a tunnel junction, where not only the insulating properties of the materials are exploited but also their spin filtering capabilities, according to the orbital symmetry, or by taking advantage of the magnetic nature of the barrier to achieve different effective barrier height for each spin orientation [7], or using ferroelectric tunnel junctions to modulate the effective barrier thickness by controlling the ferroelectric polarization orientation of the barrier. These so-called "multifunctional materials" are being studied for their exciting potential towards device miniaturization [8].

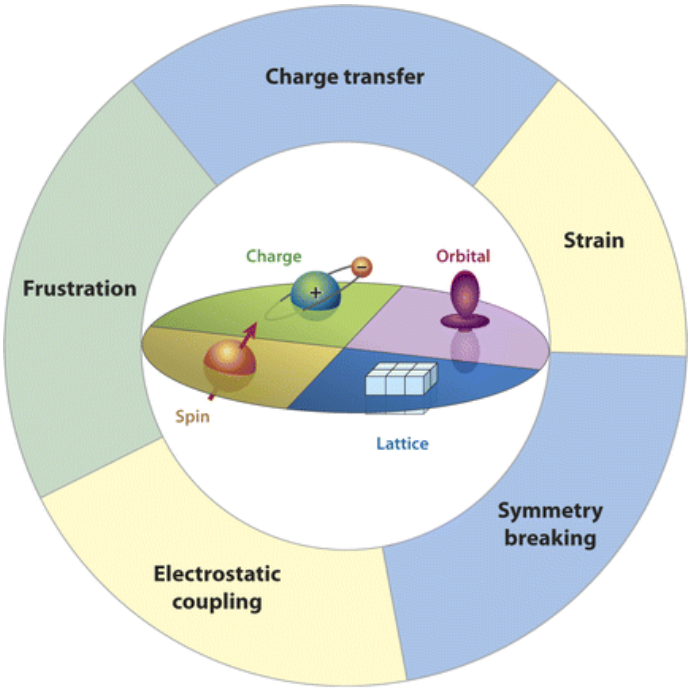

Fig 1.1. Sketch of the degrees of freedom of transition-metal oxides (at the centre) and various phenomena which may take place at the interfaces between oxides (taken from [9])

As the advancement of nanoscale science goes on, the role of the spin will probably gain greater relevance since the length scale of spin-dependent exchange interactions is

of the order of a few atomic distances. This is why spin-dependent properties are so sensitive to the atomic scale structure [1]. However, the advancement of oxide spintronics requires the parallel advancement of material science aspects (thin film growth and characterization, device fabrication procedures) [6,10] as improved control and quality at the nanoscale of the structures greatly influences the final device performance. In particular, interfaces between complex oxides exhibit exciting new and exotic phenomena –including charge transfer, strain, frustration, electrostatic coupling and symmetry breaking effects- [11,12] and the novel functionalities which arise also depend on the interface quality, so that advanced preparation methods are also critical towards detection of subtle effects, which may still unveil hidden physics.

Besides the technological potential of transition metal oxides (spintronic materials, superconductors, superionic conductors, catalysts…), understanding and mastering such strongly correlated systems remains an important and stimulating challenge to condensed matter physics. Concomitant to the search for increased response of the device performance, characterization of physical properties of devices using different tools such as, for instance, tunneling conduction processes, is an excellent way to achieve information about the interfacial states and properties. We are, therefore, working in a field where applications and fundamental physics are advancing hand in hand.

1.2 AIM AND OUTLOOK OF THIS THESIS

The **aim** of this thesis is the **study of tunnelling conduction processes in oxide-based heterostructures which use the optimally doped manganite LSMO** as one of the electrodes**. In particular, we focus our work on the magnetoresistive properties of such tunnelling devices.** In this sense, three different systems have been considered. The first, we have worked on the optimization of thin films of an insulating ferromagnetic material, La_2CoMnO_6 (LCMO), whose growth by sputtering had not yet been reported, to study its suitability as spin filtering barrier in combination with the half-metallic LSMO. LCMO/LSMO heterostructures have been grown and characterized, although their magnetotransport properties have not yet been measured. The second and third systems, we have prepared two kinds of tunnelling devices and studied their magnetoresistive responses as a function of temperature: (i) tunnel junctions with a single ferromagnetic electrode made from LSMO/$LaAlO_3$(LAO)/Pt heterostructures, which will enable the study of the LAO barrier quality, as well as the magnetoresistive response of the LSMO/LAO interface, and (ii) magnetic tunnel junctions made from LSMO/MgO/Fe heterostructures, which exhibit spin-filtering properties due to the formation of an FeO_X at the MgO/Fe interface. The different contributions to the magnetoresistive response are discussed.

As we have already mentioned in the previous section, the preparation of the samples is decisive towards the good performance of the devices. This is why we have dedicated

much of the thesis to the optimization of the growth of the films and heterostructures and their characterization, as well and the fabrication process of our devices.

Therefore, the thesis is divided into six parts (**Parts I-VI**):

Part I provides an introduction to the thesis; in particular, **Chapter 2** reviews the most relevant general concepts used throughout this thesis. The main structural, electronic and magnetic properties of transition metal oxides are explained, as they are at the origin of the behaviour of these materials. A brief description of the various existing magnetoresistive phenomena is provided, as well as the basics for two types of devices: magnetic tunnel junctions and spin filter junctions. Finally, some of the most relevant factors for thin film growth are mentioned.

Part II is devoted to the growth and characterization of the films and heterostructures. **Chapter 3** considers the optimization of the parameters for the growth by sputtering of films and heterostructures containing various oxides, Fe and metallic cappings. The preparation of each material is optimized according to the role for which we intend the material; for the well-known half-metallic LSMO, we search for the maximum T_C; for MgO, we focus on its crystallinity; for Fe, we must avoid oxidation as much as possible. Interfacial effects are studied and discussed for stacks such as MgO/LSMO, Pt/MgO/LSMO or Pt/Fe/MgO/LSMO. **Chapter 4** consists in the study of the growth of La_2CoMnO_6 (LCMO) thin films by sputtering. A complete characterization has been done to explore both its fundamental properties and the suitability of this material as spin filtering barrier. To that end, the magnetic properties are analysed for films with reduced thickness (down to 3-5 nm) and of LCMO/LSMO heterostructures.

Part III (Chapter 5) considers the fabrication of the tunnel junction devices. The selected configuration is discussed and their nano- and microstructuration, using various lithographic and etching steps, is detailed.

Part IV is dedicated to the magnetotransport measurements performed for the different devices. In **Chapter 6** we perform tunnelling transport measurements on a Pt/$LaAlO_3$/$La_{0.7}Sr_{0.3}MnO_3$ junction as a way of characterizing the $LaAlO_3$ barrier. Dependencies on temperature and magnetic field are analysed and the tunnelling anisotropic magnetoresistance exhibited by the junction is discussed. **Chapter 7** collects the magnetotransport results of LSMO/MgO/Fe magnetic tunnel junctions. Some suggestions regarding the modest values of tunnelling magnetoresistance measured for such junctions are offered, and the origin of the unexpected temperature and magnetic field orientation dependences is assigned to interfacial effects, namely the formation of FeO_x at the Fe/MgO interface.

Finally, in **Part V** (**Chapter 8)** we state the main conclusions resulting from this work.

In addition, **Part VI** is an appendix to the main text. **Appendix A** provides explanations of the different techniques used during this work, including those used for characterization, for patterning and for transport measurements. They are meant as a

reminder or a brief introduction for a reader which is not familiar with such techniques. **Appendix B** covers relevant details for the characterization of La_2CoMnO_6.

1.3 REFERENCES

[1] Kawakami R., McCreary K., Li Y.; Fundamentals of Spintronics in Metal and Semiconductor Systems. In: Korkin A, Rosei F, editors. Nanoelectron. Photonics, Springer New York; **2008**, p. 59–114. doi:10.1007/978-0-387-76499-3_5.

[2] Prestgard M.C., Siegel G.P., Tiwari A.; "Oxides for spintronics : A review of engineered materials for spin injection". *Adv. Mater. Lett.* 5; **2014**: 242–7. doi:10.5185/amlett.2014.amwc1032.

[3] Das Sarma S., Fabian J., Hu X., Zutic I.; "Spin electronics and spin computation". *Solid State Commun.* 119; **2001**: 207–15. doi:10.1016/S0038-1098(01)00111-9.

[4] Slaughter J.M.; "Materials for Magnetoresistive Random Access Memory". *Annu. Rev. Mater. Res.* 39; **2009**: 277–96. doi:10.1146/annurev-matsci-082908-145355.

[5] Coey J.M.D., Venkatesan M.; "Half-metallic ferromagnetism: Example of CrO2 (invited)". *J. Appl. Phys.* 91; **2002**: 8345. doi:10.1063/1.1447879.

[6] Bibes M., Barthelemy A.; "Oxide spintronics". *IEEE Trans. Electron Devices* 54; **2007**: 1003–23. doi:10.1109/ted.2007.894366.

[7] Moussy J.-B.; "Ultimate magnetism: Oxides in spintronics". *Clefs Du CEA* online.

[8] Bibes M., Villegas J.E., Barthélémy A.; "Ultrathin oxide films and interfaces for electronics and spintronics". *Adv. Phys.* 60; **2011**: 5–84. doi:10.1080/00018732.2010.534865.

[9] Zubko P., Gariglio S., Gabay M., Ghosez P., Triscone J.-M.; "Interface Physics in Complex Oxide Heterostructures". *Annu. Rev. Condens. Matter Phys.* 2; **2011**: 141–65. doi:10.1146/annurev-conmatphys-062910-140445.

[10] Heber J.; "Materials science: Enter the oxides.". *Nature* 459; **2009**: 28–30. doi:10.1038/459028a.

[11] "The interface is still the device.". *Nat. Mater.* 11; **2012**: 91. doi:10.1038/nmat3244.

[12] Hwang H.Y., Iwasa Y., Kawasaki M., Keimer B., Nagaosa N., Tokura Y.; "Emergent phenomena at oxide interfaces". *Nat. Mater.* 11; **2012**: 103–13. doi:10.1038/nmat3223.

CHAPTER 2. GENERAL CONCEPTS

2.1 BASIC PROPERTIES OF TRANSITION-METAL OXIDES: MANGANITES AND COBALTITES

Transition-metal oxides exhibit a wide range of electronic and magnetic properties as a consequence of the strong interaction of the outer *d*-shell electrons of the transition metal element (strongly correlated electrons). Their electronic properties are no longer explained by the band model, which considers free electrons, but result from the delicate balance between charge, spin and orbital degrees of freedom [1]. This grants transition-metal oxides a rich phenomenology [2] which includes colossal magnetoresistance (as in the case of $La_{0.7}Sr_{0.3}MnO_3$), high temperature superconductivity [3], piezoelectricity, ferroelectricity, pyroelectricity, electrooptical or thermal effects, etc.

In this section, we briefly explain the main physical properties of transition metal oxides, such as the crystalline and electronic structure, the magnetic interactions and the magnetoresistive phenomena, which are key to understanding the basic behaviour of these materials. We pay special attention to the two ferromagnetic transition metal oxides used in this work: $La_{0.7}Sr_{0.3}MnO_3$ (LSMO) and La_2CoMnO_6 (LCMO). LSMO has been widely studied, in bulk and in thin films, its main interest being the half-metallic character which is promising towards spintronic applications. LCMO has also been studied in bulk form but studies in thin film form are scarce, its main interest being its magnetoelectric properties. In our case, we will focus on its ferromagnetic insulating character for spin-filtering perspectives.

2.1.1 CRYSTALLINE STRUCTURE: PEROVSKITE

The crystalline structure of an ABO_3 perovskite is depicted in Fig 2.1a. It consists of a cube with A ions on its vertices (often a rare earth element), a smaller B ion at the centre of the cube (usually a magnetic ion), and an octahedron of oxygens surrounding the latter. The compounds receive the name according to the magnetic ion: for example, if B=Mn, we obtain the family of "manganites" whereas if B=Co, we obtain the family of "cobaltites".

The octahedron of oxygens provides great stability to the structure, enabling substitution of the A and B positions, and also ion vacancies. For example, taking $LaMnO_3$ as parent compound, $La_{0.7}Sr_{0.3}MnO_3$ is achieved from A-site substitution (La^{3+}/Sr^{2+}). This substitution (sometimes also referred to as doping) may completely alter the properties of the compound: from the complex phase diagram of $La_{1-x}Sr_xMnO_3$ as a function of Sr doping x, see that $LaMnO_3$ compound is insulator whilst $La_{0.7}Sr_{0.3}MnO_3$ is metallic (Fig 2.2).

Substitution of the B-site of the same $LaMnO_3$ parent compound with Co gives rise to La_2CoMnO_6, also called $LaCo_{0.5}Mn_{0.5}O_3$. In that case, the B-site substitution (Mn^{4+}/Co^{2+}) takes place for half the B sites (given the ratio 1:1 for Co:Mn), so if the Co/Mn ions are ordered inside the structure, the latter becomes a "double perovskite".

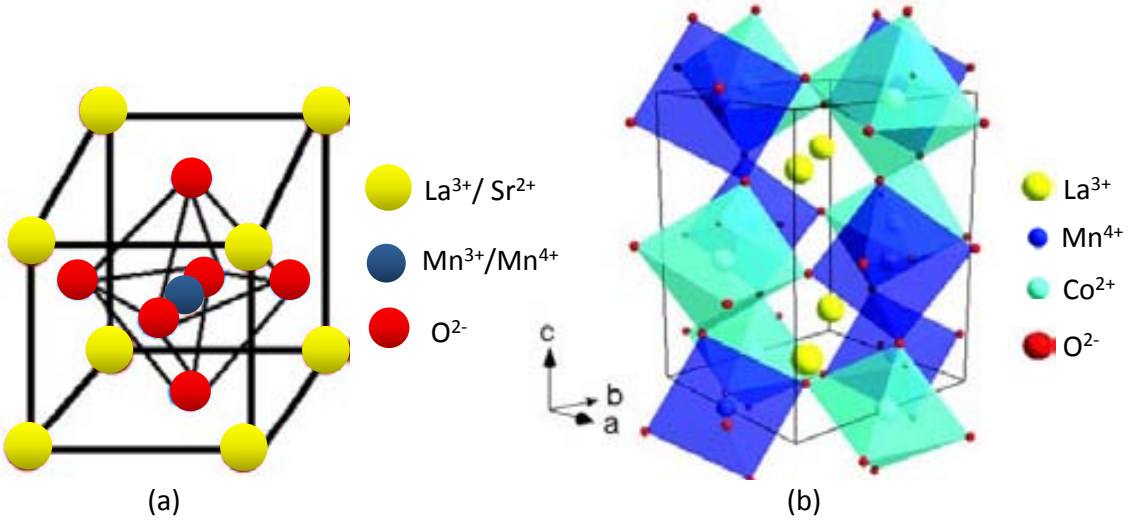

Fig 2.1. (a) Sketch of the perovskite structure applied to $(La,Sr)MnO_3$ (taken from Ref [4]) and (b) double perovskite structure for an ordered La_2CoMnO_6 sample.

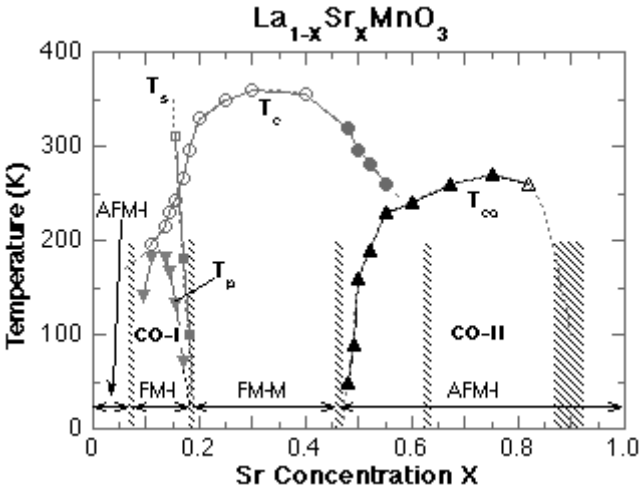

Fig 2.2. Phase diagram of $La_{1-x}Sr_xMnO_3$ as a function of Sr concentration x. In this picture, FM and AFM stand for ferromagnetic and antiferromagnetic, M and I stand for metallic and insulating and CO stands for charge order. Taken from [4].

Depending mostly on the ionic radii of the different species occupying the A and B sites, the structure tends to deviate from the ideal cubic perovskite to accommodate a certain distortion. This distortion is quantified by the tolerance factor:

$$t = \frac{(r_A + r_O)}{\sqrt{2}(r_B + r_O)} \qquad [2.1]$$

where r_i is the mean ionic radii of the ion occupying the *i*-site and r_0 is the radius of the anion. If $t = 1$, the perovkite structure is cubic and the structure is stable. However, in most cases, a distortion occurs and (i) the oxygen octahedron may distort (Jahn-Teller distortion), (ii) cation B may shift from the centre of its octahedron or (iii) the BO_6 octahedra may tilt as rigid units, along one or more symmetry axis, maintaining the regularity and the connectivity between vertices. In the case of LCMO, the octahedra distort slightly (as shown in Fig 2.1b), so that the spatial group is Pnma for disordered Co/Mn cations, and $P2_1/n$ for total Co/Mn ordering [5].

If an A ion is doped or substituted by an A' ion with different valence (i.e. oxidation state), the charge neutrality may require a non-integer valence of the B ion. In that case, different oxidation states of the B ion are present to obtain charge neutrality, leading to mixed-valence compounds. This is the case for LSMO, where Mn^{3+} and Mn^{4+} coexist.

For some mixed-valence compounds, lowering temperature can cause the ordering of the B cations with different valences, the so-called charge ordering (CO). Thought to originate from strong Coulomb interaction, this localization of the electrons in certain positions of the lattice leads to an increase of the electrical resistance [6]. Ordering of the orbitals or the spins may also take place under certain conditions, and result in anisotropic electron transfer [7].

2.1.2 ELECTRONIC STRUCTURE

Transition metals have an electronic structure with an incomplete d-shell (*l*=2). The interatomic interaction which tends to align spins parallely (Hund interatomic coupling) gives rise to two different energy bands, one for each spin orientation (spin up and spin down band), the energy difference being Δ_{ex}.

In addition, in the perovskite structure of the transition metal oxide, the degeneration of the five d-orbitals (*m*=-2,-1,0,+1,+2) is broken due to the octahedral crystal field originated from the Coulomb repulsion with the O^{2-}. Orbitals split into two groups: the e_g doublet ($3z^2$-r^2 and x^2-y^2 orbitals), and the t_{2g} triplet (zx, yz and xy orbitals). The energy difference Δ_{CF} between e_g and t_{2g} orbitals depends on the transition metal, its valence and the distance to the oxygen ions. Both the Δ_{CF} and the Δ_{ex} splitting are represented in Fig 2.3. In the case of manganites, Δ_{CF}~1.5eV and the splitting for Mn^{3+} and Mn^{4+} is Δ_{ex}~2.5eV, so that $\Delta_{ex} >> \Delta_{CF}$ and the spin down band only starts filling in if the spin up band is completely occupied.

The electronic configuration of Mn^{3+} is: $[Mn^{3+}] = [Ar]3d^4$ and that of Mn^{4+} is: $[Mn^{4+}] = [Ar]3d^3$. Three spin-up electrons fill the t_{2g} band in both cases, but in the case of Mn^{3+}, there is another spin-up electron in the e_g band. In the case of compounds with Mn^{3+} (d^4), the energy may be further lowered by distortions of the BO_6 octahedra, breaking the degeneracy of the e_g and t_{2g} as a result (as sketched in Fig 2.4). This is known as a "Jahn-Teller distortion".

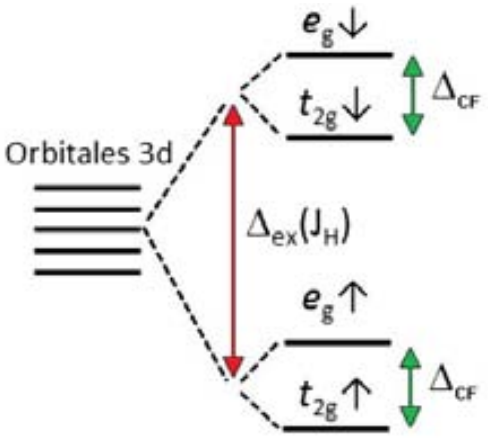

Fig 2.3. Schematic representation of the energy levels of the Mn ions: the degeneration of the d-level electrons is broken due to the interatomic interaction (Δ_{ex}) and to the crystal field gap (Δ_{CF}). Adapted from [8].

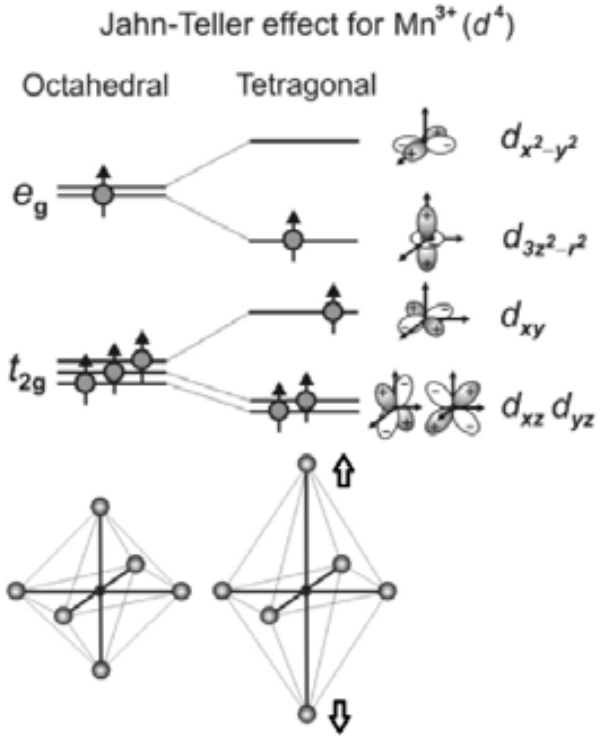

Fig 2.4. Jahn-Teller distortion present in Mn^{3+} breaks the degeneration of the e_g and the t_{2g} orbitals. Adapted from [9].

In the case of cobaltites, however, both splittings are of the same order ($\Delta_{CF} \sim \Delta_{ex}$). This originates different filling of the orbitals, giving rise to different spin states, depending on the strength of the crystal field. As an example, Fig 2.5b shows the energy levels for a Co^{2+} ion, which has 7 electrons in its d-shell (d^7). A weak crystal field ($\Delta_{CF} < J_H$) favours the filling of the spin up band before the t_{2g} electrons of the spin down band, so that the spin is S=3/2 (and we say that Co^{2+} is in the "high spin state"). However, under a strong crystal field ($\Delta_{CF} > J_H$) –as represented in Fig 2.5c- the t_{2g} orbitals for both spin

orientations have lower energy than the e_g orbitals for the spin up band, thereby giving rise to "low-spin state", with S=1/2.

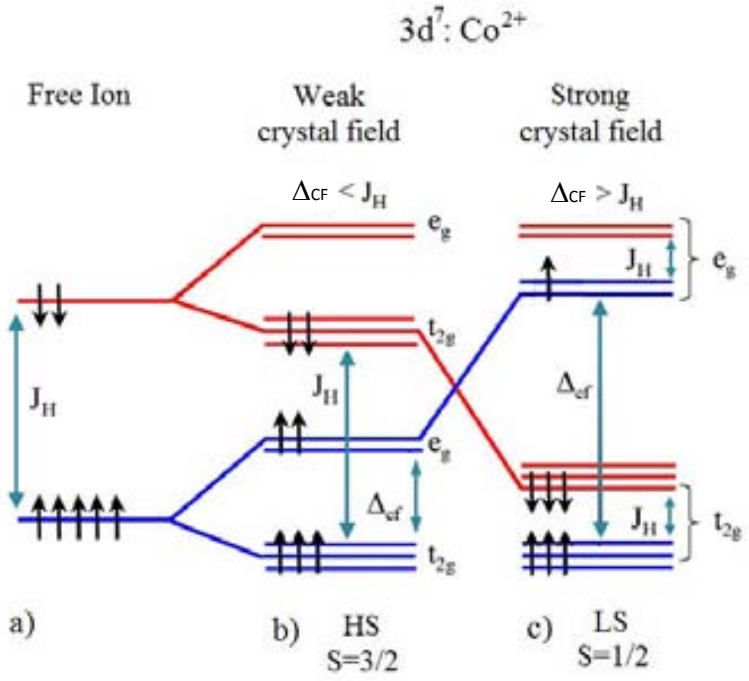

Fig 2.5. Schematic representation of the energy levels of the Co^{2+} ion. (a) represents the free ion, (b) and (c) represent the energy levels when the Co^{2+} ion is under a weak and a strong crystal field, respectively. These cases correspond to the high spin (HS) configuration and the low spin (LS) configuration. This figure has been adapted from [6].

Both cell volume and saturation magnetization are influenced by spin state. In the LCMO compound we will consider high spin, as is established in the literature [10].

2.1.3 MAGNETIC INTERACTIONS

The wavefunction of the *d*-orbitals of the transition metals in a perovskite structure do not overlap because of the relatively large distance between them. The transport is therefore mediated through the hybridization with the *p*-orbital of the oxygen in between them, in what is called "indirect exchange". The two possible magnetic interactions of this kind that are particularly important in transition-metal oxides are the superexchange (SE) and the double exchange (DE) mechanisms.

In double perovskites such as La_2CoMnO_6, ferromagnetic coupling arises from 180º-SE interaction between the two transition-metal cations. In mixed-valence manganites such as $La_{1-x}Sr_xMnO_3$, however, SE and DE mechanisms compete, favouring antiferromagnetism (AF) and ferromagnetism (FM) respectively, thus explaining the complex phase diagram of these compounds (see Fig 2.2).

2.1.3.1 SUPEREXCHANGE

The superexchange interaction is a magnetic interaction, mediated by an oxygen ion, which takes place when the electron occupancy at the *d*-shell of both metallic ions is the same or differs by 2. Electrons do not actually move between the ions, so there is no real charge transport associated to the magnetic interaction. The sign (positive for FM and negative for AF) and strength of superexchange interaction depend on the bonding angle (for ex. Co^{2+}-O^{2-}-Co^{2+}) but also on the *d*-orbitals involved in the bond. The Goodenough-Kanamori rules allow predicting the sign of the magnetic interaction [11].

In the case of 180º cation-anion-cation interaction, as for La_2CoMnO_6, three different cases are considered, depending on the last half-filled orbitals:

(i) e_g-e_g: gives strong AF interaction,

(ii) t_{2g}-t_{2g}: the resulting AF interaction is weaker than for (i),

(iii) e_g-t_{2g}: the interaction is FM and moderate.

So, La_2CoMnO_6 featuring Co^{2+} in high spin configuration (t_{2g}) and Mn^{4+} (full t_{2g} and empty e_g) gives rise to FM interaction for Co^{2+}-O- Mn^{4+}. If the Mn/Co are not fully ordered, AF interactions for Co^{2+}-O- Co^{2+} and Mn^{4+}-O- Mn^{4+} may also contribute.

In the case of single-valence manganites, such as $LaMnO_3$, the interaction is also AF.

2.1.3.2 DOUBLE EXCHANGE

To explain the relationship between the transport and magnetism in mixed-valence manganites, Zener proposed the double exchange mechanism [12]. This consists in the simultaneous transfer of the e_g electron from Mn^{3+} to the O^{2-} and another electron from the O^{2-} to the Mn^{4+} (Fig 2.6a). The itinerant electron is the e_g from the Mn^{3+}, but it can only be transferred to the Mn^{4+} through the oxygen if the t_{2g} electrons from Mn^{3+} and the Mn^{4+} are aligned ferromagnetically (see Fig 2.6b,c), due to the conservation of the magnetic moment. On the other hand, the Mn^{3+}-O^{2-}-Mn^{4+} bonding angle determines the mobility of the e_g electron, the probability of the electron transition being proportional to $\cos(\Theta/2)$, where Θ is the angle between neighbouring spins.

This DE mechanism explains the origin of the simultaneity of the metal to insulator (M-I) transition and the ferromagnetic to paramagnetic (FM-PM) transition in manganites. The only itinerant e_g electrons conduct (metal state -M) when the ions are aligned ferromagnetically. When the ions lose the FM alignment (PM), e_g electrons can no longer jump, thereby an insulating state is achieved (I).

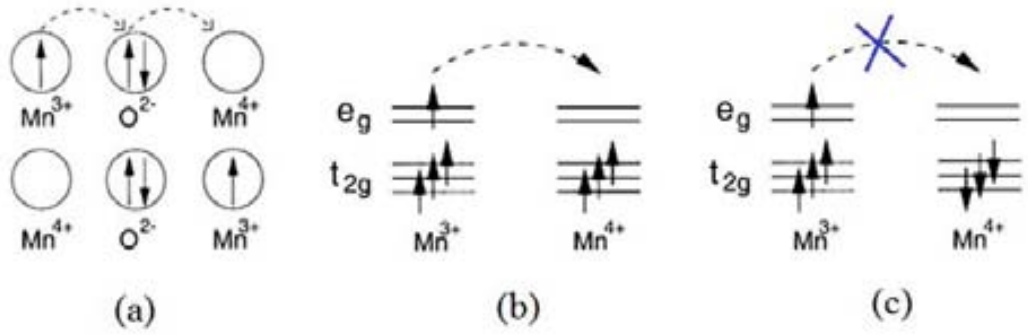

Fig 2.6. (a) Double exchange mechanism, between Mn^{3+} and Mn^{4+} ions. This mechanism is possible for ions ordered ferromagnetically (b), but not for those with antiferromagnetic interaction (c).

2.1.4 SPIN POLARIZATION AND HALF-METALLICITY

A ferromagnetic material possesses an intrinsic internal magnetic field (Weiss field) which creates an imbalance between the number of electrons of both spin orientations (see Fig 2.7, which compares a paramagnetic material (a) and a FM one (b)). The orientation which has more population is called the "majority spin", whilst the less-populated orientation is called the "minority spin". As the magnetic moment has inverted sign with respect to the spin ($m = -g\mu_B s$), the minority spins are aligned with the total magnetization. The often used terms "spin-up" and "spin-down" require a quantization direction, which we take to be that of the external magnetic field $\vec{H}$ used to align the total magnetization of the sample, $\vec{M}$. So that, in this case, spin-up and spin down correspond to minority and majority spin populations, respectively. For an external magnetic field antiparallel to $\vec{M}$, the spin up and spin down labels are reversed [9].

According to the "two-current model" proposed by Nevill Mott [13], FM metals conduct in two independent channels of conduction, one for each spin orientation. These two currents are coupled by spin mixing (which takes into account spin-flip scattering, mainly from electron-magnon scattering). At room temperature, this tends to equilibrate the spin-up and spin-down currents [14]. However, some materials present different density of states for each orientation at the Fermi level. This difference defines the "spin polarization":

$$P = \frac{\mathrm{DOS}(\mathrm{E_F})_{\mathrm{maj}} - \mathrm{DOS}(\mathrm{E_F})_{\mathrm{min}}}{\mathrm{DOS}(\mathrm{E_F})_{\mathrm{maj}} + \mathrm{DOS}(\mathrm{E_F})_{\mathrm{min}}} \qquad [2.2]$$

where $\mathrm{DOS}(E_F)_{maj}$ and $\mathrm{DOS}(E_F)_{min}$ are the density of states at the Fermi level for the majority and minority-spin population. Therefore, if there is a predominance of majority spin carriers at the Fermi level (as in Fig 2.7b), the material has positive spin polarization, as is the most common case. If, however, at the Fermi level there are more minority spin electrons (as in Fig 2.7c), the material has negative spin polarization. This is the case of Fe and Fe_3O_4, for example.

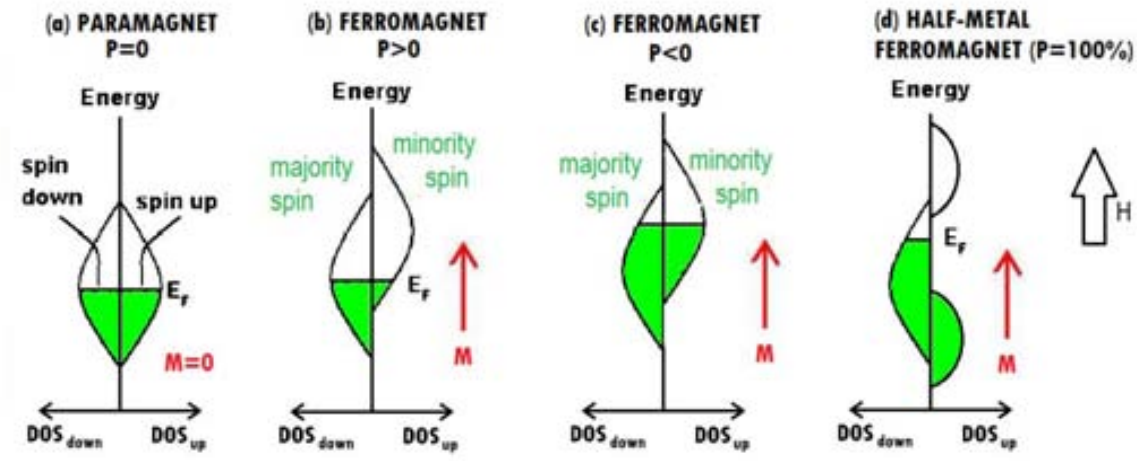

Fig 2.7. Schematic representation the spin-up and spin-down band for (a) a paramagnet; (b) a ferromagnet with positive spin polarization P, where the spin carriers are majority spins; (c) a ferromagnet with negative spin polarization P, where the carriers are minority spins; (d) a specific case of FM with P=100%, half-metal ferromagnet.

Half-metals are a particular case of spin polarized FM, where P=100%: the density of states at the Fermi level is zero for one spin direction and non-zero for the other, as sketched in Fig 2.7d. As the name suggests, this material has metallic properties for one spin orientation and an insulating gap for the other spin orientation. This is the case of the mixed-valence manganite LSMO.

2.2 MAGNETORESISTIVE PHENOMENA

We define magnetoresistance as the change in electrical resistance of a conducting material under the application of an external magnetic field (H). This section is devoted to the classification of such magnetoresistive phenomena according to their physical origin.

2.2.1 NORMAL MAGNETORESISTANCE (MR)

Conducting materials under a magnetic field experiment a change in resistance with respect to the zero magnetic field. This is called "normal magnetoresistance" and its origin lies in the Lorentz force exerted on the carriers due to the magnetic field. The normal magnetoresistance can be calculated as:

$$MR(\%) = \frac{R(H) - R(H=0)}{R(H=0)} \times 100 \qquad [2.3]$$

Where R(H) is the resistance at a certain applied magnetic field and R(H=0) is the zero-magnetic field resistance. In this case, the MR is limited to 100%. However, to appreciate changes when the MR is close to 100%, the expression used is:

$$MR(\%) = \frac{R(H) - R(H=0)}{R(H)} \times 100 \qquad [2.4]$$

2.2.2 ANISOTROPIC MAGNETORESISTANCE (AMR)

The change of resistance obtained in a magnetic material by changing the direction of an external magnetic field (H) with respect to the direction of the current ($\vec{j}$) is called the anisotropic magnetoresistance (AMR), which is calculated by the following relationship:

$$AMR(\%) = \frac{\rho_{xx} - \rho_{xy}}{\frac{1}{3}\rho_{xx} - \frac{2}{3}\rho_{xy}} \times 100 \qquad [2.5]$$

Where ρ_{xx} and ρ_{xy} are the resistivities when the current flows parallel and perpendicular to the magnetization of the material, respectively.

The origin of AMR lies in the spin-orbit coupling [14]. The total angular momentum $\vec{J}$ in a magnetic material is a sum of the orbital ($\vec{L}$) and the spin ($\vec{S}$) momenta: $\vec{J} = \vec{L} + \vec{S}$. The application of an external magnetic field causes the alignment of the magnetization ($\vec{M}$), and the total angular momentum ($\vec{J}$) along the same direction. Due to the spin-orbit coupling, if $\vec{J}$ changes orientation, so does $\vec{L}$; this means that the electrons' orbit around the nucleus is modified. This causes the electrons from the current to feel a different electrostatic repulsion, and therefore, the resistivity will change.

Although the AMR effect is around 1-2%, this property is used in magnetic field sensors.

2.2.3 GIANT MAGNETORESISTANCE (GMR)

The GMR received this name because of the large effect observed in multilayers which alternate ferromagnetic with non-magnetic materials. In this kind of systems, the in-plane measured resistance is high for H=0 and decreases sharply for increasing field (as can be seen in Fig 2.8a).

In this case, the magnetoresistance is not due to the interaction between the conduction electrons and magnetic field, but to their interaction with the FM layers via spin-dependent scattering. The coherence length for spin is of a few tens of nanometers, larger than the thickness of the multilayers. It can be assumed, therefore, that the conduction takes place in two separate conduction channels, one for each spin orientation. Scattering of electrons depends on the orientation of their spin with respect to the magnetization of the layer. At H=0, the magnetizations of the FM layers tend to be rotated 180º from each other (because the interaction between layers is antiferromagnetic), and scattering is important. At increasing field, however, the magnetization of the different layers align so that they are parallel to each other, and the scattering is reduced [8,15]. This can be understood in terms of a simple model of resistances, as sketched in Fig 2.8b.

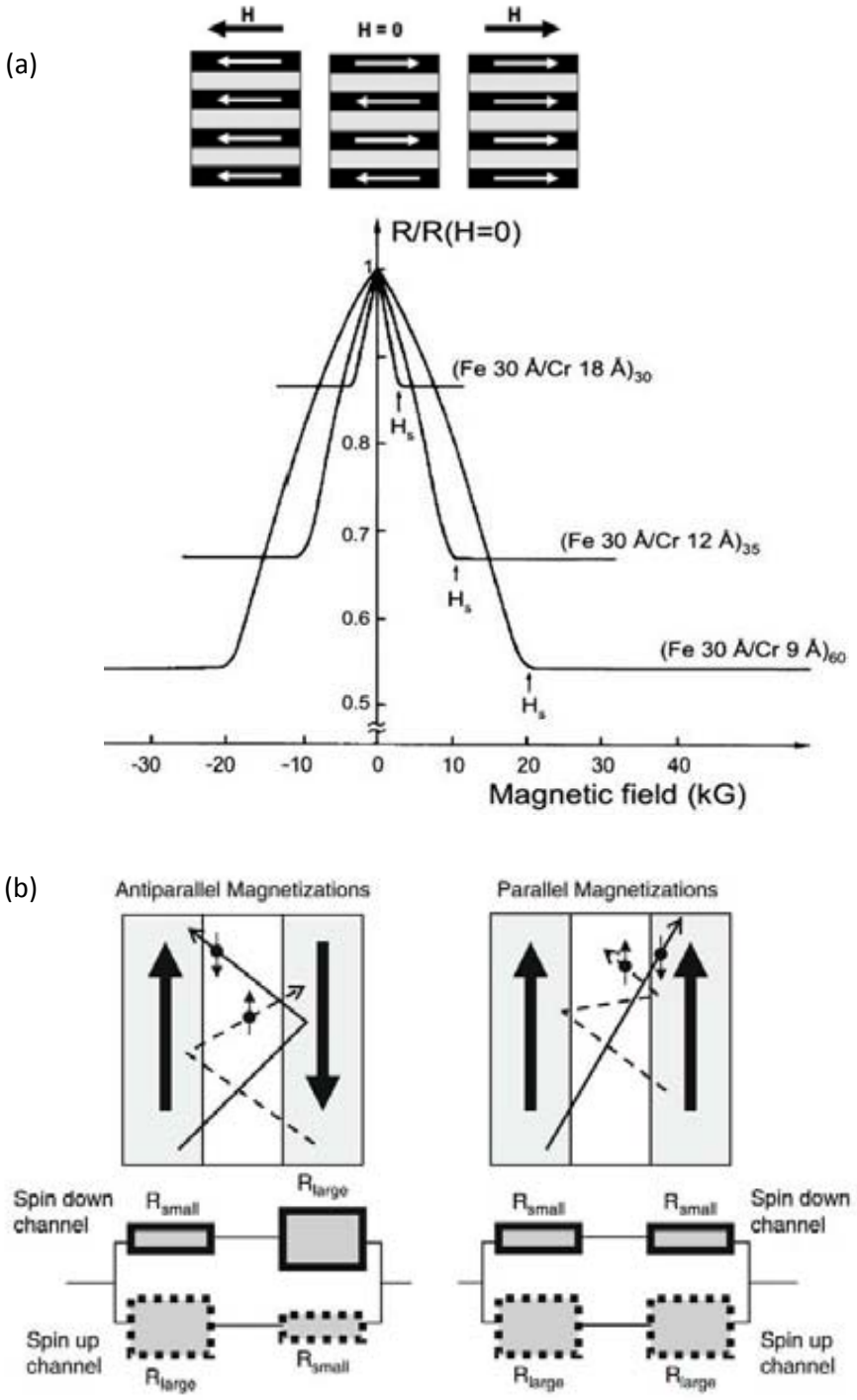

Fig 2.8. (a) Giant magnetoresistance observed in multilayers. Magnetic field controls parallel or antiparallel magnetization of the FM layers, and spin-dependent scattering modifies resistance; (b) Two channel model for GMR. Figures taken from [16].

Although this phenomena has also been observed in granular systems [17], the GMR discovery was possible because of the technological advances, which enabled the growth of thin enough films to obtain AF coupling. This is a clear example of the

importance of the growth and fabrication process for the unveiling of physical phenomena.

2.2.4 COLOSSAL MAGNETORESISTANCE (CMR)

The close relationship between transport and magnetism in systems such as mixed-valence manganites (fruit of the double exchange mechanism) leads to the phenomenon known as colossal magnetoresistance (CMR). The existence of a metal to insulating transition and the fact that the temperature at which it takes place can be modulated by H causes large variations of resistance under an applied field around this temperature [7]. An example of resistance *vs.* temperature curves at different magnetic fields for an 47 nm LSMO sample is plotted in Fig 2.9, were the magnitude of this effect reaches 60% for H=90 kOe. However, as high magnetic fields are required, CMR is not of easy use in technological applications.

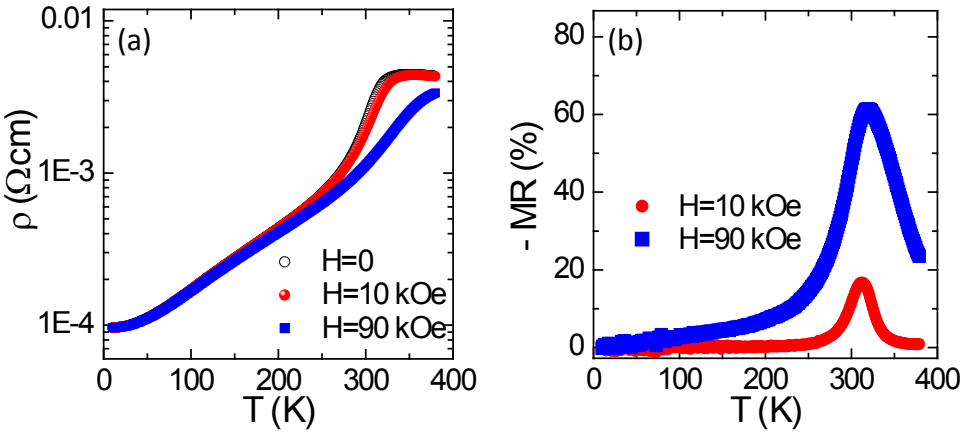

Fig 2.9. (a) Resistivity vs temperature curves for a 47 nm-LSMO sample at different applied magnetic fields (H=0, 10 and 90 kOe) and (b) its corresponding calculated CMR.

2.2.5 TUNNELLING MAGNETORESISTANCE (TMR)

Tunnelling magnetoresistance occurs in trilayer systems made of two ferromagnetic electrodes separated by a thin insulating barrier, a structure which will be hereby called "magnetic tunnel junction" (MTJ). Electrons tunnel through the insulating barrier, and the resistance of the whole device depends on the relative direction of the magnetization of both electrodes (parallel or antiparallel). The physical origin of this effect is complex but relies on the fact that during the tunnelling process, electrons keep their spin orientation and the probability of tunnelling from one electrode to the next depends on the number of states with the same spin direction available in the second electrode (so, it is related to the spin polarization of the electrodes, although the "tunnelling spin polarization" must also take into account other factors).

The order of magnitude of the TMR has reached ~500% at room temperature (RT), and ~1000% at 5 K, for an MTJ with MgO barrier and $(Co_{25}Fe_{75})_{80}B_{20}$ electrodes [18]. A more detailed explanation of the dependencies of the TMR is found in section 2.4, but

both understanding the tunnelling process and achieving good quality of the interfaces is required. Therefore, in the following sections, we explain the tunnelling process and some concepts on thin film growth.

2.2.6 TUNNELLING ANISOTROPIC MAGNETORESISTANCE (TAMR)

Tunnelling anisotropic magnetoresistance (TAMR) is found for systems with a ferromagnetic electrode with large spin-orbit coupling in contact with a tunnel barrier. It reflects the dependence of the tunnelling density of states of the FM layer on the orientation of the magnetization with respect to the current direction or the crystallographic axes [19]. This anisotropic effect may show a richer response than conventional AMR, with the magnitude and sign of the MR dependent on the magnetic field orientation and electric fields. Its main advantage lies on its versatility, as it does not require two decoupled FM electrodes and spin-coherent tunnelling [20]. For a system with a single ferromagnetic electrode, we define TAMR as the following:

$$TAMR(\%) = \frac{R(\phi) - R(\phi = 0)}{R(\phi = 0)} \times 100 \qquad [2.6]$$

Where ϕ is the angle between the magnetization and the current direction. This anisotropy can be probed in-plane or out-of-plane. The latter case is sketched in Fig 2.10.

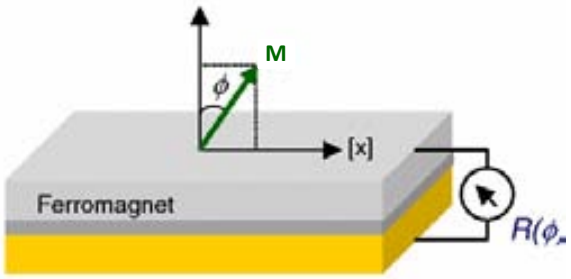

Fig 2.10. TAMR out-of-plane measurement configuration for junctions in which only one electrode is ferromagnetic. Adapted from [21].

Systems with two ferromagnetic electrodes may also show TAMR, in which case the relative orientation of both FM layers, θ, must also be taken into account, leading to the following expression:

$$TAMR(\%) = \frac{R(\theta,\phi) - R(\theta,\phi = 0)}{R(\theta,\phi = 0)} \times 100 \qquad [2.7]$$

2.3 TUNNELLING PHENOMENON

Electron tunnelling is a quantum mechanical effect –although it can be regarded as a wave phenomenon- which explains how electric current can flow through a very thin insulating layer. When a certain bias voltage (V) is applied across a metal-insulator-

metal stack, the Fermi level of one of the electrodes shifts by eV with respect to that of the other electrode. The insulating region may be considered as a potential barrier, and electrons have a finite probability of crossing it. This probability has an exponential dependence on the thickness of the insulating layer ("tunnel barrier thickness", *d*)

$$P \propto \exp(-\kappa d) \qquad [2.8]$$

where the decay constant, κ, depends on the difference between the electron's energy and the energy of the potential barrier ("barrier height", Φ) [22]. This probability also takes into account the density of states at a certain energy for both electrodes; in short, the amount of electrons available for tunnelling in electrode 1 and the amount of unoccupied positions at the electrode 2, so that the tunnelling electrons can fill the available positions.

However, this is the simplified picture (illustrated in Fig 2.18a). In fact, the short electron wavelength at the Fermi energy in a typical metal renders the tunnelling process extremely sensitive to the atomic-scale details of the metal-insulator interface. Also, the decay constant in the insulating region is dictated by evanescent states from the metal electrode, so the really complex electronic structure of the insulator and its coupling to the metal electrodes must be taken into account [22].

The current *vs*. voltage curves, I(V), for the tunnelling process are non-linear. And their asymmetry depends on the difference between the workfunctions of both electrode materials. If both electrodes are made of the same material, symmetric I-V curves are expected and we can extract the thickness and height of the barrier by fitting Simmons' equation [23] to the J(V). For asymmetric I(V) curves, Brinkman's equation [24] also provides an extra "asymmetry term" in order to correctly characterize the barrier.

Depending on the quality of the barrier and the energy provided to the electrons, the conduction through the insulating layer may take place in different modes. Some of them, sketched in Fig 2.11, include:

(a) **Direct tunnelling**: electrons tunnel through the whole thickness of the barrier (*d*), maintaining their energy from the Fermi Energy of the first electrode.

(b) **Tunnelling in the Fowler-Nordheim regime**: a considerably large voltage applied to the junction induces the barrier to become almost triangular, so that the "effective" barrier thickness for tunnelling electrons is reduced for one or both spin orientations.

(c) Defect assisted-tunnelling: if the barrier has defect states (or traps), the electrons may hop from one defect state to another until they reach the other electrode. The presence of traps splits the barrier into multiple thinner tunnel barriers, thus increasing the tunnelling probability (from equation 2.8) [25].

(d) **Thermionic emission**: if the electrons' thermal energy overcomes the binding potential (or work function) of the electrode, the electrons flow over the potential energy barrier instead of tunnelling.

Even if there is no clear experimental frontier between these transport mechanisms, voltage and temperature dependencies of the electronic current may allow their identification [26]. For example, as thermionic emission is an activated process, strong temperature dependence is expected, contrary to direct tunnelling. In the case of Fowler Nordheim regime, the decrease in the effective thickness leads to large increase of the tunnel probability when increasing voltage.

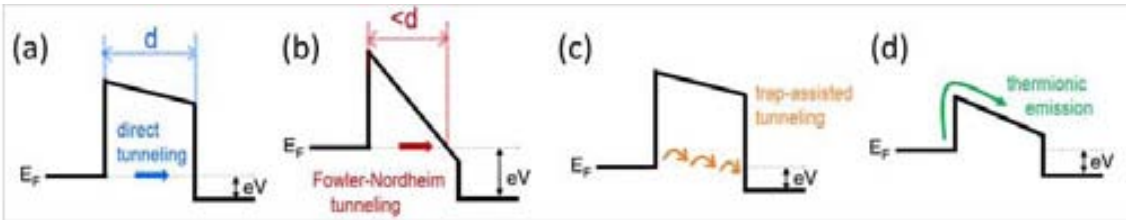

Fig 2.11. Sketch of four possible conduction mechanisms through insulating barriers: direct tunnelling (a), Fowler-Nordheim tunnelling (b), trap-assisted tunnelling (c) and thermionic emission (d). Adapted from [26].

2.4 MAGNETIC TUNNEL JUNCTIONS

A magnetic tunnel junction is a heterostructure made of two ferromagnetic electrodes separated by a thin insulating barrier (of a few nm or less). When biasing the junction, current can tunnel across the barrier and the resistance has two defined states depending on the relative orientation of the magnetization of both electrodes (parallel or antiparallel). To quantify the change in resistance, we define the *tunnelling magnetoresistance* (TMR) as:

$$\mathrm{TMR}(\%) = \frac{R_{AP} - R_P}{R_P} \times 100 \qquad [2.9]$$

Being R_{AP} the resistance of the antiparallel state and R_P that of the parallel state.

As we can see from equation 2.9, positive TMR implies that the antiparallel (AP) state presents higher resistance than the parallel (P) state, whilst when it presents lower resistance, the TMR is negative.

To probe the P and AP configurations of the magnetization of the electrodes (which give the two states of different resistance), both electrodes must be able to switch independently when sweeping an applied external magnetic field. Two possible configurations are shown in Fig 2.12: (a) the two electrodes must be decoupled and possess different coercive fields or (b) one of the electrodes must be pinned through the exchange bias effect by an adjacent AF layer, whilst the other must be free to switch with the external magnetic field. The main advantage of the first mentioned configuration resides in the smaller amount of layers that must be grown in the

magnetic tunnel junction stack, but in the second mentioned configuration we achieve greater magnetic stability and the transition from one resistive state to the other is closer to zero magnetic field.

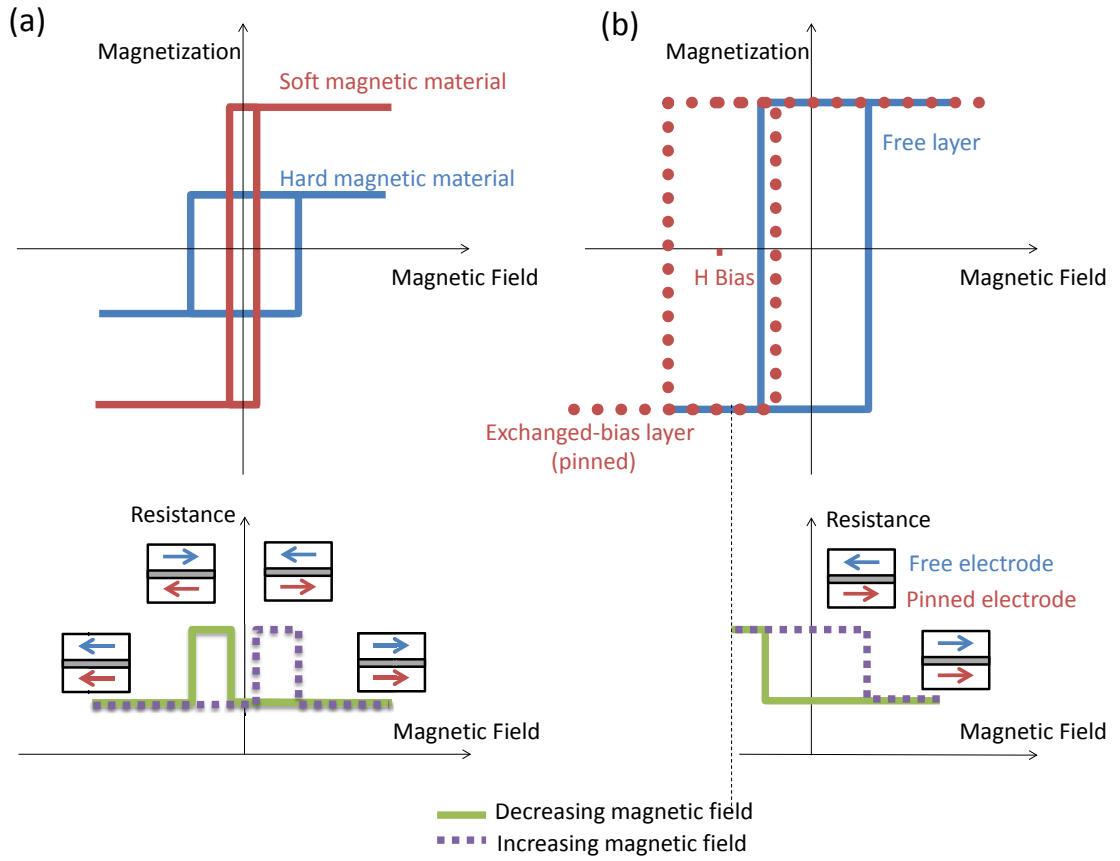

Fig 2.12. Sketch of the hysteresis loops with their corresponding R(H) graphs for two different MTJ configurations; (a) relies on the different coercive fields of the two magnetic electrodes and (b) possesses a pinned electrode (from exchange bias effect).

2.4.1 Electrodes dependence

The origin of the tunnelling magnetoresistance effect lies in the different probability of an electron to tunnel through the barrier depending on its Fermi wave-vector. A ferromagnetic material has exchange-split electronic bands, therefore different wave-vector for spin up and for spin down electrons. In this way, the tunnelling probability depends on the spin. Jullière proposed a simple model to relate the TMR with the spin polarizations of the ferromagnetic electrodes [27]. His model takes into account the density of states for each spin orientation for both electrodes (via their spin polarization):

$$TMR = \frac{2P_1P_2}{1-P_1P_2} \qquad [2.10]$$

As spins tunnel from one electrode to the other maintaining their spin orientation (spin up or spin down), if the majority spin direction coincides for both electrodes, there is an

optimum match of filled majority spin states in one electrode with empty majority spin states in the other electrode. Thus, the resulting resistance is low (thick red arrow at Fig 2.13a represents high conductivity). But if the majority electrons of the first electrode tunnel towards the minority spin band in the second electrode (or inversely, the minority spin electrons tunnel towards the majority spin band), the resistance is high (for both channels, the conductivity is low, as represented by red and blue thin arrows at Fig 2.13b).

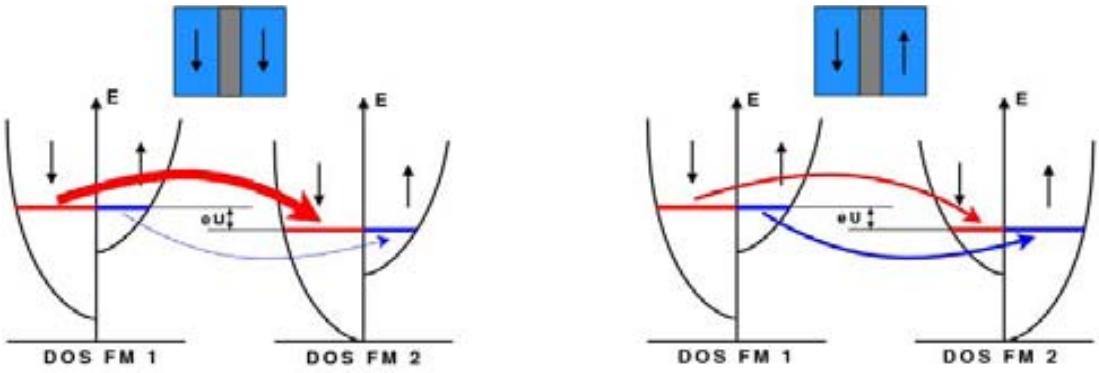

(a) High conductivity (low R) (b) Low conductivity (high R)

Fig 2.13. Schematic illustration of the origin of TMR, according to Jullière's model. The density of states (DOS) at the Fermi energy for both electrodes determines the probability of the tunnelling process, in which spin orientation is conserved. (a) and (b) represent the low and high resistance states, respectively.

This picture is a simplified view of the magnetic tunnelling process. Stearns [28] specified that only the density of states of itinerant electrons should be taken into account. Subsequent studies, however, revealed that the tunnelling spin polarization also depends on the structural quality of the magnetic tunnel junction, on the choice of tunnelling barrier and on the electronic structure of the interfaces [29]. Thus, the complexity of this phenomenon requires that we specify that the spin polarization of the electrodes is not directly the tunnelling spin polarization.

In what follows, we briefly comment on the TMR dependences on voltage, temperature and barrier. A more complete review of these (and other) dependencies can be found elsewhere [30–32].

2.4.1.1 Use of half-metallic Electrode: LSMO-based MTJ

As already mentioned in section 2.1.4, LSMO is a half-metal with total spin polarization. Spin-polarized photoemission spectroscopy experiments have confirmed the half-metallic character of LSMO [33], and tunnelling experiments have shown magnetoresistance ratios above 1800 % at 4 K for LSMO/STO/LSMO junctions, suggesting a spin polarization of at least 95 % [34]. From these findings, LSMO shows potential as a spin analyser or as fully spin polarized current source in epitaxial oxide heterostructures, and MTJ based on manganites are expected to give very high TMR (from equation 2.10).

Besides the potential for high TMR responses, the use of LSMO as electrode is also interesting from the fundamental point of view. Combining the use of an LSMO and some other FM, for instance, the tunnelling measurements provide some insight on the electronic properties of that FM [35].

Despite the reported high TMR for LSMO-based MTJ, unfortunately the high spin polarization at low temperatures vanishes below RT, much below the T_C of bulk LSMO (360 K). This effect is attributed to either spin flips caused by defects in the tunnel barrier or to degraded magnetic properties at the manganite/barrier interfaces (such as oxygen deficiency, phase separation, …)[35]. In fact, the spin polarization, derived from the TMR of LSMO/I/LSMO with I=LAO, STO,TiO_2, reproduces the same shape as the magnetization of bulk LSMO – following the Bloch $T^{3/2}$ law- but with a lower critical temperature (around 60 K below). This decay is much smoother at interfaces than at surfaces [36], underlining the importance of the continuity of the oxygen ions at the interfaces in the determination of the magnetic properties.

2.4.2 VOLTAGE DEPENDENCE

The voltage dependence of TMR can be probed either directly (from the resistance *vs.* magnetic field measurements taken at different applied voltages) or indirectly (from the difference between two current *vs.* voltage curves taken in the two states of parallel and antiparallel magnetization of the electrodes). In most magnetic tunnel junctions, TMR strongly decreases monotonically with increasing bias voltage. The figure of merit to quantify this effect is the voltage at which the TMR has decreased by half with respect to the maximum obtained value. Different experimental results point towards various possible origins for this TMR decrease with voltage, which include the following [30,32]:

(a) Higher voltage enhances inelastic scattering by magnon excitations. This means that electrons tunnelling through the barrier arrive as "hot electrons" at the second electrode, with higher energy than that of the Fermi Energy of the second electrode. They lose this excess energy emitting a magnon, flipping the electron spin. This loss of polarization leads to a decrease in the TMR.

(b) the presence of localized trap states in the amorphous barrier, so that impurity-assisted tunnelling takes place.

The spin-dependent electronic structure of the ferromagnets changes as a function of the energy. As different applied biases give rise to different energies, the voltage dependence may also reflect the variation of the density of states (DOS) with energy. Therefore, we represent conductance as G(DOS(E(V))) [24]. As an example, in Fig 2.14 (a,b) we represent the density of states (DOS) of LSMO –derived from photoemission- and from Co(100) surface –calculated- for each spin orientation, respectively. The change of sign of the TMR of a Co/STO/LSMO MTJ, which can be seen in Fig 2.14, is related to the spin polarization of the Co/STO interface.

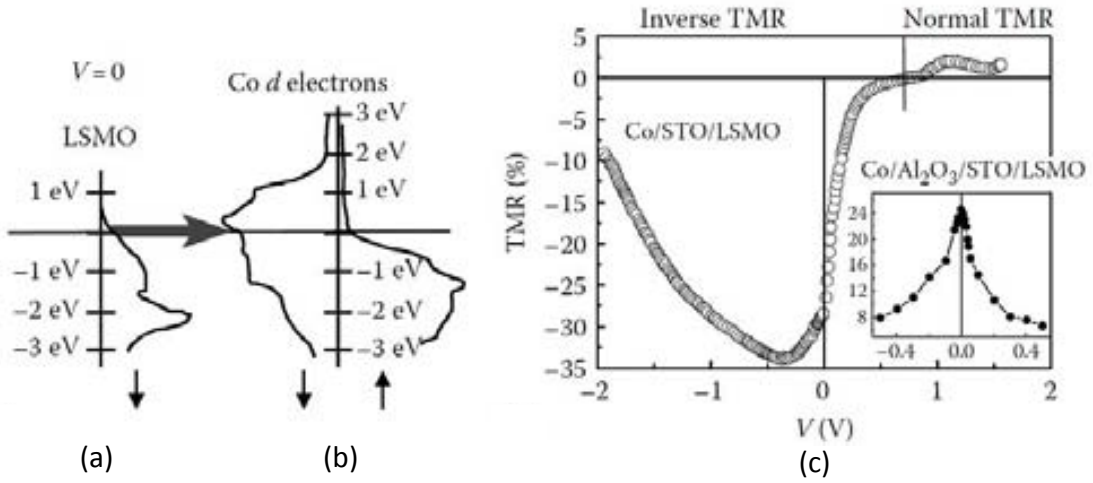

Fig 2.14. (a), (b) Schematic illustration of the spin-polarized densities of states of LSMO and Co(100) surface, respectively. (c) TMR *vs.* V for a Co/STO/LSMO junction at T=5 K, which shows that the change of sign of the TMR is related to the negative spin polarization of Co/STO. Inset shows bias dependence for a $Co/Al_2O_3/STO/LSMO$ junction [taken from [22]].

2.4.3 TEMPERATURE DEPENDENCE:

A drop of the TMR with increasing temperature –besides the contribution from the ferromagnet's loss of polarization with temperature, which is relevant close to T_C- can be attributed to various factors [30]:

(a) Spin-wave excitations (magnons), which are responsible for the decrease in the tunnelling spin polarization and in the surface magnetization with increasing temperature. As TMR is proportional to the tunnelling spin polarizations, TMR drops with temperature.

(b) Magnetic impurities in the barrier cause spin-flip scattering and the number of electrons involved in this process increases with temperature. Even inelastic scattering events which do not flip the spin are detrimental to the TMR.

2.4.4 BARRIER DEPENDENCE

The barrier material, quality and thickness are also critical parameters for the optimization of the performance of a device.

We define as completely *incoherent tunnelling* the process by which Bloch states possessing different symmetries tunnel with the same probability (as illustrated in Fig 2.15a). In contrast, for *completely coherent* tunnelling, the tunnelling probability depends on the symmetry of each Bloch state. In this case, only highly spin-polarized states tunnel through the barrier conserving the phase coherence (so, considering no scattering processes) and this gives rise to high TMR (represented in Fig 2.15b). Even if realistic tunnelling is neither completely coherent nor completely incoherent, amorphous barriers tend to incoherent tunnelling and crystalline barriers tend to

coherent tunnelling, revealing that the crystalline quality of the barrier is of great importance.

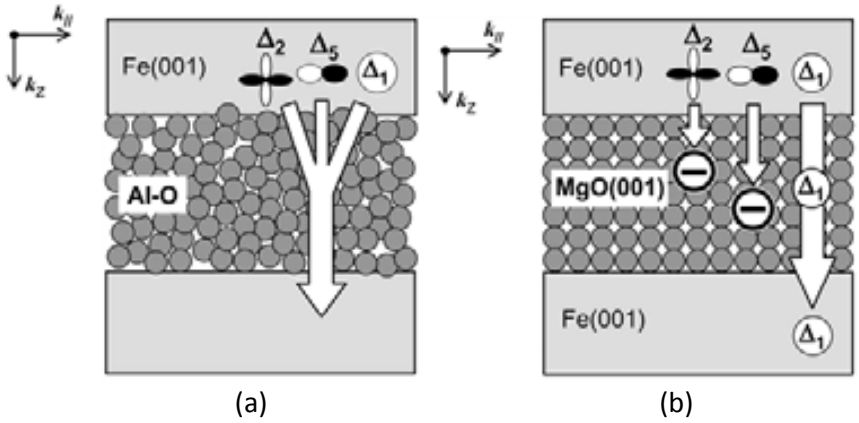

Fig 2.15. Schematic illustration of (a) incoherent tunnelling through an Al-O amorphous barrier and (b) coherent tunnelling through a MgO crystalline barrier. Taken from [37].

The barrier material must also be chosen carefully: as already mentioned, the electronic structure of the interfaces does not solely depend on the ferromagnetic electrodes, but may give different results for the same electrodes and different insulating barrier material. This was probed for Co and LSMO electrodes, finding different TMR signs for different barriers: negative TMR for $SrTiO_3$ and $Ce_{0.69}La_{0.31}O_{1.845}$, and positive TMR for Al_2O_3 and $Al_2O_3/SrTiO_3$ [29]. Therefore, even if Jullière's model explained positive or negative TMR based on the spin polarization sign of the ferromagnetic electrodes, the real "tunnelling spin polarization" depends on the materials on both sides of the interface FM/I (see section 2.5.3 in which this particular example of interfacial dependence is explained). If the barrier material is magnetic or ferroelectric, it receives the name of "active" barrier, as its role in the device behaviour is even more complex. A brief explanation and examples of active barriers can be found in section 2.5.

Thin barrier thicknesses (a few nm) are sought in order to lower the junction resistance, and therefore also the resistance × area product ($R \times A$). However, in the case of symmetry filtering effects (explained in section 2.5.1), very thin barriers may not ensure fast enough decay of other symmetries [38]. Thin barriers also represent a greater technological challenge, and they require better quality of the thin layer, to avoid pinholes or inhomogeneities in the barrier due to surface roughness. The effect of pinholes and also their influence on some possible magnetic coupling is explained in the following section.

2.4.4.1 PINHOLES AND CRITERIA FOR DIRECT TUNNELLING CONFIRMATION

Pinholes are paths between the electrodes, across the insulating barrier, where the conductance is quite high. These metallic short-circuits may come from insufficient oxidation of oxidized barriers or, for very thin barriers, from incomplete coverage of the bottom metallic electrode. Pinholes cause the decrease of TMR in two ways. First, they favour magnetic coupling between the electrodes where the electrodes are in direct

contact with each other. Also, the transport of electrons is no longer by tunnelling as most of the current runs through the normal metallic contact created by the pinhole [39].

As pinholes are very small, direct visualization is hard. However, indirect methods have been reported. According to Rowell, the fulfilment of three criteria would confirm the absence of pinholes [24]: (i) the resistance should depend exponentially on the barrier thickness, (ii) I-V curves should be parabolic and (iii) the temperature dependence of the conductance, G(T), should display a weak insulator-like temperature dependence. In the case of FM/I/FM heterostructures experimental evidences demonstrate that the fulfilment of criteria (i) and (ii) are not sufficient to rule out the presence of pinholes: Oliver *et al.* [40] report that only the study of dielectric breakdown may discriminate between the presence or absence of pinholes (the drawback of this method is its destructive nature). Akerman *et al.* [41] consider that only the third criteria is reliable, and show artificial temperature dependences of both the resistance and the apparent fitted barrier parameters for intentionally shorted tunnel barriers.

2.5 ACTIVE BARRIERS

The selection of certain tunnel barrier materials may improve the device performance or even extend the functionality of the MTJ. Besides their insulating character, tunnel barrier materials may play an active role in the tunnelling process, such as, for instance, spin filtering according to orbital symmetry or multiferroicity to modify barrier height by applying different stimuli. Using a ferroelectric barrier combined with ferromagnetic electrodes, in a so-called "multiferroic tunnel junction", we achieve a 4-state resistance device, whose transport properties depend on the magnetization orientations of the electrodes (just as in regular MTJ) but also on the ferroelectric polarization of the barrier. Another way of achieving a multiferroic tunnel junction is by using a ferromagnetic and ferroelectric barrier in combination with a ferromagnetic electrode [42].

In this section, we will focus on the spin-filtering effect resulting from the use of the Fe/MgO combination, on the use of ferromagnetic tunnel barriers (spin-filter junctions) and on interfacial oxidation which may result in spin-filtering.

2.5.1 MGO/FE SPIN FILTERING

As predicted by Butler and Mathon [43–45], Fe/MgO system may act as a spin filter due to the symmetry filtering in the MgO barrier, combined with the choice of FM which selects one spin for a certain symmetry.

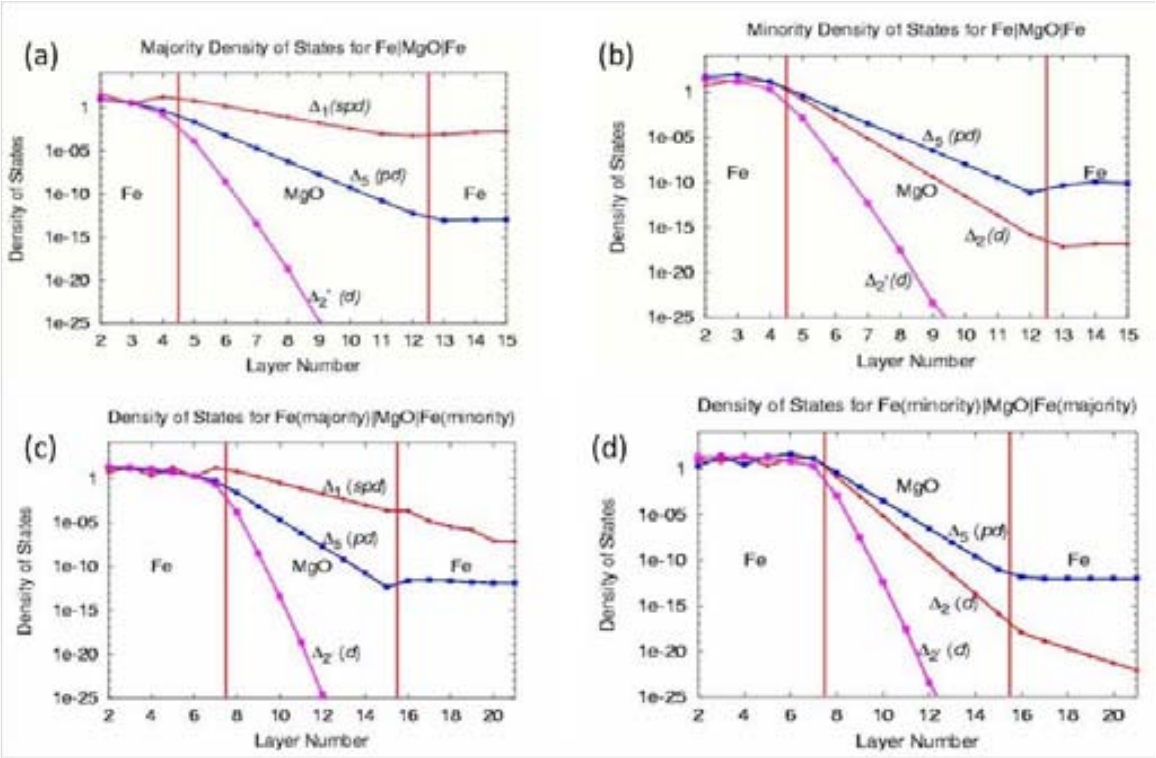

Fig 2.16. Schematic for the transmission of Bloch functions of different symmetries across the Fe/MgO/Fe system. Parallel configuration of electrodes is depicted in (a) and (b), for majority-majority and minority-minority channels respectively. Antiparallel configuration of electrodes is depicted in (c) and (d), for majority-minority and minority-majority channels, respectively. Image taken from [45].

When tunnelling through MgO, wavefunctions of different symmetries decay at different rates. In other words, wavefunctions of certain symmetries are transmitted preferentially (see Fig 2.16: Δ_1 is the preferentially transmitted because of the lower decay rate).

The FM electrodes are chosen to fulfill three requirements:

(i) The wavefunction of the preferred symmetry is only present at one of the spin orientations and not the other.
(ii) The FM possesses the same 2-D symmetry parallel to the interface as MgO (the correspondence between the different orbital symmetries and the 2-D Block state symmetries compatible with a square lattice are shown in Fig 2.17b).
(iii) The growth must be epitaxial.

In the case of Fe, we plotits band diagram for different symmetries and spin orientations in Fig 2.17a: Δ_1 majority spins are present at the Fermi Energy, but not Δ_1 minority spins. If a certain symmetry is not present in the receiving electrode, the wavefunction continues its decay even in the electrode region. This is the case for Δ_1 for Fig 2.16c or for Δ_2 in Fig 2.16d.

By combining this simple symmetry-filtering barrier with such FM electrodes (Fe, Co, FeCo are some examples), we obtain spin filtering properties [45]. Even if this spin-

filtering is enhanced for thicker insulating barriers, the resistance of the current increases exponentially.

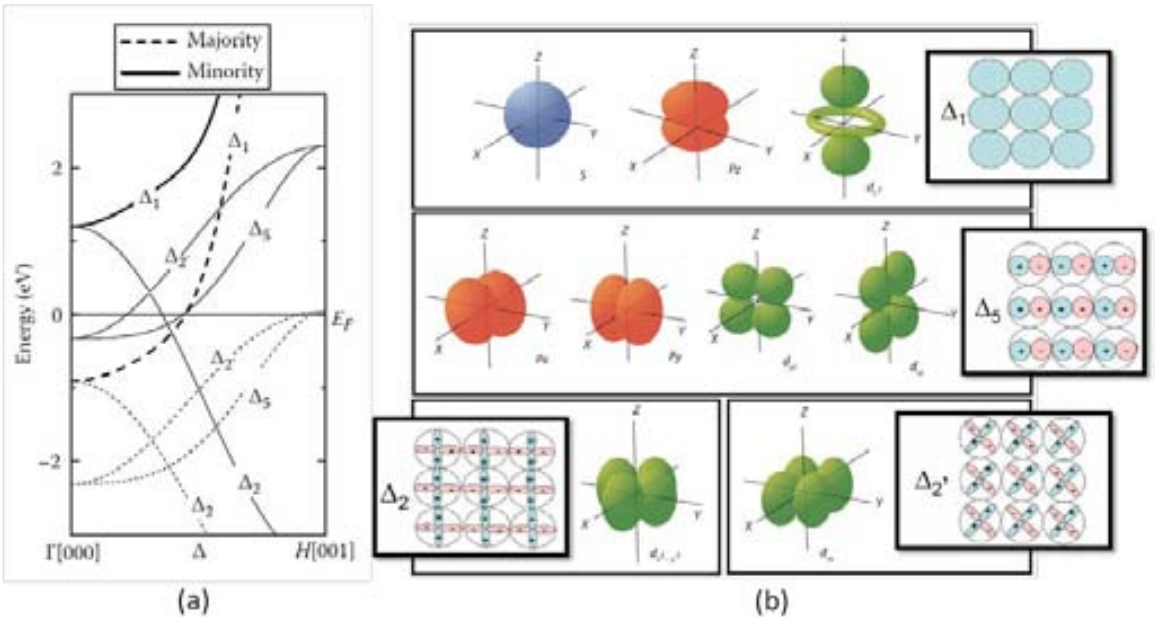

Fig 2.17. (a) Band diagram of Fe in the (001) direction, for majority (solid lines) and minority (dashed lines) spin bands. The different symmetries (Δ_1, Δ_2, $\Delta_{2'}$ and Δ_5) are taken into account. From [46], (b) Correspondence between the different orbital symmetries and the 2-D Bloch state symmetries compatible with square lattice in the x-y plane. Mix from [45] and [47].

The symmetry filtering effect for Fe/MgO combination has been confirmed experimentally, and very high TMR values have been achieved for Fe/MgO/Fe MTJ. Strong effort was devoted to preventing the oxidation of the Fe layer at the Fe/MgO interface, which was predicted to result in an exponential decrease of the TMR [48], although it was later demonstrated experimentally to be less detrimental than expected [49]. In late 2004, TMR of 180% at RT was found both for MBE-grown Fe-MgO-Fe [50] and sputtered CoFe-MgO-CoFe [51] electrodes. In late 2007, 500 % TMR was achieved at RT (1010 % at low T) for $(Co_{25}Fe_{75})_{80}B_{20}$ electrodes [18].

2.5.2 FERROMAGNETIC BARRIERS (SPIN-FILTER JUNCTIONS)

Aiming at high TMR, an alternative to magnetic tunnel junctions (FM/I/FM stack) is to use a FM electrode and a spin-selective tunnel barrier. Such barriers are made from insulating magnetic materials, therefore sensitive to spin orientation: below their ordering temperature (T_C for FM), the exchange splitting of the conduction band ($2\Delta E_{ex}$) gives rise to different barrier heights for spin down and spin up electrons ($\Phi_\uparrow$ and $\Phi_\downarrow$). Since tunnelling depends exponentially on barrier height through the decay constant κ (see equation 2.8), the probability of tunnelling for one spin orientation (the one with lower barrier height) is greatly increased with respect to the other spin orientation, thus yielding a highly spin-polarized current. This effect is called "spin filtering" and is illustrated in Fig 2.18b for two non-magnetic metallic electrodes. Combining such a barrier with another FM electrode may yield high TMR [52].

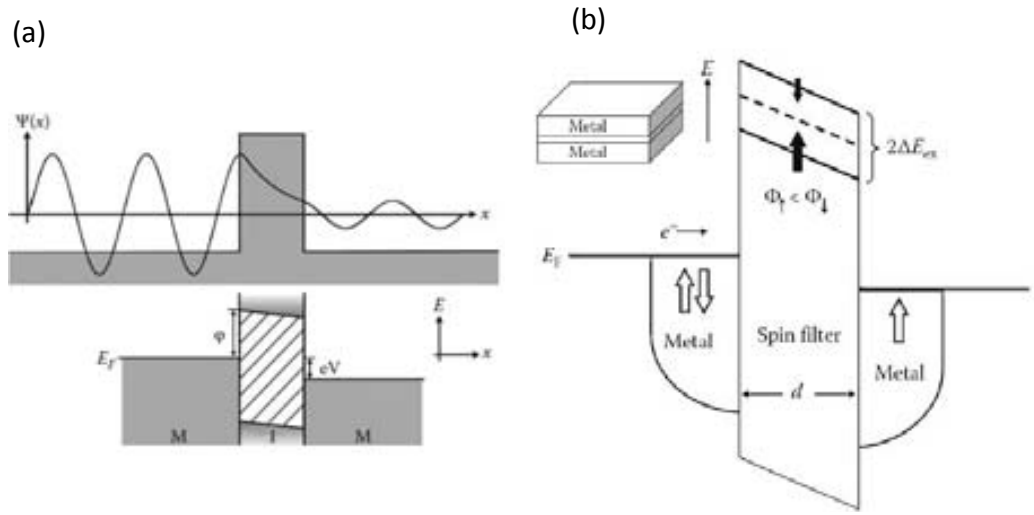

Fig 2.18. Sketch of tunnelling process in a metal-insulator-metal, for non-magnetic electrodes. In (a) the insulating barrier is non-magnetic, whilst in (b) the insulating barrier is FM and therefore it acts as spin filter and electrons with opposite spin orientations see different barrier heights, resulting in spin-polarized current. Figs taken from [22] and [52], respectively.

EuSe, EuS and EuO were tested as spin-filter materials, but although an interesting behaviour was observed (field-dependent spin filtering for EuS, for example), their main disadvantage is their low ordering temperatures (5, 17 and 70 K, respectively). Perovskites and ferrites present larger T_C: as a ferroelectric, La-doped $BiMnO_3$ is a promising choice, although its T_C=105 K is well below RT. Ferrites exhibit the largest T_C, above RT. Although the predicted TMR at RT was not found for LSMO/ $NiFe_2O_4$, a small TMR signal of -3% was found at RT for $CoFe_2O_4/Al_2O_3$/Co (-18% at 2 K). The high quality of this fully epitaxial system is considered a main factor in the successful spin transport experiment. A more extended review of the spin-filtering materials can be found in Ref [52].

2.5.3 Effect of oxidation at the interface

In this section, we mention a specific example of the role of interfaces, concerning the oxidation of the electrode materials at their interface with the barrier, in particular when the barrier is Fe or Co.

Non-oxidized Fe interfaces exhibit negative spin polarization, in accordance to the negative spin polarization of bulk Fe. However, a theoretical study demonstrates the switching of the spin polarization sign when Fe is oxidized due to hybridization of the Fe 3d- O 2p orbitals [53]. In the case of Co, a monolayer of oxygen on the Co surface creates a spin-filter effect due to the Co-O bonding, which produces an additional tunnel barrier in the minority-spin channel. This results in the reversal of the sign of the spin polarization from negative to positive for oxidized interfaces [38]. In fact, this effect – which reveals the decisive role of interface bonding in spin-dependent tunnelling- also provides an explanation for the previously mentioned case of tunnelling across LSMO and Co electrodes, in which TMR is positive or negative depending on the barrier

material [29]: the predominant O-termination of Co/Al_2O_3 interfaces thus explains the change from negative to positive TMR, with respect to non-oxidized interfaces.

2.6 THIN FILM GROWTH: SOME CONCEPTS

Thin films show different properties with respect to their bulk counterparts. Besides the reduction in dimensionality (which leads to a strong influence of surface and interface effects), the films may be under stress and they possess different defect structure. The different steps in thin film growth are basically: separation of particles from source, transport and condensation on the substrate. This last step includes thermal accommodation, binding formation, surface diffusion (which is typically larger than bulk diffusion), nucleation on defects...

Energy considerations govern the growth mode and crystalline quality of thin films. But it is not an equilibrium process: thermodynamic and kinetic arguments compete to create a complex scenario where the properties of each material and the deposition conditions (temperature, pressure, rate..) are crucial to the final properties of the films or heterostructures.

2.6.1 STRAINED OR RELAXED FILM

The difference between lattice parameters for the substrate material and the grown material (in bulk form) is the main responsible for the strained state of a film. We define lattice mismatch strain as: $f = (a_s - a_f)/a_f$, where a_s is the bulk lattice constant of the substrate and a_f is the bulk lattice constant of the film. This value may take either sign, $f > 0$ for tensile and $f < 0$ for compressive strain. In some cases, if the mismatch is low ($abs(f) < 1\%$), a thin film grows coherently (pseudomorphic), which means that the film is totally strained. For cubic structures, this causes a tetragonal distortion of the film unit cells: whilst the in-plane parameter $a_{\parallel}$ adapts to the in-plane parameter of the substrate, the out-of-plane parameter $a_{\perp}$ extends or shrinks with respect to the bulk value (see Fig 2.19a). As the film thickness increases, so does the strain energy –until we reach a critical thickness. Above that critical thickness, it becomes energetically favourable to relax some of the mismatch strain by introducing misfit dislocations at the interface. The in-plane parameters of the film will no longer be the same as the substrate's, but will tend to evolve towards the bulk value, the so-called *relaxed* lattice parameter of the material (as in Fig 2.19b) [54].

The residual strain does not depend exclusively on the mismatch and layer thickness, but also on the growth conditions and post-growth thermal treatments. These influence the kinetic barriers to lattice relaxation, associated to the generation and movement of dislocations [55].

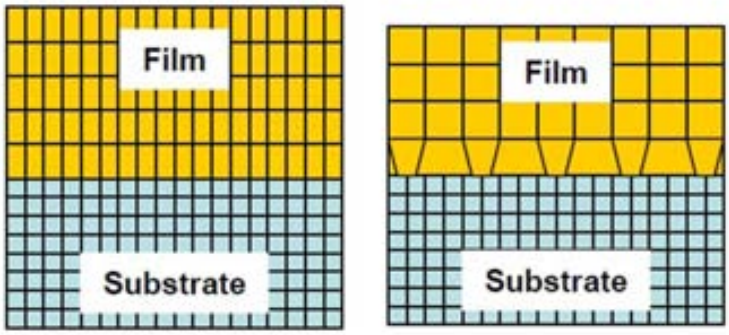

(a) strained (b) relaxed

Fig 2.19. Sketch of a strained lattice grown pseudomorphically on a substrate (a), and a film which is grown on a substrate with large mismatch, the film growing relaxed after one monolayer (b).

The strained state of the film strongly influences its properties. For manganites, it may even determine the electron occupancy of electronic orbitals, effect that could be specially relevant for surface and interfacial properties [56] - defining the wettability, corrugation and hydrophobicity of the film surface- and may even tune the transport and magnetic properties of the film [57].

2.6.2 GROWTH MODES, SURFACE ENERGIES AND SURFACE DIFFUSION

From a thermodynamic point of view, the morphology of a material A grown on top of material B will depend on the free surface energies of the substrate (or previously deposited film) γ_B, on that of the material being deposited γ_A, and on that of the interface γ_i [58]. From these considerations, we can distinguish three distinct growth modes. If $\Delta\gamma = \gamma_A + \gamma_i - \gamma_B \leq 0$, the first atomic layer of A coats all the material B surface in order to reduce the energy. If after the deposition of a first layer of material A, we still have $\Delta\gamma \leq 0$, a "layer-by-layer" growth mode is achieved, also known as "Frank-van der Merwe" (Fig 2.20a). However, if the complete first layer of material A grows accommodating its lattice parameters to those of the substrate, the interfacial tension causes elastic energy to be stored in the film, and after a certain thickness it will give $\Delta\gamma > 0$, so that 3D agregates will start to nucleate, thus reaching "Stranski-Krastanov" or "layer-plus-island" growth morphology (Fig 2.20b). On the other hand, if before any A material is deposited $\Delta\gamma > 0$, 3-D agregates will condense as islands and material B will not be fully covered. This "island" growth mode also receives the name of "Volmer-Weber" (Fig 2.20c).

For thin film heterostructures, the layer by layer growth mode is the most desired and when a material coats another while reproducing the morphology of the non-coated surface, we say it "wets" well.

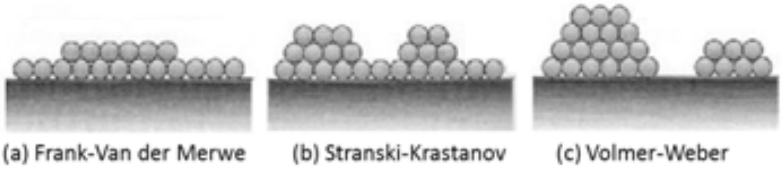

Fig 2.20. Surface morphology for different growth modes: (a) Frank-van der Merwe mode, or "layer-by-layer" has fully covered layers; (b) Stranski-Krastanov growth mode has a full first monolayer after which aggregates condense in 3-D manner; (c) Volmer-Weber mode has no complete coverage of substrate (or previous film), but material condensates in 3-D aggregates. Image adapted from [59].

However, as we have already mentioned, the real deposition conditions are far from thermodynamic equilibrium, and kinetic factors such as deposition and surface diffusion rates largely influence the surface morphology. For stepped (vicinal) surfaces, the 3-D growth modes can be generalized to 2-D growth modes, by substituting the free surface energies for step energies. In this case, atoms are repelled or attracted to the steps. But atoms can move along a terrace –necessary for a good wetting of the substrate surface- only when their energy is enough to overcome the Ehrlich-Schwoebel barrier[1]. For temperatures lower and growth rates higher than those of quasi-equilibrium, non-equilibrium 2D growth occurs, and diffusion is reduced. In Fig 2.21, the sketch represents the different diffusion processes on a stepped surface.

So, the main parameters to take into account are the growth rate (controlling the deposition temperature, the distance between the magnetron and the substrate, and RF power), and substrate temperature during deposition. A clear example of control of the thermodynamic and kinetic competition is the formation of heterostructures A/B/A with sharp interfaces, which would not be feasible only from a thermodynamic point of view[2].

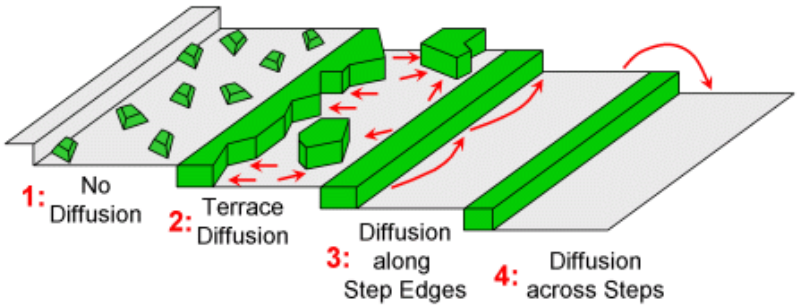

Fig 2.21. Surface morphology. Taken from [60].

[1] For a stepped surface, on the lower terrace close to the step there is larger binding energy due to larger number of nearest neighbours with respect to the other terrace sites. When crossing a step, atoms need to overcome an additional diffusion barrier because they pass through an area of lower coordination.

[2] Thermodynamically speaking, if A/B interface is energetically favourable, the B/A interface it not so.

2.6.3 SURFACE ROUGHNESS AND OTHER INTERFACIAL EFFECTS

Surface or interfacial quality is another important parameter to take into account for heterostructure growth. As depicted in Fig 2.22a-d, interfaces can be abrupt and flat, or on the contrary, rough, with interdiffusion[3] or intermixing phenomena or even reactive, where a new chemical compound is created. This will depend on the diffusion constants, reaction rates and times, and, of course, the temperature. For a more complete description, see Ref [61].

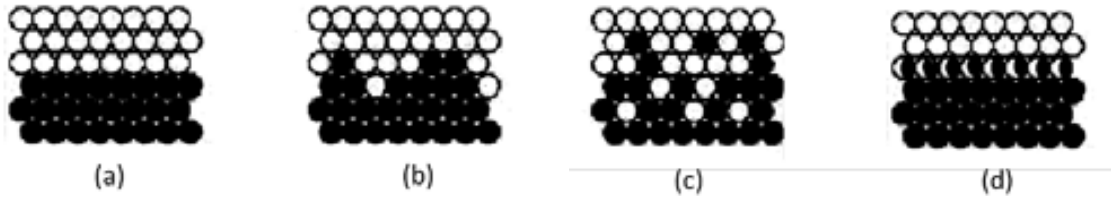

Fig 2.22. Interfacial quality examples: (a) sharp interface; (b) rough interface; (c) interdiffusive interface; (d) reactive interface, new chemical compound is created. Fig adapted from [62].

In applications such as magnetic tunnel junctions, for example, abrupt interfaces are a mandatory requirement. As the insulating barrier grown on top of the lower electrode is extremely thin, a rough surface of the electrode causes indetermination in the value of the barrier thickness, may favour the formation of pinholes or result in an excessively thin path for the electrons to tunnel which produces the breakdown of the junction. Another possible complication is that a correlated roughness in the barrier may cause Néel coupling. This consists in the accumulation of magnetic "charges" at each interface of the insulating barrier, thereby raising the field energy for antiparallel magnetization of the electrodes (see Fig 2.23).

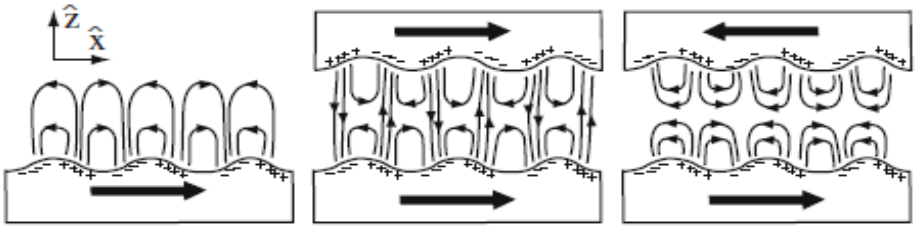

Fig 2.23. Sketch of the effect of Néel coupling of two magnetic layers due to correlated roughness. Image taken from [63].

Interdiffusion is enhanced for high temperature processing, because of higher atom diffusion [64]. However, high annealing temperatures are required to achieve good crystallization of the tunnel barriers. A possible solution is to perform ultrafast (flash) annealings, which allow good recrystallization while preventing interdiffusion.

[3] Large number of atoms (even islands or layers) bury themselves in the substrate.

In a FM/non-magnetic interface, interdiffusion of interfacial atoms and hybridization of electron states also supress magnetic moments. This sometimes results in a magnetic "dead layer" at the interface and the order parameter at the surface often decreases faster with increasing temperature than the bulk order parameter. The concept of "magnetic interface" is created. The "magnetic roughness" determines the coercivity of the films, and both the chemical and the magnetic roughnesses strongly affect the transport properties across magnetic layers and spin-dependent transport [65].

As we have explained in this section, growing films or heterostructures is a complicated process with many variables that influence the final properties of the material (surface morphology, crystallinity and strain state among others), with crucial effects on the functionality that these may provide. The correct control of the growth parameters is necessary to ensure good quality of the films, and optimal performance of the devices prepared with them.

2.7 REFERENCES

[1] Tokura Y.; "Orbital Physics in Transition-Metal Oxides". *Science (80-.).* 288; **2000**: 462–8. doi:10.1126/science.288.5465.462.

[2] Rao C.N.R.; "Transition Metal Oxides". *Annu. Rev. Phys. Chem.* 40; **1989**: 291–326. doi:10.1146/annurev.pc.40.100189.001451.

[3] Sleight A.W.; "Chemistry of high-temperature superconductors.". *Science* 242; **1988**: 1519–27. doi:10.1126/science.242.4885.1519.

[4] Majumdar S., van Dijken S.; "Pulsed laser deposition of La1-xSrxMnO3: thin-film properties and spintronic applications". *J. Phys. D-Applied Phys.* 47; **2014**. doi:10.1088/0022-3727/47/3/034010.

[5] Woodward P.M.; "Octahedral Tilting in Perovskites. I. Geometrical Considerations". *Acta Crystallogr. Sect. B Struct. Sci.* 53; **1997**: 32–43. doi:10.1107/S0108768196010713.

[6] Barón-González A.J., Garcia J.L.; Estudio de los mecanismos electrónicos en perovskitas de cobalto Pr0.5Ca0.5CoO3, (Pr, Y, Ca) CoO3 y La2 MnCoO6. Universitat Autònoma de Barcelona, **2011**.

[7] Aktas B., Mikailov F., editors; Advances in Nanoscale Magnetism. vol. 122, Proceedings of the International Conference on Nanoscale Magnetism ICNM-2007, June 25 -29, Istanbul, Turkey: Springer Proceedings in Physics; **2009**.

[8] Peña Guédez L., Martínez Perea B.; Sistemas Nanoestructurados y Propiedades de Transporte en Capas Delgadas de Manganita. Universitat de Barcelona, **2014**.

[9] Stöhr J., Siegmann H.C.; "Magnetism: from Fundamentals to Nanoscale Dynamics". vol. 152. **2006**.

[10] Baidya S., Saha-Dasgupta T.; "Electronic structure and phonons in La_{2}CoMnO_{6}: A ferromagnetic insulator driven by Coulomb-assisted spin-orbit coupling". *Phys. Rev. B* 84; **2011**: 035131. doi:10.1103/PhysRevB.84.035131.

[11] Robinson D.W.; "Magnetism and the Chemical Bond. John B. Goodenough. Interscience (Wiley), New York, 1963. xvi + 394 pp. Illus. $12.50". *Science (80-.).* 143; **1964**: 33–4. doi:10.1126/science.143.3601.33-a.

[12] Zener C.; "Interaction between the d-Shells in the Transition Metals. II. Ferromagnetic Compounds of Manganese with Perovskite Structure". *Phys. Rev.* 82; **1951**: 403–5. doi:10.1103/PhysRev.82.403.

[13] Mott N.F.; "The Electrical Conductivity of Transition Metals". *Proc. A* 153; **1936**: 699–718 . doi:10.1098/rspa.1936.0031.

[14] Fontcuberta i Griñó J.; "Albert Fert i Peter Grünberg: Premis Nobel de Física 2007". *Rev. Física V4* **2010**: p. 29–37. http://www.raco.cat/index.php/RevistaFisica/article/view/174207.

[15] Kawakami R., McCreary K., Li Y.; Fundamentals of Spintronics in Metal and Semiconductor Systems. In: Korkin A, Rosei F, editors. Nanoelectron. Photonics, Springer New York; **2008**, p. 59–114. doi:10.1007/978-0-387-76499-3_5.

[16] Kawakami R.K., McCreary K., Li Y.; Fundamentals of Spintronics in Metal and Semiconductor Systems. In: Korkin A, Rosei F, editors. Nanoelectron. Photonics, Springer New York; **2008**, p. 59–114. doi:10.1007/978-0-387-76499-3_5.

[17] Berkowitz A., Mitchell J., Carey M., Young A., Zhang S., Spada F., et al.; "Giant magnetoresistance in heterogeneous Cu-Co alloys". *Phys. Rev. Lett.* 68; **1992**: 3745–8. doi:10.1103/PhysRevLett.68.3745.

[18] Lee Y.M., Hayakawa J., Ikeda S., Matsukura F., Ohno H.; "Effect of electrode composition on the tunnel magnetoresistance of pseudo-spin-valve magnetic tunnel junction with a MgO tunnel barrier". *Appl. Phys. Lett.* 90; **2007**: 212507. doi:10.1063/1.2742576.

[19] Giddings A., Khalid M., Jungwirth T., Wunderlich J., Yasin S., Campion R., et al.; "Large Tunneling Anisotropic Magnetoresistance in (Ga,Mn)As Nanoconstrictions". *Phys. Rev. Lett.* 94; **2005**: 127202. doi:10.1103/PhysRevLett.94.127202.

[20] Park B.G., Wunderlich J., Williams D.A., Joo S.J., Jung K.Y., Shin K.H., et al.; "Tunneling Anisotropic Magnetoresistance in Multilayer-(Co/Pt)/AlO_{x}/Pt Structures". *Phys. Rev. Lett.* 100; **2008**: 087204. doi:10.1103/PhysRevLett.100.087204.

[21] Matos-Abiague A., Fabian J.; "Anisotropic tunneling magnetoresistance and tunneling anisotropic magnetoresistance: Spin-orbit coupling in magnetic tunnel junctions". *Phys. Rev. B* 79; **2009**: 155303. doi:10.1103/PhysRevB.79.155303.

[22] LeClair P.R., Moodera J.S.; Tunneling Magnetoresistance: Experiment (Non-MgO Magentic Tunnel Junctions). Handb. Spin Transp. Magn., Taylor & Francis; **2011**, p. pp. 197–216.

[23] Simmons J.G.; "Generalized formula for electric tunnel effect between similar electrodes separated by a thin insulating film". *J. Appl. Phys.* 34; **1963**: 1793 – &. doi:10.1063/1.1702682.

[24] Brinkman W.F.; "Tunneling Conductance of Asymmetrical Barriers". *J. Appl. Phys.* 41; **1970**: 1915. doi:10.1063/1.1659141.

[25] Driussi F.; "Trap Assisted Tunneling (TAT) processes" online. http://www.diegm.uniud.it/driussi/biografia/dottorato/node47.html.

[26] Garcia V., Bibes M.; "Ferroelectric tunnel junctions for information storage and processing". *Nat. Commun.* 5; **2014**: 4289. doi:10.1038/ncomms5289.

[27] Julliere M.; "Tunneling between ferromagnetic films". *Phys. Lett. A* 54; **1975**: 225–6. doi:http://dx.doi.org/10.1016/0375-9601(75)90174-7.

[28] Beth Stearns M.; "Simple explanation of tunneling spin-polarization of Fe, Co, Ni and its alloys". *J. Magn. Magn. Mater.* 5; **1977**: 167–71. doi:10.1016/0304-8853(77)90185-8.

[29] De Teresa J.M., Barthelemy A., Fert A., Contour J.P., Montaigne F., Seneor P.; "Role of metal-oxide interface in determining the spin polarization of magnetic tunnel junctions". *Science (80-.).* 286; **1999**: 507–9. doi:10.1126/science.286.5439.507.

[30] Tsymbal E.Y., Mryasov O.N., LeClair P.R.; "Spin-dependent tunnelling in magnetic tunnel junctions". *J. Phys. Condens. Matter* 15; **2003**: R109–42. doi:10.1088/0953-8984/15/4/201.

[31] Spin Transport and Magnetism in Magnetic Metallic Multilayers. Handb. Spin Transp. Magn., Chapman and Hall/CRC; **2011**, p. 18–9. doi:10.1201/b11086-4 10.1201/b11086-4.

[32] Bowen M.O., Fert A.; Experimental Insights into Spin-Polarized Solid State Tunneling. Université de Paris-Sud, U.F.R. Scientifique d'Orsay, **2003**.

[33] Park J.-H., Vescovo E., Kim H.-J., Kwon C., Ramesh R., Venkatesan T.; "Direct evidence for a half-metallic ferromagnet" 392; **1998**: 794–6. doi:10.1038/33883.

[34] Bowen M., Bibes M., Barthélémy A., Contour J.-P., Anane A., Lemaître Y., et al.; "Nearly total spin polarization in La2/3Sr1/3MnO3 from tunneling experiments". *Appl. Phys. Lett.* 82; **2003**: 233–5. doi:doi:http://dx.doi.org/10.1063/1.1534619.

[35] Bibes M., Barthelemy A.; "Oxide spintronics". *IEEE Trans. Electron Devices* 54; **2007**: 1003–23. doi:10.1109/ted.2007.894366.

[36] Garcia V., Bibes M., Barthelemy A., Bowen M., Jacquet E., Contour J.P., et al.; "Temperature dependence of the interfacial spin polarization of La2/3Sr1/3MnO3". *Phys. Rev. B* 69; **2004**. doi:10.1103/PhysRevB.69.052403.

[37] Yuasa S., Djayaprawira D.D.; "Giant tunnel magnetoresistance in magnetic tunnel junctions with a crystalline MgO(001) barrier". *J. Phys. D-Applied Phys.* 40; **2007**: R337–54. doi:10.1088/0022-3727/40/21/r01.

[38] Belashchenko K.D., Tsymbal E.Y., van Schilfgaarde M., Stewart D.A., Oleynik I.I., Jaswal S.S.; "Effect of interface bonding on spin-dependent tunneling from the oxidized Co surface". *Phys. Rev. B* 69; **2004**: 7. doi:10.1103/PhysRevB.69.174408.

[39] Swagten H.J.M.; "Chapter One Spin-Dependent Tunneling in Magnetic Junctions". *Handb. Magn. Mater.* 17; **2007**: 1–121. doi:10.1016/S1567-2719(07)17001-3.

[40] Oliver B., He Q., Tang X., Nowak J.; "Tunneling criteria and breakdown for low resistive magnetic tunnel junctions". *J. Appl. Phys.* 94; **2003**: 1783. doi:10.1063/1.1590064.

[41] Akerman J.J., Escudero R., Leighton C., Kim S., Rabson D.A., Dave R.W., et al.; "Criteria for ferromagnetic-insulator-ferromagnetic tunneling". *J. Magn. Magn. Mater.* 240; **2002**: 86–91. doi:10.1016/s0304-8853(01)00712-0.

[42] Gajek M., Bibes M., Fusil S., Bouzehouane K., Fontcuberta J., Barthélémy A., et al.; "Tunnel junctions with multiferroic barriers.". *Nat. Mater.* 6; **2007**: 296–302. doi:10.1038/nmat1860.

[43] Butler W.H., Zhang X.G., Schulthess T.C., MacLaren J.M.; "Spin-dependent tunneling conductance of Fe vertical bar MgO vertical bar Fe sandwiches". *Phys. Rev. B* 63; **2001**. doi:10.1103/PhysRevB.63.054416.

[44] Mathon J., Umerski A.; "Theory of tunneling magnetoresistance of an epitaxial Fe/MgO/Fe(001) junction". *Phys. Rev. B* 63; **2001**. doi:10.1103/PhysRevB.63.220403.

[45] Butler W.H.; "Tunneling magnetoresistance from a symmetry filtering effect". *Sci. Technol. Adv. Mater.* 9; **2008**. doi:10.1088/1468-6996/9/1/014106.

[46] Kirill D.B., Evgeny Y.T.; Tunneling Magnetoresistance. Handb. Spin Transp. Magn., Chapman and Hall/CRC; **2011**, p. 233–50. doi:doi:10.1201/b11086-16 10.1201/b11086-16.

[47] Ball D.W.; "Introductory Chemistry, v. 1.0" online. http://catalog.flatworldknowledge.com/bookhub/reader/2273?e=ball-ch08_s02.

[48] Zhang X.-G., Butler W., Bandyopadhyay A.; "Effects of the iron-oxide layer in Fe-FeO-MgO-Fe tunneling junctions". *Phys. Rev. B* 68; **2003**: 092402. doi:10.1103/PhysRevB.68.092402.

[49] Zermatten P.-J., Bonell F., Andrieu S., Chshiev M., Tiusan C., Schuhl A., et al.; "Influence of Oxygen Monolayer at Fe/MgO Interface on Transport Properties in Fe/MgO/Fe(001) Magnetic Tunnel Junctions". *Appl. Phys. Express* 5; **2012**: 023001. doi:10.1143/APEX.5.023001.

[50] Yuasa S., Nagahama T., Fukushima A., Suzuki Y., Ando K.; "Giant room-temperature magnetoresistance in single-crystal Fe/MgO/Fe magnetic tunnel junctions". *Nat. Mater.* 3; **2004**: 868–71. doi:10.1038/nmat1257.

[51] Parkin S.S.P., Kaiser C., Panchula A., Rice P.M., Hughes B., Samant M., et al.; "Giant tunnelling magnetoresistance at room temperature with MgO (100) tunnel barriers". *Nat. Mater.* 3; **2004**: 862–7. doi:10.1038/nmat1256.

[52] Tiffany S.S., Jagadeesh S.M.; Spin-Filter Tunneling. Handb. Spin Transp. Magn., Chapman and Hall/CRC; **2011**, p. 251–66. doi:10.1201/b11086-17 10.1201/b11086-17.

[53] Tsymbal E.Y., Oleinik I.I., Pettifor D.G.; "Oxygen-induced positive spin polarization from Fe into the vacuum barrier". *J. Appl. Phys.* 87; **2000**: 5230–2. doi:10.1063/1.373304.

[54] Birkholz M.; "Thin Film Analysis by X-Ray Scattering". Wiley-VCH Verlag GmbH & Co. KGaA; **2006**. doi:10.1002/3527607595.

[55] Ayers J.E.; "Heteroepitaxy of Semiconductors: Theory, Growth and Characterization". 1st ed. Taylor & Francis Group, LLC; **2007**.

[56] Pesquera D., Herranz G., Barla A., Pellegrin E., Bondino F., Magnano E., et al.; "Surface symmetry-breaking and strain effects on orbital occupancy in transition metal perovskite epitaxial films". *Nat. Commun.* 3; **2012**. doi:10.1038/ncomms2189.

[57] Konishi Y., Fang Z., Izumi M., Manako T., Kasai M., Kuwahara H., et al.; "Orbital-State-Mediated Phase-Control of Manganites". *J. Phys. Soc. Japan* 68; **1999**: 3790–3. doi:10.1143/jpsj.68.3790.

[58] Gilmer G.H., Grabow M.H.; "Models of Thin Film Growth Modes". *J. Met.* 39; **1987**: 19–23. doi:10.1007/bf03258055.

[59] "Surfaces, Growth and Strain Relaxation". *Warwick, Dep. Phys.* **2010**. http://www2.warwick.ac.uk/fac/sci/physics/current/postgraduate/regs/mpags/ex5/strainedlayer/surfgrwth/ (accessed July 02, 2014).

[60] Petrovykh D.; "Biointerface: Nanostructures" **2014**. http://biointerface.org/nano/nanostructures/ (accessed July 26, 2014).

[61] Lüth H.; "Solid Surfaces, Interfaces and Thin Films". Fifth Edit. Springer; **2010**. doi:10.1007/978-3-642-13592-7.

[62] Martínez Boubeta C., Cebollada Navarro P.A.; Heteroestructuras Fe/MgO(001): Epitaxia y Propiedades Magnéticas. Universidad Complutense de Madrid, **2003**.

[63] Stiles M.D.; Interlayer Exchange Coupling. In: Bland JAC, Heinrich B, editors. Ultrathin Magn. Struct. III, **2005**.

[64] Venables J.; "Introduction to Surface and Thin Film Processes". Cambridge University Press; **2000**.

[65] Fullerton E.E., Sinha S.K.; X-ray Scattering Studies of Ultrathin Metallic Structures. In: Bland JAC, editor. Ultrathin Magn. Struct. III, **2005**.

PART II:

GROWTH AND CHARACTERIZATION OF THIN FILMS AND HETEROSTRUCTURES

CHAPTER 3. THIN FILMS AND INTERFACES FOR TUNNEL JUNCTIONS

The film heterostructures in this thesis have been grown by RF magnetron sputtering on (100)-oriented $SrTiO_3$(STO) substrates. In Chapter 2, we already introduced some basic concepts related to growth of thin films and the relevant physical parameters which determine the growth modes and the quality of the final heterostructures. The present chapter is devoted to the preparation of such heterostructures. An initial optimization of the growth parameters is performed for each material separately (LSMO, MgO, LAO and Fe), followed by the corresponding characterization of the obtained films. The basic characterization usually consists in atomic force microscopy (AFM), X-ray diffraction (XRD) and magnetic measurements in the Superconducting Quantum Interference device (SQUID), but we shall focus on different properties depending on the material and its role in the final structure. When heterostructures are prepared, the stack properties are not necessarily the combination of those of the different layer materials, and interfaces can play a very significant role, one of the most popular examples being the conductive interface between the two insulators LAO and STO [1]. In the case of LSMO-based heterostructures, for instance, the Curie temperature (T_C) of LSMO depends on the capping materials and the growth conditions. So, interfacial phenomena play a key role that we seek to elucidate in order to optimize the final properties of the heterostructure.

3.1 PREPARATION OF STO SUBSTRATES

The substrates we have used are 5x5 mm^2 (001)-single crystals of STO. These are widely used for deposition of high quality manganite films because of the compatibility in the lattice constant [2], and its chemical and compositional stability (high melting temperature) enables deposition at high temperatures [3], as required for oxides.

STO is an insulator with perovksite structure (its cubic lattice parameter is 3.905 Å), which can be understood as alternating TiO_2 planes and SrO planes (separated half a unit cell). The substrates are not cut perfectly parallel to the unit cell, but form a certain angle from the in-plane crystallographic planes, which receives the name of "miscut" (see Fig 3.1). This entails that at the untreated surface we have both TiO_2 and SrO-terminated regions. Sometimes, a single termination may be useful to impose a certain stacking sequence and a smooth morphology [3]. It is easier to obtain TiO_2-terminated substrates by a thermal treatment of the substrate than to obtain SrO ones[1]. For single-

[1] Considering the coordination number in STO of Sr (12 for bulk atoms and 8 for surface atoms) and of Ti (6 for bulk atoms and 5 for surface atoms), TiO_2 termination is expected to be more stable because fewer relative bonds must be broken at the surface.

terminated substrates, the surface morphology of the sample is of steps and terraces – and the terraces may be larger or shorter depending on the miscut angle.

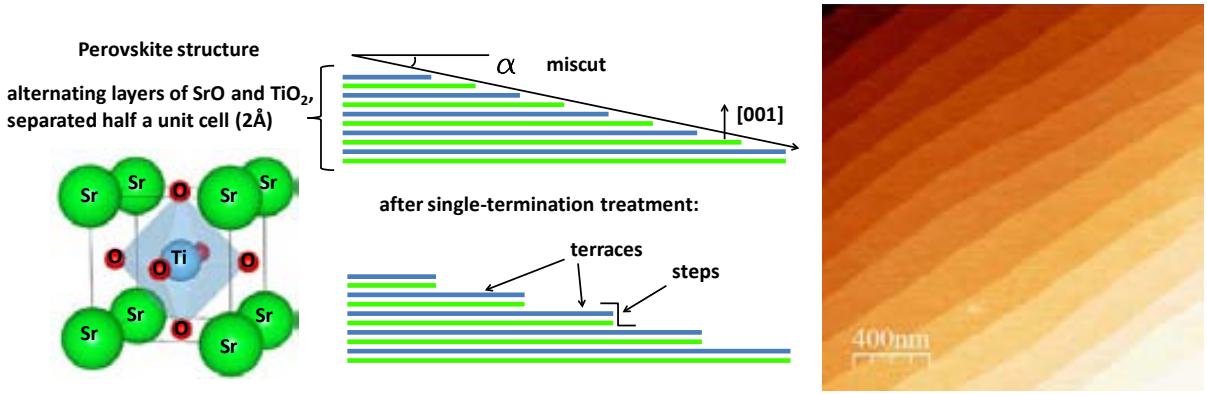

Fig 3.1. Perovskite structure of STO and miscut of the substrate that forms step-and-terrace morphology when single-termination is achieved, as shown in the AFM image at the right.

In this thesis, our substrates are TiO_2-terminated, prepared as in Ref [4]: we clean the as-received one-side polished non-terminated (100)-STO substrate with acetone and ethanol[2]. We sonicate[3] it in ultrapure MilliQ water ($\rho = 18.2\ M\Omega \cdot cm$ at 25ºC) for 5 minutes and perform an annealing[4] in air at high temperature (1000ºC) for 2 h [5]. Finally, we always check the substrate by AFM to ensure single termination, with 0.4 nm-high steps (see AFM image at the right of Fig 3.1).

3.2 Growth optimization of LSMO//STO(100)

Bulk LSMO is a half-metallic ferromagnet with bulk T_C of 370 K. It has a perovskite structure and its pseudo-cubic lattice parameter is 3.876 Å. In this section, we explain the optimization of LSMO films on STO substrates.

3.2.1 Previous LSMO optimization and characterization

LSMO films have been grown and the deposition conditions optimized in our group for a long time. As Sandiumenge et al. [6] report, LSMO films grow fully strained on STO substrates, $a_{\parallel}(LSMO) = a_{\parallel}(STO)$ even for thicknesses above 100 nm. The out-of-plane parameter of the film, however, depends on the film thickness, as can be seen in Fig 3.2a. This is due to the misfit relaxation mechanisms, which induce distortions in the lattice (by octahedron tilts) that depend on the thickness of the film. For films of thicknesses above 2.5 nm, this results in the formation of twins, which can be detected

[2] This is meant to clean the surface from any contaminants like CO_2 and H_2O.
[3] The aim is to remove the distorted and stressed layers caused by the polishing of the substrate, and ultrasonic agitation maintains the STO stoichiometry contrary to sputtering –because Ti, O and Sr have different sputter yields.
[4] The annealing is used to treat the crystallinity and obtain atomically flat terraces and sharp steps at the surface of the STO.

through XRD, or seen in Scanning Electron Microscopy (SEM) images (by slightly tilting the sample).

Other properties like magnetization and resistivity also depend on the film thickness; the magnetic moment and T_C increase with film thickness until bulk properties are achieved (as in Fig 3.2c) and films go from insulating to metallic concomitantly with the twin formation (Fig 3.2b).

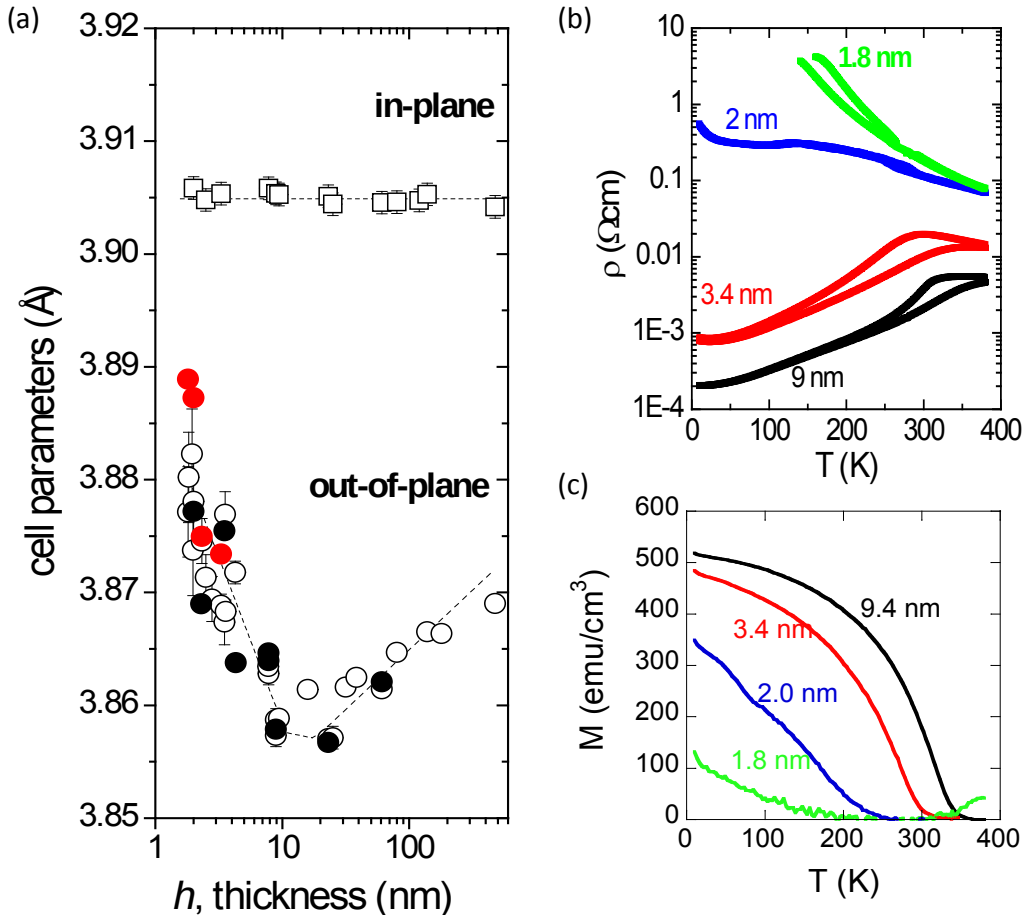

Fig 3.2. Thickness dependence of in-plane and out-of-plane cell parameters, resistivity and magnetization curves at 5 kOe of the LSMO thin films. Image adapted from [6].

For thicknesses around 10 nm, the T_C achieved is already above 340 K, not far from the bulk LSMO. In this thesis, we will therefore grow films of thicknesses above 10 nm – with high T_C, metallic behaviour and fully strained, with the same in-plane cell parameters as the STO substrate underneath.

We use the previously optimized parameters detailed in the supplementary material of reference [6][5]. However, it is important to note that the oxygen partial pressure values must be optimized every time we change the target, or if the sputtering conditions are somehow modified. This is the aim of the following section.

[5] T= 900°C and 1h of annealing at 350 Torr also at 900°C.

3.2.2 OXGYEN PARTIAL PRESSURE OPTIMIZATION

LSMO films (of thicknesses around 20 nm) were grown with oxygen partial pressures ranging from 100-240 mTorr. AFM images of their topography, in Fig 3.3, show flat surfaces for all the samples. However, two distinctive growth modes can be appreciated: for lower oxygen partial pressures, the LSMO film grown on top of STO wets the surface of the substrate, completely reproducing the steps of the TiO_2-terminated substrates. Below 160 mTorr, the edges of the steps are not well defined but form kind of meanders. By increasing the pressure slightly (around 180-190 mTorr), nicely defined terraces and steps are achieved. On the other hand, for higher pressures (above 200 mTorr), 3D growth mode is promoted.

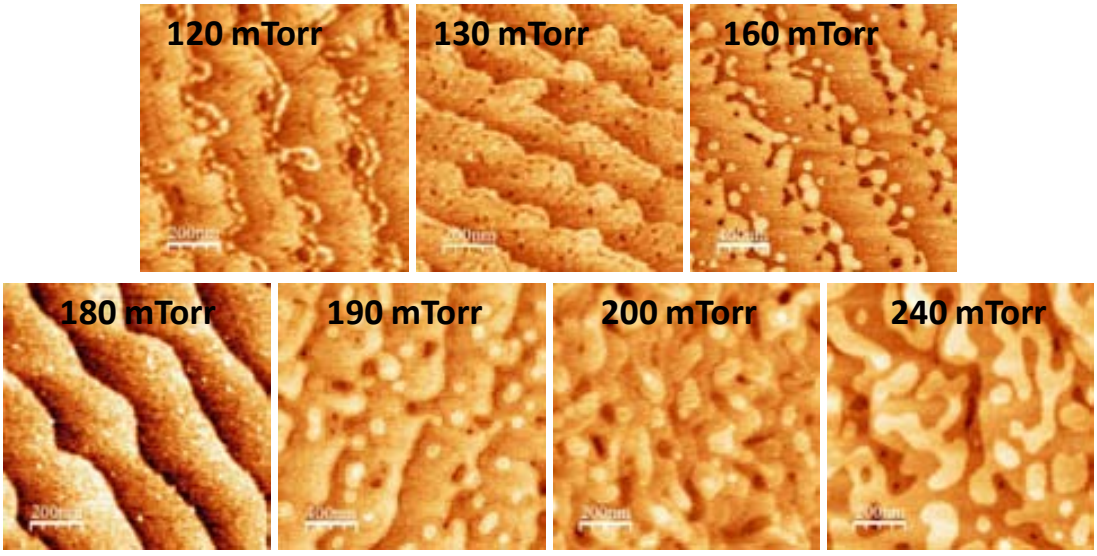

Fig 3.3. AFM images of LSMO grown on STO substrate using different oxygen partial pressures (at 900 ºC, 20 sccm O_2 and 20 W and 1h annealing at 350 Torr) reveal different growth modes depending on the growth conditions.

To grow thin film heterostructures, and particularly for the fabrication of trilayers for magnetic tunnelling junction applications, we are interested in a layer by layer growth which defines terraces and steps to ensure the continuity of the layer for very thin films, and avoid pinhole formation. According to Fig 3.3, the optimized pressures are around 180 mTorr. However, as we already mentioned, any change in the target requires a new pressure optimization. This means that we cannot take the value of the oxygen partial pressure as an absolute, but the tendency of the different growth modes for the oxygen partial pressure variation is indeed reliable.

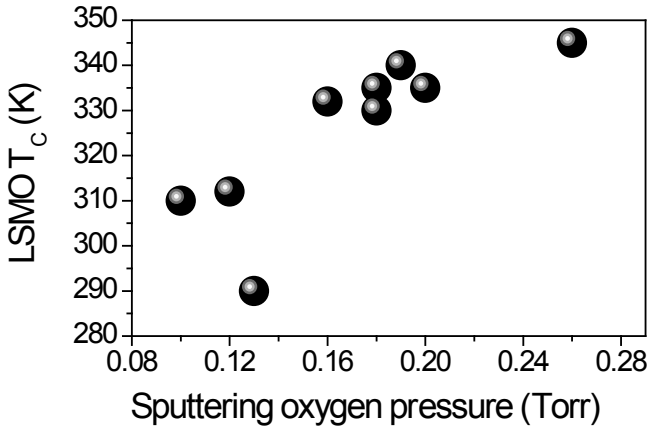

Fig 3.4. Curie Temperature of LSMO grown in different oxygen partial pressures, 900º C, 20 sccm O_2, 20 W and 1 h annealing at 350 K.

Besides the flat surface, we are also interested in the highest possible T_C of the LSMO thin film, so we compare the different values of T_C (taken from the interpolation of the final slope of the magnetization *vs*. T curve) for the films grown at different oxygen partial pressures. As depicted in Fig 3.4, the T_C of LSMO thin films seems to increase with oxygen partial pressure for the studied range. The dependence of magnetic properties on oxygen partial pressure is not surprising because the magnetic interaction is through double exchange mechanism (as explained in Chapter 2), where Mn ions exchange spins through an oxygen ion, so the oxygen contents influences the magnetic properties.

Besides the deposition pressure, another way to introduce oxygen into the LSMO structure is by annealing processes. Our standard growth conditions include 1 h of annealing at 900ºC and 350 Torr of Oxygen partial pressure, as for sample shown in Fig 3.5a. Comparing it with a sample grown at the same conditions but without annealing (b), we see that the non-annealed sample has clearly less defined contours of the terrace and steps, making it easier to distinguish –at the surface- the twinning structure that thin films of LSMO use to relax. In Fig 3.5c, we show that the annealed sample maintains higher magnetization at higher temperature, whilst the non-annealed sample presents a gradual drop at lower temperature.

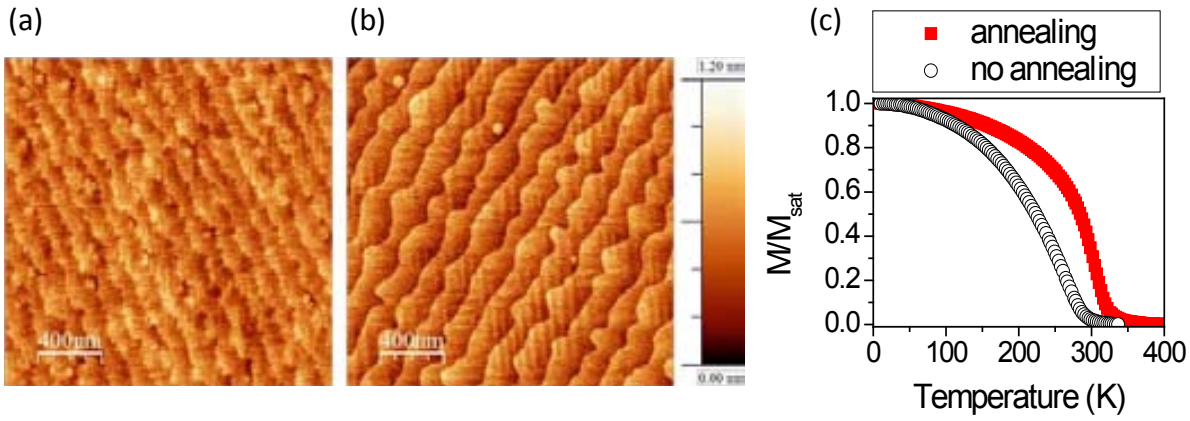

Fig 3.5. AFM images of samples grown at the same optimized pressure conditions, 20 W, 900° C, (a) with no *in-situ* annealing, (b) with an *in-situ* annealing of 1 h at 350 Torr. (c) Normalized magnetization *vs*. T measurements comparing both samples.

3.3 GROWTH OPTIMIZATION OF MgO//STO(100)

Bulk MgO is an insulator with a bandgap of 7.8 eV. Its structure is rock salt and its lattice constant is 4.213 Å. In this section, we study its growth on STO substrates. An important challenge when growing MgO is to avoid the formation of $Mg(OH)_2$ (brucite) fruit of residual H_2O molecules present in the vacuum chamber. Nagamine et al. [7] overcome this problem by sputtering Ta on the chamber just before depositing MgO, so that Ta acts as an H_2O getter, and good crystallinity of the MgO is achieved, even for very thin films (of the order of 3 nm). Yuasa et al. [8] follow the MgO deposition by the growth of an upper electrode at high temperature to avoid adsorbed oxygen atoms on the surface of MgO(100). Tsunekawa et al. [9] report that introducing a Mg metal layer between a CoFeB bottom electrode and an MgO barrier improves the crystalline orientation of the MgO(001) layer for barriers of thickness below 1.2 nm –thereby obtaining higher TMR in magnetic tunnel junctions. For thicker barriers, it was found to be detrimental.

Using our setup and growing at high temperatures (>500ºC), we do not observe brucite formation during growth [10], although it does form at the surface when MgO becomes in contact with air. We have to take this fact into account for the fabrication of heterostructures. Previous work in our group revealed that growth of MgO samples at 800ºC promotes cation vacancies, which give rise to ferromagnetic properties of the MgO. However, the reproducibility was not very good and a loss of magnetic moment was detected with time [11]. To prevent this further complication, films were grown at lower temperature for our heterostructures, using conditions in which no magnetism had been reported or measured.

In this section, we use X-ray diffraction to optimize the crystalline quality of MgO//STO(100) as a function of the deposition temperature, taking into account that lower temperature should minimize interdiffusion effects. For magnetic tunnel junctions, we need ultrathin layers of MgO (below 3 nm), but much thicker films

(around 40 nm) are used for calibration and characterization, to detect larger X-ray diffraction signal. Q-Plots and pole figures have been measured for the most crystalline sample (grown at T=750ºC).

In Fig 3.6a, we plot the Θ/2Θ XRD pattern around the (002) MgO reflection angle for the different samples (grown from 400 to 800ºC). The more intense and narrow peak obtained for the sample grown at 750ºC indicates that this is the optimum temperature for the crystallinity of the film. In Fig 3.6b, the XRR pattern not only provides the thickness of the films (between 37 and 47 nm), but the faster decay of the signal also evidences the rougher interface of the sample grown at 700ºC.

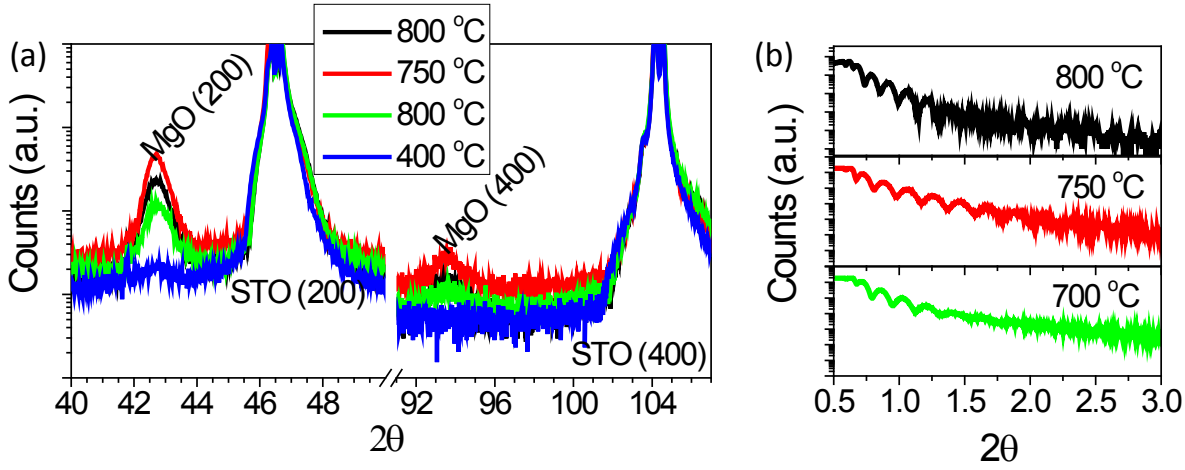

Fig 3.6. (a) Θ/2Θ scan of MgO//STO(100) samples grown at different substrate temperatures (400, 700, 750 and 800ºC); (b) XRR measurement for the MgO//STO(100) grown at 700, 750 and 800ºC, used for the thickness determination and for qualitative comparison of the surface roughness of the samples.

The out-of-plane parameter of the MgO film (determined from the position of the (200) peak of MgO on the symmetric XRD scan (Θ/2Θ)) is $c = 4.232\text{Å}$ and this value seems not to vary for the samples grown at different substrate temperatures.

In Fig 3.7 we show that the rocking curves for reflections (200) and (400) of MgO for samples grown at 750 ºC and 800 ºC. These ω-scans provide information on the angular dispersion of the observed planes. The larger full width half maximum (FWHM) found for sample grown at substrate temperature of 800ºC reveals higher dispersion of the planes than that of a sample grown at 750ºC.

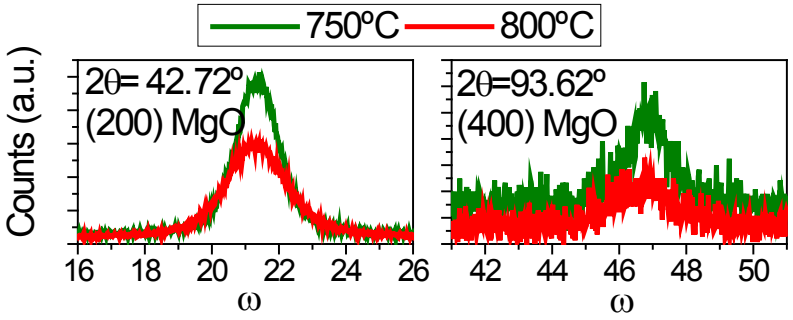

FWHM	750ºC	800ºC
(200)	1.57°	1.92°
(400)	1.6°	>2°

Fig 3.7. Rocking curves for the MgO//STO(100) samples grown at substrate temperatures 750ºC and 800ºC; for the (200) reflection at 2Θ=42.72º, for the (400) reflection at 2Θ=93.62º, and measured values of the full width half maximum (FWHM).

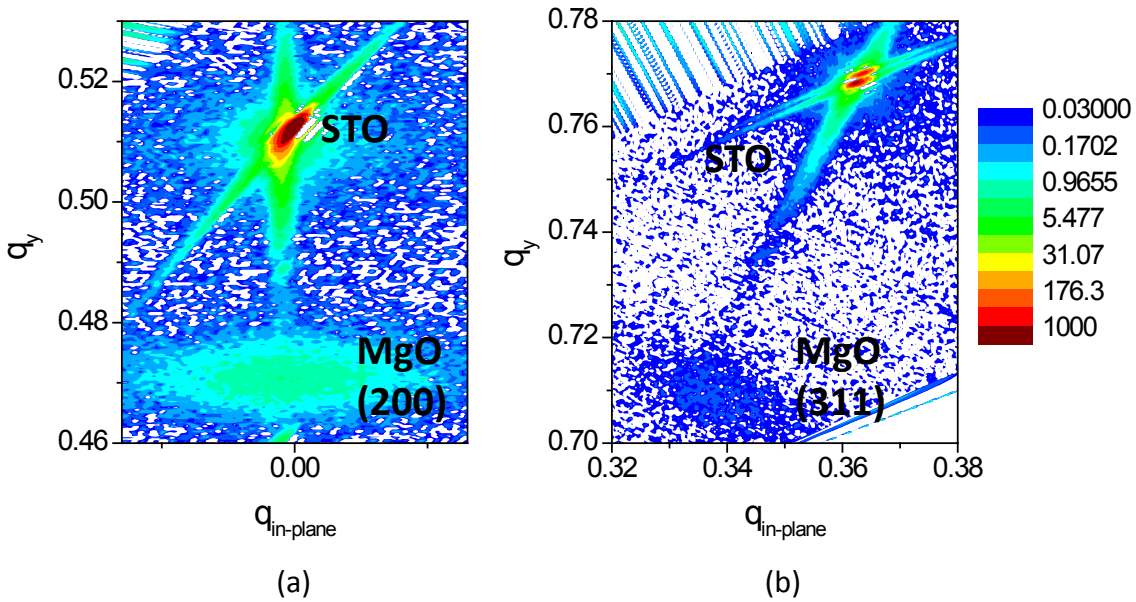

Fig 3.8. Q-plots of the (200) and the (311) reflections for a MgO(39 nm)//STO(100) sample.

We now focus on sample grown at 750ºC, which shows the best crystallinity. In Fig 3.8a we show the reciprocal space map of the (200) reflection of STO and MgO. From the q_z extracted from the graph, we obtain the out-of plane parameter: $c_{MgO} = 4.236\text{Å}$, in accordance to the value obtained from the Θ/2Θ scan (de 0.004 Å difference falls within the error range).

From the (311) reflection (shown in Fig 3.8b), we extract both out-of-plane and in-plane parameter. Although the (311) reflection is very weak, we cannot scan for longer times because the substrate signal saturates the detector. However, we can perform a quick scan (where the reflections of both substrate and MgO appear) followed by a longer

scan of only the MgO (311) reflection, without moving the position of the sample. This way, the position correction using the substrate as reference is the same for both measurements. From this long scan we can extract a more reliable value of the MgO parameters than for Fig 3.8b. We obtain: $c_{MgO} = 4.234\text{Å}, a_{MgO} = 4.193\text{Å}$, so we see that MgO grows slightly relaxed on top of the STO substrate.

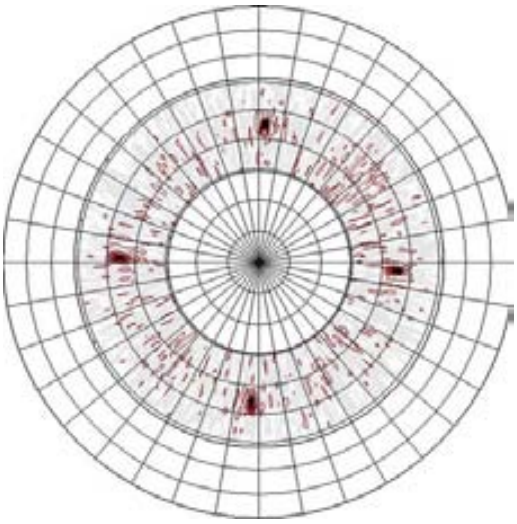

Fig 3.9. Pole figure displaying the (220) peak of MgO (in red) superposed to the pole figure of (220) peak of STO (in black).

The pole figure of the (220) reflections of STO and MgO (see Fig 3.9) confirms that MgO grows epitaxially on top of STO, both layers having cubic symmetric, and we see that the growth is cube on cube, with no rotation between the MgO and the LSMO crystallographic directions.

3.4 GROWTH OF Fe

Fe is a ferromagnetic metal of T_C=1043 K. Its structure below T_C is a body-centered cubic with bulk cell lattice parameter of 2.8665 Å. During this work, Fe has been grown in two different laboratories (IMM and ICMAB). In this section, we detail the parameters used for its non-oxidized growth, but further characterization of the Fe can also be deduced from the characterization of the heterostructures containing Fe in the following sections.

3.4.1 GROWN IN ULTRA HIGH VACUUM

An ultra-high vacuum chamber was used at the IMM-CNM to grow Fe following conditions very similar to the already optimized ones for Fe//MgO(100) [12], as printed in Table 3.1. From the hysteresis loop at 300 K, shown in Fig 3.10, we obtain a saturation magnetization of Fe of 1650 emu/cm^3, close to that of bulk Fe magnetization (1700 emu/cm^3 at 300 K). This difference may be due to a small imprecision on the determination of the Fe layer thickness. Its coercive field is very low, 14 Oe, as

expected. As can be seen later in Fe/MgO/LSMO heterostructures (see section 3.8.2), Fe grows textured.

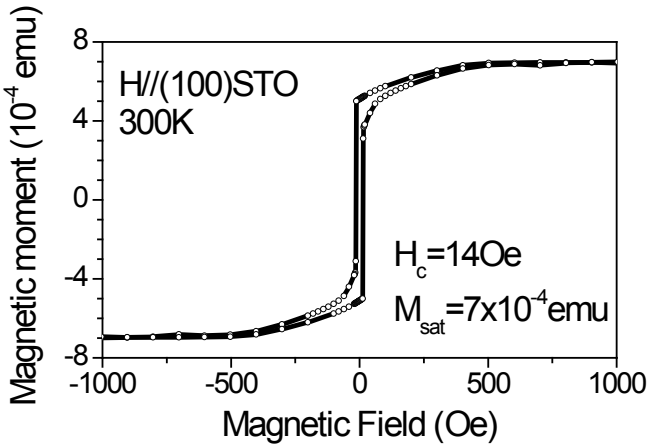

Fig 3.10. Hysteresis cycle at 300 K for Au(10 m)/Ti (2 nm)/Fe(17nm)//STO(100) grown at IMM-CNM.

3.4.2 GROWN IN HIGH VACUUM

At the ICMAB-CSIC, the sputtering chamber is not an ultra-high vacuum system, so Fe is prone to oxidation. That was the case for the first attempts at Fe growth, which were measured by XPS and found to be oxidized[6]. To avoid that, two modifications of the sputtering chamber have been performed. By XPS we verify that Fe grows metallic with each of the two modifications, using the optimized conditions listed in Table 3.1. The first consists in the use of reductive atmosphere, made of 95% Ar and 5% H_2, during the growth. However, as explained in section 3.9.1, the use of the reductive atmosphere affected the T_C of LSMO of our LSMO/MgO/Fe heterostructures. The second is the introduction of a liquid nitrogen cold finger acting as trap of water vapour and condensable gases like oxygen, to decrease the chamber base pressure from 10^{-6} Torr to 10^{-7} Torr. Ar-only atmosphere was used in this second case.

Table 3.1. Fe growth conditions at the IMM-CNM and ICMAB-CSIC.

Ultra-high vacuum conditions (IMM-CNM)	
Ultra-high-vacuum chamber.	40 W, 0.75 mTorr and approximately room temperature. A subsequent annealing at for 30 min was performed to favour good crystallinity of the Fe .
High vacuum conditions (ICMAB-CSIC)	
95% Ar-5% H_2 reductive atmosphere	12 mTorr, 10 sccm (Ar-H_2), 20 W, ~room temperature (optional 30min annealing at the deposition pressure, 400 ºC)
Ar-only atmosphere and cold finger	12 mTorr, 20 sccm Ar, 20 W, room temperature (optional 20 min annealing at the deposition pressure, 400 ºC)

[6] This explains the need for the ex-situ Fe deposition at the IMM until the chamber modifications allowed non-oxidized Fe *in-situ* deposition.

3.5 CAPPING LAYERS AND METALLIC CONTACTS

Au and Pt are metals widely used as contacts, as they are some of the rare transition metals which maintain their properties when exposed to air, due to their low standard oxidation potential E^0_{ox}=-1.5 V [12]. Pt has much better adherence to ceramics or substrates because its surface can form bridging oxygen bonds to the substrate. Au, being a noble metal, cannot oxidize, so a non-oxide-forming non-noble metal is often deposited first (Ti, Ta, W...) to favour good adherence. However, these adherent layers fail at high T because oxidizable metals diffuse along grain boundaries in the noble metal layer to get oxidised at the free surface.

In most stacks, we use Pt as capping layer or even as metallic contacts on top, grown at room temperature and P=6×10^{-3} Torr in Ar atmosphere. In the *ex-situ* heterostructures, grown at IMM, we use Au/Ti capping layers (Au prevents oxidation, Ti favours good adherence).

3.6 GROWTH OF LAO/LSMO//STO(100)

Bulk LAO is an insulator with a large bandgap of 5-6 eV [13] and perovskite structure with a cell parameter of 3.790 Å. Heterostructures containing LSMO and LAO had been previously optimized in our group [14,15], so the same conditions were used for the growth of LAO (140 mTorr, 20 sscm of oxygen flux, and 800ºC). As can be seen from the TEM image in Fig 3.11a, the stack is highly crystalline with a STO(001)/LSMO(001)/LAO(001) epitaxial relationship and sharp clean interfaces. TEM images corroborate that the thickness of the LAO layer is of about 1.5 nm.

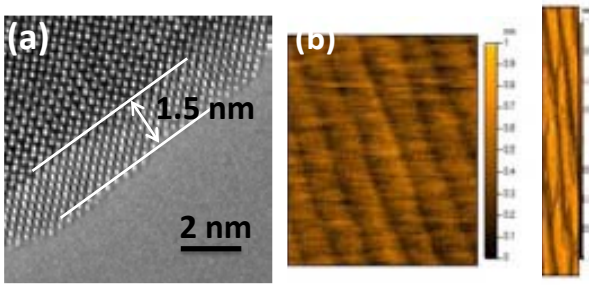

Fig 3.11. (a) TEM image of the LAO/LSMO interface; (b) AFM image of the LAO/LSMO//STO stack surface.

As seen from the AFM images in Fig 3.11b, LAO layer wets the surface of LSMO completely, exhibiting at the surface a terrace-steps morphology mimicking that of the LSMO surface beneath originated from the single termination of the STO substrate. The surface roughness of LCMO/LAO bilayers turns out to be very small [root mean squared roughness (R_{rms}) of 0.2 nm] and steps of about 0.4 nm, corresponding to one unit cell, are clearly visible.

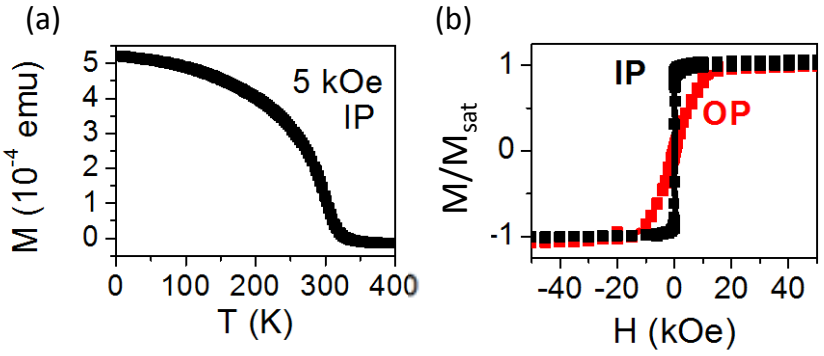

Fig 3.12. Magnetic measurements for a LAO/LSMO stack; (a) In-plane magnetization *vs.* T taken at 5 kOe, (b) In-plane and out-of-plane normalized magnetization *vs.* applied field at 10 K.

Magnetic measurements of the stack reveal in-plane anisotropy (shown in Fig 3.12) and no diminution of the T_C of LSMO caused by the growth of the LAO layer on top.

3.7 LSMO/MgO *VS.* LSMO/MgO/Pt

An LSMO//STO(100) film grown with no capping on top is optimized to a T_C of around 350 K, as explained in section 3.2, with a certain variability between batch of samples (the important point is to compare samples grown in the same batch). However, certain capping layers on top of an LSMO film grown in the same optimized conditions may alter its magnetic properties. This is the case of MgO/LSMO//STO bilayer, as illustrated in Fig 3.13. A reduction of T_C and a 5% reduction in saturation magnetization has already been reported for MgO/LSMO//STO and MgO/LSMO//STO [16] concomitant with a 15-18% increase in the Mn^{4+} content at the interface. In that case, the authors suggested the formation of $MgMnO_3$. For other cappings such as Au, STO and LAO, no such reduction of the T_C or increase in the oxidation state of the Mn ions was found.

A series of samples with and without Pt capping layers have been grown (samples A-D, their specifications listed in Table 3.2) and their magnetization *vs* temperature curves are depicted in Fig 3.13(left). As we have just mentioned, a bilayer of MgO on LSMO grown on an STO (sample B) has noticeably reduced T_C with respect to the bare LSMO film (sample A). This reduction of T_C is concomitant with a reduction of saturation magnetization at low temperatures. However, when we deposit *in situ* a capping layer of Pt on top of the bilayer (sample C), the original high T_C of bare LSMO is maintained.

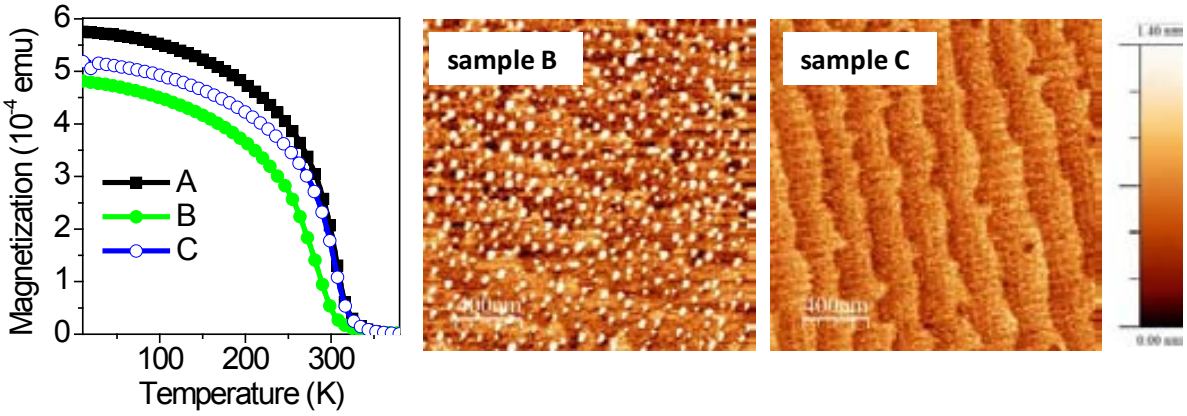

Fig 3.13. (left) Magnetization *vs*. temperature curves at 5 kOe for samples A,B and C, in which we focus on the loss of T_C for sample B; (centre and right) AFM topography images of samples B and C. For sample B, some "droplets are visible above the terraces, probably to brucite formation.

Table 3.2. Growth conditions for heterostructures containing LSMO and MgO prepared by RF magnetron sputtering.

Heterostructure (thickness in nm)		**relevant growth conditions**	**T_C (K)**	**c_{LSMO} (Å)**
A	LSMO		325	
B	LSMO/MgO(3)		300	3.8753
C	LSMO/MgO(3)/Pt		325	3.8719
D	LSMO/MgO(3)	MgO *ex-situ*	325	

In Fig 3.13 we show the AFM images of sample B and C. These illustrate that MgO wets well the LSMO layer, and the terraces from the TiO_2-terminated STO substrate are visible in both cases –even when Pt is grown on top the layer is very flat. However, for sample B, the uncapped MgO surface is full of small (and high) droplets, probably due to the deterioration of the surface resulting from the formation of brucite.

Besides this deterioration of the surface, which cannot –in principle- account for the loss of T_C of LSMO, a slight change in the lattice constant parameters of the LSMO is detected with high-resolution XRD. The non-capped sample (sample B) has an out-of-plane parameter of 3.8753Å, whilst for the Pt-capped sample (sample C) we obtain a value of 3.8719Å. This suggests it could have something to do with the oxygen contents of the LSMO: the sample with no Pt capping having a slightly superior cell parameter is coherent with a lower oxygen content of the LSMO underneath, resulting from the ionic radii increase when changing from Mn^{4+} to Mn^{3+} (or the creation of an oxygen vacancy). If that were indeed the case, we should conclude that Pt acts as a barrier for oxygen diffusion in this trilayer system.

Surprisingly, when growing the MgO *ex-situ*, the stack MgO/LSMO//STO (sample D) exhibits the same T_C as the optimized LSMO. We attribute this fact to the carbonation of the LSMO surface layer when exposed to air, which is hard to remove even with

relatively high T annealings, therefore suggesting that pumping of oxygen from the LSMO through the MgO only takes place when the LSMO/MgO interface is perfectly clean.

To probe the reversibility of this pumping of oxygen from the LSMO, a subsequent annealing was performed on sample B. The annealing conditions were those of LSMO (at 900 ºC during 1h) and a capping layer of Pt was *in-situ* sputtered after the annealing. However, after this process we did not recover larger T_C, so either the process is not reversible or the surface of the sample had been too damaged by hydroxylation.

To further inspect the LSMO/MgO interface, and test its cube on cube growth, we perform X-ray diffraction measurements (using a 2D area detector) for an *in-situ* grown Pt/MgO(40 nm)/LSMO//STO stack. The MgO [7] thickness was increased to ensure enough signal from diffraction. Fig 3.14 demonstrates perfect alignment between MgO(002) and LSMO(002) -hardly visible because of the proximity in lattice parameter with STO(200)-, as well as for Pt(111).

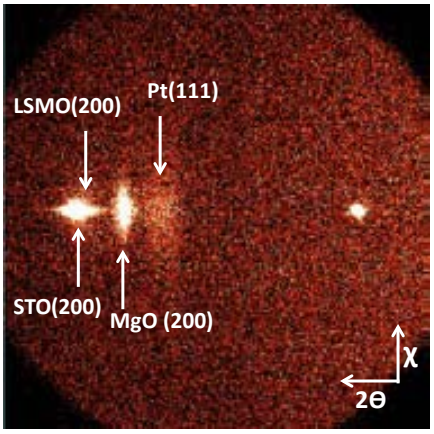

Fig 3.14. Θ-2Θ scan in a 2D detector (GADDS) of a Pt/MgO/LSMO//STO stack.

3.8 *EX-SITU* Au/Ti/Fe/MgO/LSMO//STO HETEROSTRUCTURES

An exploratory study of a magnetic tunnel junction is intended in Chapter 7. This section details the growth process for the Au/Ti/Fe/MgO/LSMO//STO samples and the performed characterization. Although the growth of a similar stack consisting of Fe/MgO/LSMO has already been reported using an MgO buffer layer in between the trilayer and the STO substrate [2], we decide not to use the buffer layer because of the better crystalline and magnetic properties of LSMO when grown directly on the STO substrate.

[7] MgO in this sample was grown at 600ºC, for better comparison with samples from section 3.8.

3.8.1 GROWTH CONDITIONS

Au(10 nm)/Ti(2 nm)/Fe(20 nm)/MgO(*t*)/LSMO(42 nm)//STO(100) samples were grown varying the MgO layer thickness. The heterostructures were grown in two different sputtering chambers. First, at the ICMAB, an LSMO layer was grown on an STO(100) substrate at the previously optimized conditions[8], followed by the deposition of MgO[9]. The thickness of the MgO layers varied from one sample to another from 2 to 6 unit cells (which corresponds to t=0.8 to 2.4 nm). The sample was then transferred to an ultra-high vacuum sputtering chamber in Instituto de Microelectrónica de Madrid (IMM-CNM). A 30 min annealing at 400 ºC was done to eliminate any possible contamination or hydroxylation of the MgO surface. After that, the Fe layer was grown using the parameters detailed in Table 3.1(IMM). Finally, Ti and Au capping layers were deposited[10].

3.8.2 X-RAY DIFFRACTION AND MAGNETIC CHARACTERIZATION

The lattice parameter of bcc Fe is 2.866Å, whilst MgO is rock salt structure of lattice parameter 4.213Å. The large difference between cell parameter causes Fe to adapt to the MgO lattice by an in-plane rotation of 45º (the diagonal of the Fe lattice parameter is $diag_{Fe} = \sqrt{2}a_{Fe} = 4{,}05$Å): Fe(001)[110]//MgO(001)[100], largely reducing the mismatch [12].

From the Θ/2Θ scan plotted in Fig 3.15a, we see that Au, Fe, LSMO and the substrate share the same out-of-plane orientation. The MgO layer is most surely too thin to give enough signal to be distinguishable from the background. To verify that we have epitaxial Fe and that a and b crystallographic orientations of all Fe crystallites are aligned, we probe one of its non-symmetric planes. We tilt the sample Ψ=45º with respect to the sample surface and scan along φ. As expected, we find 4 peaks corresponding to the planes (011), $(0\bar{1}1)$, $(\bar{1}01)$ and (101), which are related by simmetry (rotation around the z axis) (see Fig 3.15(b)).

To complete the X-ray characterization of the stack, we perform ω-scans of one of the reflections of STO, LSMO, Fe and Au. The full-width half maximum (FWHM) values of the observed peaks (0.21º, 0.26º, 2.4º and 2.8º, respectively, as shown in Fig 3.15c-f) give us an idea of the dispersion of the crystallites; more dispersion results in larger FWHM. All the obtained values (below 3º) are quite good.

[8] The conditions were 20 sccm O_2 flux, 0.25 Torr, 900 ºC and annealed 1 h at 350 Torr and 900 ºC.
[9] The conditions were 19 sccm O_2 flux, 247 mTorr, and 600 ºC.
[10] Both at an Ar pressure of 1.13 mTorr and room temperature.

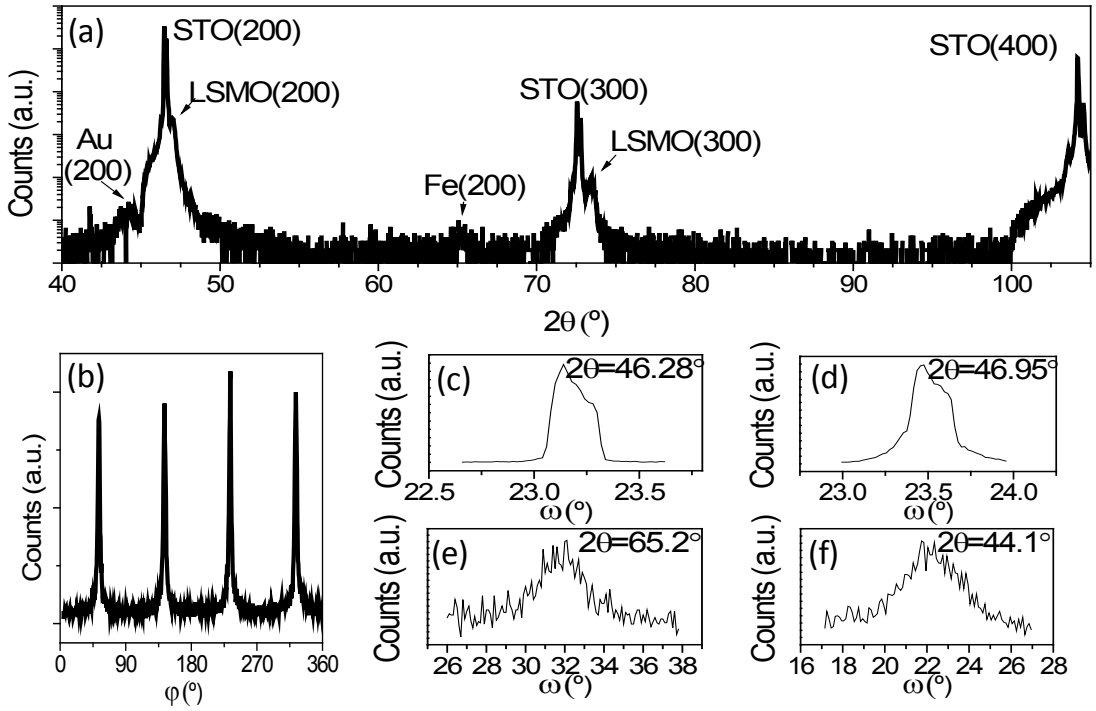

Fig 3.15. X-ray diffraction characterization of Au/Ti/Fe/MgO(2.4 nm)/LSMO//STO stack. (a) Θ-2Θ scan of the stack; (b) ϕ-scan (at ψ=45º) shows the epitaxiallity of the Fe layer; (c) ω-scan of the STO(200), (d) of the LSMO(200) peak;(e) peak of the Fe(200) peak ;(f) of the Au(200) peak.

The magnetic properties of a stack of Au(10 nm)/Ti(2 nm)/Fe(17 nm)/Mg(t)/LSMO (42 nm)//STO(100), for t=0.8 nm, are presented in Fig 3.16. Hysteresis loops for such a structure were performed by fixing the magnetic field along the (110) crystallographic orientation of the STO substrate (see Fig 3.16a), but equivalent measurements along the (100)STO were also carried out, presenting no notable magnetic anisotropy. The temperature dependence of magnetization, M(T), depicted in Fig 3.16b, reveals that the T_C of the LSMO bottom electrode has suffered a slight reduction with respect to its optimized value above RT.

Because of the reduced T_C of LSMO, at 300 K only the Fe electrode contributes to the magnetization of the stack. Thus, the coercive field (H_C) extracted from the M(H) measurement at 300 K (Fig 3.16a) for the Fe electrode is much larger than expected (we recall from section 3.4.1 that individual Fe films possess H_C=14 Oe). We may ascribe this larger coercive field to the presence of iron oxide FeO_x at the MgO/Fe interface, as will be further discussed in subsequent sections. Measurements for different stacks with different MgO thicknesses (t = 0.8, 1.2 and 2.4 nm were probed) show hysteresis loop with a single coercive field at 10 K. To explain the absence of a double loop we offer two possible explanations:

(1) First, the absence of a biloop is often interpreted as magnetic coupling existing between the electrodes. This is not a desirable condition, but the patterning of the junctions may change the coupling between electrodes (because of the

reduction in dimensionality and because only the top electrode is patterned in our configuration, as explained in Chapter 5).

(2) Second, it is worth noting that both electrodes possess similar H_C: in this case, the small difference between H_C of LSMO (around 50 Oe) and that of Fe-FeO_x (also ~50 Oe) could explain the impossibility of distinguishing two uncoupled switchings of the electrodes in the hysteresis cycles at 10 K. The low resolution from the measurement depicted at Fig 3.16a does not allow further interpretation.

The loss of Tc of the LSMO in an *in-situ*-grown Fe/MgO/LSMO trilayer will be studied more deeply in section 3.9.1. In such samples, hysteresis cycles were performed with higher resolution around the ±50 Oe range, and we do notice the presence of a small biloop feature.

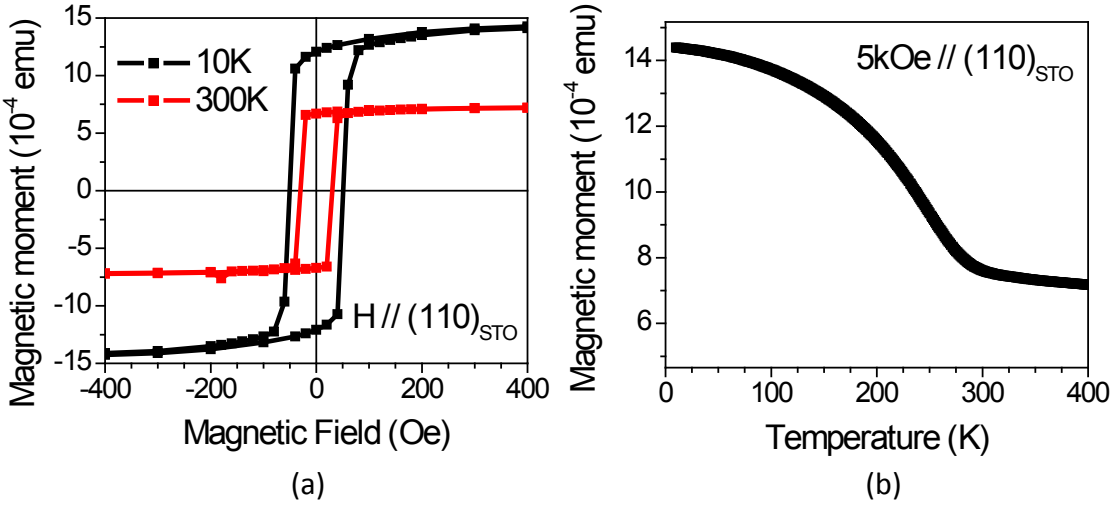

Fig 3.16. Magnetic characterization of a trilayer Au/Ti/Fe/MgO(0.8 nm)/LSMO//STO stack; (a) hysteresis loops show the electrodes are coupled, (b) magnetization *vs.* temperature curve shows reduction of Curie Temperature of the LSMO bottom electrode.

3.8.3 TEM AND EELS STUDY

After the measurement of the magnetic tunnel junctions (in Chapter 7), a cross section of the heterostructure is prepared by focused ion beam (FIB). The direction of the cut is along the (110)STO to maximize the possibility of distinguishing Mg and O atoms, as can be seen from Fig 3.17. A TEM image of the cross-section of the Au/Ti/Fe/MgO/LSMO//STO heterostructure is shown in Fig 3.18 in low magnification.

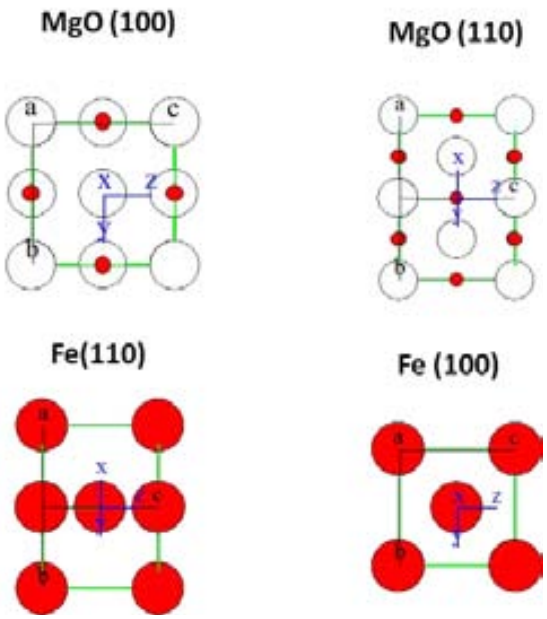

Fig 3.17. Sketch of the structure of MgO and Fe in the various orientations.

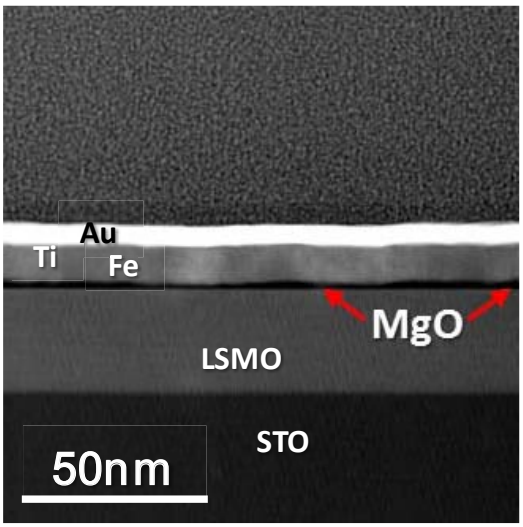

Fig 3.18. TEM image of the Au/Ti/Fe/MgO/LSMO//STO stack.

From the High-Angle Annular Dark field scanning transmission electron microscopy (HAADF-STEM) image in high magnification shown in Fig 3.19a, we determine that LSMO, MgO and Fe grow almost epitaxially following the relationship: (001)[110]LSMO// (001)[110]MgO// (001) [100]Fe. Whilst the LSMO/MgO interface is only slightly rough, the MgO/Fe interface is extremely wavy and poorly defined. From the diffraction pattern of all the layers in the stack (the superposition of which is found in Fig 3.19e), we establish that in the shown area, the MgO layer -as well as, consequently, the Fe layer- grows 2º offaxis with respect to the LSMO. The growth front is rotated about 2º for the MgO and Fe in this case, although in some other regions the rotation was even higher (around 4º), creating rough surfaces and leading to the

misalignment of the interfaces. Power spectra obtained in the different regions of the heterostructure confirm the epitaxial relationship between the layers (Fig 3.19, right).

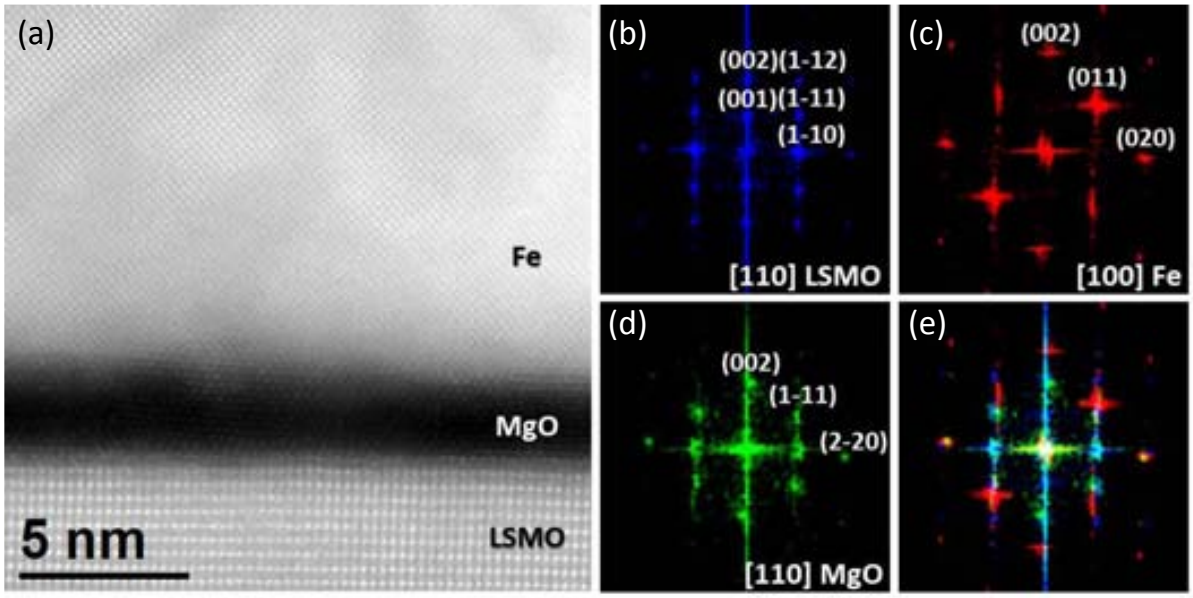

Fig 3.19. (a) High-angle annular dark field scanning transmission electron microscopy (HAADF-STEM) image of the cross-section of the trilayer Fe/MgO/LSMO and diffraction pattern for (b) LSMO,(c) Fe, (d) MgO and (e) superposition of the three diffraction patterns. In the latter, we see a slight tilt of the Fe and MgO diffraction peaks with respect to the ones for LSMO, thus indicating a slight tilt of the *c* axis for the MgO and the Fe with respect to the LSMO layer.

As we observed for *in-situ* growth of Pt/MgO/LSMO//STO, very flat surfaces are obtained (from AFM image in Fig 3.13c), where STO terraces are clearly visible, and a perfect cube-on-cube relationship is demonstrated between MgO and LSMO (discussed in Fig 3.14). Therefore, we attribute the observed 2-4º out-of-plane rotation between MgO and LSMO in the this *ex-situ*-grown stack to the fact that the grown MgO layer was very thin and exposed to air during the transport between the different deposition chambers, so that brucite was surely formed. Even if the annealing at 400ºC performed before the deposition of Fe eliminates all brucite, it may not recover the as-grown MgO layer, which is damaged: both effects of 2-4º misalignment and the MgO surface roughness before the Fe deposition are thus a consequence of such process.

A closer look to Fig 3.19 also reveals an intermediate layer composed of oxidized Fe, with presence of MgO too: this may be due to the roughness of the interface in the direction perpendicular to the image or to intermixing (leading to the the formation of some kind of iron oxide) –possibly both effects are present. Unfortunately, an EELS study of the cross section did not reveal any more significant information because the FIB procedure to obtain the cross section resulted in an inevitable reduction of the species and implantation of Ga ions, thus preventing the determination of the oxidation state of the Fe at the MgO/Fe interface and of the Mn valence at the LSMO/MgO interface.

We have seen in this section that *ex-situ* growth of Au/Ti/Fe/MgO/LSMO//STO heterostructures result in good crystallographic properties, although power spectra of TEM images point to a 2-4º rotation of the MgO film with respect to the LSMO layer, attributed to the consequence of formation of brucite due to exposure of MgO to air. TEM images also reveal a considerably rough Fe/MgO interface, with possible FeO_x. Magnetic measurements also show a reduced T_C for the LSMO layer, but we cannot conclude whether the Fe/MgO electrodes are magnetically coupled with each other, as the presence of FeO_x changes the coercive field of the top electrode and its value is extremely similar to that of the LSMO electrode (see next section). Magnetoresistive measurements of junctions made out of such samples (with MgO thicknesses of t=0.8, 1.2 and 2.4 nm) are analysed in Chapter 7.

Avoiding the brucite formation by *in-situ* growth of the whole stack is therefore expected to result in high T_C of LSMO, flat interfaces and cube-on-cube relationship between LSMO and MgO layers. Therefore, in the next section, *in-situ* heterostructures are grown and characterized, seeking to understand and to overcome these various setbacks. The oxidation at the Fe/MgO interface will also be addressed.

3.9 *IN-SITU* GROWTH OF Pt/Fe/MgO/LSMO//STO HETEROSTRUCTURES

From section 3.6, we have seen that *ex-situ* grown Pt/Fe/MgO/LSMO//STO samples do not show optimal properties. In this section we tackle the two main problems that we have found for *ex-situ* growth: (1) the reduced T_C for LSMO in the stack and (2) the oxidation of Fe at the Fe/MgO interface. A third problem, the 2-4º rotation of MgO with respect to LSMO, is already attributed to the *ex-situ* preparation conditions (from comparison with *in-situ* grown Pt/MgO/LSMO heterostructures). To that end, we characterize various *in-situ* grown Pt/Fe/MgO/LSMO//STO heterostructures and study the origin of the reduction of the T_C of LSMO for certain deposition conditions and the formation of FeO_x at the Fe/MgO interfaces inherent to the *in-situ* growth of such heterostructures.

3.9.1 T_C REDUCTION IN LSMO/MgO/Fe/Pt *IN-SITU*-GROWN HETEROSTRUCTURES

The growth of a stack consisting of Pt/Fe/MgO/LSMO//STO is done using different deposition conditions for Fe layer growth (at IC MAB), as already mentioned in section 3.4.

For Fe deposited in a reductive atmosphere (95%Ar + 5%H_2), similar to that used in Ref [17], we measure a drastic reduction of T_C for LSMO (T_C below 250K). Annealings at various temperatures (up to 750ºC) in reductive Ar-H_2 atmosphere of an LSMO//STO sample (with T_C=325K) do not change its magnetic properties. The same holds for *ex-situ* grown MgO/LSMO//STO stacks. However, when Fe (Ar-H_2) is grown, the Tc of LSMO drops considerably.

To elucidate whether Fe could be absorbing oxygen from the LSMO through the MgO barrier, we tried introducing an intermediate layer of $LaAlO_3$ (LAO) between the LSMO and the MgO. As pinhole-free LAO is impermeable to oxygen and its interface with LSMO does not modify the valence of Mn [14], a high T_C for this heterostructure would indicate that the origin of the loss of T_C resides in the MgO/LSMO interface, maybe through the formation of $MgMnO_3$. However, the T_C found for LSMO in the heterostructure Pt/Fe/MgO/LAO/LSMO//STO was even more reduced (below 170K).

XRD measurements showed that the reduction of T_C in these samples (with and without LAO intermediate layer) was concomitant with the adjustment of the lattice parameters of LSMO to those of the STO substrate. These results suggest that the origin of the reduction of T_C in the case of the growth of Fe in Ar-H_2 atmosphere is related to the formation of the plasma with reductive atmosphere, which reduces the LSMO by creating oxygen vacancies, also increasing the cell parameter.

Therefore, we proceed to grow Fe in non-reductive conditions. For Fe grown in Ar-only atmosphere (using a cold finger to prevent Fe oxidation), a stack of Pt/Fe/MgO/LSMO//STO does not show such dramatic reduction of the T_C of LSMO, but a T_C just above room temperature. In what follows, we discuss the oxidation at the MgO/Fe interface and the difference in T_C between two samples with and without annealing after Fe growth.

3.9.2 Effects of annealing after Fe deposition on the formation of FeO_x

It is worth mentioning that a lot of discussion about the presence or absence of an interfacial oxide layer between Fe-based ferromagnets (FM) and MgO has been reported [18]. This is particularly important for FM/MgO/FM tunnel junctions with bcc FM such as Fe, CoFe and CoFeB, as the quality of the interfaces is critical for the performance of such devices. The presence of an FeO_x layer is predicted to result in a dramatic reduction of the TMR ratio, although experimental results show a more modest reduction [19]. Studies using numerous characterization techniques reveal presence of FeO_x in most cases –but for a few exceptions. These seem to point towards the relevance of the growth technique; only e-beam deposition produces very little or no FeO_x at the interface. A thermal annealing is reported to result in a large improvement of the tunnelling magnetoresistance for these magnetic tunnel junctions. Besides decreasing interfacial roughness, the annealing process also changes de oxidation state of the FeO_x layer present in most of these structures [18].

In this work, we have studied the influence of the *in-situ* annealing after the Fe deposition in the final properties of the whole Pt/Fe/MgO/LSMO//STO stack. For that purpose, two different samples were grown of this heterostructure, one with annealed Fe and the other one with no *in-situ* annealing after the Fe deposition. Both structures present a very flat surface for both (as visible from the AFM images in Fig 3.20, where the R_{rms} is below 2.4 Å) and a study of the magnetic properties reveals that there is little

difference in T_C between the annealed and non-annealed Fe samples (see Fig 3.21a and inset).

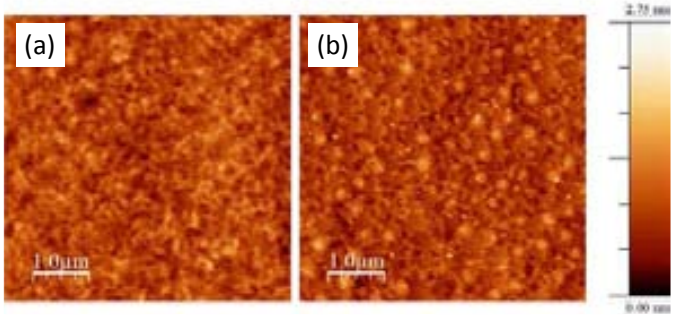

Fig 3.20. AFM images of Pt/Fe/MgO/LSMO//STO (a) without and (b) with annealing after Fe deposition reveal extremely flat surfaces, which indicate a R_{rms} below 2.4 Å.

The hysteresis loops from Fig 3.21b also show different shape for both samples, both presenting a "biloop" structure, most surely indicative of a certain decoupling between both ferromagnetic electrodes. The non-annealed-Fe sample presents a biloop (which can be more easily seen at the inset), with two very similar coercive fields around 30 Oe. The annealed-Fe sample also shows a small coercive field around 30 Oe, besides a larger coercive field of around 80 Oe, which is not as abrupt but more rotation-like switching. We suggest that the LSMO is responsible for the coercive field around 30 Oe, and the coupling of the Fe and the different FeO_x present at the interface. The main difference resides in the higher-H_C contribution for the annealed Fe sample. For both samples, we can see biloops indicating decoupled LSMO and Fe electrodes.

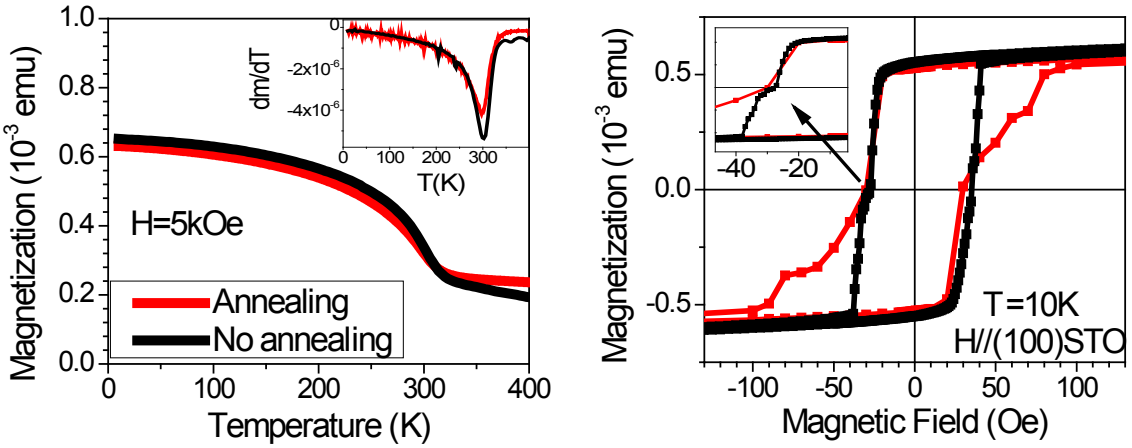

Fig 3.21. Magnetic measurements for samples of Pt/Fe/MgO/LSMO//STO where Fe has been grown with no *in-situ* post annealing (in red) and after an *in-situ* post annealing (in black). (a) Magnetization vs Temperature curves for both samples, inset shows its derivative. (b) Hysteresis loops at 10K show different biloop shapes.

To probe the quality of the Fe/MgO interface, we performed XPS measurements before and after various etch cycles, which use Ar ions. In Fig 3.22 we plot the XPS spectra in

the Fe 2p and Mg 1s regions for two samples of Pt/Fe/MgO(3.7 nm)/LSMO(~40 nm)//STO. In (b) the Fe layer was annealed *in-situ* at 400 ºC during 30 min after its deposition, whilst in (a) the Fe layer was not annealed. Black curves show the XPS spectra before etching, but the presence of the Pt top layer considerably weakens the XPS signal of Fe. However, it is sufficient to see that there is no oxidation at the Pt/Fe interface. In red (etch cycle 1), we show the spectra after the first etch of 30 s, in which the metallic Fe peak is clearly visible in both samples. For etch cycle 3, an extra peak at around 710 eV in Binding Energy appears in both samples, concomitant with the apparition of the Mg 1*s* peak around 1304 eV. This occurs in both samples, although the metallic peak is much less intense in the Fe-annealed sample (shown in (b)). This peak at around 710 eV is quite wide and could be attributed to a coexistence of Fe_2O_3 (709.6 eV) and Fe_3O_4 (710.6 eV). For etch cycle 4, in both samples the peak becomes thinner and tends to higher energies, suggesting only Fe_3O_4 is present [20].

It is worth noting that metals can easily suffer reduction when sputtered by Ar ions, even at low energies. But as our results indicate higher oxidation of the Fe for each sputter cycle, no doubts arise about the reliability of these data interpretation.

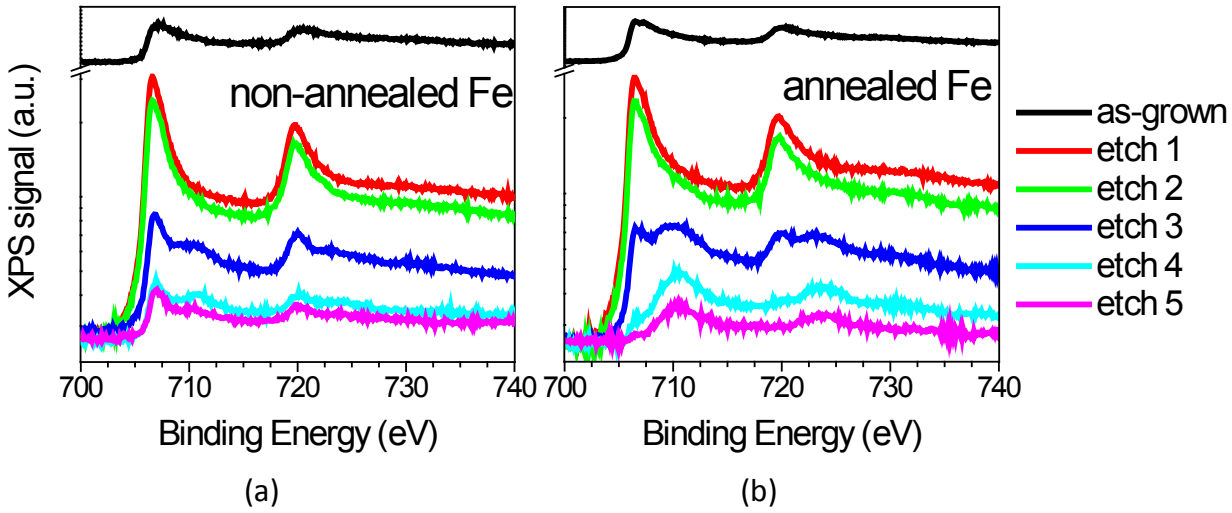

Fig 3.22. XPS spectra in the Fe 2*p* and Mg 1*s* regions of a Pt/Fe/MgO/LSMO//STO stack for different sample preparation conditions: (a) Fe grown with no *in-situ* annealing after deposition and (b) Fe grown with an *in-situ* annealing at 400ºC for 30m in after the deposition, in the presence of the cold finger.

As we have evidenced from the XPS measurements, a larger oxidation of the Fe layer is found for annealed Fe samples. Although this is contrary to the tendency reported for MgO/Fe interfaces in Fe/MgO/Fe structures, note that in our case the LSMO electrode may provide an extra source of oxygen for the Fe interface to oxidize. At the same time, an increase in the out-of-plane cell parameter of LSMO for the Fe-annealed sample is seen through high-resolution XRD (shown in Fig 3.23b). This is also coherent with the reduction of Mn^{4+} to Mn^{3+} or the formation of oxygen vacancies. Thus, Fe may be

pumping oxygen from the LSMO through the MgO layer. At the same time, a shift in the peak position of (200)Fe indicates larger cell parameter, fruit of the relaxation of the structure caused by the annealing (see Fig 3.23a and inset). The Fe thickness is 8.4 nm for both samples and there is no difference in peak width between the samples that could suggest less crystallinity or oxidation of Fe. Surprisingly, a peak appears for (111)-oriented Pt for the Fe-annealed sample. This could indicate that annealing flattens the Fe surface, although further study would be required to confirm this fact.

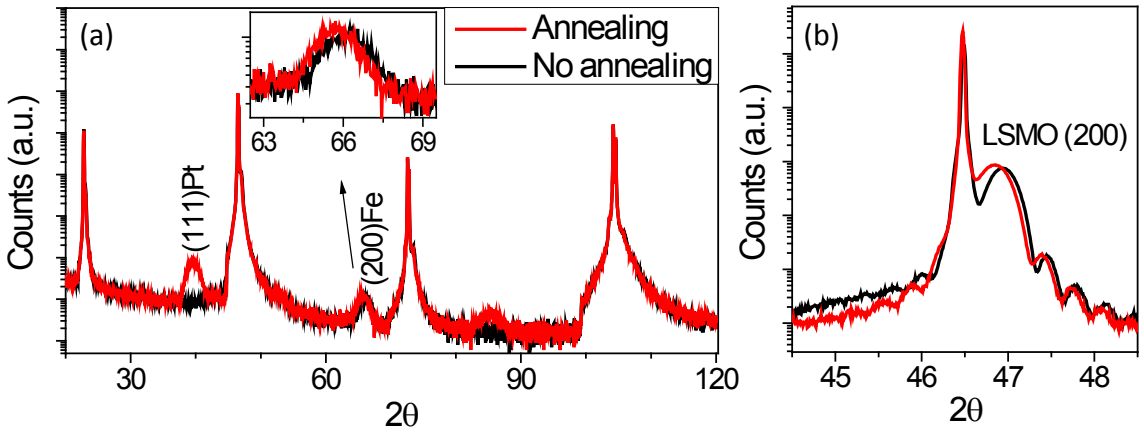

Fig 3.23. High resolution XRD for Pt/Fe/MgO/LSMO//STO samples with and without *in-situ* annealing after Fe deposition; (a) Θ/2Θ scan for all the range, inset focuses on the Fe(200); (b) (200) LSMO peak.

From this section we conclude that it is not possible to grow *in-situ* Fe/MgO/LSMO heterostructures with high T_C and non-oxidized MgO/Fe interfaces. Sputtering in reductive (Ar-H_2) atmosphere has a powerful effect of creating oxygen vacancies in the LSMO layer, even if the latter is capped by a thin MgO layer or an LAO layer, thus strongly diminishing its T_C. But even for sputtering in Ar-only atmosphere (and using the cold finger), for perfectly clean LSMO/MgO interfaces (as is the case for *in-situ* growth) Fe absorbs oxygen from the LSMO –through the MgO layer. We found that this effect is further enhanced when an annealing is performed after the Fe growth.

3.10 SUMMARY

This chapter focuses on the optimization of thin films to grow heterostructures for tunnel junctions with an LSMO bottom electrode. After an initial optimization of the growth process of each material separately, interfacial effects are carefully analysed. *In-situ*-grown MgO/LSMO bilayers have revealed a decrease in the T_C of LSMO, which is avoided if Pt is *in-situ* grown on top. We suggest irreversible loss of oxygen in LSMO –through the MgO layer- as origin of this reduction. However, Pt/MgO/LSMO layers show very flat surface, high epitaxiallity and cube-on-cube growth of MgO on LSMO.

Special effort has been devoted to the growth of Fe/MgO/LSMO stacks for magnetic tunnel junctions with filtering properties. For Fe/MgO/LSMO heterostructures grown *ex-situ*, three main problems have been detected: (1) a reduced T_C of LSMO in the stack, (2) a 2-4º rotation of the out-of-plane parameter for MgO with respect to the LSMO bottom layer and (3) a rough MgO/Fe interface, with the formation of FeO_x. Due to the *ex-situ* growth conditions, we can ascribe the low T_C to the mentioned reduction of LSMO due to the extraction of oxygen in MgO/LSMO bilayers. Furthermore, we point to a damaged MgO thin layer after hydroxylation from air exposure (even after eliminating brucite by an annealing) as the cause for the 2-4º rotation of MgO with respect to LSMO and for the rough MgO surface (prior to Fe deposition).

The mentioned problems being linked to the *ex-situ* growth, one would expect that they would be avoided by preventing MgO exposure to air. However, the analysis of *in-situ* Pt/Fe/MgO/LSMO stacks reveals a much more complex scenario. *In-situ*-grown Pt/Fe/MgO/LSMO stacks are prepared in different conditions. The use of Ar-H_2 atmosphere is observed to dramatically reduce the T_C of LSMO and increment the lattice parameter –indicative of the presence of oxygen vacancies-, so it is ruled out. But growing Fe in Ar-only atmosphere also yields a small reduction of T_C and the formation of FeO_x at the MgO/Fe interface is observed. An *in-situ* annealing after the Fe deposition is not found to improve the properties of the stack, but enhances the formation of FeO_x. Therefore, we conclude that we cannot grow *in-situ* Fe/MgO/LSMO heterostructures with high T_C and without FeO_x at the Fe/MgO interface, and suggest that transfer of oxygen from LSMO to MgO/Fe interface is at the core of both effects. *Ex-situ* growth of MgO on LSMO is found to maintain the high T_C of LSMO, which we attribute to carbonation of the LSMO surface, so further study on that point may provide insight as to the fabrication of LSMO/MgO/Fe magnetic tunnel junctions with improved performances.

3.11 REFERENCES

[1] Ohtomo A., Hwang H.Y.; "A high-mobility electron gas at the LaAlO3/SrTiO3 heterointerface". *Nature* 427; **2004**: 423–6. doi:10.1038/nature02308.

[2] Martinez-Boubeta C., Konstantinovic Z., Balcells L., Estrade S., Arbiol J., Cebollada A., et al.; "Epitaxial Integration of La2/3Sr1/3MnO3 and Fe Films by the Use of a MgO Spacer". *Cryst. Growth Des.* 10; **2010**: 1017–20. doi:10.1021/cg900866g.

[3] Koster G., Rijnders G., Blank D.H.A., Rogalla H.; "Surface morphology determined by (001) single-crystal SrTiO3 termination". *Phys. C* 339; **2000**: 215–30. doi:10.1016/s0921-4534(00)00363-4.

[4] Valencia S., Gaupp A., Gudat W., Abad L., Balcells L., Martinez B.; "Impact of microstructure on the Mn valence of La2/3Ca1/3MnO3 thin films". *Phys. Rev. B* 75; **2007**. doi:10.1103/PhysRevB.75.184431.

[5] Iwahori K., Watanabe S., Kawai M., Mizuno K., Sasaki K., Yoshimoto M.; "Nanoscale composition analysis of atomically flat SrTiO3(001) by friction force microscopy". *J. Appl. Phys.* 88; **2000**: 7099–103. doi:10.1063/1.1328065.

[6] Sandiumenge F., Santiso J., Balcells L., Konstantinovic Z., Roqueta J., Pomar A., et al.; "Competing Misfit Relaxation Mechanisms in Epitaxial Correlated Oxides". *Phys. Rev. Lett.* 110; **2013**. doi:10.1103/PhysRevLett.110.107206.

[7] Nagamine Y., Maehara H., Tsunekawa K., Djayaprawira D.D., Watanabe N., Yuasa S., et al.; "Ultralow resistance-area product of 0.4 Omega(mu m)(2) and high magnetoresistance above 50% in CoFeB/MgO/CoFeB magnetic tunnel junctions". *Appl. Phys. Lett.* 89; **2006**. doi:10.1063/1.2352046.

[8] Yuasa S., Nagahama T., Fukushima A., Suzuki Y., Ando K.; "Giant room-temperature magnetoresistance in single-crystal Fe/MgO/Fe magnetic tunnel junctions". *Nat. Mater.* 3; **2004**: 868–71. doi:10.1038/nmat1257.

[9] Tsunekawa K., Djayaprawira D.D., Nagai M., Maehara H., Yamagata S., Watanabe N., et al.; "Giant tunneling magnetoresistance effect in low-resistance CoFeB/MgO(001)/CoFeB magnetic tunnel junctions for read-head applications". *Appl. Phys. Lett.* 87; **2005**. doi:10.1063/1.2012525.

[10] Martínez-Boubeta C., Beltrán J.I., Balcells L., Konstantinović Z., Valencia S., Schmitz D., et al.; "Ferromagnetism in transparent thin films of MgO". *Phys. Rev. B* 82; **2010**: 024405. doi:10.1103/PhysRevB.82.024405.

[11] Balcells L., Beltran J.I., Martinez-Boubeta C., Konstantinovic Z., Arbiol J., Martinez B.; "Aging of magnetic properties in MgO films". *Appl. Phys. Lett.* 97; **2010**. doi:10.1063/1.3527963.

[12] Martínez Boubeta C., Cebollada Navarro P.A.; Heteroestructuras Fe/MgO(001): Epitaxia y Propiedades Magnéticas. Universidad Complutense de Madrid, **2003**.

[13] Lim S.-G., Kriventsov S., Jackson T.N., Haeni J.H., Schlom D.G., Balbashov A.M., et al.; "Dielectric functions and optical bandgaps of high-K dielectrics for metal-oxide-semiconductor field-effect transistors by far ultraviolet spectroscopic ellipsometry". *J. Appl. Phys.* 91; **2002**: 4500. doi:10.1063/1.1456246.

[14] Valencia S., Konstantinovic Z., Schmitz D., Gaupp A., Balcells L., Martinez B.; "Interfacial effects in manganite thin films with different capping layers of interest for spintronic applications". *Phys. Rev. B* 84; **2011**: 024413. doi:024413 10.1103/PhysRevB.84.024413.

[15] Valencia S., Peña L., Konstantinovic Z., Balcells L., Galceran R., Schmitz D., et al.; "Intrinsic antiferromagnetic/insulating phase at manganite surfaces and interfaces.". *J. Phys. Condens. Matter* 26; **2014**: 166001. doi:10.1088/0953-8984/26/16/166001.

[16] Valencia S., Konstantinovic Z., Gaupp A., Schmitz D., Balcells L., Martinez B.; "Interfacial effects in La(2/3)Sr(1/3)MnO(3) thin films with different complex oxide capping layers". *J. Appl. Phys.* 109; **2011**. doi:07d718 10.1063/1.3545814.

[17] Wu X., Zhang Z., Meng J.; "Breakdown by magnetic field in a La0.7Sr0.3MnO3/MgO/Fe spin valve". *Appl. Phys. Lett.* 100; **2012**. doi:10.1063/1.3696670.

[18] Telesca D., Sinkovic B., Yang S.-H., Parkin S.S.P.; "X-ray studies of interface Fe-oxide in annealed MgO based magnetic tunneling junctions". *J. Electron Spectros. Relat. Phenomena* 185; **2012**: 133–9. doi:10.1016/j.elspec.2012.04.002.

[19] Zermatten P.-J., Bonell F., Andrieu S., Chshiev M., Tiusan C., Schuhl A., et al.; "Influence of Oxygen Monolayer at Fe/MgO Interface on Transport Properties in

Fe/MgO/Fe(001) Magnetic Tunnel Junctions". *Appl. Phys. Express* 5; **2012**: 023001. doi:10.1143/APEX.5.023001.

[20] "Thermo Scientific XPS" 2014; online. http://xpssimplified.com/ (accessed December 22, 2014).

CHAPTER 4. La_2CoMnO_6 FOR SPIN FILTERING APPLICATIONS

The main issue regarding spin filter junctions is the scarcity of ferromagnetic insulators [1,2]. The most simple ones (EuO, EuS, EuSe) have already been assayed, as well as some perovskites ($BiMnO_3$ or $YTiO_3$), but their main drawback is their T_C below 120 K [3]. In this sense, ferrites are promising candidates because of their T_C above room temperature. Such is the case for $NiFe_2O_6$, for example, although its TMR has been seen to vanish by 150 K. For $CoFe_2O_6$, TMR has been achieved up to room temperature, probably due to the high quality of the barrier. Indeed, obtaining high-quality thin films is crucial towards achieving high spin-filter efficiency.

La_2CoMnO_6 is an insulating ferromagnet and as such, could be a good candidate for magnetically active insulating barriers in spin filters. Its structure is a double perovskite $A_2BB'O_6$ with B and B' sites occupied by Mn and Co ions, as in Fig 2.1b. This material has already been studied in bulk (but very few reports on PLD-grown films) due to its potential as magnetodielectric [4–8]. Its T_C in bulk is around 230 K and its low T magnetization is 6 μ_B/f.u. for samples with high degree of Mn/Co ordering. This is the expected value for a FM ordering of Co^{2+} (in high spin state, S=3) and Mn^{4+} (S=3).

In this chapter, we strive to obtain high-quality thin films of this material, and characterize them to test their suitability in spin-filter barriers.

4.1 OPTIMIZATION OF La_2CoMnO_6 THIN FILMS

In this section, we optimize the growth of La_2CoMnO_6 (LCMO) thin films on STO(100) substrates by RF magnetron sputtering, for samples around 20 nm. The use of such films for devices such as spin filters requires even thinner films. However, the optimization has been done for ~20 nm-thick films because of the intrinsic difficulty of characterizing thinner films (of the order of 5 nm, for example). In the literature, thicker films of around 100 nm have been grown by pulsed laser deposition (PLD) [9]. These previous experimental reports suggest that magnetic properties are strongly dependent on growth conditions: when samples are grown under low oxygen pressure the T_C is around 100 K while increasing oxygen partial pressure (0.2 Torr and above) T_C values around 230 K are achieved. Nevertheless, there is no clear consensus on whether this variation of T_C comes from differences on the Co/Mn cationic ordering [10] or from changes in the oxygen stoichiometry [11]. In this section we justify why we attribute the variation of T_C to different oxygen stoichiometry. After that, we take three representative samples with different oxygen content and perform a full magnetic and structural characterization, to establish whether our samples are fully ordered and to probe the different properties which are indispensable for a spin filter barrier.

4.1.1 INFLUENCE OF GROWTH PARAMETERS ON THE CURIE TEMPERATURE

The films in this work were grown by sputtering from a target prepared by solid state route according to the details in reference [12]. The heater temperatures were between 800 ºC and 900 ºC (substrate temperature must be slightly below heater temperature), the partial oxygen pressure (p_{O2}) ranged from 0.2 to 0.4 Torr and different in situ thermal treatments after deposition were tried. The thickness of LCMO films, determined by X-ray reflectivity, depends on the oxygen pressure and spans from 35 nm (0.2 Torr) to 20 nm (0.4 Torr).

Fig 4.1(a-c) shows the magnetization *vs.* temperature curves, measured following a zero-field-cooling field-cooling (ZFC-FC) process under H =1 kOe, for the most representative samples (their preparation conditions are shown in Table 4.1). Top panel illustrates the dependence of magnetic properties on growth temperature (T_g): increasing T_g from 800 ºC to 900 ºC promotes an increase of T_C from ~130 K to ~160 K. The dependence of T_C on p_{O2} at a fixed T_g is evidenced in Fig 4.1(b), which reveals that lowering p_{O2} from 400 to 300 mTorr promotes the reduction of T_C down to ~120 K.

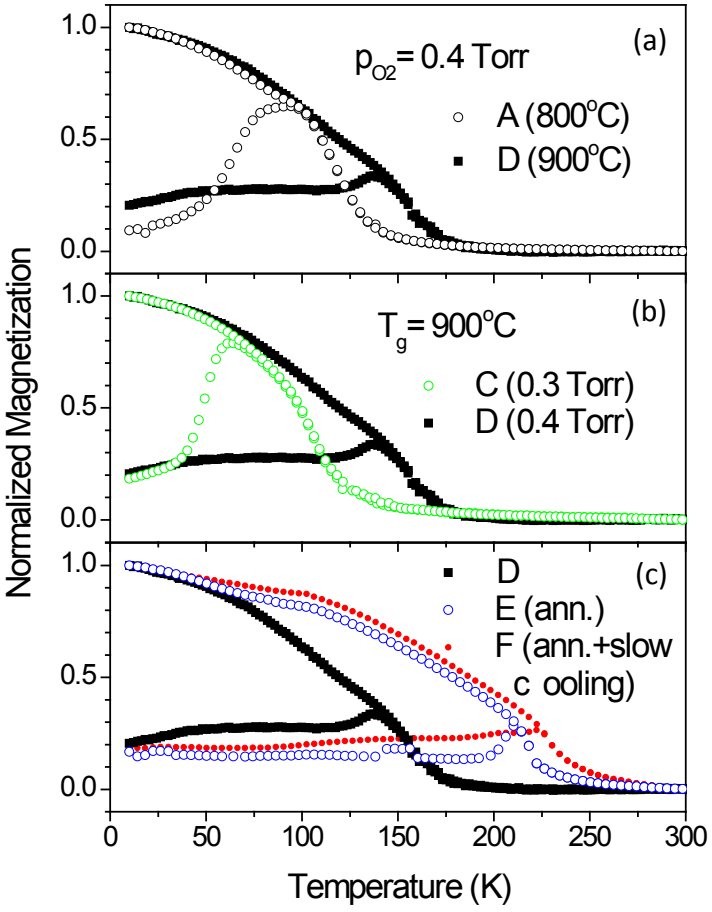

Fig 4.1. Normalized M(T) of different LCMO films for H||$(100)_{STO}$ (H=1 kOe); (a) effect of growth temperature; (b) effect of oxygen partial pressure and (c) effect of annealing at 400Torr and effect of lowering cooling rate.

To further enhance T_C, we have performed different *in-situ* annealing processes and depicted the results in Fig 4.1c. This figure shows that by annealing at 900 ºC and p_{O2}= 400 Torr we obtain T_C values of about 225 K, close to that reported for bulk samples [13,14] and films grown by PLD [9–11]. However, we note that in some reported cases, PLD films were grown at 800 ºC and no annealing process, further that a relatively fast cooling down to room temperature, was needed to obtain a high T_C, whilst for RF sputtered films T_g=800 ºC is not enough, even after an *in-situ* annealing at p_{O2}=400 Torr (sample B, not shown). Furthermore, we have evaluated the influence of lowering the cooling rate after the annealing (sample F), observing a slight increase of Tc (~230 K).

Table 4.1. Growth conditions of the La_2CoMnO_6 films prepared by RF magnetron sputtering.

Name	T(ºC)	p_{O2} (Torr)	T_C(K)	Thermal treatment
A	800	0.4	130	Fast Cooling (25 ºC/min, p_{O2}=0.4 Torr)
B	800	0.4	140	Annealing 1 h@800 ºC, p_{O2}=0.4 Torr; cooling 10 ºC/min
C	900	0.3	120	Fast Cooling (25 ºC/min, p_{O2}=0.3 Torr)
D	900	0.4	160	Fast Cooling (25 ºC/min, p_{O2}=0.4 Torr)
E	900	0.4	225	Annealing 1 h@900 ºC, p_{O2}=400 Torr; cooling 10 ºC/min
F	900	0.4	230	Annealing 1 h@900 ºC, p_{O2}=400 Torr; cooling 1 ºC/min
G	900	0.4	150	Annealing 1 h@900 ºC, p_{O2}=2×10^{-6} Torr; cooling 10 ºC/min
H	900	0.4	150	Annealing 1 h@900 ºC, p_{O2}=0.4 Torr; cooling 10 ºC/min

The differences in the growth conditions of the studied samples are the thermal treatment and the p_{O2} in the chamber during the annealing. In order to discern which of these two factors determines the change in T_C, we have prepared a new sample (G) that was annealed at 900 ºC during 1 hour but under vacuum conditions (2×10^{-6} Torr), in contrast to the 400 Torr used for samples E and F. This sample exhibits low T_C (~150 K) very similar to that of sample D, even when its thermal history is identical to that of sample E, but with a reduced p_{O2} pressure during the annealing. Therefore, we attribute the increase of T_C to the larger oxygen content in the films annealed at high p_{O2} (and at high enough temperature, vide ultra). This result is in accordance with previous studies in bulk $La_2CoMnO_{6-\delta}$ samples [13] where low T_C (~150 K) was reported for samples with $\delta \geq 0.05(1)$ but high T_C (~225 K) was found when the oxygen deficiency is $\delta \leq 0.02(1)$; and also in agreement with the conclusions derived in reference [11] for thin films grown by PLD, where the change in T_C is attributed to variations of oxygen stoichiometry. However, the annealing temperature also plays a relevant role. As shown

in the case of sample B, an annealing process at 800 ºC (and p_{O2}=400 Torr) is not enough to increase T_C, which indicates low oxygen content, even for high p_{O2}. This result proves that oxygen diffusion proceeds slowly at 800 ºC but much faster at 900 ºC. Hence, a threshold temperature, between these two values, must be surpassed to reach an efficient oxygen uptake and diffusion inside the films. The behaviour shown by sample F (slowly cooled from 900 ºC) can be explained when considering that the slow cooling process implies a longer time above this threshold temperature, so resulting in a larger oxygen uptake. In fact, samples with prolonged annealing time (two hours or more) exhibit similar magnetic behaviour to that of sample F. In other words, final oxygen content of the sample depends on the oxygen pressure and temperature during the annealing (and its duration).

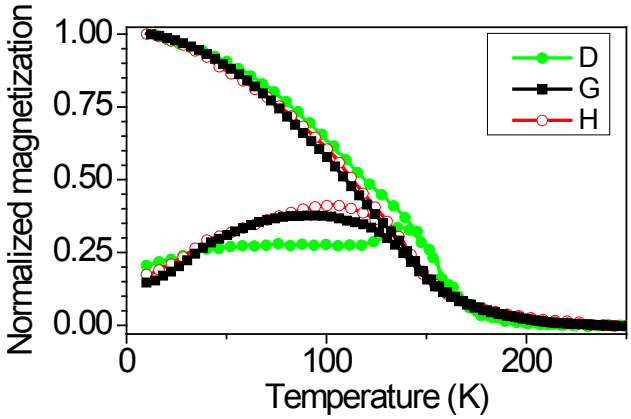

Fig 4.2. Normalized in-plane M(T) (taken at H=1 kOe) of films D (not annealed), G (annealed in vacuum) and H (annealed at low p_{O2}=0.4 Torr).

According to our reasoning, sample D (which has not received extra thermal treatment after the LCMO deposition) should have the same T_C or slightly lower than that of samples G and H, which have spent larger amount of time at high temperature. As shown in Fig 4.2 and also in Table 4.1, sample D shows slightly higher T_C. We must point out, however, that at such low oxygen pressures as 0.4 Torr or less, we do not expect oxygen uptake. It also happens that for low oxygenated samples (those without annealing at high pressure and temperature), the T_C may show a slight variation that we attribute to small variations in the oxygen content as they have not reached a well-defined equilibrium point. In any case, these variations are far from the 60-70 K of increase in T_C when the high-temperature high-p_{O2} annealing is performed whilst the differences in T_C between sample D and samples G and H are within this dispersion.

Moreover, one has to take into account that the reactivity of the oxygen pressure when the sputtering plasma is on (during the growth) is much higher than when the sputtering plasma is off. Thus, if oxygen pressure is not increased from the growth process to the annealing process, the reactivity of oxygen decreases and even a loss of oxygen could take place during the annealing process.

Fig 4.2 also reveals a change of shape of the ZFC-FC measurement between non-annealed sample (D) and annealed ones (G and H). We attribute this to a homogenization of the oxygen content throughout the film due to the annealing. This homogenization can make regions with higher oxygen to become less oxygenated giving rise to a certain change (decrease) in T_C.

4.1.2 STRUCTURAL CHARACTERIZATION

To clarify the possible relation between the magnetic behaviour and the structure of the samples we have carefully analysed samples C, D and F by means of synchrotron diffraction at KMC2 beamline (BESSY-II at Helmholtz-Zentrum, Berlin), which is equipped with a two dimensional General Area Detector Diffraction System (GADDS) for a deeper structural characterization.

The reciprocal space maps of the (103) diffraction peak (indexed with respect to STO, and shown in Fig 4.3) reveal that the films are epitaxial with the same in-plane lattice parameters as the STO substrate. Therefore, no relaxation of the tensile strain due to lattice mismatch with the substrate occurs during annealing processes. Rods along Q_Z show thickness fringes revealing the high crystal quality of the prepared films.

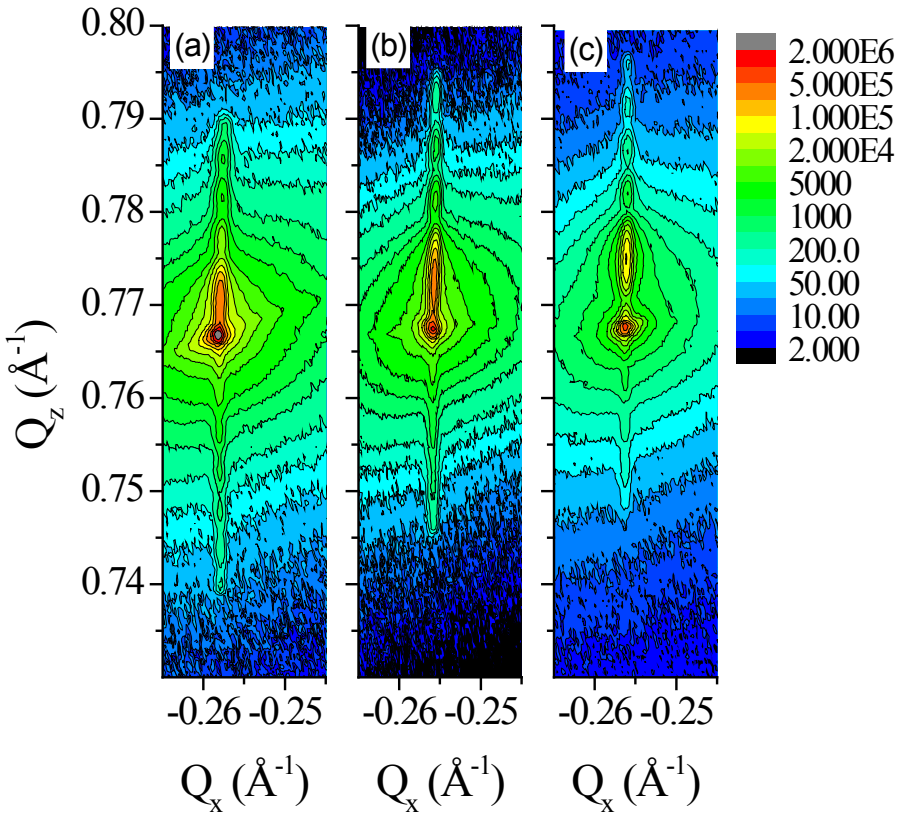

Fig 4.3. Reciprocal space map of the (103) reflection measured by using synchrotron radiation for the three selected samples with increasing oxygen content: (a) sample C, (b) sample E, (c) sample F.

To elucidate if LCMO grows with *c*-parameter in-plane or out-of-plane with respect to STO (sketch a t t he t op of Fig 4.4), w e m easured t he $(0\ \bar{3}\ \frac{5}{2})$ and $(0\ \frac{\bar{5}}{2}\ 3)$ diffraction peaks (referred to STO reciprocal lattice) which appear exclusively when the *c*-axis of LCMO is out-of-plane or in-plane, respectively[1]. We performed phi-scans around their positions in reciprocal space and plot the projections along Q_x of the collected intensity in Fig 4.4. The orientation of c-axis strongly varies with preparation conditions.

- For s ample C , r eflection $(0\ \bar{3}\ \frac{5}{2})$ is m uch s tronger t han t he $(0\ \frac{\bar{5}}{2}\ 3)$ one (see Fig 4.4(a,b)), pr oving t hat bot h or ientations c oexist but that t he *c*-in pl ane orientation is predominant.
- For s ample E bot h pe aks pr esent s imilar i ntensities, t hus i ndicating t hat bot h orientations coexist in similar proportions.
- Finally, sample F presents only the $(0\ \frac{\bar{5}}{2}\ 3)$ reflection, representative of a unique crystallographic orientation (*c*-out of plane).

For the phase with *c*-out of plane, the *c* lattice parameter decreases monotonically with the fraction of t hat ph ase: 7.803(5), 7.762(5) a nd 7.736(5) Å for s amples C , E and F respectively. However, this change of *c* parameter cannot be attributed to a relaxation of structural s train, as m entioned a bove. S o, i ts variation a lso s upports the i dea of a progressive i ncrease o f t he ox ygen c ontent. T he variation of t he c ell vol ume (59.494, 59.181, 58.983 $Å^3$) for s amples C , E a nd F r espectively also tends to that reported for the bul k va lue (58.771 $Å^3$ [12]). T his s hrinkage of t he *c*-parameter with t he o xygen content is coherent with the reduction of the cationic radii under oxidation (ionic radii of Mn^{3+} and Mn^{4+} are 0.785 and 0.670 Å respectively [15][2]). The out-of-plane parameters for the in-plane phase are 7.800 and 7.770 Å for samples C and E, respectively.

[1] See Appendix B.2.

[2] From a Co^{2+}/Mn^{4+} valence scheme, that has been confirmed by XANES measurements on s amples w ith hi gh a nd l ow T_C [14] and by ne utron pow der di ffraction [12] on samples w ith hi gh a nd l ow de gree of M n/Co or dering, ox ygen va cancies c an onl y b e compensated b y r educing f rom Mn^{4+} to Mn^{3+}. Reduction f rom Co^{2+} to Co^{+} is v ery unlikely.

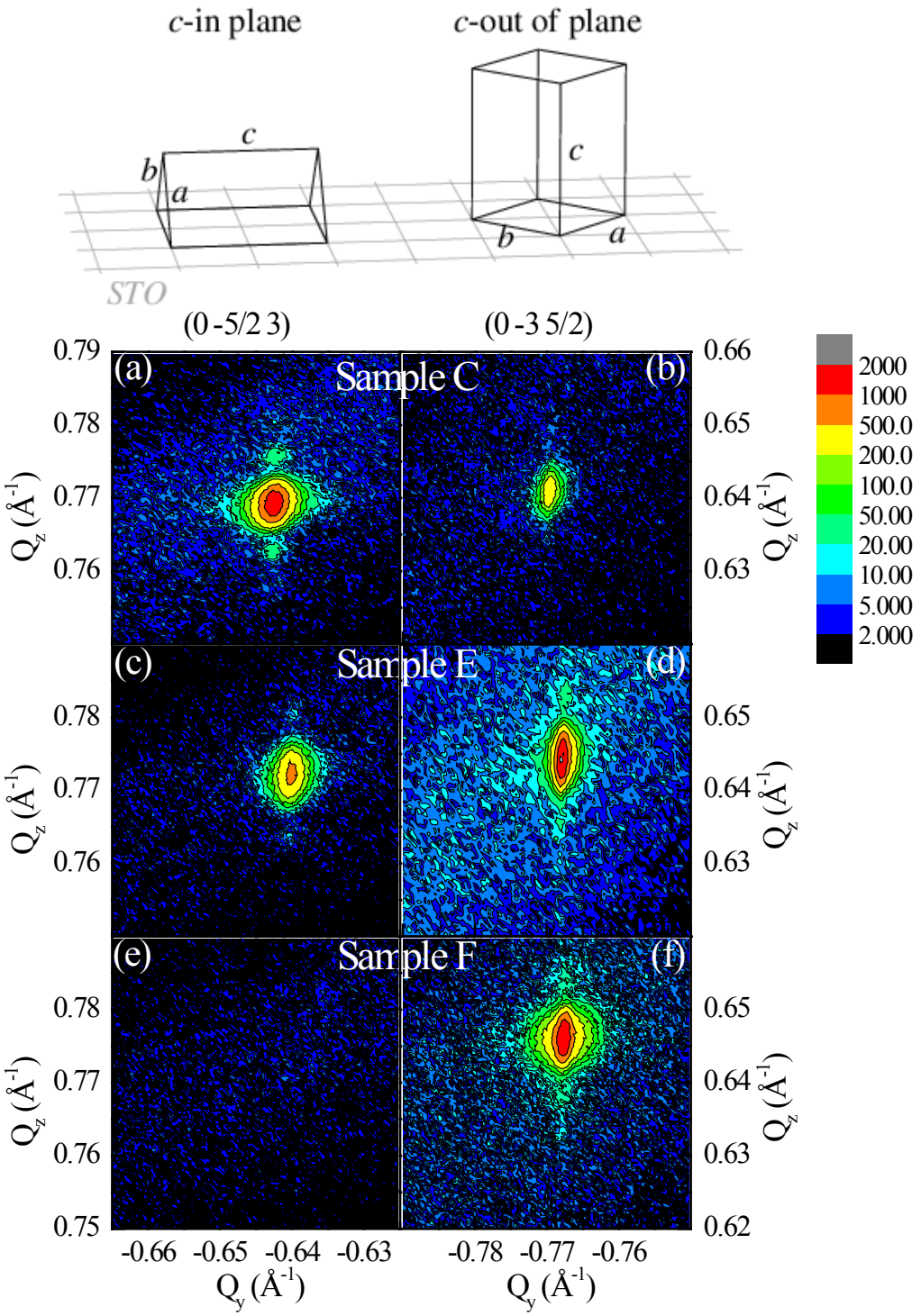

Fig 4.4. Reciprocal space maps measured by synchrotron X-ray diffraction for samples with the lowest and higher T_C; (right column) $(0\ \bar{3}\ \frac{5}{2})$ reflection, only present for La_2CoMnO_6 with *c*-out of plane, (left column) $(0\ \frac{\bar{5}}{2}\ 3)$ reflection, only present for La_2CoMnO_6 with *c*-in plane. The sketch at the top of the figure illustrates the two possible orientations of the film on the top of STO.

In order to confirm the correlation between oxygen content and crystallographic orientation, we must discard that only the increased time at high temperature (so, the thermal history of the samples) might lead to the change from mostly *c*-in plane (sample C) to only *c*-out of plane (sample E). With this objective, we performed high-resolution X-ray diffraction for $(0\ \bar{3}\ \frac{5}{2})$ and $(0\ \frac{\bar{5}}{2}\ 3)$ diffraction peaks of sample G. The results, depicted in Fig 4.5, evidence a clear predominance of *c*-in plane orientation: for the $(0\ \frac{\bar{5}}{2}\ 3)$ reflection, corresponding to the *c*-in plane orientation, the peak shows considerable intensity, whilst the peak for the $(0\ \bar{3}\ \frac{5}{2})$ reflection is hardly visible (so, much less intense). Therefore, samples C and G have very similar oxygen content and the same crystallographic orientation, whilst samples G and E have the same thermal history but different orientations. This clearly indicates that on increasing the oxygen content, the amount of phase with *c*-out of plane increases, so it confirms that it is indeed the oxygen content, and not only the thermal treatment, that determines the crystallographic orientation.

With this X-ray diffraction study, we evidence a clear correlation between oxygen stoichiometry and the two different crystallographic orientations: on increasing the oxygen content, the amount of phase with *c*-out of plane increases.

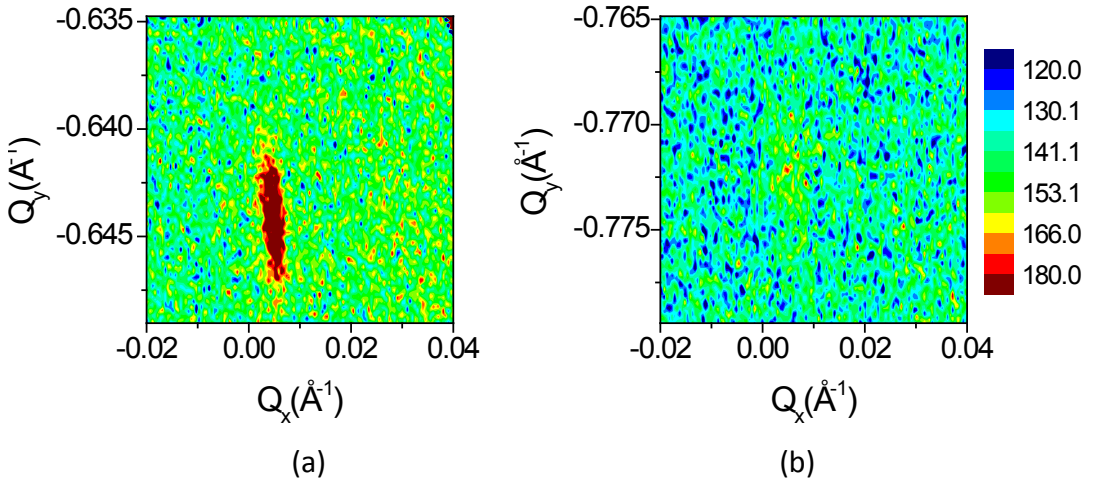

Fig 4.5. Reciprocal space maps measured by X-ray diffraction for sample G: (a) $(0\ \frac{\bar{5}}{2}\ 3)$ reflection, only present for La_2CoMnO_6 with *c*-in-plane, (b) $(0\ \bar{3}\ \frac{5}{2})$ reflection, only present for La_2CoMnO_6 with *c*-out-of-plane.

4.1.3 Magnetic hysteresis loops

4.1.3.1 Subtraction of the diamagnetic contribution

The subtraction of the diamagnetic contribution in the hysteresis loops of the LCMO thin films has proven to be a critical and difficult task, mainly because when measured in-plane, these films do not saturate at the maximum applied magnetic fields (70 kOe) and because the substrate contribution is very important with respect to the thin films

we measure. The determination of the exact thickness of the films by RRX is also required.

The method used for correcting the diamagnetic contribution of the STO has been the subtraction of the corresponding M(H) loops measured at 350 K. The accuracy of such an approximation is discussed in Appendix B.1.

4.1.3.2 M(H) FOR H ALONG (100)STO

Fig 4.6 plots the M(H) hysteresis loops corresponding to samples with low and high T_C (C, E, and F) measured at 10 K with H applied in-plane. In the case of low T_C (sample C), we find a coercive field of H_C~5200 Oe, with maximum magnetization M_S~5.0 μ_B/f.u. at H =70 kOe. For high T_C samples, the coercive field is H_C~7100-7500 Oe. This larger H_C compared to sample C can be explained because of their lower thickness (we refer the reader to section 4.1.7.2). The magnetic loop in sample F presents irreversibility up to very high fields (~50 kOe). In fact magnetization attains a value near 4.3 μ_B/f.u. (at H =70 kOe) but it is still far from reaching the saturation regime. In the case of sample E (T_C~225 K, slightly below that of sample F), which was annealed in the same conditions that sample F but cooled down at a faster cooling rate, the magnetization does not show signals of saturation at the highest attainable field. The latter mentioned sample also presents a subtle biloop feature. The presence of similar biloop features has been previously reported and considered as evidence of the existence of a bidomain structure [10], but in our case, we ascribe it to misalignment of the sample during the measurement (as discussed in Appendix B.3).

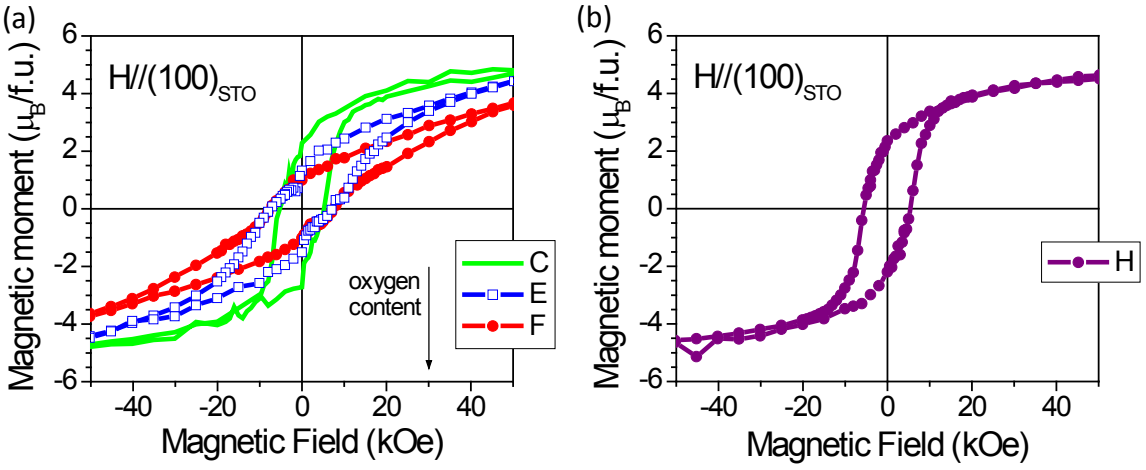

Fig 4.6. (a) M(H) measured at 10 K with H applied along (100) of STO. Curves have been corrected for the diamagnetic contribution from the STO substrate as explained in section 4.1.3.1. For simplicity, colour code is consistent with coloured M(T) curves from Fig 4.1; (b) M(H) at 10 K for sample H, for the magnetic field applied in the same direction.

In Fig 4.6b we present the hysteresis loop for sample H. The study as a function of the film LCMO film thickness in section 4.1.7.1 is done for samples grown in the same conditions as this one, which in the case of 20 nm-thickness yields low T_C but relatively high remnant magnetization for H in-plane.

4.1.3.3 MAGNETIC ANISOTROPY

Magnetic hysteresis loops performed with the magnetic field applied perpendicular to the film surface (out-of-plane) saturate for H ~10 kOe and show a square-like loop, especially for sample F (see Fig 4.7). High T_C samples (E and F) reach a saturation value of ~6 μ_B/f.u. –even if it slightly exceeds this value in Fig 4.7, the extra amount falls within the error introduced when dividing by the sample thickness. The difference in hysteresis loop shape between sample E and F is attributed to the measurement (as explained in Appendix B.3). On the other hand, samples with low T_C (such as G and H) display lower saturation values (around 5 μ_B/f.u.). This difference, which in the literature is ascribed to cationic ordering considerations, is discussed in section 4.1.5.

The shape of these loops indicates that the out-of-plane axis is clearly the magnetization easy axis for all samples, and that there is a larger contribution to the anisotropy than the shape anisotropy, which tends to align the magnetization in-plane (thin film). In addition, this perpendicular magnetic anisotropy (PMA) is found to be independent on the crystallographic orientation of the sample (c-in plane or c-out-of-plane). As we do not reach saturation for measurements with H applied in-plane, the anisotropy field remains unknown and torque measurements are required.

In the case of bulk LCMO, there are no conclusive studies to determine the direction of the ordered magnetic moment. Powder diffraction data suggest that the direction of the ordered magnetic moment is along the *b*-axis (we recall that for bulk, $a \neq b$), defined as the direction of smallest distance between cations of the same element –although authors admit the difficulty in convincingly determine this from powder diffraction [12]. Be that as it may, the magnetic easy axis for our thin films does not coincide with the *b* axis, which would correspond to 45º with respect to the sample surface, but is out-of-plane, so further work is required to understand its origin in LCMO thin films, which was unexpected.

In any case, it is worth noting that materials with large PMA are currently being studied because of their interest towards applications in spin-transfer-torque (STT)-MRAM: they provide better thermal stability, the switching current is lower compared to materials with in-plane anisotropy and they possess improved shape uniformity [16].

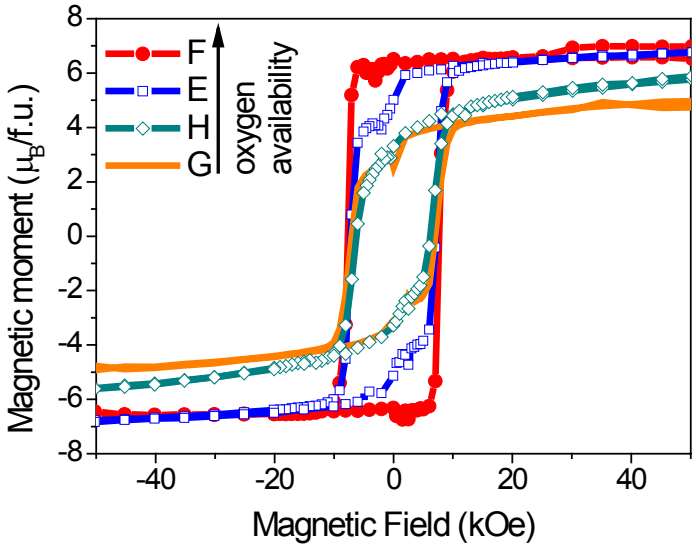

Fig 4.7. M(H) measured with H applied out-of-plane at 10 K, which reveals the out-of-plane anisotropy, especially for fully oxygenated samples (F).

4.1.4 Surface imaging

Topography of all films was investigated by atomic force microscopy (AFM) in tapping mode, revealing a flat surface with terraces-and-steps morphology which follows the STO surface morphology. In Fig 4.8 we show the topography of three representative samples (C, E and F), which correspond to the lowest and highest T_C obtained, and which we will further examine in detail in the following sections. All AFM images evidence that the surface of the different samples follow the terraces-and-steps morphology of the STO substrate beneath, with very low roughness. This is indicative of a 2D growth mode, although we do not have sufficient statistics. The process of annealing at high oxygen partial pressure favours the formation of well-defined terraces (from the STO substrate).

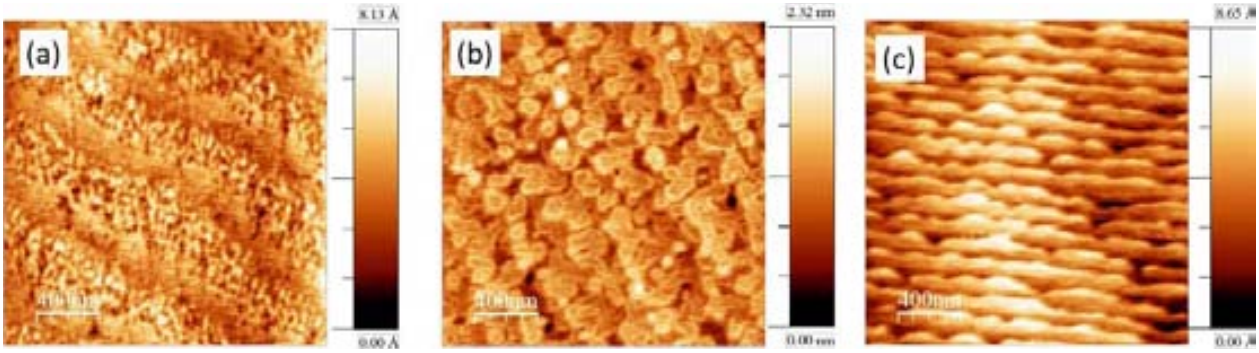

Fig 4.8. Topography from AFM in tapping mode of three representative LCMO samples: (a) sample C, (b) sample E, (c) sample F.

The structure at the surface of the sample is also probed by SEM in retrodispersive mode, see Fig 4.9, for the three representative samples. For homogeneous samples, this detection mode probes the crystalline structure by channelling effect. The sample is tilted slightly (a few degrees) in order to obtain better contrast. Samples E and F show

the presence of twins, although they are not very well-defined. In sample C we have not been able to see further than what is represented in Fig 4.9 (left). It is possible that the films present different twinning structure, due to the presence of the two different crystallographic orientations (in-plane and out-of-plane) as commented in section 4.1.2. However, the fact that the samples are insulating and that our SEM does not enable rotation in both directions, prevents us to draw further conclusions.

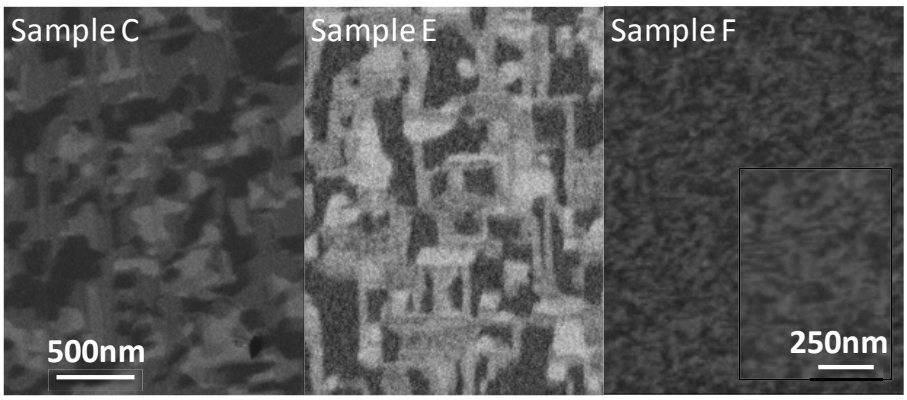

Fig 4.9. Scanning electron microscope images in retrodispersive mode and with sample tilted a few degrees from the electron beam.

4.1.5 ORDERING OF THE SAMPLES

Cationic ordering is a key parameter for controlling the magnetic properties of bulk LCMO [12,14,17]. Previous studies report low temperature hysteresis loops with a saturation magnetization close to 6 μ_B [9–11], i.e., the expected value of spin-only saturation magnetization in the case of ferromagnetic ordering of Mn^{4+} and Co^{2+} (in high spin state) ions. The existence of disorder in the cation's occupancy of the double perovskite structure, namely the presence of Mn ions placed in Co sublattice and *vice versa* (antisites), will introduce t_{2g}-t_{2g} (Mn^{4+}-Mn^{4+}) and e_g-e_g (Co^{2+}-Co^{2+}) superexchange interactions that according to Goodenough-Kanamori-Anderson rules [18–20] are antiferromagnetic. Therefore, it is expected that the existence of antisites will reduce the saturation magnetization from 6 μ_B.

The effect of Co/Mn disorder on the magnetic properties has been previously studied in bulk samples (where order can be precisely quantified by means of neutron powder diffraction) [12]. These studies show that hysteresis loops become wider (with higher coercive field and lower remanence) in the presence of disorder [12–14]. Co/Mn ordering temperature is around 1125 ºC and the ordering process is blocked below 1000 ºC due to extremely large relaxation times [17]. The reported valences for Co and Mn are 2+ and 4+ respectively and barely change with the degree of cationic ordering [12,17].

However, the determination of the cationic order in thin films cannot be done by neutron powder diffraction. In previous works on thin films prepared by PLD, cationic ordering was inferred in base of M_S values at low T close to 6 μ_B/f.u., the expected

value for spin-only fully-ordered $La_2Co^{2+}Mn^{4+}O_6$ ferromagnet [9–11]. Although such value is not achieved when H is applied in-plane (up to 9 T), high T_C samples show a saturation of 6 μ_B/f.u. for H applied out-of-plane (see Fig 4.7), which leads us to conclude that in these films, the degree of Mn/Co ordering is very high. Keeping in mind that ordering is blocked below 1000ºC and that films are prepared at 900ºC, the following question arises: why are these films ordered? The fact that during the process temperatures are below 1000 ºC may be compensated by the mobility of the cations in the plasma during the sputtering process. However, as the only difference in preparation between the low and high-T_C samples is an extra annealing at 900ºC (in the absence of plasma), we would not expect any difference in the ordering between high and low T_C samples. As we have determined in section 4.1.1, the lower T_C is due to lower oxygenation, indicating that the reduction in oxygen affects the magnetic properties. However, be sides modifying magnetic interactions, lower oxygen content may also induce changes in the Co spin state, which could explain the smaller saturation value of the low T_C samples.

4.1.6 Resistivity measurements

The use of LCMO as tunnel barriers in spin filter junctions requires an insulating behaviour of the films, so transport properties are measured as a function of temperature. Resistivity *vs.* T curves exhibit insulating behaviour -as expected- for all the samples. However, different preparation conditions also yield different behaviour, which should not be surprising given that oxygen contents in the films -tuned through the growth and annealing parameters- is determinant towards the transport mechanism. In Fig 4.10 we depict the R (T) curves for the three samples with different oxygen content (samples C, E and F). Reference [10] suggests two kind of transport mechanisms for thin films of LCMO: polaronic hopping and thermally activated conduction. Their films show similar thermal activation energy and polaronic hopping energy, leading them to conclude that both mechanisms are present for the temperature range they study (250 to 400 K approx.). For the temperature range considered in Fig 4.10, none of these two mechanisms fit our data, so further work is required to establish the transport mechanism in such films.

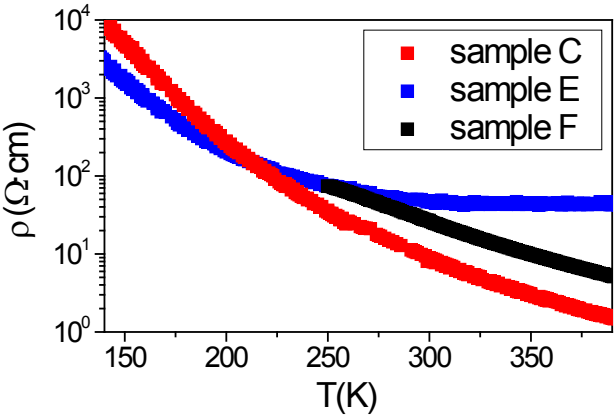

Fig 4.10. Resistivity *vs.* temperature curves for samples C, E and F, all of which display insulating behaviour.

4.1.7 MAGNETIZATION DEPENDENCE ON FILM THICKNESS

For the use of LCMO as magnetic barrier in spintronic devices such as spin filters, we are interested in relatively thin samples with flat surface and good T_C. In this section, we study the magnetic properties of increasingly thinner LCMO layers. As the resistance of LCMO is not as high as in other materials such as MgO, for example, it is probable that we do not need such thin films to obtain reasonable resistances.

4.1.7.1 LESS-OXYGENATED SAMPLES

The magnetic properties for LCMO films grown in the same conditions as sample H (which includes 1 h of annealing at 0.4 Torr) have been plotted as a function of the sample thickness in Fig 4.11. Such growth conditions have been chosen because of the higher remanence of its hysteresis loop for in-plane applied H (see Fig 4.6). Surprisingly, for 15 nm-thick samples we obtain the same T_C as for oxygenated samples, fact which requires further study –but may be related to changes in the oxygenation with the film thickness. For the tested thicknesses (from 20 to 2.5 nm), all of the samples display ferromagnetic character. Below 15 nm, T_C decreases as thickness is reduced. This is the expected behaviour for ultrathin films because of the predominance of the surface contribution, which entails lower effective magnetic coupling, tendency to spin canting and disorder due to surface termination of the crystal structure.

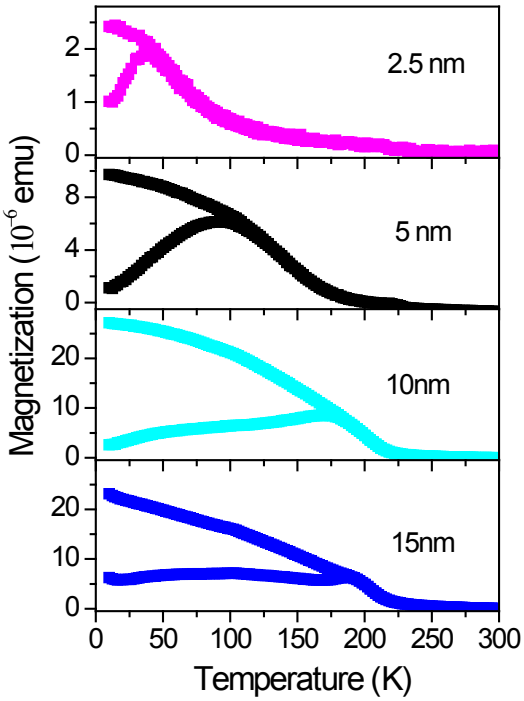

Fig 4.11. Magnetic properties of low-oxygenated LCMO films as a function of thickness, from 15 nm to 2.5 nm, measured with H||(100)$_{STO}$.

4.1.7.2 MORE-OXYGENATED SAMPLES

The study of magnetic properties of LCMO films as a function of their thickness is also performed for films grown in more oxygenated conditions (2 h of annealing *in-situ* at 400 Torr), which yield practically square hysteretic loops for H applied out-of-plane. Fig 4.12a shows the high T_C obtained for all probed thicknesses. As an example, 5 nm-films, shown at the inset for clarity, present T_C around 200 K. Fig 4.12b shows their hysteresis loops: besides a reduction of the coercive field as thickness is increased (see top inset), the saturation magnetization (taken at 20 kOe) is found to scale with thickness (as visible from the M(H) at bottom inset). The double loop, present for all thicknesses, is attributed to the misalignment of the field with respect to the film during the measurement (see Appendix B.3), so more accurate measurements are required to determine the exact M(H) loops.

Towards magnetoresistive devices, highly-oxygenated samples are much more advantageous due to the high T_C and higher magnetization they present. Their practically square hysteresis loop when measured out-of-plane, and for such reduced thicknesses is also promising.

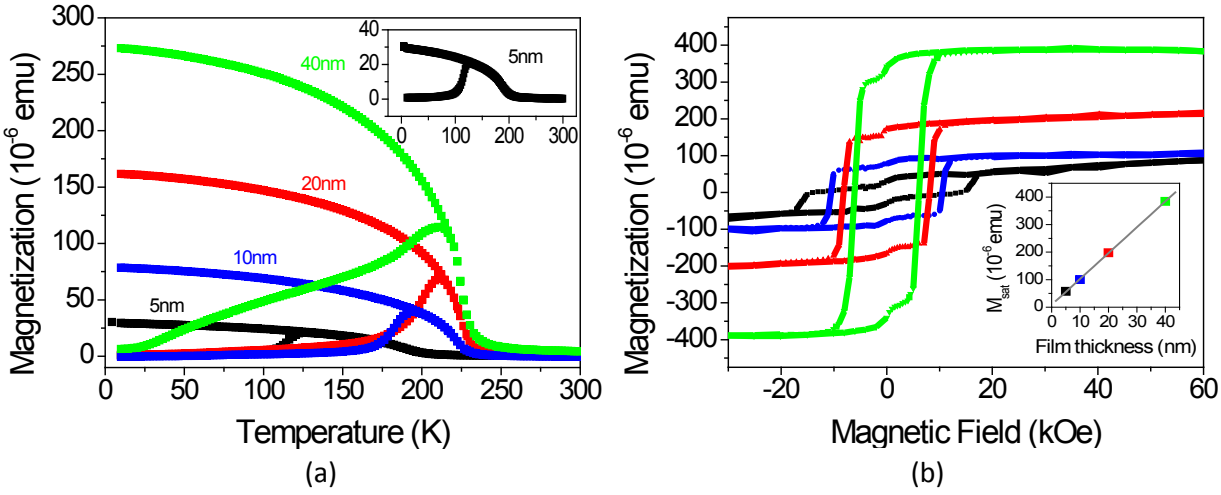

Fig 4.12. Magnetic properties of fully-oxygenated LCMO films as a function of thickness, from 40 to 5 nm, measured with H||(001)$_{STO}$. (a) ZFC-FC measurements reveal high T_C for all probed thicknesses, (inset) 5 nm-LCMO film; (b) Magnetization *vs.* magnetic field loops. Bottom inset shows magnetic moment is constant for all film thicknesses, and top inset shows decrease in coercive field with thickness.

4.2 Pt/LCMO/LSMO HETEROSTRUCTURES

To test the possibility of using LCMO as an insulating ferromagnetic barrier in a spin filter device with LSMO as bottom electrode, we must first test the quality of the heterostructure. To that end, two different heterostructures of Pt/LCMO(5 nm)/LSMO(40 nm)//STO are grown, using the conditions for the growth of LCMO from sections 4.1.7.1 and 4.1.7.2 (low and high-oxygenation, respectively).

For the sample with LCMO grown in the low-oxygenation conditions (conditions from sample H), the magnetic moment *vs.* temperature curve taken at 5 kOe is plotted in Fig 4.13a. A slight overestimation of the T_C of LCMO can be obtained from its derivative (in the inset), we recall that the other LCMO ZFC-FC measurements were performed at 1 kOe. However, two distinct transition temperatures are observed at ~310 K and ~ 180 K, thus suggesting the two materials (LSMO and LCMO) are separated.

On the other hand, for the heterostructure with LCMO grown in high-oxygen conditions, the temperature dependence of its magnetization reveals a single T_C below 300 K for the whole stack, but no peak around the expected T_C of LCMO, as can be seen from the M(T) in Fig 4.13b and the derivative in the inset. The same conditions are tested for a sample with thicker LCMO layer, LCMO(10 nm)/LSMO(20 nm), so that LCMO contribution should be much more visible. In this case, the in-plane and out-of-plane magnetizations are tested and depicted in Fig 4.13c, but besides showing the same T_C around 200 K, and much larger magnetization than that expected for the LSMO or LCMO layers separately, no other T_C is detected.

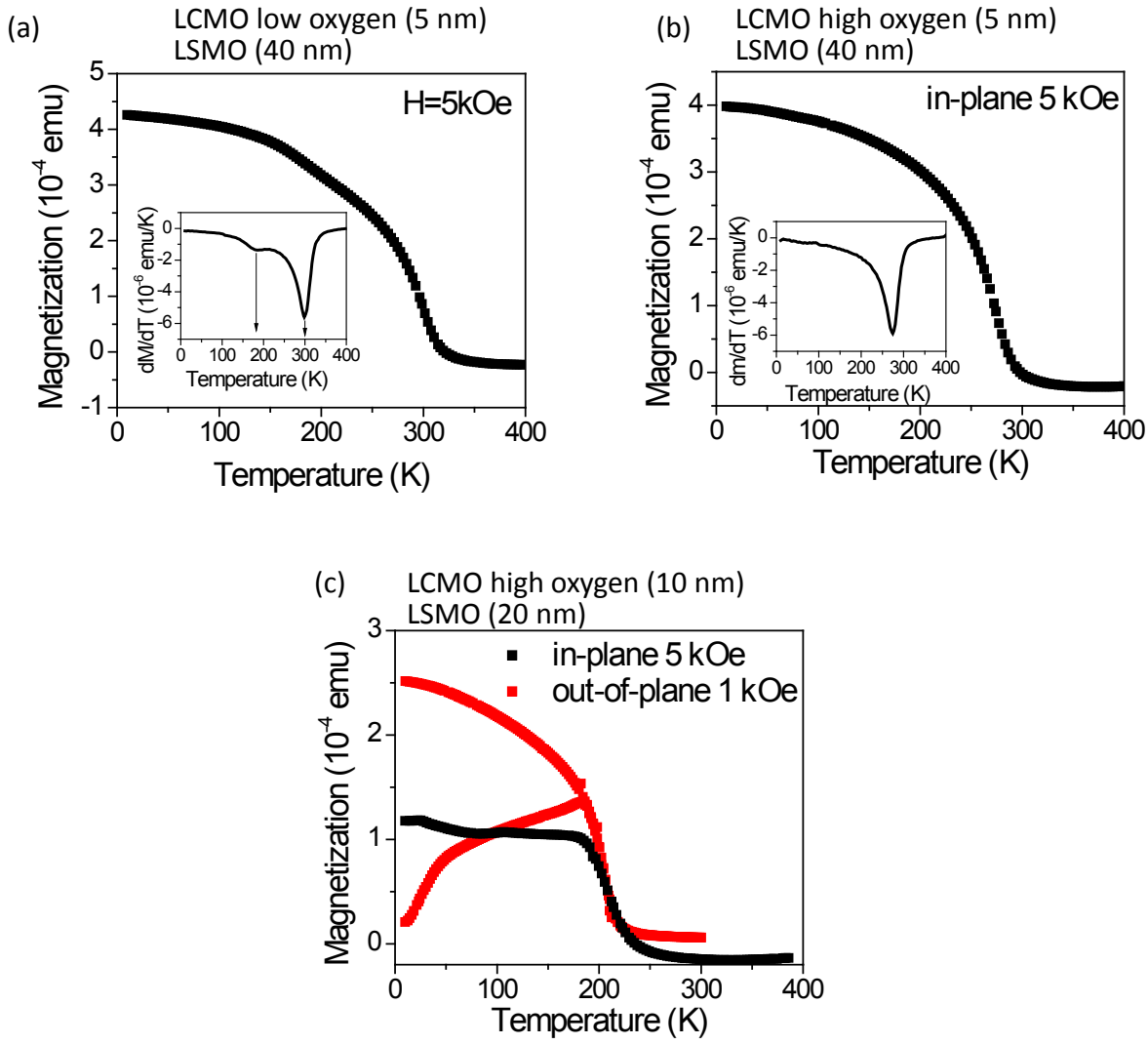

Fig 4.13. In-plane M(T) measurements for Pt/LCMO(5 nm)/LSMO(40 nm)//STO measured at 5 kOe with LCMO layer grown at (a) low-oxygen conditions and (b) high-oxygen conditions. Their derivatives are plotted at the insets. (c) In- and out-of-plane M(T) measurements for Pt/LSMO(10 nm)/LSMO(20 nm)//STO measured at 5 and 1 kOe, respectively, for LCMO layer grown in high-oxygen conditions.

We proceed to characterize the stack grown at low-oxygenation conditions. Although these growth conditions entail lower T_C, the lower time the films spend at high temperature and lower oxygen pressure during the annealing may help prevent interdiffusion.

The M(H) of the whole stack was measured, but the LCMO is not distinguishable from the LSMO (see inset in Fig 4.14), probably because of its small signal and the difficulty in the measurement. Therefore, we measure a single LCMO(5nm)//STO, and plot its magnetization *vs.* magnetic field curve in Fig 4.14.

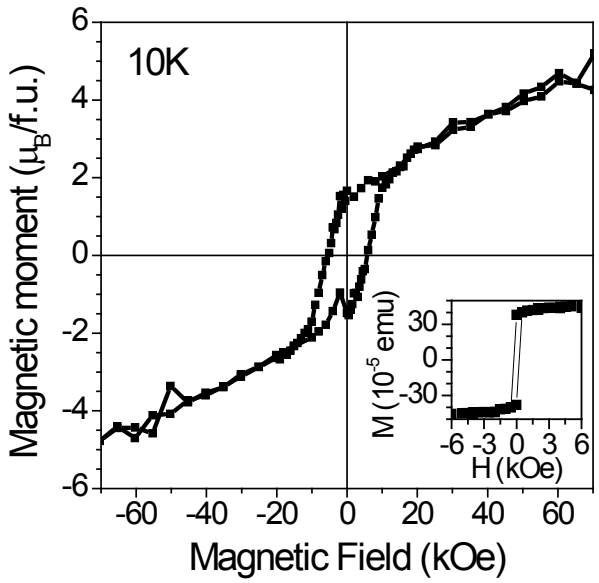

Fig 4.14. Hysteresis cycle of a nominally 5 nm-thick LCMO film, taken at 10 K and in-plane H, with diamagnetic contribution corrected from the measured susceptibility at 350 K. Inset shows M(H) from the Pt/LCMO/LSMO//STO stack with LCMO grown at low-oxygen conditions.

As we are unable to determine the quality of the latter heterostructure by magnetic measurements, we have performed TEM images of the stack. In Fig 4.15a, the high epitaxiallity of the layers can be seen from the high-resolution TEM image, although it shows no contrast between the LSMO and the LCMO films. This fact is coherent with their similar perovskite (or double perovskites) structure and the similarity between the atomic number of Co and Mn. However, the contrast from TEM also provides information about the strained state of the materials: in Fig 4.15b, a lower magnification TEM image, the interfaces between materials may be guessed.

Energy-filtered-TEM images allow mapping of the different elements of the structure. Such a map for the Co and Mn energy ranges is shown in Fig 4.15c. This allows confirming that there is no interdiffusion of the Co to the LSMO layer, as it is confined to a small layer close to the Pt interface, as expected from the growth process.

Exploratory I(V) curves of junctions made from this Pt/LCMO/LSMO//STO stack (taken at room temperature and with bias voltages up to 1 V) resulted in Ohmic behaviour, but further work (at lower temperatures) is required to analyse the tunnelling behaviour and the suitability of this system as spin-filter.

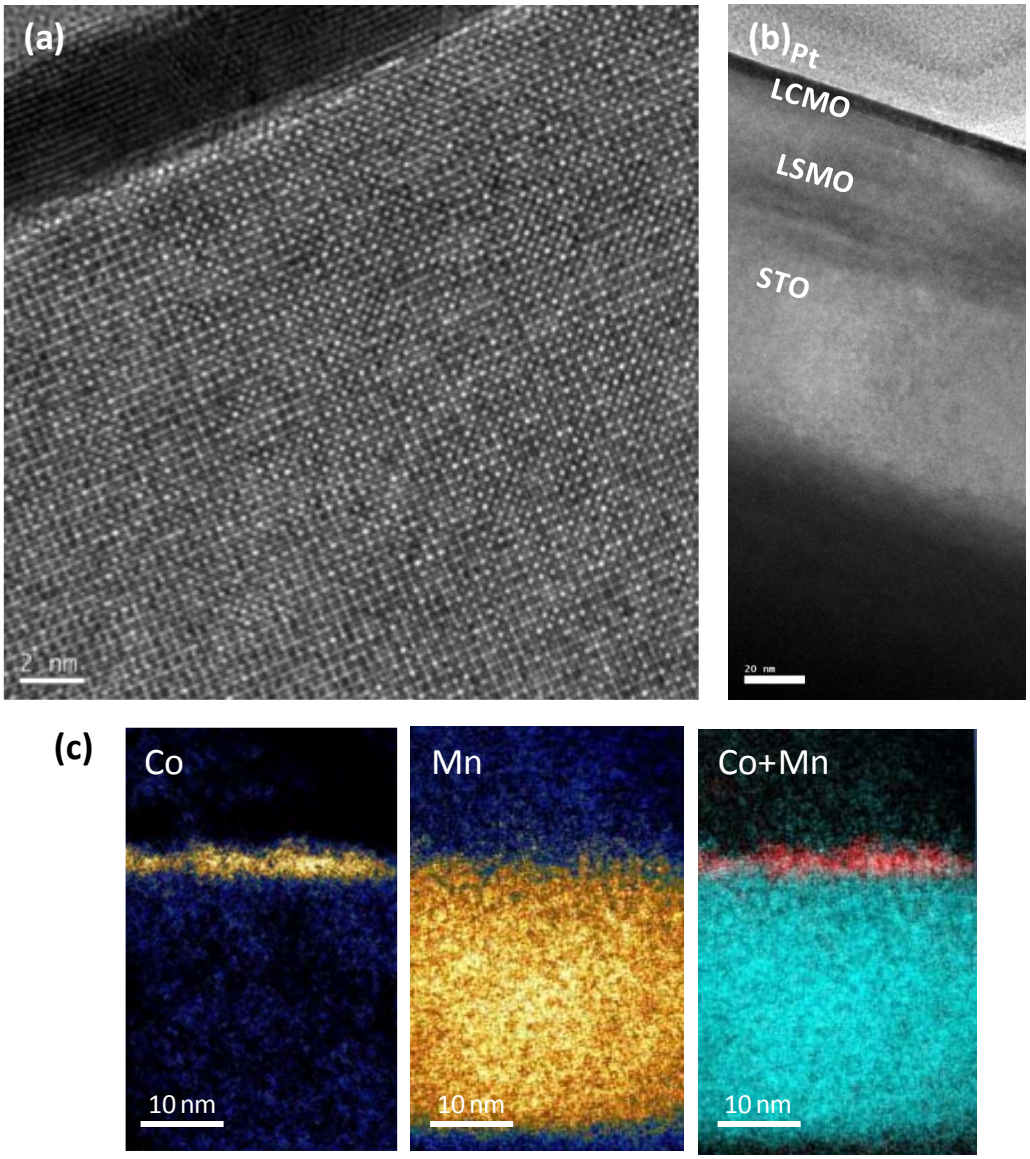

Fig 4.15. TEM image of the Pt/LCMO(5 nm)/LSMO(40 nm)//STO stack with LCMO grown with conditions of sample H, (a) high resolution image, (b) lower magnification image, (c) Energy-filtered-TEM image shows composition maps for Co, for Mn and for both.

4.3 SUMMARY

This chapter focuses on the optimization of ferromagnetic insulating LCMO thin films for spin-filtering applications, in particular for tunnel junctions based on LCMO/LSMO heterostructures.

We have optimized the growth of LCMO thin films by sputtering, achieving ferromagnetic and insulating layers. In-situ annealed films present a high T_C similar to that of bulk, which we attribute to an increase of oxygen content. This change of content is concomitant with the change of crystallographic orientation of the LCMO on the STO substrate: from *c*-in plane to *c*-out of plane for increasing oxygen content, as examined by XRD. Out-of-plane anisotropy is found from the hysteresis cycles, thus confirming that LCMO has its magnetic easy axis out-of-plane, regardless of the crystallographic

directions orientation on the STO substrate. A magnetic moment of 6 μ_B/f.u. is found for high-T_C samples measured out-of-plane, indicative of full cationic ordering of the double perovskite. A saturation magnetization of 5 μ_B/f.u. reached for low-T_C samples is suggested to come from lower oxygen contents and change of the Co spin state.

The thickness dependence of the magnetic properties is probed for the two different growth conditions which yield the most remanent magnetization in-plane and out-of-plane, respectively. At reduced thicknesses (tested up to 2.5 nm in-plane and 5 nm out-of-plane), the films are still ferromagnetic. Finally, two different Pt/LCMO/LSMO heterostructures are grown using the low-oxygen and high-oxygen growth for the LCMO. Magnetic measurements suggest that important interdiffusion may be taking place in the stack where the high-oxygen growth has been used for LCMO, as the bilayer presents a single T_C around 200 K. On the other hand, the stack with LCMO grown in low-oxygen conditions exhibits two distinct T_C and TEM and energy-filtered TEM suggest high epitaxiallity and no interdiffusion of the Co into the LSMO layer. Characterization of the magnetic hysteresis loop of the latter structure does not show the expected bi loop, suggesting problems in the measurement or ferromagnetic coupling between both magnetic layers.

4.4 REFERENCES

[1] Wolf S.A., Awschalom D.D., Buhrman R.A., Daughton J.M., von Molnár S., Roukes M.L., et al.; "Spintronics: a spin-based electronics vision for the future.". *Science* 294; **2001**: 1488–95. doi:10.1126/science.1065389.

[2] Rogado N.S., Li J., Sleight A.W., Subramanian M.A.; "Magnetocapacitance and Magnetoresistance Near Room Temperature in a Ferromagnetic Semiconductor: La2NiMnO6". *Adv. Mater.* 17; **2005**: 2225–7. doi:10.1002/adma.200500737.

[3] Tiffany S.S., Jagadeesh S.M.; Spin-Filter Tunneling. Handb. Spin Transp. Magn., Chapman and Hall/CRC; **2011**, p. 251–66. doi:10.1201/b11086-17 10.1201/b11086-17.

[4] Singh M.P., Truong K.D., Fournier P.; "Magnetodielectric effect in double perovskite La[sub 2]CoMnO[sub 6] thin films". *Appl. Phys. Lett.* 91; **2007**: 042504. doi:10.1063/1.2762292.

[5] Yanez-Vilar S., Castro-Couceiro A., Rivas-Murias B., Fondado A., Mira J., Rivas J., et al.; "Study of the dielectric properties of the perovskite LaMn0.5Co0.5O3-delta". *Zeitschrift Fur Anorg. Und Allg. Chemie* 631; **2005**: 2265–72. doi:10.1002/zaac.200570055.

[6] Yáñez-Vilar S., Sánchez-Andújar M., Rivas J., Señarís-Rodríguez M.A.; "Influence of the cationic ordering in the dielectric properties of the La2MnCoO6 perovskite". *J. Alloys Compd.* 485; **2009**: 82–7. doi:10.1016/j.jallcom.2009.05.103.

[7] Lin Y.Q., Chen X.M.; "Dielectric, Ferromagnetic Characteristics, and Room-Temperature Magnetodielectric Effects in Double Perovskite La2CoMnO6 Ceramics". *J. Am. Ceram. Soc.* 94; **2011**: 782–7. doi:10.1111/j.1551-2916.2010.04139.x.

[8] Manna K., Joshi R.S., Elizabeth S., Anil Kumar P.S.; "Evaluation of the intrinsic magneto-dielectric coupling in LaMn0.5Co0.5O3 single crystals". *Appl. Phys. Lett.* 104; **2014**: 202905. doi:10.1063/1.4879642.

[9] Guo H.Z., Gupta A., Calvarese T.G., Subramanian M.A.; "Structural and magnetic properties of epitaxial thin films of the ordered double perovskite La2CoMnO6". *Appl. Phys. Lett.* 89; **2006**. doi:10.1063/1.2422878.

[10] Singh M.P., Charpentier S., Truong K.D., Fournier P.; "Evidence of bidomain structure in double-perovskite La2CoMnO6 thin films". *Appl. Phys. Lett.* 90; **2007**. doi:10.1063/1.2743387.

[11] Guo H.Z., Gupta A., Zhang J., Varela M., Pennycook S.J.; "Effect of oxygen concentration on the magnetic properties of La2CoMnO6 thin films". *Appl. Phys. Lett.* 91; **2007**. doi:10.1063/1.2814919.

[12] Baron-Gonzalez A.J., Frontera C., Garcia-Munoz J.L., Rivas-Murias B., Blasco J.; "Effect of cation disorder on structural, magnetic and dielectric properties of La2MnCoO6 double perovskite". *J. Physics-Condensed Matter* 23; **2011**. doi:10.1088/0953-8984/23/49/496003.

[13] Dass R.I., Goodenough J.B.; "Multiple magnetic phases of La2CoMnO6-delta (0 <=delta <= 0.05)". *Phys. Rev. B* 67; **2003**. doi:10.1103/PhysRevB.67.014401.

[14] Kyomen T., Yamazaki R., Itoh M.; "Correlation between magnetic properties and Mn/Co atomic order in LaMn0.5Co0.5O3+delta. 2. Magnetic and calorimetric properties". *Chem. Mater.* 16; **2004**: 179–84. doi:10.1021/cm030279t.

[15] Shannon R.D.; "Revised effective ionic-radii and systematic studies of interatomic distances in halides and chalcogenides". *Acta Crystallogr. Sect. A* 32; **1976**: 751–67. doi:10.1107/s0567739476001551.

[16] Sbiaa R., Meng H., Piramanayagam S.N.; "Materials with perpendicular magnetic anisotropy for magnetic random access memory". *Phys. Status Solidi - Rapid Res. Lett.* 5; **2011**: 413–9. doi:10.1002/pssr.201105420.

[17] Kyomen T., Yamazaki R., Itoh M.; "Correlation between magnetic properties and Mn/Co atomic order in LaMn0.5CO0.5O3+delta: I. Second-order nature in Mn/Co atomic ordering and valence state". *Chem. Mater.* 15; **2003**: 4798–803. doi:10.1021/cm0302781.

[18] Anderson P.W.; "Antiferromagnetism - theory of superexchange interaction". *Phys. Rev.* 79; **1950**: 350–6. doi:10.1103/PhysRev.79.350.

[19] Goodenough J.B.; "An interpretation of the magnetic properties of the perovskite-type mixed crystals La1-xSrxCoO3-l". *J. Phys. Chem. Solids* 6; **1958**: 287–97. doi:10.1016/0022-3697(58)90107-0.

[20] Kanamori J.; "Superexchange interaction and symmetry properties of electron orbitals". *J. Phys. Chem. Solids* 10; **1959**: 87–98. doi:10.1016/0022-3697(59)90061-7.

PART III:

MICRO AND NANO-FABRICATION OF TUNNEL JUNCTION DEVICES

CHAPTER 5. FABRICATION OF MICRO AND NANODEVICES

5.1 INTRODUCTION

The improved mastering of the nanofabrication processes and the nanostructuration has made possible not only the reduction in sizes of the devices and the improved performance of the latter, but also provided the means to study novel physical phenomena at smaller scales. In order to study interfacial effects and phenomena at small scales, good nanofabrication procedures must ensure clean interfaces and the non-modification of the good structural qualities of the materials during the patterning. Each step of the fabrication process may introduce modifications which alter the properties of the material or stack of materials, the functionality of the device changing drastically from what may be initially pursued. This is especially true in the case of complex oxides, which are extremely sensitive to any small distortion; any small modification may result in completely different behaviour of the material. Therefore, a good optimization and calibration of the parameters for each fabrication step can make a huge difference in the performance of the fabricated devices.

During this thesis, a strong effort has been devoted to optimize the micro/nano fabrication process of the samples. This chapter aims at giving a detailed account of the procedures that have been used to fabricate the two device structures we will focus on.

Section 5.2 focuses on <1 μm^2-sized Pt/LAO/LSMO non-magnetic tunnel junctions, our interest being the study of the tunnelling properties through the insulating layer, using the smallest contact zone possible (the results are presented in Chapter 6). Section 5.3, on the other hand, reviews the fabrication of 100 μm^2-sized magnetic tunnel junctions (the magnetoresistive results of which are discussed in Chapter 7), from the choice of measurement configuration (sketched in Fig 5.10b) to the various patterning steps.

5.2 FABRICATION OF NON-MAGNETIC TUNNEL JUNCTION NANODOTS

In order to fabricate the device represented in Fig 5.1, the LAO/LSMO//STO(100) heterostructure was grown by sputtering (conditions detailed in Chapter 3). 5 large squares of 350×350 μm^2 and a 6×5 matrix of different-sized nanodots are patterned by e-beam lithography –to achieve sub-micron resolution- and the deposition of Pt macrocontacts is performed through a shadowmask. The resist sensitive to electrons (PMMA) is used to electrically isolate the Pt macrocontacts from the LAO layer. In section 5.2.1 we perform an optimization of some of the lithographic conditions to achieve the resolution limit of the smallest-sized nanodots possible. The fabrication of a shadowmask is reviewed in section 5.2.2 and, finally, in section 5.2.3, the nanodots' sizes are determined by SEM images across the deposited Pt macrocontacts.

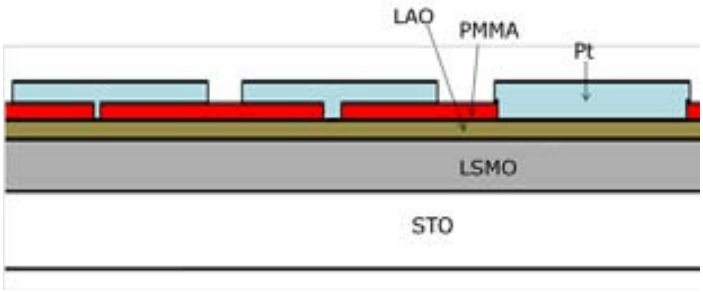

Fig 5.1. Sketch of the cross-section of the desired configuration for the non-magnetic tunnel junction nanodots: we represent two nanocontacts of different size and a macrocontact (on the right).

5.2.1 Optimization of e-beam lithography parameters

With the aim to achieve the minimum sized nanodots, we are interested in determining the resolution limit for platinum or gold deposited contacts (henceforth referred to as "dots") using electron beam lithography. The choice of resist and the number of layers, the exposition dose and the deposited material and technique are the parameters we can tune, so in this section we perform the optimization of these parameters on LSMO samples.

5.2.1.1 Type of resist

To start with, we focus on the type of electron-sensitive resist spin-coated on the sample surface. The most common positive[1] resists used in e-beam lithography are PMMA (Polymethyl methacrylate) and MMA (Methyl methacrylate). The most relevant difference between them is that MMA is more sensitive than PMMA, resulting in less resolution. However, the combination of both PMMA and MMA can be particularly useful in the case of adhesion problems between the sample surface and the deposited material. Once we have the deposited material (Pt or Au, for example) on top of the resist after performing the lithography, the remaining (unexposed) resin is dissolved using acetone and ethanol, so that the layer of Pt or Au is removed. This process is called lift-off. Only the parts where the material touches the sample directly, i.e. the ones previously exposed, should remain.

In the image below (Fig 5.2), a matrix of squares was patterned on an LSMO sample and a thin layer of Au was deposited on top. After lift-off, we found that the Au had been removed not only from the unexposed parts, but that some squares of Au had been ripped off too due to adhesion problems.

[1] Positive resist: the exposed part of the resin is the one whose properties change and dissolve after the developing.

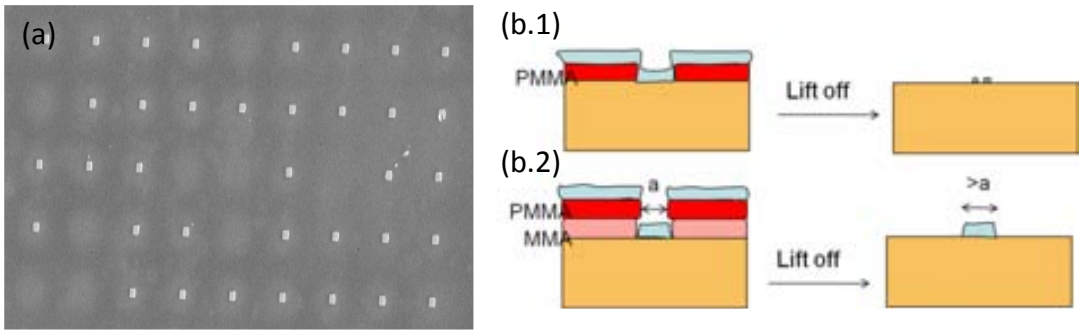

Fig 5.2. (a) Matrix of 0.5 μm^2-sized Au squares with adhesion problems due to lift-off: lithography using a single PMMA layer; (b) Sketch of the effect of adhesion problems when we use a single PMMA layer: the deposited region may be ripped off when PMMA is dissolved (b1). The use of double layer of MMA+PMMA can help solve this effect, in detriment of resolution (b2).

These adhesion problems can be solved in detriment of resolution by using a double layer of MMA+PMMA. To illustrate the loss of resolution, in Fig 5.3 we show some SEM images of two Pt-deposited 1 µm nominal-sized squares, both using the same parameters in the e-beam lithography: for a single PMMA layer, the square shape is maintained (see Fig 5.3a) but for double layer of MMA+PMMA, the designed square pattern becomes a circle and a double contrast can be appreciated (see Fig 5.3b). The square-shaped higher contrast in the middle of the dot corresponds to the vertical projection of the patterned opening in the PMMA. However, as the opening of the MMA underneath is larger (because of its higher sensitivity to the electron beam), the square becomes a disc (with lower contrast in the extended regions) due to the limited directionallity of the sputtering deposition (see Fig 5.2b.1). In summary, as MMA is more sensitive, the opening in the MMA is greater than the opening in the PMMA layer on top, and Pt is also deposited for the whole opened area.

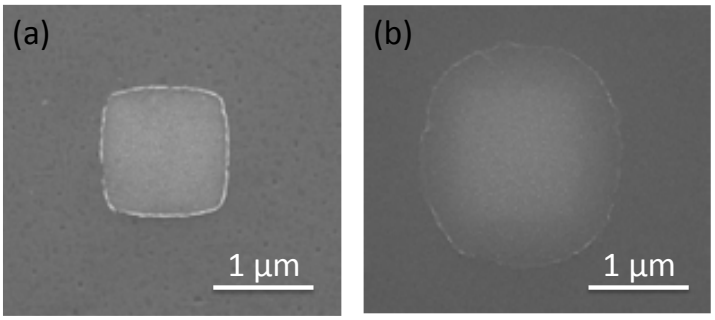

Fig 5.3. Pt sputter-deposited squares of 1x1 μm^2 nominal-size, using e-beam lithography with 160 $\mu As/cm^2$ dose. (a) use of a single layer of PMMA; (b) use of double layer of MMA+PMMA, which leads to a double contrast due to the not complete directionality of the sputtering technique and the high sensitivity of the MMA layer. See Fig 5.2.

For good adherence with our LSMO samples, we have found that for Au deposition a double layer of MMA+PMMA is required, whilst for Pt deposition a layer of PMMA is sufficient and provides good resolution.

5.2.1.2 DEPOSITED MATERIAL AND TECHNIQUE

The deposited material and used technique are also relevant issues. Magnetron sputtering is a less directional technique than thermal evaporation. The reason is that the pressure of the evaporation chamber is greater for sputtering (due to the need of creating a plasma), so that target atoms collide with the existing chamber gas ions. This less directional deposition results in less defined contours (less resolution) for the designed objects, because a shadow mask does not act as shield to the deposited atoms if they do not reach the sample perpendicularly.

The choice of the deposited material is sometimes linked to a certain technique (depending on its boiling point, for example), but must also take into account the material's adherence properties. In our case, we have used evaporation for Au and sputtering for Pt.

5.2.1.3 EXPOSITION DOSE

As mentioned in Appendix A, the applied e-beam dose is the electronic radiation needed to remove the resin thickness in a lithographic process. The required dose depends on the size of the designed element, so that by overdosing small enough designed squares we obtain dots. Overdosing has yet another effect: performing lithography for the same nominal size elements, the higher the dose, the bigger the final element size. This effect can be seen in the SEM images in Fig 5.4a,b: squares were designed of same sizes (100×100 nm^2), and yet the sizes of the resulting Au dots depends on the applied dose. In Fig 5.4c, the squares were designed with even smaller nominal sizes (50×50 nm^2) but the resulting dot is much larger because of the larger dose applied during the exposure.

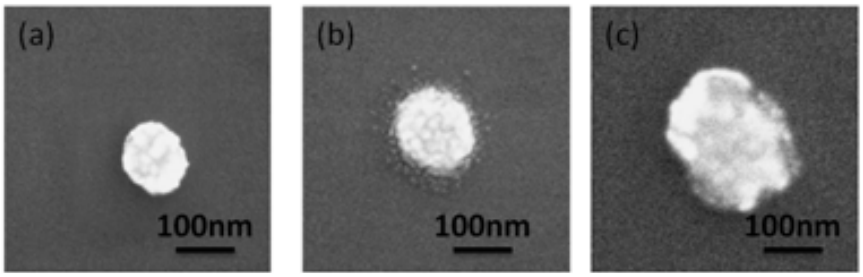

Fig 5.4. Au evaporated on squared-shape lithography performed on with a double layer of resist (MMA+PMMA) (a) square of 100×100 nm^2 of nominal size exposed at 120 μAs/cm^2 dose; (b) square of 100×100nm^2 of nominal size exposed at 160 μAs/cm^2 dose; (c) square of 50×50 nm^2 of nominal size exposed at 200 μAs/cm^2 dose.

As for the resolution, we have found the following size limit: for Pt sputtering on PMMA layer, we can obtain the smallest well defined circles designing squares of 50-90 nm nominal size and exposing at a 160 μAs/cm^2 dose and 10 kV, to obtain 100 nm diameter circles. For Au evaporation on MMA+PMMA layer, the best dose is 120 μAs/cm^2, for which 100 nm-sized nominal squares become 100 nm diameter circles (Table 5.1 provides a summary of the obtained diameters for each dose and nominal size).

Table 5.1. Optimization of the lithographic parameters for the definition of nanodots: dose (μAs/cm^2), nominal size of the square of side L performed by e-beam lithography at 10 kV and the measured diameter of the resulting dot.

Single PMMA resist, Pt deposition			
DOSE (μAs/cm^2)	120	160	
Nominal size (L)	40 nm	40 nm	From 50 nm to 90 nm
Measured diameter	40-50 nm, not circular shape	60-100 nm	100 nm
MMA+PMMA resist, Au deposition			
DOSE (μAs/cm^2)	120	160	200
Nominal size (L)	100 nm	100 nm	50 nm
Measured diameter	100 nm	120 nm	100 nm, not perfectly circular shape

5.2.2 SHADOW MASK FABRICATION

We need a shadow mask to perform a sputtering deposition on macrocontacts on top of nanocontacts. Our goal is to obtain a matrix of 6×6 square platinum macrocontacts with a side length of L_{Pt}=250 μm each in a 5×5 mm^2 sample.

The shadow mask is created from a silicon substrate covered with a thin layer of Si_3N_4 on both sides. Its surface is (10×10) mm^2 and its thickness is t=280 μm. The different steps of the fabrication process are (sketched in Fig 5.6):

1) The first step towards the creation of a shadow mask is spin coating a photoresist on top of the sample, using a spinner in order to achieve a thin homogeneous layer of photoresist on top of the Si_3N_4.
2) We design the desired pattern (in our case, it is a matrix of different sized squares) and expose the photoresist to light using a microwriter. The sample is dipped in a developer solution which dissolves exposed photoresist. Conditions: sensitivity 120, 5 μm-spot laser.
   Taking into account that the wet etching of Si with KOH (step 5) will be crystallographically oriented [1,2], we have to compute the length of the squares we have to design. A simple calculation provides the lithography parameters (Fig 5.5): tg(54.7º)=t/x where $L_{design} = (2x + L_{Pt}) \sim 650$ μm is the designed length we require, with a spacing of 100 μm between one macrocontact and the next.

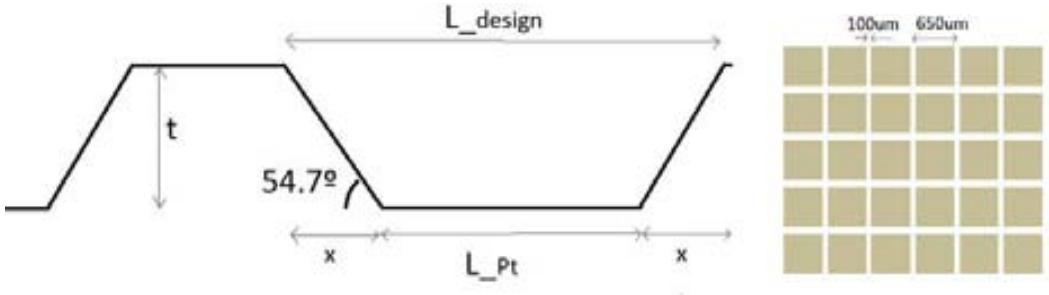

Fig 5.5. Determination of the lithographic parameters for the shadow mask.

3) Using Reactive Ion Etching (RIE), which attacks the surface with gas ions, the thin layer of Si_3N_4 is removed from the areas where there is no photoresist left on top. We used the following conditions: 150 W, 50 mTorr, RT, 5 sccm O_2 and 20 sccm CHF_3, 2 min.
4) With the Si substrate exposed, a quick dip of the sample in HF is needed to cleanse the surface and avoid possible oxidation due to contact with the atmosphere. It is also necessary to rinse the sample using acetone and ethanol to get rid of the remaining photoresist.
5) After that, we proceed to a long bath of KOH using the parameters detailed in Table 5.2. KOH attacks the Si substrate and the Si_3N_4 selectively, so that the velocity of attack of Si is much faster, and dependent on the crystallographic orientation.
6) Ideally, the KOH bath would result in a thin membrane of Si_3N_4 below the patterned windows and an ultrasound bath would break the membrane and provide us with the desired openings.

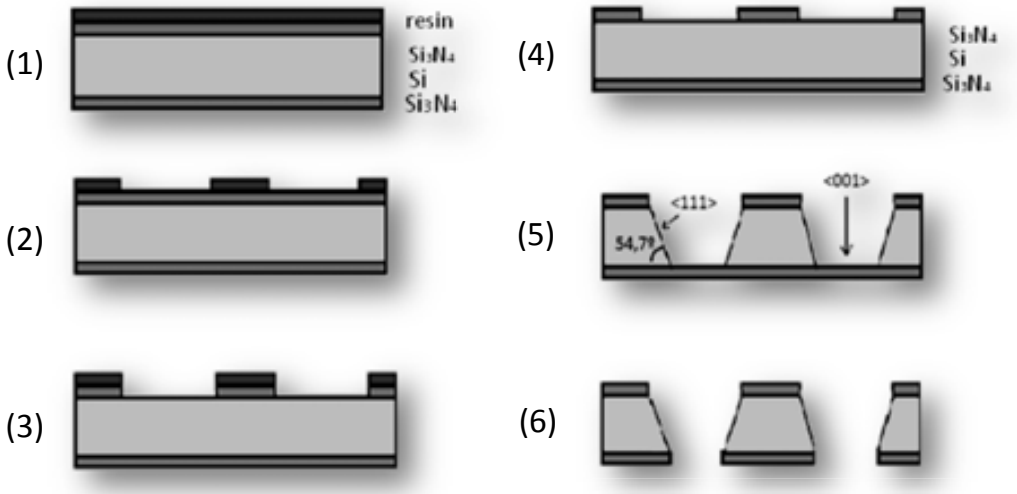

Fig 5.6. Step by step sketch of the shadow mask creation procedure

After attempting to use the samples with the mentioned thickness (280 μm), we realized that the Si_3N_4 layer that protects the Si is too thin, so that the bath of KOH etches the thin layer of Si_3N_4 completely and dissolves the silicon underneath. We repeated the

process for 500 µm thick samples (which have a Si_3N_4 layer of around 200 nm), without changing the previous lithographic parameters, so that the crystallographic axes <111> meet at a depth of 460 µm, just before reaching the other side of the sample. So, finally, we must polish the surface opposite to the one where we have performed the lithography until we reach the desired size for the openings (see Fig 5.7a).

Table 5.2. Etching recipe using KOH to etch silicon [1,2].

Etchant	Recipe	Temperature (ºC)	Etch rate (100)(μm^{-1})	Selectivity (100)/(111)	Typical mask
KOH (water)	44 g 100 cm^2	60	16	>1000	Si_3N_4 (<1 $Åmin^{-1}$) SiO_2 (14 $Åmin^{-1}$)

(a) (b) (c)

Fig 5.7. (a) Shadow mask openings. Note the crystallographic orientation type of etching; (b) shadowmasks for different number of macrocontacts in a square matrix; (c) alternative way of making 3×3 matrix of macrocontacts using long thin strips of foil.

To deposit different number of macrocontacts on other samples, we prepare various different shadow masks (see Fig 5.7b) or must otherwise use the alternative of long thin strips of foil, which is feasible for 3×3 matrix (as in Fig 5.7c) but gets more difficult for larger number of macrocontacts in a 5×5mm^2 sample.

5.2.3 NANODOTS DEFINITION, DEPOSITION OF MACROCONTACTS AND SIZE DETERMINATION

The sizes of the prescribed nanodots range from 0.01 to 110 μm^2 and the lithography is done using a single layer of PMMA, a voltage of 10 kV and a dose of 160 $\mu As/cm^2$ (from the calibration in section 5.2.1). We use a shadowmask (the fabrication of which is explained in section 5.2.2) to deposit the final Pt macrocontacts on top of the resin. A careful positioning of the shadowmask with respect to the sample must be done in the optical microscope to ensure that the macrocontacts are on top of the patterned dots.

For the macrocontacts, we deposit around 50 nm of Pt by sputtering. Just before the deposition, however, a UVO cleanse[2] of 30 s is done, to clean the sample surface and

[2] UVO cleaning: it is a fast and soft cleaning method. UV radiation excites and/or dissociates contaminant molecules from photoresists, human skin oils, residues from cleaning solvents, etc. The products from this process react with atomic oxygen to form simpler volatile molecules which are removed from the sample surface [20].

favour good adherence of the Pt to the sample. Even after the Pt deposition, the nanodots can be seen, through the macrocontacts, by SEM (as shown in Fig 5.8). This will provide a good estimation of the areas of the nanodots, which are the contact areas between the film and our macroscopic metallic contact.

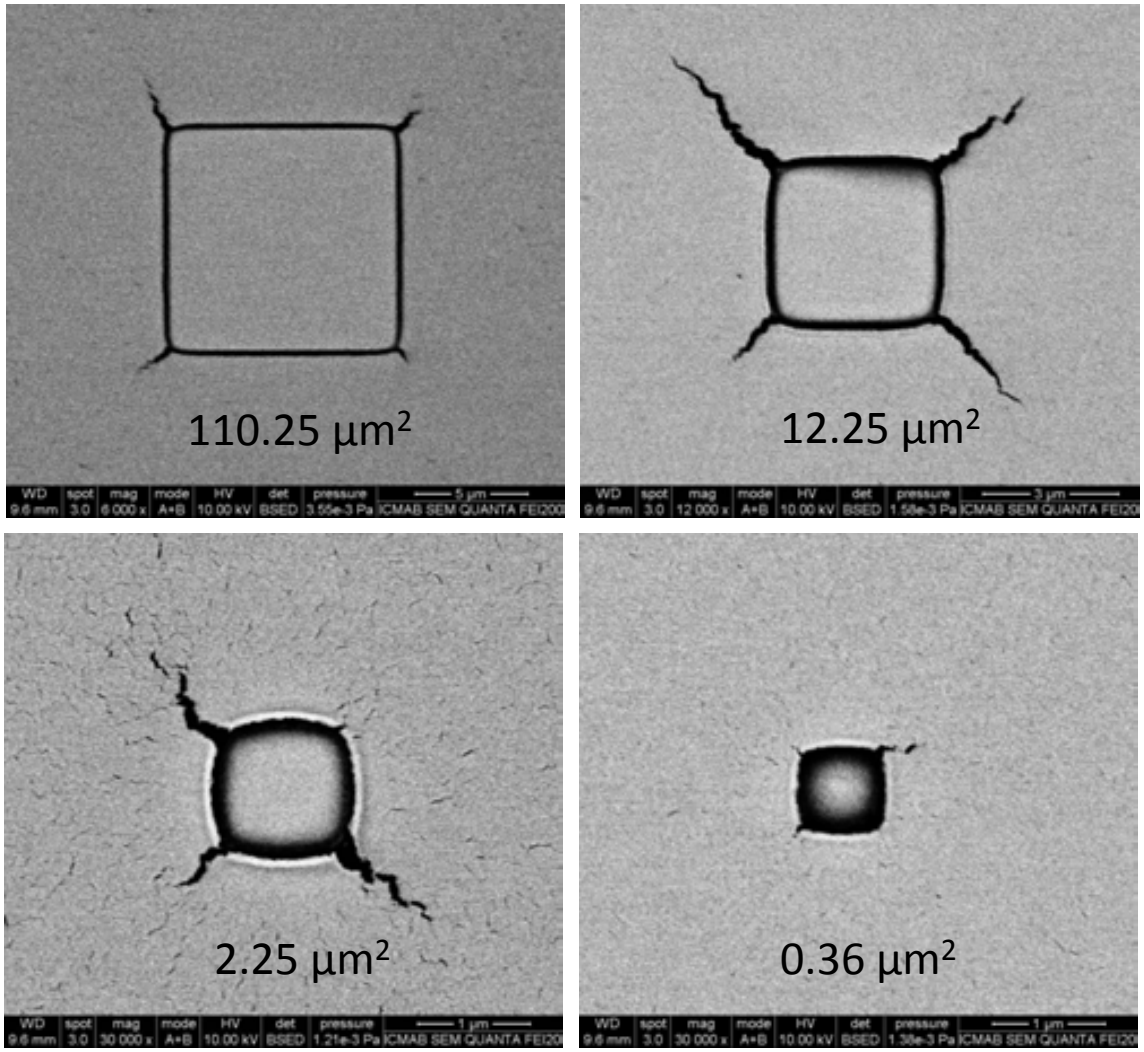

Fig 5.8. SEM images of different-sized nanodots seen through the Pt macrocontacts.

In Graphic 5.1, we compare the nominal areas prescribed in the lithographic process with these measured dot areas taken from the SEM images. The slope of the graph is practically unity, confirming that the chosen dose is quite appropriate.

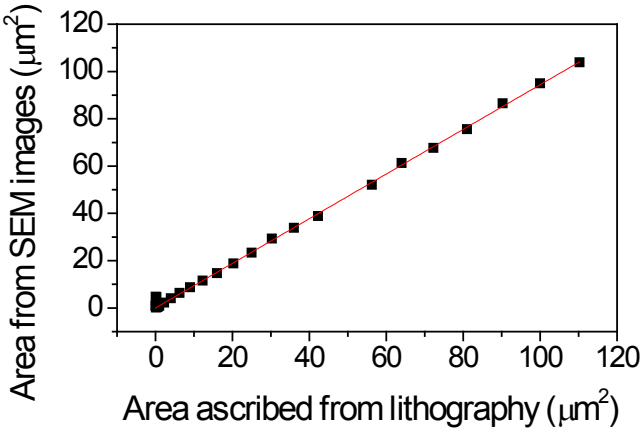

Graphic 5.1. Comparison of the areas of the dots measured from the SEM images (from Fig 5.8 and similar ones) with the areas prescribed during the e-beam lithographic process.

After this process, the conduction through the nanodots is ready to be measured and the results are detailed in Chapter 6.

5.3 FABRICATION OF MAGNETIC TUNNEL JUNCTIONS (MTJ)

In this section, we discuss the configuration we develop –simplified with respect to the MTJ stack used for magnetic random access memories (MRAMs). Next, we review some of the design considerations which can help to optimize the switching behaviour of the junctions. After that, the four following sections are devoted to each of the different steps of the magnetic tunnel junction device fabrication: (1) the definition of the tunnel junctions by lithography, (2) the etching, (3) the alignment and second lithography step and, finally, (4) the deposition of the macrocontacts.

During this thesis, magnetic tunnel junctions were fabricated in two different laboratories: in Universidad Complutense de Madrid, at the Grupo de Física de Materiales Complejos, where the magnetic tunnel junction fabrication and measurement had already been optimized; and at the Institut de Ciència de Materials de Barcelona (CSIC), where we have started our fabrication and measurement of magnetic tunnel junctions using different equipment. The main difference in equipment is related to the lithographic process, so we explain the process used for both techniques.

5.3.1 CONFIGURATION

Though a magnetic tunnel junction is defined as a trilayer of two ferromagnetic electrodes sandwiching a thin insulating barrier, MTJs for practical applications – Magnetic Random Access Memories- require even more complex structures [3]. These structures comprise a pinned layer structure (bottom electrode), a tunnel barrier, the top electrode (acting as a free layer, which means that its magnetization can be inverted upon the application of a magnetic field) and capping layers.

The pinned layer structure is achieved by growing an AF layer with a synthetic antiferromagnet (SAF) on top (see Fig 5.9). The SAF –two ferromagnetic layers strongly coupled antiferromagnetically[3]- closes the magnetic flux within it, preventing the magnetization of the bottom electrode to cause stray fields which could act on the free layer (top electrode). The upmost layer of the SAF is called the "reference layer", and as the SAF it is coupled to the AF, the magnetic moment of the reference layer is pinned; this robust exchange bias is useful to decouple the magnetization of both electrodes, enabling two different resistance states to exist at zero applied magnetic field H, interesting for applications with low energy consumption.

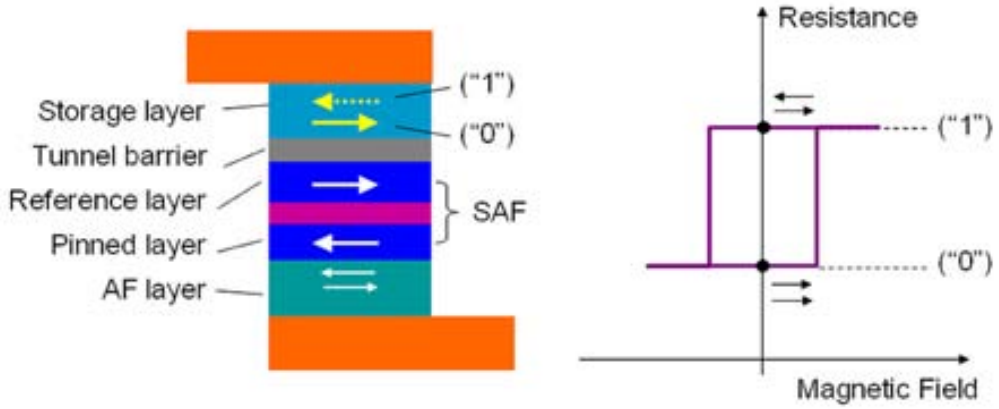

Fig 5.9. Sketch of the stacking layers of the MTJ used in MRAMs. Depending on the magnetization direction of the storage layer, which is the only one which is not pinned, two resistance states can be achieved. Image taken from [4].

Besides these mentioned necessary stacking layers, the optimal growth of the electrodes and tunnel barrier may also introduce other requirements. In the case of CoFeB/MgO/CoFeB MTJ, for example, to attain in-stack symmetry compatibility, the CoFeB electrodes must be grown amorphous and made to crystallize in a subsequent annealing [5,6], materials which are good B getters must be introduced to avoid B segregation at the barrier interface [7,8] and capping layer materials must also be selected carefully [9].

The standard procedure to fabricate and measure tunnel junctions (at an experimental level) entails a long process of lithographic and etching steps towards the fabrication of a relatively robust structure [10]. After defining the MTJ pillars, the whole sample is covered in an oxide layer -acting as insulator-, and the oxide is then patterned to open a hole just on top of the pillars (see Fig 5.10a). Some macrocontacts are then deposited on top of the holes to be able to measure the pillar resistance through the macrocontacts on top.

[3] They are coupled through the Ruderman-Kittel-Kasuya-Yosida (RKKY) interaction, which depends on the thickness of the spacer layer grown in between.

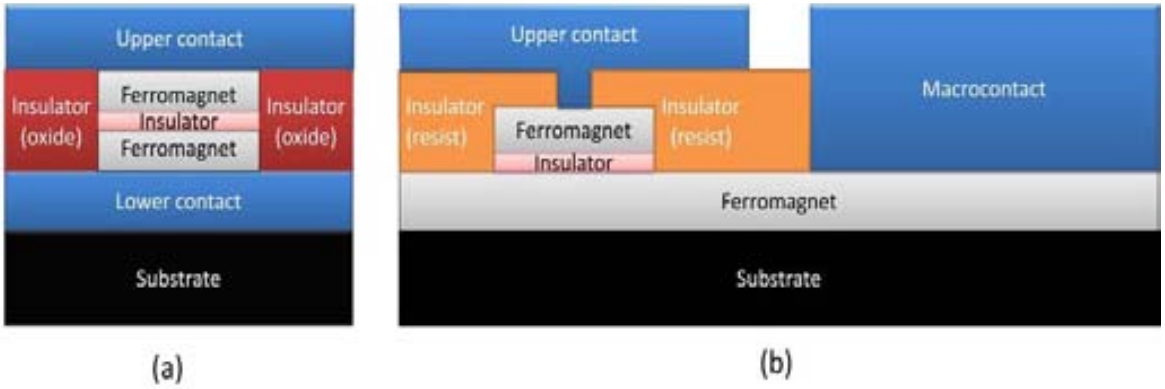

Fig 5.10. (a) Typical configuration for magnetic tunnel junctions includes lower and upper contact and an oxide is used as insulator. (b) Sketch of our configuration, where we use the same photoresist for the opening of the MTJ as insulator, and the bottom FM is not patterned.

As our aim is to make an initial exploratory study of the system and to study the interfacial phenomena related to it, far from any immediate technological application pretention, we take a simpler approach and do not grow a pinned layer structure but a simple single bottom electrode. Furthermore, in this thesis, we have tried a new device measurement configuration which is a bit less robust than that depicted in Fig 5.10a, but reduces the preparation process in a few steps, with the thought of circumventing some of the technical complications that may arise from these steps. This slightly simpler configuration consists in eliminating the deposition of an oxide layer to insulate the structure from the macrocontacts. Instead, we use as insulator material the same resist deposited for the opening of the gaps on top of the MTJ stacks (by lithography), as in Fig 5.10b.

5.3.2 Design considerations

When designing a magnetic tunnel junction device, we must consider some aspects that can optimize the switching behaviour, and therefore improve its performance. Such aspects are basically related to promoting uniaxial anisotropy in the direction of the element, in view to achieve the maximum abruptness in the switch, and avoid non-coherent rotation of the magnetization within each electrode. These aspects go from the choice of materials to the actual shape of the MTJ element designed.

Choice of **materials for the electrodes**: besides the suitability in terms of spin polarization (discussed in Chapter 2), the natural magnetic anisotropy of electrode materials can also be an interesting factor to consider: whether it possesses strong uniaxial or biaxial anisotropy; whether it tends to be magnetized in-plane or out of plane; the crystallographic orientation of its easy axis, etc. Applying an external magnetic field during the deposition of the electrodes can also induce a preferential uniaxial magnetic anisotropy [10].

Also, a difference between the coercive fields between the two electrodes (also dependent on the thickness and the junction sizes) is vital to have de coupled magnetization switching of both electrodes.

Selection of **electrode thicknesses**: for most materials grown in thin films, the magnetization tends to be oriented in-plane, and lower thickness increases in-plane anisotropy. Thick films also tend to present rougher surfaces; if that is the case for the lower electrode of a magnetic tunnel junction, we risk having "orange-peel coupling" [11] hot-spots and pinholes in the thin insulating tunnel barrier deposited on top. These issues have been discussed in Chapter 3.

Towards the **definition of the switching element**, various factors must be considered:

Orientation: to favour a step-like change of resistance visible in the resistance versus magnetic field sweep, the external magnetic field must be applied in the direction of the easy axis of the materials of the electrodes, where the hysteresis cycle will saturate at smaller applied magnetic field.

Shape, aspect ratio and width: to benefit from shape anisotropy, the MTJs are designed to have an enlarged shape in the direction of the magnetic field. In this way, we keep the magnetic moment in the structure always along the long axis of the element. However, the thermal stability due to shape anisotropy also depends on the aspect ratio $k = length/width$.

Stoner-Wohlfarth's single domain model [12] postulates that switching fields increase with higher k and shrinkage of MTJ sizes, and that lower k results in the formation of multi-domains and a decrease of the remnant magnetization. Increasing the aspect ratio also frustrates flux closure through the formation of magnetization vortices. However, the width of the element also affects vortex formation [13]. Besides, above a certain value of aspect ratio (around 2) the switching is no longer coherent, so that switching by nucleation and propagation of domain walls must be considered.

Besides the aspect ratio, the actual shape also matters: the magnetic moment orientation on a rectangular MTJ generates magnetic poles at the ends of the element, so depending on the specific shape of this ends, the switching threshold can vary notably [4]. Depending on the edge domains that are formed, different magnetic configurations are achieved (as can be seen for rectangular-shaped elements in Fig 5.11), which causes lack of reproducibility of the switching fields over repeated magnetization reversals. The difference between the switching fields increases with magnetic film thickness because of the increase of magnetostatic energy in the system [14]. Sharp ends would eliminate the possibility of domain creation, but it is technologically challenging because the MTJ fabrication naturally favours shapes with rounded corners (like the shape labelled "a practical element" in Fig 5.11).

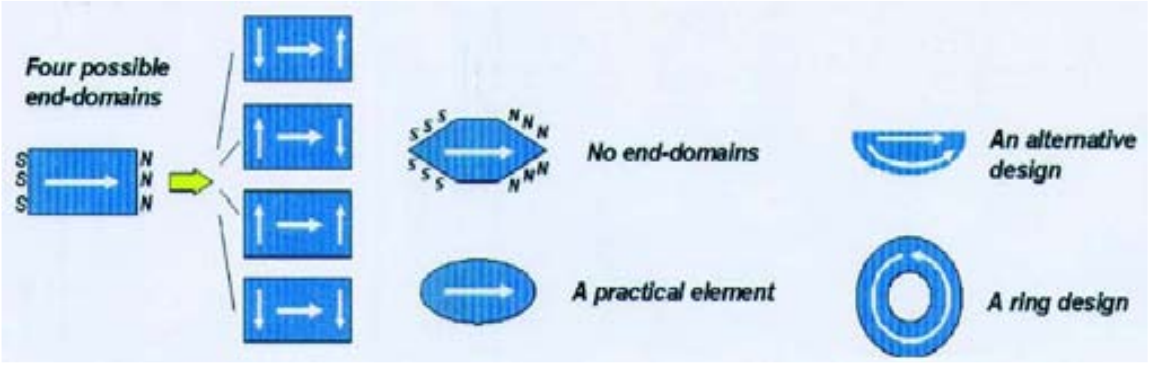

Fig 5.11. Different end configurations for rectangle-shaped switching elements (which give non-repeatable magnetic switching), and alternative shapes to control end domains. Figure adapted from [15].

Materials with perpendicular anisotropy are also being used in out-of-plane magnetized MTJ, displaying various advantages with respect to in-plane magnetized MTJ. In perpendicularly magnetized MTJ there is no magnetization curling at the edges. This allows low aspect ratio of 1, the MTJ size therefore reduced; and there is no switching field fluctuations, which are problematic for practical applications [16].

In our case, we have a stack of Au/Ti/Fe(110)/MgO(100)/LSMO(100)//STO(100). The growth conditions and optimization can be found in Chapter 3. Fe grows rotated 45º in-plane from the MgO, LSMO and STO, as already mentioned there. Taking into account that LSMO thin films have in-plane magnetization with practically no easy axis and that the easy axis of Fe is (100) [17], we pattern the rectangular-shaped MTJ along the (100) Fe direction, corresponding to the (110) crystallographic orientation of LSMO, MgO and STO.

Even if rectangular shape is not the optimum, as explained just above, we will define rectangle-shaped MTJ with slightly rounded corners, for simplicity. The aspect ratios used are between 2 and 3, and the whole process is detailed in the following sections.

5.3.3 Definition of the junction pillars by lithography

The first step towards the definition of the magnetic tunnel junction pillars is the patterning by lithography, defining the size and shape of the elements, and their orientation with respect to the substrate. As explained at the beginning of section 5.3, we use different optical lithography equipment in two different laboratories (GFMC at the Universidad Complutense and ICMAB), with different optimization or conditions:

5.3.3.1 With UV lamp and optical mask

To perform the lithography of the whole sample in a single step, we expose the sample to UV light through an optical mask with rectangle motifs of sizes 10×5, 15×5 and 18×9 μm^2, aligned 45º with respect to the substrate crystallographic axes. These motifs, hereafter called MTJ, are separated from each other forming a 3×3 matrix on a 5×5 mm^2 sample, except in one of the corners, where a macro-contact will be set. Surrounding the

central MTJ there are also some alignment marks necessary for the second lithographic step.

The optical mask and the sample are brought together until the mask is in contact with the photoresist. The UV light is shone on top of the mask during 17 seconds, changing the properties of the exposed photoresist. After developing, all the resin is removed except for the one below the MTJ rectangles, the alignment marks and sometimes even the borders of the sample (larger thickness of resist at the borders of the sample causes the direct contact between the mask and the resist, hardening the latter so that it is not removed as easily, see Fig 5.13c).

The actual recipe used was the following: spinning primer[4] 30'' at 6krpm, spinning photoresist MEGAPOSIT SPR700 30'' at 6 krpm, soft bake 80'' at 95 ºC on a contact hotplate, exposure to UV lamp 17 s and hard bake 80'' at 115 ºC on hot plate. The developer solution was 5 mL H_2O + 10 mL MF319 and the developing time is decided by visual inspection, when we can perceive a change in the colour of the solution surrounding the sample due to the fact that the photoresist has dyed the product in red.

5.3.3.2 WITH MICROWRITER

To perform the lithography with a UV raster-scan exposition, we use the microwriter. In this case, the motifs are designed using the program CleWin Layout Editor Version 4.3.5.0 and a UV laser beam is scanned above all the region of the sample from where we want to remove the photoresist. The main advantage of this method is the absence of photoresist remaining at the borders of the sample and the fact that no alignment marks are required. However, the process is much more time-consuming.

The recipe used and the following: manual focus, 1µm spot laser, exposure with dose of 200 mJ/cm^2. We use the laser with 1 µm spot because the laser with spot 0.6 µm is excessively focus dependent.

In Fig 5.12 we show an image taken by SEM of marks performed at an optimized dose of 220 mJ/cm^2, while testing the different radii, spot laser and focus in the microwriter. Four rows of dots were prescribed, the three above using laser with spot 0.6 µm (with radii of 0.6 µm, 0.8 µm and 1 µm) and the last one using laser with spot 1 µm (with increasing radii from 0.6 to 3.5 µm). No dots for the 0.6 µm-spot and 0.6 µm radius were visualized. The dependence on the focus correction for 0.6 µm-spot laser was very critical, whilst the 1 µm-spot laser seemed to be correctly focused with no focus correction.

[4] Primer is a substance which is used to promote the adhesion of photoresist onto a surface. It is useful because oxidized surfaces tend to create long range hydrogen bonds with adsorbed water from the air, so that photoresist adheres to the water vapour rather than to the surface, resulting in poor adhesion [21].

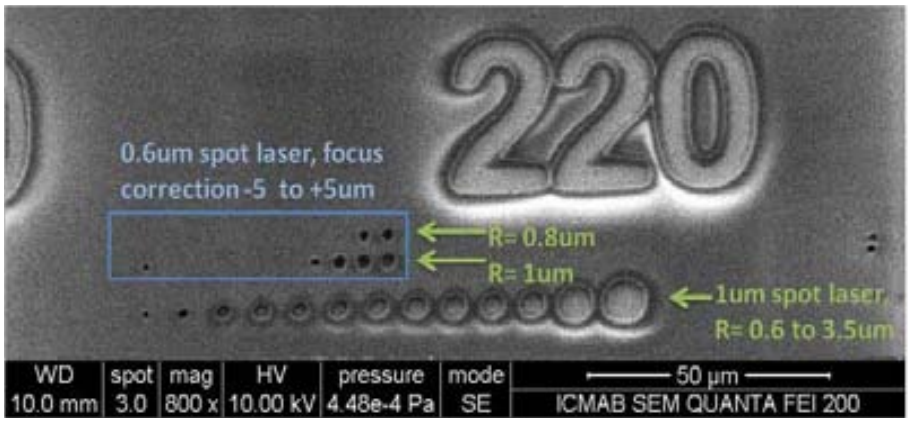

Fig 5.12. SEM image of test of radii and focus, using the 0.6 µm and the 1 µm spot laser in the microwriter. For 1 µm-spot laser, all dots were produced (radii ranging from 0.6 to 3.5 µm). With 0.6 µm-spot laser and radii 0.8 and 1 µm, a focus correction of -5, -4, -3, -2, -1, 0, +1, +2, +3, +4 and +5 µm was tested and the result was found to be very much dependent on the focus, and the sample had been very difficult to focus (see that dots are present for very high positive focus corrections).

5.3.4 ETCHING

The etching step consists in removing the top electrode (Fe and capping layers) from the unprotected regions of the sample. We initially tried with Reactive Ion Etching (RIE) with Ar, and with chemical etching which is fast and material dependent. However, we did not obtain the desired result and finally we used Ion Beam Etching and managed to etch down to the bottom electrode.

5.3.4.1 FAILED ATTEMPTS: REACTIVE ION ETCHING AND CHEMICAL ETCHING

Some first steps were done by reactive ion etching (RIE), which proves useful for etching LSMO or other compounds. After 10min of RIE with Ar (at the following conditions: 199 W, 200 Torr), from AFM we can see that a stack of Ti(5 nm)/Fe(17 nm)//MgO has only been etched 3-5 nm, so it is very slow. When increasing the amount of time to 30 min, we etch away all the resin before having removed all the Fe. We thought that the sample might be retaining charge due to the fact that the MgO substrate is insulating, so we tried again using a metallic structure which connects the surface of the sample with the cathode of the RIE. However, after successive failures in our attempts to effectively remove the Fe layer, we conclude that this method was not appropriated for the patterning process in our case.

Next, we attempted at using chemical etching, whose main advantage of which is the lower energy required than in physical etching, hence being less aggressive to the material and eliminating the possibility of ion implantation during the process [18]. We prepared a solution of HCl with concentration of 37 % diluted to 1/1000: 1 mL of HCl on 10 mL of deionized water and stirring, 1 mL of the previous solution on 100 mL of deionized water. After testing in various test samples, we conclude that the right time is in between 50 s and 2 min. However, to avoid inhomogeneities appearing at short times, we decide to attack a real sample for 2 min. Having done that, we obtain a well-defined

pattern on the sample, but unluckily we have removed the entire LSMO manganite bottom electrode, and the sample no longer conducts because the substrate is insulator.

5.3.4.2 FINAL CALIBRATION FOR IBE

Finally, we decided to proceed with the removal of Fe using Ion Beam Etching (IBE) and sent the samples to our co-workers in NanoGUNE (San Sebastián).

The milling was performed with the sample tilted 80º with respect to the incident beam (the milling conditions used were the following: Ar flux of 15 sccm, 300 V beam voltage, 50 mA beam current and 50 V of acceleration voltage). The height of the photoresist (1 µm) seems to cause shadows in the element edges during the etching process. To minimize this effect, the sample is being continuously rotated (spin speed of 15 rpm). Another option would be to mill at 90º, although it is not recommended because of a reduction in the efficiency and the fact that the surface of the sample gets dirtier. In the 80º configuration, the photoresist is easily removed with an acetone bath.

In Fig 5.13 we show optical images of the magnetic tunnel junction pillars and the corner of the sample (patterned with UV lamp) after Ion Beam Etching for 360 seconds the Au/Ti/Fe/MgO/LSMO//STO(100) stack. We can appreciate the shadowing effect mentioned above, which is more noticeable in some junctions and practically inexistent in others. Also, the corners have not been etched because they were protected by the photoresist that had been in contact with the physical mask.

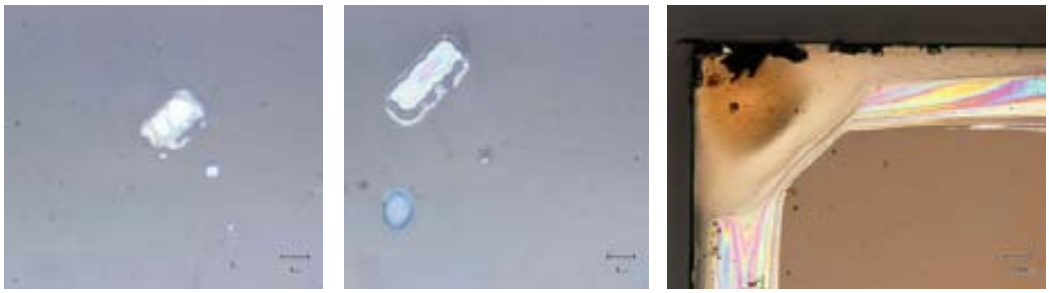

(a) (b) (c)

Fig 5.13. (a-b)The MTJ pillars after the Ion Beam Etching step: the borders of the MTJ pillars are etched irregularly due to shadowing (see Appendix A). (c) The corners of the sample which has been lithographiated with the UV lamp and physical mask are not etched because the pressure of the mask on the photoresist prevents the resist from dissolving in the developer solution.

To confirm the total elimination of the top electrode other than at the MTJ stacks, we perform some EDAX using the SEM. In Fig 5.14a we show the image from the backscattered electrons of one of the alignment marks from the lithography with the UV lamp and compare the attacked regions (in dark colour at the backscattered electrons image) with the protected regions (in white at the backscattered electrons image), and Fig 5.14b is a table with the quantitative information about the percentages of each element in various regions of the sample after the IBE etch.

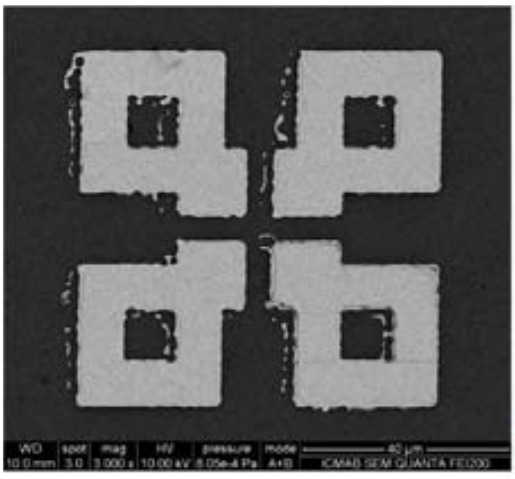

(a)

	attacked area (dark in the BSE)		Non-attacked area (white in the BSE)	
Element	Wt%	At%	Wt%	At%
CK	4.01	13.09	11.34	36.22
OK	19.03	46.56	10.24	24.56
MgK	0.13	0.21	0.16	0.26
SrL	37.05	16.55	24.16	10.58
TiK	16.68	13.63	10.78	8.63
LaL	15.11	4.26	13.29	3.67
MnK	7.98	5.69	6.45	4.50
AuM	-	-	9.37	1.83
FeK	-	-	14.20	9.76

(b)

Fig 5.14. (a) SEM image of an alignment mark after Ion Beam Etching, corresponding to the backscattered electrons (BSE) signal, which provides contrast for the differences in the sample composition; (b) results of the EDAX analysis: weight and atomic percentage of each element for both analysed zones: the attacked area and the non-attacked area.

After the etching process, there is no presence of Au or Fe in the attacked area. But as we detect the presence of Mg (from the MgO layer), we suspect that we have attacked just at the limit. To ensure that the attack is complete, we decide to slightly increase the milling time for the rest of the samples (360 s+40 s). To calibrate the etching rate, some extra samples were prepared and profilometry measurements gave us the approximate etching rates, listed in Table 5.3. Given the thickness of the bottom LSMO electrode, even if we etch some LSMO it is not critical. However, overetching the LSMO electrode may be the cause of stray fields, which we should avoid [19].

On the other hand, an important problem with ion milling is the possible redeposition of the removed material on the walls of the patterned elements, which can cause electrical shorts of the junctions if the redeposited material is conductive. Overmilling helps removing the deposited sidewalls if the patterned elements are sufficiently far apart, the problem remaining for small and dense geometries required for commercial MRAM. Other possibilities include the use of reactive chemistries to induce the creation of etch products which can be more easily removed from the sample surface [15].

Table 5.3. Estimation of IBE rates, obtained from perfilometry measurements in some test samples.

Etching materials	Etching rates (nm/min)
Fe	2.8 - 3.3
LSMO	1 - 1.16
STO	3
Pt	7.5

5.3.5 ALIGNMENT AND SECOND LITHOGRAPHY STEP

The aim of this step is to perform a second lithography to open some holes on top of the MTJ stack in order to contact the sample to the macrocontacts that we will deposit on top. The alignment in this step is critical, because the motifs are small and the holes on the photoresist must not be too much on the edge of the MTJ stack, to prevent the deposited material to reach the lower electrode, short-circuiting the junction. After this second lithography step we do not remove the photoresist, but leave it on the sample to profit from its insulating properties.

Again, as in section 5.3.3, the process has been done with two different lithographic techniques; using the optical lamp with chromium mask and using the microwriter.

5.3.5.1 WITH OPTICAL MASK

The optical mask pattern for this second lithography step (pattern II) consists in an opaque square of the size of the sample with some transparent rectangle motifs of smaller sizes (2/3 of those in pattern I). They are also aligned 45º with respect to the substrate. Some alignment marks are also engraved.

The sample is approached to the optical mask, held in a fixed position, and the relative positioning of the sample with respect to the optical mask can be adjusted using three micrometric screws: one moves vertically, another moves horizontally and the other performs a rotation. The alignment consists in successive adjustment of these three parameters until the alignment pattern from the first lithography (where we define the MTJ rectangles) matches the alignment pattern of this second lithography (where we open a gap on top of the MTJ stacks). A useful tip is to adjust the rotation taking as reference the corner of the sample which is opposite to the rotation axis of the positioning system in the lamp, and adjust the vertical and horizontal movements using the corner next to the rotation axis. After a few iterations, a correct alignment should be reached. The conditions for this second lithography step are the same as the ones detailed in section 5.3.3.1, differing only in the exposure time.

5.3.5.2 WITH MICROWRITER

Once the MTJ pillars have been defined and attacked, we make use of the combination of two lasers in the microwriter: a red laser, which does not modify the photoresist properties, and a blue laser, which does expose the photoresist. The red laser scans the position where we expect the pillar to be, so we use it to centre the second lithography pattern (an opening just on top of the pillar). In Fig 5.15a we can see how the contrast between the pillar and the non-attacked region is clear and enables us to do a good alignment.

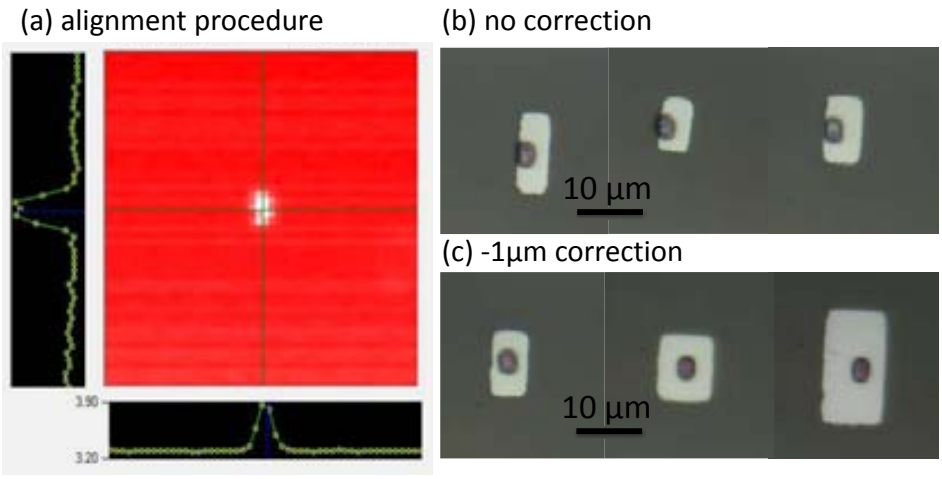

Fig 5.15. (a) Alignment of the pattern II on top of the MTJ stack using the red laser. (right) Calibration of the misalignment between the red and the blue laser. Optical images corresponding to squares patterned on the photoresist on top of Pt, introducing a corrective factor with respect to the alignment procedure of (b) 0 µm, (c) -1 µm.

However, we detect a certain misalignment between the positioning of the red laser (used to centre the sample in this second step) and the blue laser (used to expose and effectively alter the photoresist properties). So, just before performing this second lithography step, we perform the alignment and exposure on a test sample to check the value of the misalignment, and use this corrective factor (usually -1 µm) in the positioning of the motifs.

The recipe used is the following: independent focus for each junction, red laser scan to obtain position (we will take into account the corrective factor), 1 µm-spot laser exposure with dose of 230-260 J/cm^2 depending on the position and the size of the patterned element (higher dose is required closer to the edge of the sample because of the non-homogenous deposition of photoresist; and smaller exposed areas need higher dose). The minimum size for the rectangle in this second lithography step, in order to have a real opening and reach the metallic surface of the MTJ stack, is 2×3 µm^2. The large macrocontact was done in dose 600 J/cm^2.

5.3.6 CONTACTS

Finally, the macrocontacts must be deposited; we either evaporate Au or sputter Pt on top of the openings. Whenever possible, we also perform 30 s UVO cleanse to minimize the probability of any photoresist residue on top on the junction opening. To perform transport measurements, we perform hand-made electrical contacts because wirebonding may destroy the tunnel junction. In Fig 5.16a we show a TEM image of the cross-section of the Fe/MgO/LSMO heterostructure after the evaporation of Au contacts. We note that a thin layer of photoresist (black contrast) remains between the Au layers, so that further effort must be done to ensure its complete removal. In Fig 5.16b we show an image taken by SEM of a magnetic tunnel junction after it has

been measured and the sample has been cleaned. After the lift-off process, some Au from the deposited macrocontact still remains.

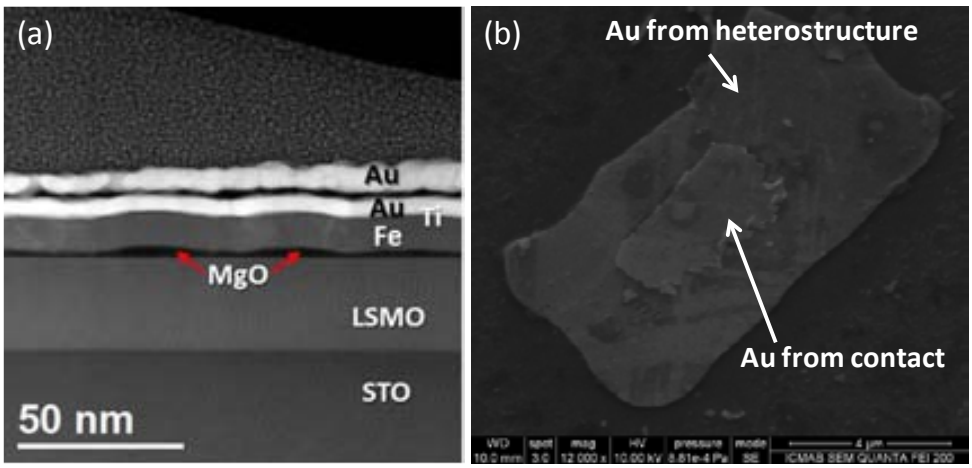

Fig 5.16. (a) TEM image of the heterostructure for a contacted region, where resist (black contrast) remains between the Au layers; (b) SEM image of a magnetic tunnel junction after it has been measured.

5.4 SUMMARY

In this chapter we have described the fabrication process for two types of tunnel junction devices tested in this thesis: (i) junctions of Pt/LAO/LSMO patterned by e-beam lithography to yield small-area junctions, and (ii) magnetic tunnel junctions of Fe/MgO/LSMO patterned by UV-lithography. In both cases, the final configuration includes the resist from the patterning process, so that we take advantage of its insulating properties.

For the first case, electron-beam lithography parameters are previously optimized to yield the small-sized dots: Pt dots with a diameter of 100 nm are achieved by using a single PMMA layer and defining squares of nominal sizes of 50-90 nm. The exposure is performed using a dose of 160 $\mu As/cm^2$ and 10 kV. A shadowmask is also fabricated. For the fabrication of the Pt/LAO/LSMO tunnel junctions, junctions with different areas are defined by e-beam lithography using the mentioned parameters and Pt is sputtered through the shadowmask to define the macrocontacts on top. The areas of the dots are estimated from SEM images and shown to correspond to the areas prescribed for the lithography, thus confirming a good dose has been used. In Chapter 6 we will discuss the results of magnetotransport experiments performed with such junctions. Similar junctions fabricated using the same procedure but with photoresist and using UV-lithography are also analysed.

As for the magnetic tunnel junctions of Fe/MgO/LSMO, rectangular-shaped stacks are obtained by etching the top Fe electrode and patterning some openings on top, in which the Au macrocontacts are deposited, again through the shadowmask. The junctions have larger sizes and are patterned using photoresist and two UV lithographic method: UV lamp exposure and "microwriter". The calibration of each step has been discussed. In

Chapter 7 we will discuss the magnetotransport behaviour of these magnetic tunnel junctions.

5.5 REFERENCES

[1] Collins S.D.; "Semiconductor Micromachining: Vol. II. Techniques and Industrial Applications". Wiley; **1998**.

[2] Madou M.J.; "Fundamentals of Microfabrication: the Science of Miniaturization". Second Edi. CRC Press LLC; **2000**.

[3] Shinji Y.; Tunneling Magnetoresistance. Handb. Spin Transp. Magn., Chapman and Hall/CRC; **2011**, p. 217–31. doi:doi:10.1201/b11086-15 10.1201/b11086-15.

[4] Zhu J.-G.; "Magnetoresistive Random Access Memory: The Path to Competitiveness and Scalability". *Proc. Ieee* 96; **2008**: 1786–98. doi:10.1109/jproc.2008.2004313.

[5] Djayaprawira D.D., Tsunekawa K., Nagai M., Maehara H., Yamagata S., Watanabe N., et al.; "230% room-temperature magnetoresistance in CoFeB/MgO/CoFeB magnetic tunnel junctions". *Appl. Phys. Lett.* 86; **2005**. doi:10.1063/1.1871344.

[6] Park C., Zhu J.-G., Moneck M.T., Peng Y., Laughlin D.E.; "Annealing effects on structural and transport properties of rf-sputtered CoFeB/MgO/CoFeB magnetic tunnel junctions". *J. Appl. Phys.* 99; **2006**. doi:10.1063/1.2165141.

[7] You C.Y., Ohkubo T., Takahashi Y.K., Hono K.; "Boron segregation in crystallized MgO/amorphous-Co40Fe40B20 thin films". *J. Appl. Phys.* 104; **2008**. doi:10.1063/1.2963709.

[8] Kozina X., Ouardi S., Balke B., Stryganyuk G., Fecher G.H., Felser C., et al.; "A nondestructive analysis of the B diffusion in Ta-CoFeB-MgO-CoFeB-Ta magnetic tunnel junctions by hard x-ray photoemission". *Appl. Phys. Lett.* 96; **2010**. doi:10.1063/1.3309702.

[9] Yuasa S., Djayaprawira D.D.; "Giant tunnel magnetoresistance in magnetic tunnel junctions with a crystalline MgO(001) barrier". *J. Phys. D-Applied Phys.* 40; **2007**: R337–54. doi:10.1088/0022-3727/40/21/r01.

[10] Gallagher W.J., Parkin S.S.P., Lu Y., Bian X.P., Marley A., Roche K.P., et al.; "Microstructured magnetic tunnel junctions". *J. Appl. Phys.* 81; **1997**: 3741–6. doi:10.1063/1.364744.

[11] Zhang J., White R.M.; "Topological coupling in spin valve type multilayers". *Ieee Trans. Magn.* 32; **1996**: 4630–5. doi:10.1109/20.539101.

[12] Stoner E.C., Wohlfarth E.P.; "A mechanism of magnetic hysteresis in heterogeneous alloys". *Philos. Trans. R. Soc. London Ser. a-Mathematical Phys. Sci.* 240; **1948**: 599–642. doi:10.1098/rsta.1948.0007.

[13] Girgis E., Schelten J., Shi J., Janesky J., Tehrani S., Goronkin H.; "Switching characteristics and magnetization vortices of thin-film cobalt in nanometer-scale patterned arrays". *Appl. Phys. Lett.* 76; **2000**: 3780–2. doi:10.1063/1.126779.

[14] Zheng Y.F., Zhu J.G.; "Switching field variation in patterned submicron magnetic film elements". *J. Appl. Phys.* 81; **1997**: 5471–3. doi:10.1063/1.364629.

[15] Ditizio R., Werbaneth P., Corporation T., and Zhu J.-G.; "Cell Shape and Patterning Considerations for Magnetic Random Access Memory (MRAM) Fabrication". *Dep. Electr. Comput. Eng. Pap. 45* **2008**.

[16] Nishimura N., Hirai T., Koganei A., Ikeda T., Okano K., Sekiguchi Y., et al.; "Magnetic tunnel junction device with perpendicular magnetization films for high-density magnetic random access memory". *J. Appl. Phys.* 91; **2002**: 5246–9. doi:10.1063/1.1459605.

[17] Spaldin N.A.; "Magnetic Materials: Fundamentals and Applications". Second Edi. Cambridge University Press; **2010**.

[18] Peña Guédez L., Martínez Perea B.; Sistemas Nanoestructurados y Propiedades de Transporte en Capas Delgadas de Manganita. Universitat de Barcelona, **2014**.

[19] Bowen M.O., Fert A.; Experimental Insights into Spin-Polarized Solid State Tunneling. Université de Paris-Sud, U.F.R. Scientifique d'Orsay, **2003**.

[20] "UVO-Cleaner (R) Jelight Company Inc" online. http://www.jelight.com/uv-ozone-cleaning.html (accessed April 02, 2014).

[21] "Photolithography Resist Processes and Capabilities" online. http://www.cnf.cornell.edu/cnf_process_photo_resists.html (accessed March 05, 2014).

PART IV:

MAGNETORESISTIVE PROPERTIES OF SPIN-DEPENDENT TUNNELING DEVICES

CHAPTER 6. PT/LAO/LSMO TUNNEL JUNCTIONS

Magnetic random access memories based on MTJs have been proposed as one of the most solid candidates for non-volatile memory devices because they combine alternatives based on new materials and/or new architectures [1]. However, in spite of the intense work already done, some technical challenges –such as the uniformity of the magnetic properties of the electrodes, the insulating barrier uniformity or the thermal stability, are still not fully resolved [2]. The characterization of barriers and interfaces is therefore of great importance and there is still much work to be done.

The use of half-metallic materials as electrodes [3–6], is expected to result in an important increase of the TMR. Nevertheless, only in the cases of optimized junctions based on manganite electrodes, such as $La_{2/3}A_{1/3}MnO_3$ (A=Sr, Ca), TMR values of several hundred percent have been reported so far [7–9], or even 1800 % at 4 K [10] for optimized pattering process, although unfortunately those TMR values become vanishing small well below room temperature. LSMO, with the highest Curie temperature ($T_C \sim 370$ K) in this family of materials, is the most interesting one for the implementation of devices, so its interface with various insulating materials (STO, MgO, LAO, $NdGaO_3$ (NGO)...) has been the subject of many works [11–13].

In particular, LAO is an insulator with a high dielectric constant, a broad band gap and a band offset with Si of about 1.8 eV which renders it one of the ideal materials for spin injection into semiconductors [14]. Besides being structurally compatible with LSMO because of its perovskite structure, LAO capping has demonstrated to be less harmful for the magnetic and electronic properties of LSMO than other oxides such as STO, NGO or MgO [11,15–18]. Furthermore, it has been shown that the temperature dependence of spin polarization of LSMO with LAO capping resembles that of the magnetization M(T), but with lower critical temperature [12].

The characterization of interfaces is not easy due to the fact that they are buried below several nanometers of material of the upper electrode, thus requiring the use of interface-selective probing techniques. High-resolution transmission electron microscopy jointly with electron energy loss spectroscopy, as well as other surface, element, and magnetic sensitive X-ray spectroscopy techniques have been used to investigate manganite-oxide interfaces [15,16,19–21]. While these techniques may offer a profound and accurate vision of the different physical and chemical aspects of the electrode/insulating barrier interface, they either require a complex sample preparation or are expensive and not of easy access.

To overcome these challenges, and taking advantage of the fact that tunnelling current is sensitive to the electronic structure of the barrier (as shown by recent results on MgO-based MTJs [13]) and the electronic properties of the electrode/barrier interface [22], direct transport measurements across the interfaces are an interesting alternative for

tunnelling barrier characterization aimed at technological applications. In previous work, other members of our group implemented a procedure to study transport properties across manganite/insulating barriers interfaces at room temperature by using atomic force microscopy working in the current sensing mode (CS-AFM) [18,23]. To avoid intrinsic problems of the CS method, related to the determination of the actual contact area between the AFM tip and the surface, they developed a nanostructured contact geometry of metallic dots. With this experimental setup a homogeneous current injection across the insulating barrier/manganite interface is obtained and the density of current is controlled by the dot area, thus allowing a fast characterization of the insulating layer avoiding the whole MTJ microfabrication process. However, this procedure does not allow studying neither magnetic field nor temperature dependence of the tunneling conduction process.

In this chapter we tackle the study of the magnetotransport properties of LAO/LSMO bilayers by using a Pt/LAO/LSMO contact geometry (explained in Chapter 5) which allows us to probe the transport properties across LAO insulating barriers as a function of temperature and applied magnetic field. In particular, we will show that Pt/LAO/LSMO tunnel junctions exhibit TAMR, i.e., a dependence of the tunnel magnetoresistance on the orientation of the magnetization of the electrodes with respect to the crystallographic axes or the current flow direction. The origin of TAMR is the interference between Bychkov-Rashba and Dresselhaus spin-orbit couplings that appears at junctions' interfaces and in the tunnelling region. Since TAMR may appear in tunnel junctions with only one magnetic electrode, it could be an alternative of much easier technological implementation than conventional tunnel magnetoresistance devices [24].

6.1 DETAILS ON SAMPLE PREPARATION AND MEASUREMENT CONFIGURATIONS

LAO(1.5 nm)/LSMO//STO heterostructures were grown as explained in Chapter 3, as in Ref. [16]. The fabrication of the structures is explained in section 4.2. Briefly, samples were covered with a PMMA layer, a series of squares (of sizes from 0.01 to 100 μm^2) were defined by electron beam lithography, UVO cleanse was performed to ensure a clean LAO surface inside the patterned apertures and Pt was deposited by evaporation through a shadow mask defining a metallic macrocontact on top of each nano-square, finally yielding the structure depicted in Fig 5.1. These junctions were measured in a 2-terminal configuration, between a large area macrocontact and much smaller-sized contact. Due to the particular configuration of the measurement setup, a careful characterization of the transport properties as a function of the area of the upper Pt electrode was performed to ensure that contribution from the electrodes was avoided.

However, this experimental setup, used in section 6.2, resulted in a failure of the contacts at low temperatures due to problems related to the thermal contraction of PMMA resist (below about 110-120 K). Given this limitation on the probed temperature

when using PMMA, we proceeded to repeat the fabrication of such junctions using UV positive photoresist instead. This small change allowed us to reach low temperatures, at the expense of larger junction areas (used in section 6.3). Therefore, measurements are performed in a 3-terminal measurement configuration to avoid contributions from the lower electrode.

Transport measurements were performed in a Physical Properties Measurement System (PPMS) by Quantum Design to control the temperature and magnetic field, but using an external Keithley source.

6.2 Evaluation of barrier parameters using Simmons' tunnelling model at intermediate voltages

6.2.1 Junction area dependence

I-V curves for Pt/LAO/LSMO junctions taken at room temperature exhibit non-linear behaviour. The density of current *vs.* voltage measured for several nanocontacts of different areas (ranging from 0.04 to 35 μm^2) is shown in Fig 6.1a (symbols).

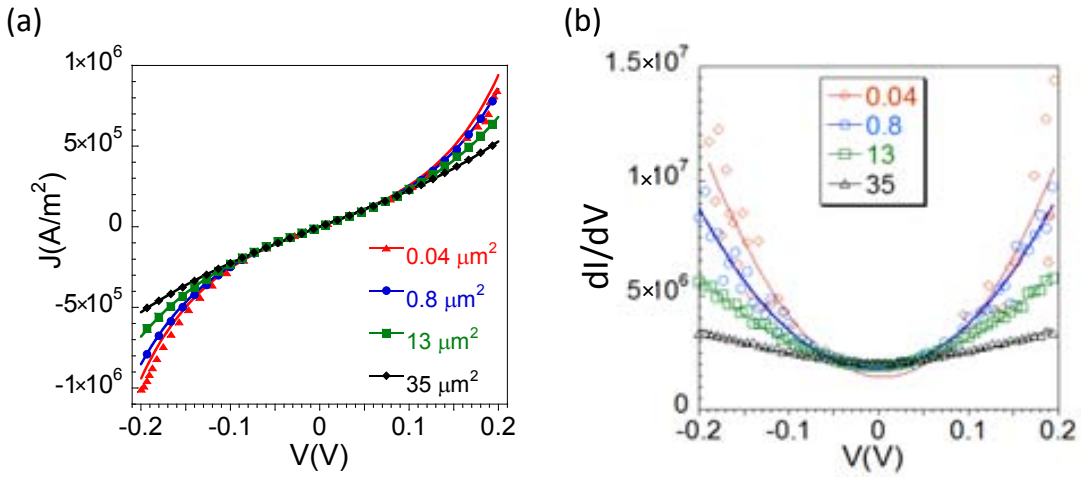

Fig 6.1. (a) Density of current *vs.* voltage curves at 300 K for different-sized nanocontacts (areas ranging from 0.04 to 35 μm^2) measured with PPMS (markers) and their corresponding Simmons' fits (solid lines); (b) Conductance *vs.* voltage curves for the same junctions fitted by using Brinkman's model.

The resistance in the ohmic region as a function of the junction area shows good agreement with a line of slope -1 in the log-log plot in Fig 6.2. This indicates that the resistance in the ohmic region is mostly inversely proportional to the nanocontact area. The constant resistance-area product entails that the thickness of the LAO is constant for all the junctions, thus confirming the good quality of the heterostructure.

The mentioned proportional relationship does not hold, however, for contacts with very small or very large areas. In the case of smaller areas, the discrepancy is attributed to problems related with the fabrication process and determination of the actual area. In the

case of larger areas, it is ascribed to the non-negligible contribution of the experimental setup to the measured resistance due to the 2-terminal configuration (the resistance between two macrocontacts is 1.7 kΩ), as well as the larger probability of inhomogeneites (pinholes, microstructural defects...). For these reasons, we discard nanocontacts with areas which do not fall within the range of 0.04 – 40 μm^2.

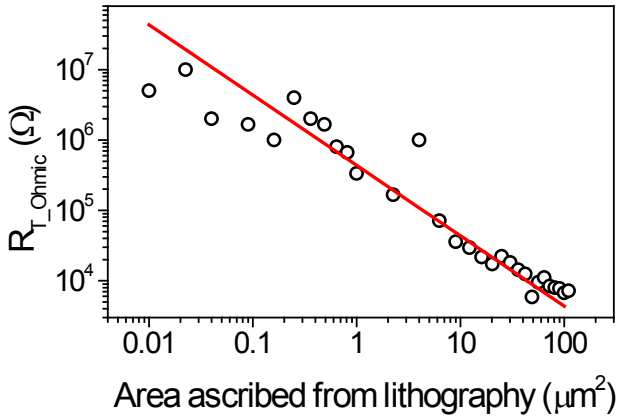

Fig 6.2. Tunnelling resistance measured in the Ohmic region for different-sized nanosquares. The red line shows that resistance is proportional to the inverse of the area because its slope is -1 in the log-log plot.

I-V curves have been analysed in the intermediate voltage regime using the Simmons model [25] given by the following equation:

$$J = \left(\frac{e}{2\pi h s^2}\right)\left\{\left(\varphi_0 - \frac{1}{2}eV\right)exp\left[-(2m)^{1/2}\frac{4\pi s}{h}\left(\varphi_0 - \frac{1}{2}eV\right)^{1/2}\right] - \left(\varphi_0 + \frac{1}{2}eV\right)exp\left[-(2m)^{1/2}\frac{4\pi s}{h}\left(\varphi_0 + \frac{1}{2}eV\right)^{1/2}\right]\right\} \quad [6.1]$$

Where J is the density of current obtained by dividing the intensities by the area of the different nanocontacts, e and m are the electron charge and mass respectively, h is Planck's constant, s the thickness of the barrier, φ_0 the energy of the barrier and V the applied voltage.

Fitting G(V) curves using Brinkman's model [26] gives similar values for φ_0 and s with a small asymmetry parameter, thus indicating I-V curves are substantially symmetric, as can be appreciated from the conductance *vs*. voltage curves (and their corresponding Brinkman fit) in Fig 6.1b, except for the case of the smallest-sized nanocontact. So, for simplicity, we use Simmons' model.

Some examples of Simmons' fits of the obtained J-V are shown in Fig 6.1a(lines) while the different obtained values of φ_0 and s corresponding to nanocontacts with different areas are depicted in Fig 6.3a. Assuming a uniform and defects free LAO layer, both φ_0 and s values should be independent of the nanocontact area. However, the figure evidences that both parameters change when large area nanocontacts are considered. This fact indicates that, as mentioned above, for large area nanocontacts the non-

negligible contribution of the experimental setup resistance to the measured resistance masks the intrinsic properties of the insulating LAO barrier. For that reason we will take into consideration results obtained for nanocontact areas smaller than 5 μm^2 only.

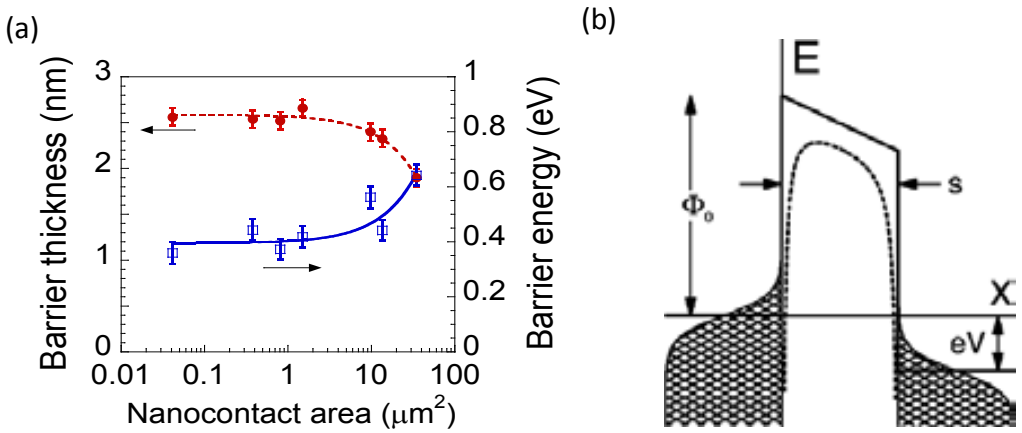

Fig 6.3. (a) Barrier thickness s (in red, referred to the left axis) and barrier energy φ_0 (in blue, referred to the right axis), determined from Simmons' fit, for I-V curves taken at 300 K from nanocontacts of different sizes. Lines are guide to the eyes; (b) Schematic representation taken from [27] of barrier thickness and energy for an ideal barrier (continuous line) and with image forces (discontinuous line).

Effective insulating barrier thickness values determined using equation 6.1 are around $s \approx$ 2.5 nm, in contrast with the ~1.5 nm nominal thickness determined from the growth rate and TEM (see Fig 3.11a). This enhancement of Δs ~1 nm of the barrier thickness has been previously observed in these systems and is attributed to interfacial effects due to the structural disruption and inversion symmetry breaking at the LSMO interface [15,16,18]. These effects promote the appearance of an insulating antiferromagnetic layer about 1 nm-thick at the topmost LSMO layers that explains the observed enhancement of the effective barrier thickness.

On the other hand, the values obtained for the barrier height, φ_0, are around 0.4 eV. Theoretically, the barrier height between LSMO and LAO is given by

$$\varphi_0 = W_{LSMO} - \phi_{LAO} \qquad [6.2]$$

where W_{LSMO} is the work function of LSMO (W_{LSMO} ~ 4.9 eV)[28] and ϕ_{LAO} is the electron affinity of LAO (ϕ_{LAO} ~2.5 eV)[29]. With experimental conditions considered –basically image forces, which take into account that the barrier does not possess an infinite dielectric constant because it is not ideal (see Fig 6.3b), and the fact that capping layers also modify the structure [30]- the barrier height should be smaller than ~2.4 eV, as experimentally found. The values derived for φ_0 are also in good agreement with both theoretical and experimental values of LAO tunnelling barriers reported previously [30,31]. However, although epitaxial cube-on-cube growth of LAO on LSMO can be seen from TEM images (see Fig 3.11a) and AFM reveals the step-and-terrace structure, as our growth does not take place in a clean room, the existence of some microstructural

defects or randomly distributed pinholes affecting the quality of the barrier cannot be fully excluded. In these circumstances the existence of conducting channels other than direct tunnelling conduction may not be fully discarded and this may be more likely as the area junction increases. In such a case, the temperature dependence of the zero-bias resistance of the heterojunction would be a reliable indicator of the quality of the barrier and the dominant role of the tunnelling conduction process. To that end, the temperature dependence of the resistance is analysed in the following section.

6.2.2 Dependence on temperature and magnetic field

I-V curves for a Pt/LAO/LSMO junction of ~0.8 μm^2 were taken lowering temperature down to 130 K. We observe that measurements taken at lower temperatures yield more resistive curves (see symbols in Fig 6.4a). Further reduction of the temperatures caused the loss of good contact properties (we suggest it is related to contraction of the PMMA resist which affected the contacts) and prevented proper transport measurements. As shown in Fig 6.4b, the temperature dependence of the junction resistance in the ohmic region exhibits an insulating behaviour indicative of a pinhole-free barrier [32] above 170 K. Noteworthy, R(T) describes a dome-like shape that peaks at about 150 K, which seems to be a common feature of junctions having manganite electrodes and whose origin has not been clarified yet. As discussed in section 6.3, a peak in the R(T) is generally reported for LSMO-based MTJ.

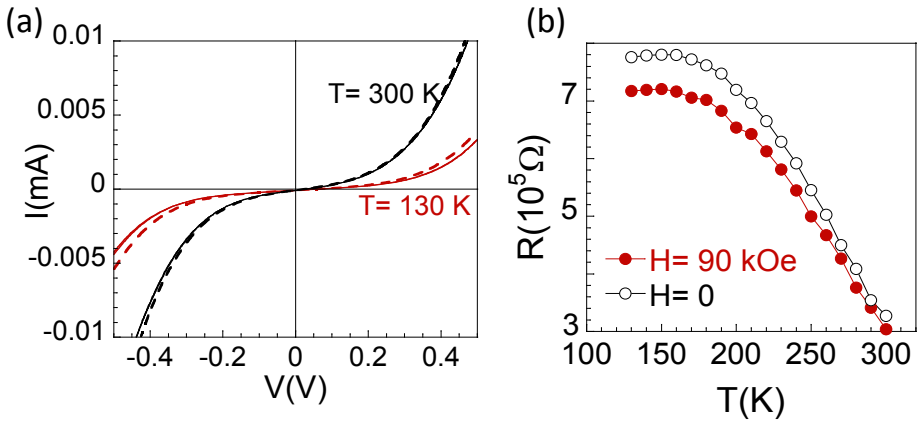

Fig 6.4. Dependence of tunnelling current and resistance on temperature and magnetic field (H=90 kOe) applied perpendicular to the sample plane; (a) I-V characteristic curves taken at 130 and 300 K for H=0 (continuous lines) and H=90 kOe (dashed lines); (b) Ohmic resistance as a function of temperature for H=0 (open dots) and H=90 kOe (solid red dots).

These I-V curves were also fitted using equation 6.1 in the low voltage regime (±0.2 V). In principle, barrier height, φ_0, and barrier thickness, s, should be almost temperature-independent. However, a progressive increase of the barrier height is detected when lowering temperature and, in parallel with this increase of φ_0, a reduction of the barrier thickness was also detected (see Fig 6.5a). Regarding this temperature dependence, it is worth mentioning that the values of φ_0 and s have been determined using equation 6.1 that does not include temperature effects. As shown by Simmons [33], the thermal

component of the tunneling current is proportional to T^2 and this contribution, which is not taken into account in equation 6.1, is reflected in our results as a decrease of φ_0 when increasing temperature. In fact, the observed variation of φ_0 (from Fig 6.5b) is clearly proportional to $1/T^2$. Other additional mechanisms, such a strong temperature dependence of the dielectric constant of LAO, the thermal expansion of the barrier volume or the increase of the thermal activation across de barrier may also affect the tunneling conductance, but in our case their effects are much smaller than the thermal broadening of Fermi-Dirac statistics [27].

On the other hand, the variation of the barrier thickness, of about a unit cell, may also have different contributions. First, thermal expansion of the barrier thickness when increasing temperature was considered: a rough approximation gives $\Delta s/s \approx 0.002$, which in a barrier of <2 nm would cause a clearly smaller effect than the observed $\Delta s \approx 0.5$ nm on increasing T from 130 K to room temperature. Other possible explanations for the change of s are related to interfacial effects in the LSMO topmost layers. However, in the case of LAO/LSMO interface intrinsic effects, structural disruption and inversion symmetry breaking at the LSMO interface seem to be dominant [15,16], thus not very likely to be temperature dependent. Nevertheless, some thermal induced disorder at the interface cannot be fully disregarded.

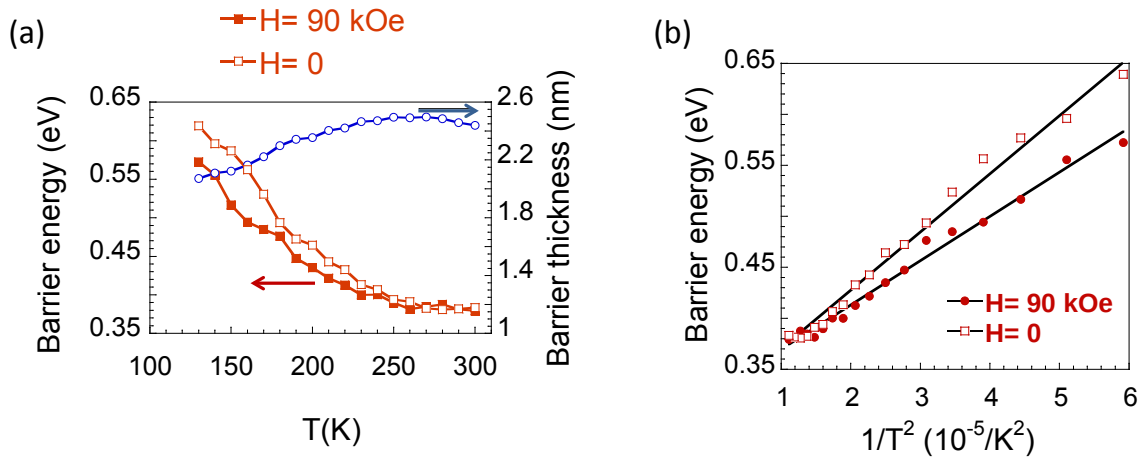

Fig 6.5. Simmons parameters as a function of temperature and magnetic field. (a) Barrier thickness (in blue, referred to the right axis) and barrier energy (in red, referred to the left axis). The latter is represented for H=0 (open symbols) and H=90 kOe (solid symbols). Variation of barrier thickness with field is within the experimental error. (b) Barrier energy (for H=0 and 90 kOe) represented as a function of $1/T^2$.

The effect of the application of a magnetic field of 90 kOe on the tunnelling current was also analysed: I-V curves measured with a magnetic field of 90 kOe applied perpendicular to the sample plane (parallel to the current) resulted in lower resistance for all tested temperatures (see dashed lines in Fig 6.4a and red dots in (b)). This magnetoresistance is especially important for the lower measured temperatures: in particular, the MR reaches ~7.5% at 130 K. Such magnetoresistance is explored more deeply in the following section, where lower temperatures were reached using positive

photoresist instead of PMMA for both the patterning process and the final measured system. The resistance is probed as a function of the magnetic field orientations to try to elucidate the origin of each magnetoresistive contribution.

6.3 TAMR IN Pt/LAO/LSMO JUNCTIONS

In this section, we present a study of the magnetoresistive response of a 16 μm^2-sized Pt/LAO/LSMO tunnel junction patterned using UV positive photoresist and measured in a 3-terminal configuration. The substitution of the PMMA resist for a positive photoresist allows reaching low temperature values, while the use of a 3-terminal configuration avoids the masking effects of the contribution of the bottom electrode to the measured junction resistance.

6.3.1 TEMPERATURE DEPENDENCE OF THE JUNCTION RESISTANCE

The junction's resistance as a function of temperature reveals a peak at around ~170 K and suggests an increase of the resistance at lower temperatures (below 10 K), as represented in Fig 6.6b (blue dots). Although this dependence seems to be similar to that of the 0.8 μm^2-sized junction for the tested range, analysed in section 6.2.2, two distinct differences must be pointed out:

- To start with, this larger-area junction possesses much smaller resistance (even when the area is taken into account –the comparison must be done for the R×A product). At room temperature, for example, the R×A products are 240 $k\Omega \cdot \mu m^2$ and 48 $k\Omega \cdot \mu m^2$ for the smaller and larger-sized junctions, respectively. This difference could be explained by the fact that a larger area of the junction increases the probability of a region with smaller thickness, which always dominates the tunnelling conduction. Or by a slight variation in the thickness of both samples –we recall that a unit cell variation of the thickness has an important impact because the dependence is exponential on the thickness (from equation 2.8).
- It must also be mentioned that the increase of the resistance (from room temperature to the maximum resistance measured for the peak) represents a 133 % and a 500 % variation of the resistance with respect to the room temperature resistance for the smaller and larger-sized junctions, respectively. Whilst the mostly linear increase of resistance with decreasing temperature for the junction in section 6.2.2 was attributed to direct tunnelling, the larger percentual variation and non-linear R(T) dependence at high temperatures for the larger-sized junction suggests alternative conduction channels besides direct tunnelling. Hopping dependence ($\propto T^{-\frac{1}{4}}$) has been tested for this temperature range but does not apply.

Furthermore, we note that the peak existence is not linked to the quality of the LSMO bottom electrode, as the R(T) of the latter yields a metal-insulator transition at higher

temperatures, close to T_C (~350 K). The R(T) curve corresponding to the bottom LSMO electrode probed in a 4-terminal configuration is shown in Fig 6.6b. As expected for canonical double-exchange LSMO, the metal to insulator-transition shifts to higher temperature when a magnetic field (H=30 kOe) is applied.

Similar behaviour for junction resistance has already been reported for many LSMO-based MTJ [8,9,34–38], although its origin is not well understood yet. Viret et al. [36] suggest that its origin may be related to an oxygen-deficient layer at the interface between the LSMO and the insulating barrier (STO, in their case), because of its resemblance with the R(T) for underdoped manganites with reduced ordering temperatures. They speculate that this reduced layer is in the paramagnetic state above the peak temperature and induces spin flipping events which decrease the magnetoresistive effects.

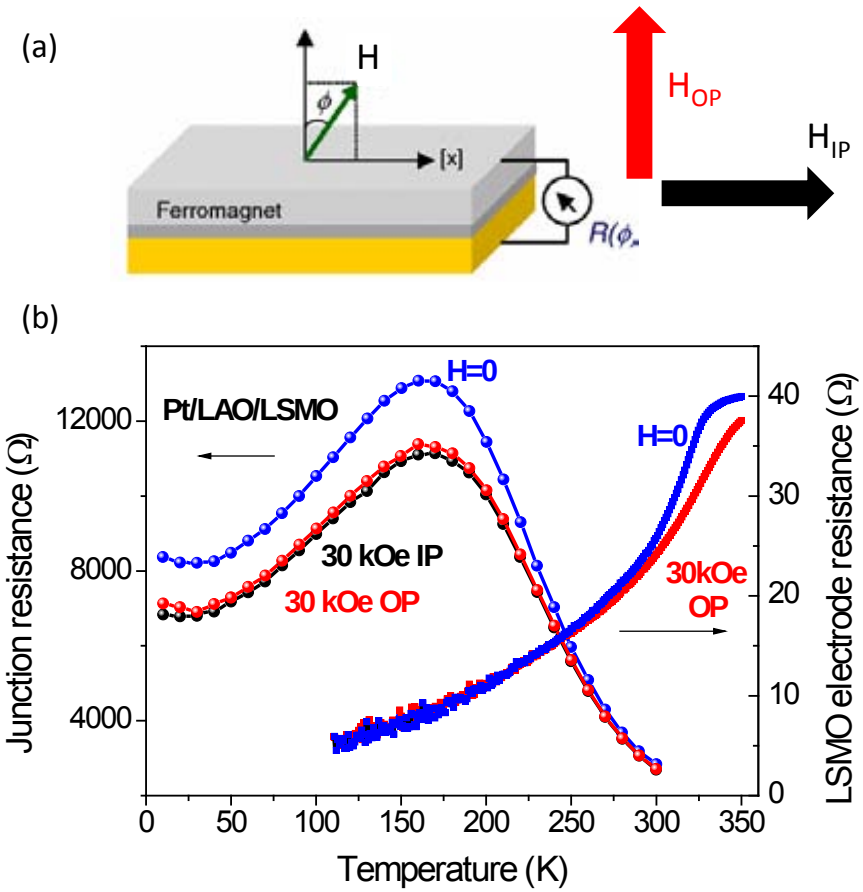

Fig 6.6. (a) Sketch of the measurement configuration for the corresponding in-plane (IP) and out-of-plane (OP) applied magnetic field, taken from [39]. (b) Dependence of the resistance on temperature; (referred to left axis) Pt/LAO/LSMO junction resistance, measured in 3-terminal configuration for applied bias voltage of 100 mV and H=0 (in blue) and 30 kOe applied IP (in black) and OP (in red); (referred to right axis) LSMO bottom electrode resistance, measured in a 4-terminal configuration at H=0 (in blue) and 30 kOe OP (in red). Note the different scale of resistance for left and right axes.

For our system, the application of a magnetic field results in an important reduction of the junction's resistance, as shown in Fig 6.6b. Interestingly, in contrast with the typical behaviour of CMR materials, no shift in the temperature of the peak of the junction resistance is observed with the application of the magnetic field (H=30 kOe). This key observation strongly suggests that the origin of the peak at ~170 K in the R(T) is not related to an oxygen-deficient layer at the LSMO/LAO interface. Another mechanism, such as the variation of the density of states by the interface and the possible contribution of alternative conduction channels other than direct tunnelling may play a role. However, more information is needed to draw further conclusions about the origin of such peak in the R(T).

6.3.2 HIGH-FIELD MR AND TAMR

It has recently been shown that magnetoresistance in magnetic tunnelling junctions may depend on the orientation of the magnetization with respect to the crystallographic axes or the direction of the current flow [40], in what is called tunnelling anisotropic magnetoresistance. To analyse this effect in our Pt/LAO/LSMO junctions, in which the current flows normal to the sample surface and the magnetization lies in the plane in the absence of magnetic field, we consider the application of H normal to the sample surface: for H=0, the magnetization and current directions are perpendicular (ϕ=90º from the setup configuration sketched in Fig 6.6a), whilst increasing H gradually orients the magnetization out-of-plane, as can be seen from the out-of-plane M(H) in Fig 6.7b. When the magnetization saturates, at ~ 10 kOe, the magnetization is parallel to the current direction (ϕ=0). Thus, the difference in resistance when H=0 and H≠0 (out-of-plane) should be a measure of the TAMR.

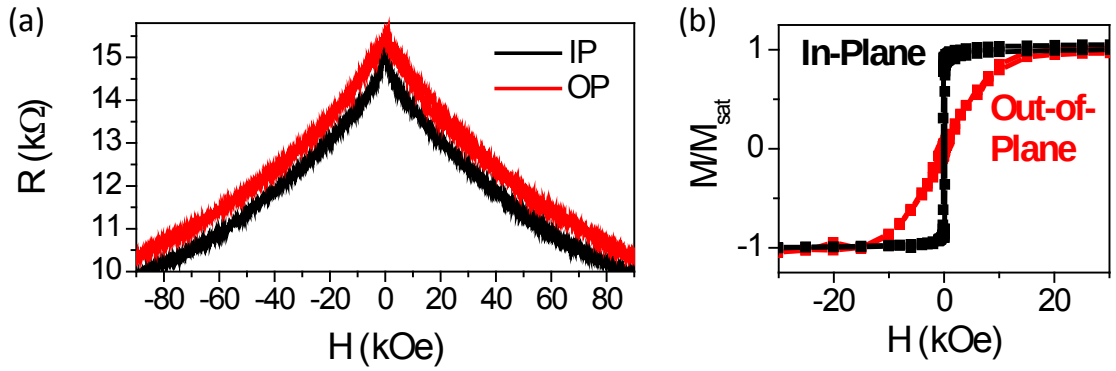

Fig 6.7. (a) Resistance *vs.* magnetic field measurements at 10 K, 10 mV and applying H in-plane (IP) and out-of-plane (OP) for a Pt/LAO/LSMO junction; (b) Corresponding magnetic hysteresis loops for the bilayer measured for both orientations, confirming its in-plane anisotropy.

It is worth noting, however, that the resistance should not vary as a function of H once the magnetization has reached saturation, contrary to what has been observed in our system (see Fig 6.7a). As a consequence, it is important to distinguish between two different contributions to the observed MR: (i) contribution due to the presence of a

magnetic field (the magnetic field changes from 0 to 30 kOe), which in this section we call "high-field MR", and (ii) contribution due to the change of the orientation of the magnetization with respect to the current flow direction (magnetization is initially in-plane but for perpendicular fields higher than 10 kOe it is saturated in the direction of the applied field, i.e. perpendicular to the film plane). This latter angular-dependent contribution, corresponding to the TAMR, is a spin-orbit coupling effect since it is the only mechanism which couples orbital and electronic spin degrees of freedom. The origins of TAMR could be diverse [41], including: (a) spin-orbit induced changes of the density of states of the ferromagnetic electrode, (b) the interference between Bychkov-Rashba and Dresselhaus spin-orbit couplings at junctions interfaces and in the tunnelling region, (c) resonant states whose coupling to the scattering channels depends on magnetization direction.

Measurements of the R(T) performed at 30 kOe for H applied in-plane and out-of-plane are depicted in Fig 6.6 (black and red dots, respectively). It is our aim to distinguish both magnetoresistive contributions (the high-field MR from the TAMR). The high-field MR contribution, which we assume to be fairly constant independently of the direction of the magnetic applied field, is therefore calculated from the difference in resistance when H=0 and H≠0 (in-plane). Depicted in Fig 6.8 (green dots), its value is of the order of 18 % at lower temperatures and decreases monotonously with temperature, although it remains constant at 15 % throughout the 50-180 K range. This high-field MR contribution could be due to a change in density of states resulting from the application of a magnetic field, even though we cannot discard magnetic disorder at the interface, which would give MR similar to granular LSMO systems. The fact that this high-field MR is larger at low temperatures (10 K) than at the peak temperature (~170 K) or the LSMO transition temperature (>300 K) suggests that this MR contribution cannot be ascribed to CMR.

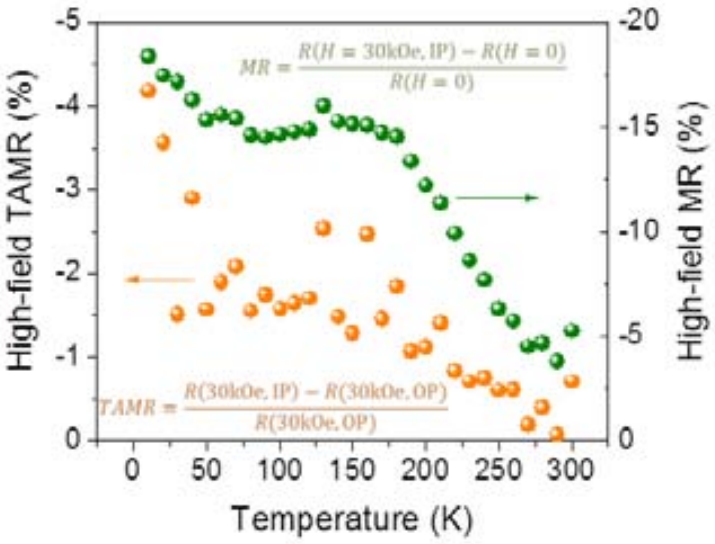

Fig 6.8. Temperature dependence of the different high-field magnetoresistive contributions for a Pt/LAO/LSMO stack measured at 100 mV. Green dots, referred to the right axis, depict the difference between the resistance at H=0 and 30 kOe applied in-plane (IP). Red dots, referred to the left axis, represent the difference in resistance for a fixed magnetic field of 30 kOe applied in-plane (IP) and out-of-plane (OP).

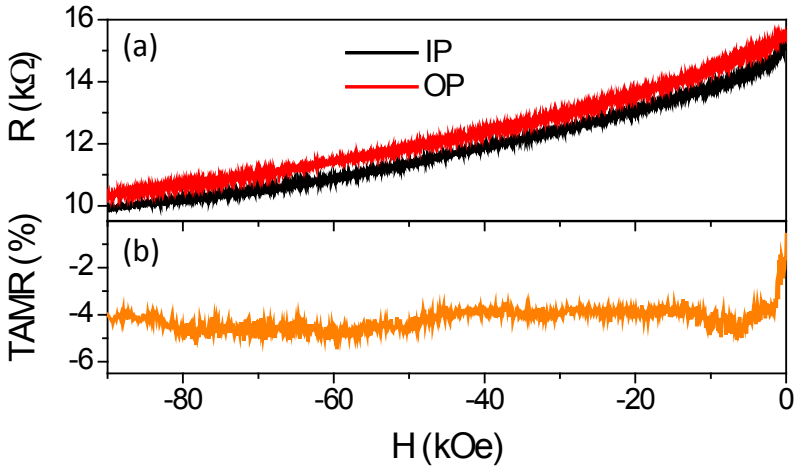

Fig 6.9. (a) Resistance *vs.* magnetic field of the Pt/LAO/LSMO junction resistance on large magnetic fields (up to 90 kOe) for the in-plane (IP) and out-of-plane (OP) configurations, measured at 10 K and 10 mV; (b) Its corresponding TAMR as a function of the magnetic field.

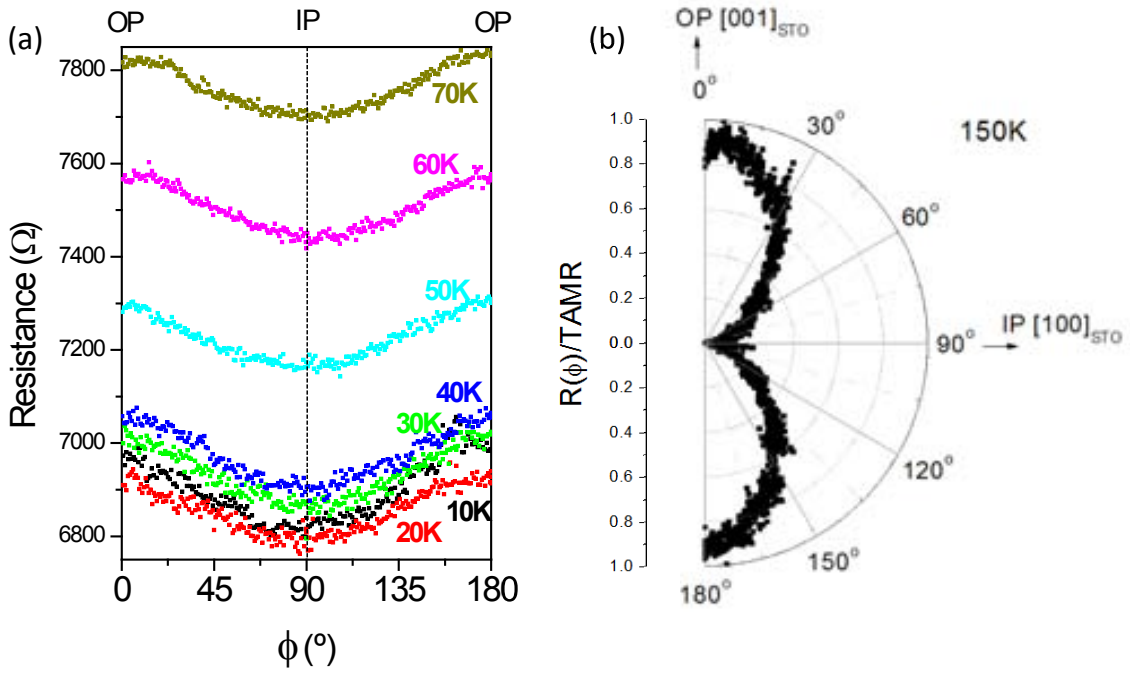

Fig 6.10. TAMR at high magnetic fields for Pt/LAO/LSMO junctions. (a) Resistance as a function of the angle between the current (normal to the sample surface) and the applied magnetic field, ϕ, for different temperatures. Different colours represent measurements taken at different temperatures, from 10 to 70 K; (b) Polar plot of the normalized R(ϕ)/TAMR at 150 K. IP and OP correspond to the configurations where magnetization is aligned in-plane and out-of-plane, respectively.

The difference between the resistance measured for the same magnetic field applied in-plane and out-of-plane, depicted in Fig 6.8 (orange dots), is associated to TAMR, reflecting a variation of the resistance of the order of 4 % at 10 K. As temperature is increased, TAMR slowly decreases and vanishes close to room temperature. The modest value of TAMR contrasts with the large value of MR (from the difference between H=0 and H=30 kOe), of the order of 15 %, as mentioned before. Its variation as a function of the magnetic field is shown in Fig 6.9: above 5 kOe and up to 90 kOe, its value remains constant. The dependence of the resistance on the orientation of H, from ϕ=0 to ϕ=180º, is depicted in Fig 6.10 for various temperatures, and its shape reflects uniaxial anisotropy up until 200 K.

6.3.3 Low-field TAMR

As for the low-field range of TAMR, we perform R(H) measurements in both magnetic field orientations (in-plane and out-of-plane). The results, shown in Fig 6.11, indicate switching between distinct resistance states, in a spin-valve-like fashion. As no TMR effect is expected due to the fact that only one of the electrodes is magnetic (LSMO), TAMR must be at the origin of such behaviour, probably through a magnetization reversal which takes place in a multi-step process [42,43], so that the jumps in resistance correspond to the rotation of different magnetic domains. In our sample, we observe that the effect is stronger for smaller bias voltages and lower temperatures, as

can be seen from comparison between the results at 10 and 100 mV. In Fig 6.11a, taken for 10 mV and 10 K, the effect is very large (the fact that data for the in-plane configuration presents an irreversibility is just a problem with the measurement). As visible in Fig 6.11d, TAMR is hardly distinguishable from the noise for the measurement taken at 150 K and 100 mV. This could be attributed to the fact that providing more energy to the system (via thermal energy or via electric field) leads to a faster magnetization reversal, with no intermediate magnetization steps.

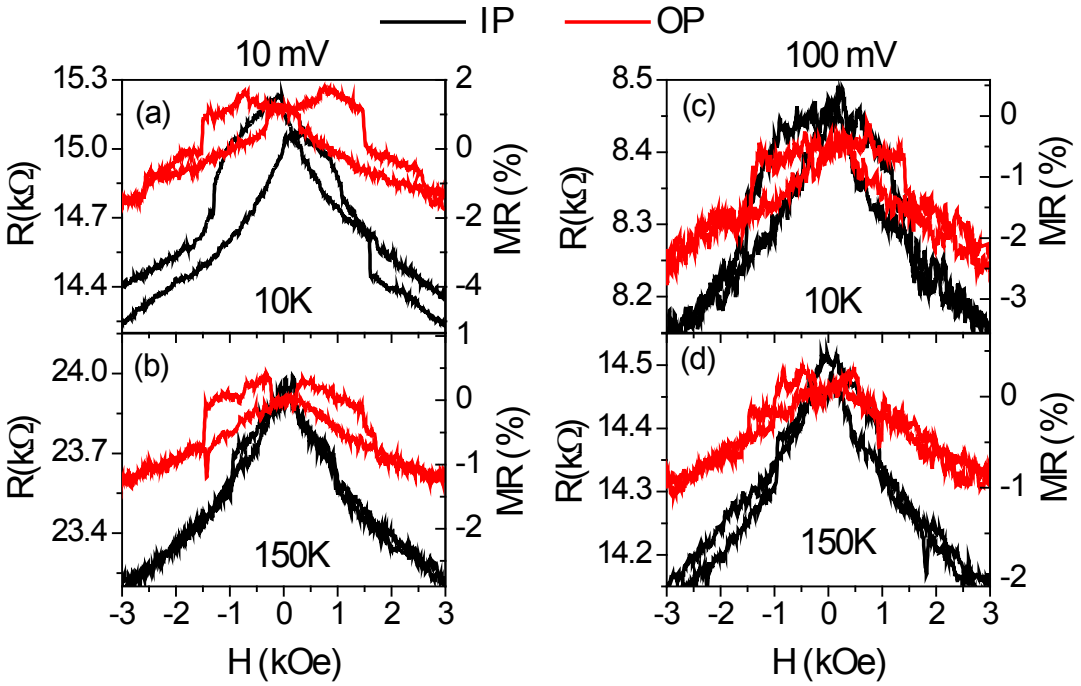

Fig 6.11. TAMR at low fields: R (H) curves taken for the in-plane (IP) and out-of-plane (OP) configuration, at 10 mV and 100 mV, for T=10 and 150 K.

The order of magnitude of the TAMR low-field switching, however, is small (<2 %) even for 10 K and 10 mV.

6.4 SUMMARY

In this chapter we have studied the properties of LAO/LSMO interface properties relevant for spintronic applications. The magnetotransport properties of LSMO/LAO/Pt tunnelling junctions have been analysed as a function of temperature and magnetic field, demonstrating that LAO barriers maintain their insulating properties down to 1-2 nm, i.e. 4 to 5 unit cells, thus being an appropriate material as a tunnel barrier and for efficient spin injection. The used configuration takes advantage of the resist from the patterning process, which acts as insulating material on top of which the electrodes are deposited. Samples with PMMA have been seen to result in poor contacts for temperatures lower than 120 K, thus hindering lower temperature measurements. We have circumvented this problem by using positive photoresist: this has enabled us to probe lower temperatures at the expense of larger-sized junctions.

LAO/LSMO interface has been studied through its tunnelling conduction properties across a 0.8 μm^2-sized junction. The temperature dependence of the junction resistance, R(T), down to about 200 K evidences that direct tunnelling transport is the dominant conduction channel. In turn, this would indicate that insulating LAO barriers are of excellent microstructural quality with no pinholes or other microstructural defects, in contrast with other results previously reported. In the low temperature regime ($T \leq 190$ K) R(T) develops a peak, as in the case of other tunnelling junctions with manganite electrodes, whose origin is not well understood yet. Our results strongly suggest that the previously reported scenario of an interfacial layer of under-doped manganite with reduced ordering temperature is very unlikely. On the other hand, the parameters of the LAO barrier, φ_0 and s, have been estimated from I-V curves by using the Simmons model in the intermediate voltage regime. Values of φ_0 (≈0.4 eV at room temperature) are in good agreement with previous theoretical and experimental estimations. A dependence of the parameters with temperature is found: we discuss that the T^2 dependence of barrier energy is only the intrinsic contribution from thermal broadening of the Fermi-Dirac statistics, whilst the barrier thickness variation could be related to thermal-induced disorder at the interface between LAO and LSMO.

The change in resistance due to the application of a magnetic field suggests the existence of tunnelling anisotropic magnetoresistance, so a careful study has been done of the magnetotransport properties of a 16 μm^2 Pt/LAO/LSMO junction. In this junction, the TAMR measured for H=30 kOe in two different perpendicular orientations (H applied in-plane and out-of-plane) is of the order of 4% at 10 K, and reflects uniaxial anisotropy. This is in striking contrast with the 15% of large-field MR coming from the difference in resistance between H=0 and H=30 kOe (in-plane). The fact that in both latter cases the magnetization and the current present a misalignment of 90º suggests that the origin of the high-field MR –constant for all fields up to 90 kOe- is not just the spin-orbit coupling, but may be related to a change in the density of states of the electrode upon the application of H, although magnetic disorder at the interface is not ruled out. However, as temperature is increased, both magnetoresistive effects decrease and become vanishingly small at room temperature, thus severely restricting potential technological applications.

6.5 REFERENCES

[1] Cowburn R.P.; "The future of universal memory". *Mater. Today* 6; **2003**: 32–8. doi:http://dx.doi.org/10.1016/S1369-7021(03)00730-2.

[2] Tsymbal E.Y., Mryasov O.N., LeClair P.R.; "Spin-dependent tunnelling in magnetic tunnel junctions". *J. Phys. Condens. Matter* 15; **2003**: R109–42. doi:10.1088/0953-8984/15/4/201.

[3] Gupta A., Li X.W., Xiao G.; "Inverse magnetoresistance in chromium-dioxide-based magnetic tunnel junctions". *Appl. Phys. Lett.* 78; **2001**: 1894. doi:10.1063/1.1356726.

[4] Leo T., Kaiser C., Yang H., Parkin S.S.P., Sperlich M., Güntherodt G., et al.; "Sign of tunneling magnetoresistance in CrO[sub 2]-based magnetic tunnel junctions". *Appl. Phys. Lett.* 91; **2007**: 252506. doi:10.1063/1.2825475.

[5] Seneor P., Fert A., Maurice J.-L., Montaigne F., Petroff F., Vaurès A.; "Large magnetoresistance in tunnel junctions with an iron oxide electrode". *Appl. Phys. Lett.* 74; **1999**: 4017. doi:10.1063/1.123246.

[6] Hu G., Suzuki Y.; "Negative spin polarization of Fe3O4 in magnetite/manganite-based junctions". *Phys. Rev. Lett.* 89; **2002**. doi:10.1103/PhysRevLett.89.276601.

[7] O'Donnell J., Andrus A.E., Oh S., Colla E. V., Eckstein J.N.; "Colossal magnetoresistance magnetic tunnel junctions grown by molecular-beam epitaxy". *Appl. Phys. Lett.* 76; **2000**: 1914. doi:10.1063/1.126210.

[8] Noh J.S., Nath T.K., Eom C.B., Sun J.Z., Tian W., Pan X.Q.; "Magnetotransport in manganite trilayer junctions grown by 90° off-axis sputtering". *Appl. Phys. Lett.* 79; **2001**: 233. doi:10.1063/1.1383276.

[9] Wertz E.T., Li Q.; "Magnetoresistance after initial demagnetization in La[sub 0.67]Sr[sub 0.33]MnO[sub 3]/SrTiO[sub 3]/La[sub 0.67]Sr[sub 0.33]MnO[sub 3] magnetic tunnel junctions". *Appl. Phys. Lett.* 90; **2007**: 142506. doi:10.1063/1.2718481.

[10] Bowen M., Bibes M., Barthélémy A., Contour J.-P., Anane A., Lemaître Y., et al.; "Nearly total spin polarization in La2/3Sr1/3MnO3 from tunneling experiments". *Appl. Phys. Lett.* 82; **2003**: 233–5. doi:doi:http://dx.doi.org/10.1063/1.1534619.

[11] Yamada H., Ogawa Y., Ishii Y., Sato H., Kawasaki M., Akoh H., et al.; "Engineered interface of magnetic oxides". *Science (80-.).* 305; **2004**: 646–8. doi:10.1126/science.1098867.

[12] Garcia V., Bibes M., Barthelemy A., Bowen M., Jacquet E., Contour J.P., et al.; "Temperature dependence of the interfacial spin polarization of La2/3Sr1/3MnO3". *Phys. Rev. B* 69; **2004**. doi:10.1103/PhysRevB.69.052403.

[13] Parkin S.S.P., Kaiser C., Panchula A., Rice P.M., Hughes B., Samant M., et al.; "Giant tunnelling magnetoresistance at room temperature with MgO (100) tunnel barriers". *Nat. Mater.* 3; **2004**: 862–7. doi:10.1038/nmat1256.

[14] Garcia V., Bibes M., Maurice J.-L., Jacquet E., Bouzehouane K., Contour J.-P., et al.; "Spin-dependent tunneling through high-k LaAlO[sub 3]". *Appl. Phys. Lett.* 87; **2005**: 212501. doi:10.1063/1.2132526.

[15] Valencia S., Konstantinovic Z., Schmitz D., Gaupp A., Balcells L., Martinez B.; "Interfacial effects in manganite thin films with different capping layers of interest for spintronic applications". *Phys. Rev. B* 84; **2011**: 024413. doi:024413 10.1103/PhysRevB.84.024413.

[16] Valencia S., Peña L., Konstantinovic Z., Balcells L., Galceran R., Schmitz D., et al.; "Intrinsic antiferromagnetic/insulating phase at manganite surfaces and interfaces.". *J. Phys. Condens. Matter* 26; **2014**: 166001. doi:10.1088/0953-8984/26/16/166001.

[17] Martinez-Boubeta C., Konstantinovic Z., Balcells L., Estrade S., Arbiol J., Cebollada A., et al.; "Epitaxial Integration of La2/3Sr1/3MnO3 and Fe Films by the Use of a MgO Spacer". *Cryst. Growth Des.* 10; **2010**: 1017–20. doi:10.1021/cg900866g.

[18] Balcells L., Abad L., Rojas H., Perez del Pino A., Estrade S., Arbiol J., et al.; "Electronic effects in manganite/insulator interfaces: interfacial enhancement of the insulating tunneling barriers.". *Small* 4; **2008**: 365–71. doi:10.1002/smll.200700537.

[19] Maurice J.-L., Imhoff D., Contour J.-P., Colliex C.; "Interfaces in {100} epitaxial heterostructures of perovskite oxides". *Philos. Mag.* 86; **2006**: 2127–46. doi:10.1080/14786430600640460.

[20] Riedl T., Gemming T., Dörr K., Luysberg M., Wetzig K.; "Mn valency at La 0.7 Sr 0.3 MnO 3/SrTiO 3 (0 0 1) thin film interfaces.". *Microsc. Microanal.* 15; **2009**: 213–21. doi:10.1017/S1431927609090229.

[21] Samet L., Imhoff D., Maurice J.-L., Contour J.-P., Gloter A., Manoubi T., et al.; "EELS study of interfaces in magnetoresistive LSMO/STO/LSMO tunnel junctions". *Eur. Phys. J. B - Condens. Matter* 34; **2003**: 179–92. doi:10.1140/epjb/e2003-00210-8.

[22] LeClair P., Swagten H., Kohlhepp J., van de Veerdonk R., de Jonge W.; "Apparent Spin Polarization Decay in Cu-Dusted Co/Al2O3/Co Tunnel Junctions". *Phys. Rev. Lett.* 84; **2000**: 2933–6. doi:10.1103/PhysRevLett.84.2933.

[23] Balcells L., Abad L., Rojas H., Perez del Pino A., Estrade S., Arbiol J., et al.; "Transport properties across the La2/3Ca1/3MnO3/SrTiO3 heterointerface". *J. Appl. Phys.* 103; **2008**: 07E303. doi:10.1063/1.2833760.

[24] Giddings A., Khalid M., Jungwirth T., Wunderlich J., Yasin S., Campion R., et al.; "Large Tunneling Anisotropic Magnetoresistance in (Ga,Mn)As Nanoconstrictions". *Phys. Rev. Lett.* 94; **2005**: 127202. doi:10.1103/PhysRevLett.94.127202.

[25] Simmons J.G.; "Generalized formula for electric tunnel effect between similar electrodes separated by a thin insulating film". *J. Appl. Phys.* 34; **1963**: 1793 – &. doi:10.1063/1.1702682.

[26] Brinkman W.F.; "Tunneling Conductance of Asymmetrical Barriers". *J. Appl. Phys.* 41; **1970**: 1915. doi:10.1063/1.1659141.

[27] Gloos K., Poikolainen R.S., Pekola J.P.; "Wide-range thermometer based on the temperature-dependent conductance of planar tunnel junctions". *Appl. Phys. Lett.* 77; **2000**: 2915. doi:10.1063/1.1320861.

[28] Reagor D.W.; "Work function of the mixed-valent manganese perovskites". *J. Appl. Phys.* 95; **2004**: 7971. doi:10.1063/1.1737802.

[29] Peacock P.W., Robertson J.; "Band offsets and Schottky barrier heights of high dielectric constant oxides". *J. Appl. Phys.* 92; **2002**: 4712. doi:10.1063/1.1506388.

[30] Cazorla C., Stengel M.; "First-principles modeling of Pt/LaAlO3/SrTiO3 capacitors under an external bias potential". *Phys. Rev. B* 85; **2012**: 075426. doi:10.1103/PhysRevB.85.075426.

[31] Wu S., Luo X., Turner S., Peng H., Lin W., Ding J., et al.; "Nonvolatile Resistive Switching in Pt/LaAlO3/SrTiO3 Heterostructures". *Phys. Rev. X* 3; **2013**: 041027. doi:10.1103/PhysRevX.3.041027.

[32] Jönsson-Åkerman B.J., Escudero R., Leighton C., Kim S., Schuller I.K., Rabson D.A.; "Reliability of normal-state current–voltage characteristics as an indicator of tunnel-junction barrier quality". *Appl. Phys. Lett.* 77; **2000**: 1870. doi:10.1063/1.1310633.

[33] Simmons J.G.; "Generalized Thermal J-V Characteristic for the Electric Tunnel Effect". *J. Appl. Phys.* 35; **1964**: 2655. doi:10.1063/1.1713820.

[34] Sun J.Z., Abraham D.W., Roche K., Parkin S.S.P.; "Temperature and bias dependence of magnetoresistance in doped manganite thin film trilayer junctions". *Appl. Phys. Lett.* 73; **1998**: 1008. doi:10.1063/1.122068.

[35] Sun J., Roche K., Parkin S.; "Interface stability in hybrid metal-oxide magnetic trilayer junctions". *Phys. Rev. B* 61; **2000**: 11244–7. doi:10.1103/PhysRevB.61.11244.

[36] Viret M., Drouet M., Nassar J., Contour J.P., Fermon C., Fert A.; "Low-field colossal magnetoresistance in manganite tunnel spin valves". *Europhys. Lett.* 39; **1997**: 545–50. doi:10.1209/epl/i1997-00391-2.

[37] Ishii Y., Yamada H., Sato H., Akoh H., Ogawa Y., Kawasaki M., et al.; "Improved tunneling magnetoresistance in interface engineered (La,Sr)MnO3 junctions". *Appl. Phys. Lett.* 89; **2006**: 042509. doi:10.1063/1.2245442.

[38] Jo M.-H., Mathur N., Todd N., Blamire M.; "Very large magnetoresistance and coherent switching in half-metallic manganite tunnel junctions". *Phys. Rev. B* 61; **2000**: R14905–8. doi:10.1103/PhysRevB.61.R14905.

[39] Matos-Abiague A., Fabian J.; "Anisotropic tunneling magnetoresistance and tunneling anisotropic magnetoresistance: Spin-orbit coupling in magnetic tunnel junctions". *Phys. Rev. B* 79; **2009**: 155303. doi:10.1103/PhysRevB.79.155303.

[40] Brey L., Tejedor C., Fernández-Rossier J.; "Tunnel magnetoresistance in GaMnAs: Going beyond Jullière formula". *Appl. Phys. Lett.* 85; **2004**: 1996. doi:10.1063/1.1789241.

[41] Khan M.N., Henk J., Bruno P.; "Anisotropic magnetoresistance in Fe/MgO/Fe tunnel junctions". *J. Phys. Condens. Matter* 20; **2008**: 155208. doi:10.1088/0953-8984/20/15/155208.

[42] Moser J., Matos-Abiague A., Schuh D., Wegscheider W., Fabian J., Weiss D.; "Tunneling Anisotropic Magnetoresistance and Spin-Orbit Coupling in Fe/GaAs/Au Tunnel Junctions". *Phys. Rev. Lett.* 99; **2007**: 056601. doi:10.1103/PhysRevLett.99.056601.

[43] Ciorga M., Schlapps M., Einwanger A., Geißler S., Sadowski J., Wegscheider W., et al.; "TAMR effect in (Ga,Mn)As-based tunnel structures". *New J. Phys.* 9; **2007**: 351–351. doi:10.1088/1367-2630/9/9/351.

CHAPTER 7. FE/MGO/LSMO MAGNETIC TUNNEL JUNCTIONS

As explained in Chapter 2, the combination of symmetry filtering from MgO barriers –which selects Δ_1 states preferentially- and Fe electrodes –which possess only one spin orientation for the Δ_1 state- results in spin filtering. The large TMR resulting from such combination has already been confirmed for Fe/MgO/Fe magnetic tunnel junctions [1].

On the other hand and also mentioned before, half-metallic materials are interesting candidates for tunnel junctions due to their potential as spin injectors. Large TMR results obtained in magnetic tunnel junctions based on LSMO at low temperature are consistent with half-metallicity, although the effect decreases notably with temperature. This is ascribed to a stronger temperature dependence of the spin polarization at interface than in bulk. In fact, interfaces are crucial towards the final performance of tunnel junctions, to the point that a single monolayer at the interface may completely determine the sign of the magnetoresistance and the magnitude of the effect [2].

In this chapter we study the magnetoresistive phenomena of an Fe/MgO/LSMO//STO(100) magnetic tunnel junction. As LSMO is a half-metal, only one spin orientation is expected to contribute to the conduction. To determine the symmetry of the electrons at the Fermi level at the surface of an LSMO film, both epitaxial strain and symmetry breaking effects at the surface or interface must be considered. Tensile (compressive) strain favours x^2-y^2 ($3z^2$-r^2) occupancy [3], surface orbital reconstruction stabilizes the d $3z^2$-r^2 orbitals –independently of dipolar fields, the chemical nature of the substrate or the presence of capping layers [4] - but whenever no orbital reconstruction is present, x^2-y^2 orbitals are favoured [5]. In particular, for films of LSMO with MgO capping layers grown in our laboratory, the $3z^2$-r^2 orbitals are stabilized at the surface [6]. These orbitals possess Δ_1 symmetry, so they may couple to the Δ_1 orbitals of the crystalline MgO. Thus, it would be expected that the combination of both the half-metallicity of LSMO and the spin-filtering system Fe/MgO would yield, in optimal conditions, very high TMR response. However, as we have seen in Chapter 3, the growth of such a heterostructure (both *in-situ* and *ex-situ*) is inevitably associated with the formation of an FeO_x at the Fe/MgO interface. Therefore, the magnetotransport measurements will be highly affected by the FeO_x layer.

Measurements of an Fe/MgO/LSMO system have already been reported by Wu *et al.* [7] to produce a giant out-of-plane negative MR ratio of 540 % at 190 K. However, this MR takes place at very high magnetic fields (>5 kOe), which suggests that it does not correspond to the rotation of the magnetization of the electrodes. In their study, they do not analyse the oxidation at the Fe/MgO interface, but focus on the breakdown of the junction (occurring for H~7-8 kOe).

The present chapter addresses the magnetoresistive behaviour of Fe/MgO/LSMO junctions (of sizes below 200 μm^2) when applying the magnetic field in-plane and out-

of-plane. For real applications, two main characteristics are sought: (i) high TMR and (ii) the device must be able to function at the higher possible temperature (in any case, above room temperature). In view of the dramatic reduction of the T_C of LSMO in such heterostructures (seen from Chapter 3) and the modest TMR obtained in magnetic tunnel junctions fabricated from them (as will be explained in this chapter), our main objective has been to understand the possible effects which occur at the interfaces which may explain why the TMR is not as large as expected and account for the unexpected temperature and magnetic field dependence of the TMR.

7.1 SAMPLES AND PHENOMENOLOGY

The Au/Ti/Fe/MgO/LSMO//STO samples measured in this chapter have been grown as indicated and characterized in section 3.8. As mentioned, three different MgO thicknesses have been probed (t=0.8, 1.2 and 2.4 nm). The patterning process has been performed as indicated in section 5.3, with junction areas ranging from 8 to 162 μm^2.

The I-V curves and temperature dependence of the resistance, whose tendency mostly coincides for all measured junctions, is discussed in section 7.3. Magnetoresistive measurements, however, present two different phenomenologies, depending on the junction: some junctions presented negative TMR throughout all the measured temperature range (junctions Neg), whilst a few others presented positive TMR at low temperatures (junctions Pos). Surprisingly, both junctions Neg and Pos were found indistinctly in the same samples, so we ascribe this discrepancy to differences in the interfacial oxidation of the Fe (we recall that the growth of Fe was done *ex-situ* after an annealing of the MgO surface). In the following of the chapter we explain the different observed magnetoresistive behaviours, which highlights the importance of interfacial effects in the final performance of the device, and the possibility of tuning the TMR response.

7.2 MEASUREMENT CONFIGURATION AND SPECIFICATIONS

Transport measurements were done using a Keithley source in the dc 2-probe configuration, with positive bias corresponding to the electrons tunnelling from the top Fe electrode to the bottom LSMO electrode, as sketched in Fig 7.1.

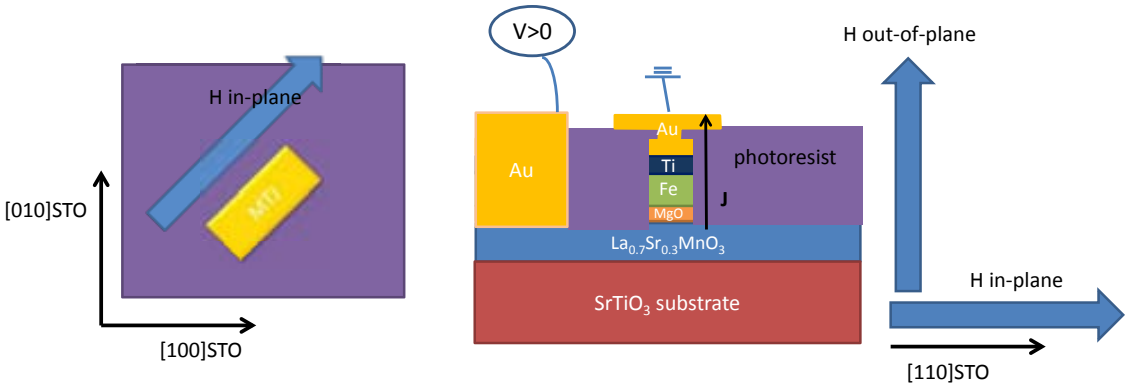

Fig 7.1 Measurement configuration for magnetic tunnel junctions.

Magnetoresistance measurements have been carried out by applying a fixed bias voltage and measuring the current through the device. The in-plane measurements have been performed with the magnetic field (H) applied parallel to the surface, along the [100] Fe easy axis, which coincides with the [110] axis of MgO and LSMO, also the long side of the patterned rectangles. The out-of-plane measurements were done with the magnetic field applied parallel to the [001] Fe, MgO and LSMO axis.

Part of the measurements were performed at the Universidad Complutense de Madrid with the existing setup (which includes an electromagnet). Another measurement setup was developed during the thesis at the ICMAB laboratory, in which both field and temperature were carefully controlled in the PPMS, and the transport properties are measured using a Keithley source. The limitations for the latter setup are discussed in Appendix A.6.2.1.

7.2.1 Magnetoresistance of the bottom LSMO electrode

In this work, most tunnelling magnetoresistance measurements have been performed in a 2-terminal configuration, as represented in Fig 7.1, which entails that measurements include the contributions of the bottom electrode, a macrocontact and the junction. In this section, we analyse the importance of such contributions compared to the junction resistance.

The resistance of the bottom LSMO electrode has been measured in a 4-terminal configuration (see Fig 7.2a, black curve). The LSMO probed in a 3-terminal configuration (depicted in Fig 7.2a, red curve) contains the contribution of a macrocontact, which adds up to the resistance from the LSMO electrode. The expected increase of resistance for the 3-contact configuration with respect to the 4-contact one, however, does not yield resistances above 1 kΩ below 300 K.

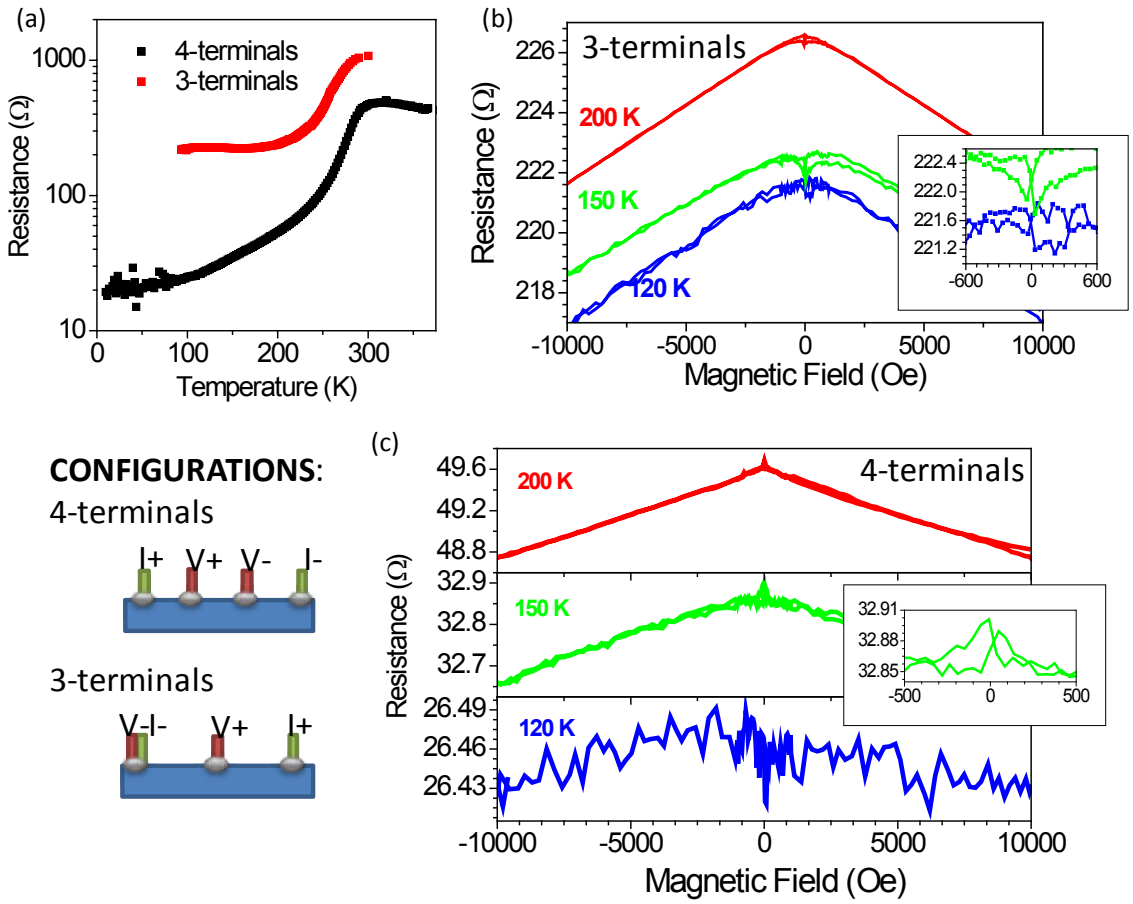

Fig 7.2. Transport and magnetoresistance in the bottom LSMO electrode using the 3- and 4-terminal configurations shown in the sketch. (a) R(T) for both configurations; R(H) at 120, 150 and 200 K for measured using (b) 3-terminal configuration and (c) 4-terminal configuration.

The magnetoresistance for 3-terminals and 4-terminals configurations are depicted in Fig 7.2b and c. The R(H) measurements of the LSMO bottom electrode, probed in the 4-contact configuration (Fig 7.2c), shows the CMR effect of LSMO, increasing with temperature –as T_C is approached. The R(H) probed in the 3-contact configuration includes the CMR from the bottom electrode and the effect of one contact. Therefore, the effect of a single contact is visible from the difference between the 3- and 4-contacts configurations. At 120 K, for example, this single contact contributes adding an extra MR of 2% at 1 T, similar to the MR observed in granular LSMO systems [8]. The small low-field MR for T~120-150 K represents a variation of resistance of the order of 1 Ω while the total resistance is around 220 Ω, so the effect is of $\Delta R3\text{-}T / R3\text{-}T = 0.45\%$.

To confirm that the measurement configuration has negligible effect on the obtained data, we point out that the R of the tunnel junction is much larger than the R arising from the electrode and contacts, so that it is safe to neglect such contributions, especially below 200 K.

7.3 I-V CURVES AND TEMPERATURE DEPENDENCE OF THE RESISTANCE

I-V curves measured by sweeping voltage are non-linear and the conductance of the junctions as a function of bias voltage is slightly asymmetric and parabolic at low bias from 10 K up to at least 220 K (Fig 7.3a), as expected because of the asymmetric FM-barrier interfaces. According to the results reported in reference [9], the junction's zero-bias resistance variations as a function of temperature provides information of barrier quality. Fig 7.3b depicts the temperature dependence of the resistance at zero field for a 18×9 μm^2 LSMO/MgO(2.4 nm)/Fe typical junction for several positive bias values, which shows an exponential increase of the resistance when temperature is lowered, contrary to the weak insulating behaviour characteristic of direct tunnelling in magnetic tunnel junctions [9,10]. This observed unexpected dependence suggests the existence of impurity assisted conduction channels through the barrier [11]. Defects levels in the bandgap of MgO due to intrinsic microstructural defects (vacancies, interstitial and interfacial states), which can provide conducting channels in the MgO layer leading to the degradation of the barrier performances, have been clearly stated previously [7]. In fact, oxygen vacancies are present even for high-TMR junctions [1], yielding a barrier height around 1.2 eV, in contrast with the 3.7 eV expected for an ideal MgO layer, which –on the other hand- would be too high for device applications.

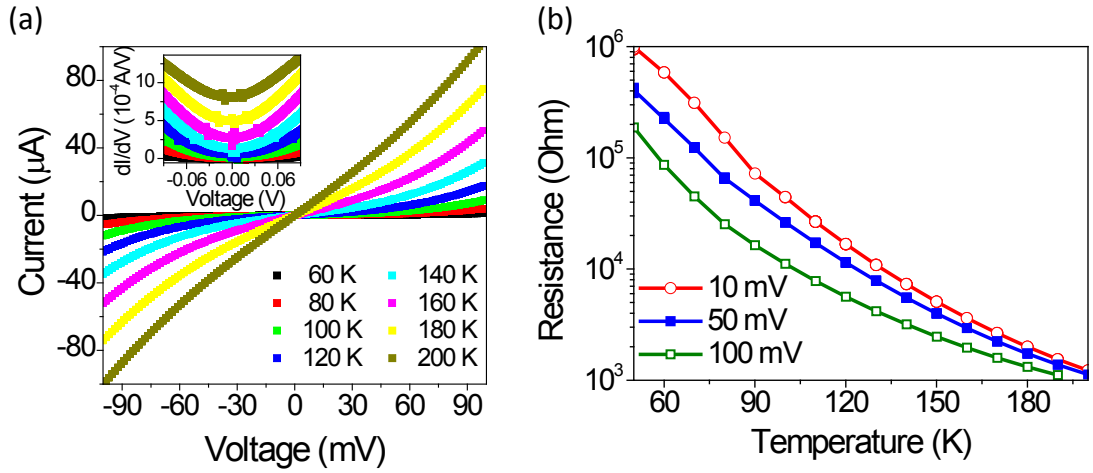

Fig 7.3 (a) Current *vs.* voltage curves taken at different temperatures for a 5×10μm^2-sized Fe/MgO(t=2.4 nm)/LSMO MTJ. Inset is the derivative of the curves, i.e. the conductance; (b) Temperature dependence of the resistance of the LSMO/MgO/Fe junctions in the low T regime for different positive bias values.

Both Simmons' [12] and Brinkman's [13] fits yield increasing barrier thickness as temperature is lowered from 200 to 50 K (a variation of ~1 nm), and decreasing barrier energy. This unexpected variation (note that, as in the case of LAO/LSMO tunnelling from chapter 5, barrier energy should increase as T^2 [14]) is a further indication that conduction in our system is not solely governed by direct tunnelling, thereby invalidating the use of such models.

7.4 MAGNETORESISTIVE MEASUREMENTS FOR JUNCTIONS NEG (NEGATIVE TMR)

We have found several junctions from different samples which display negative TMR throughout all the studied temperature range, as expected from the positive and negative spin polarization of LSMO and Fe, respectively (we call them junctions Neg). Fig 7.4 shows the TMR for a junction of area 5×10 μm^2, from a stack with MgO thickness 2.4 nm, measured at 20 K and applied bias of -600 mV: in black, the sweep from positive to negative H; in red, H was swept from negative to positive. Hereafter, we represent both sweeps in the same colour. The switch from parallel (P) configuration to antiparallel (AP) configuration – which takes place at H~50 Oe and results in a lower device resistance- is basically abrupt. However, the higher-field switch (from the lower-R antiparallel state to the high-R parallel state) is partly abrupt but seems to take place in basically two steps: a more abrupt switch at around 250-300 Oe (indicated as A) and a gradual rotation of the electrodes to gain back the parallel configuration of electrodes (indicated as B). It is also worth mentioning that the resistance at the antiparallel state is not constant, but tends to increase for higher fields, even before switch A. This could indicate that H is not exactly oriented along the easy axis of the electrodes, so that instead of viewing a single switch, a gradual rotation of the electrode's magnetization results in differences in the resistance in the AP configuration.

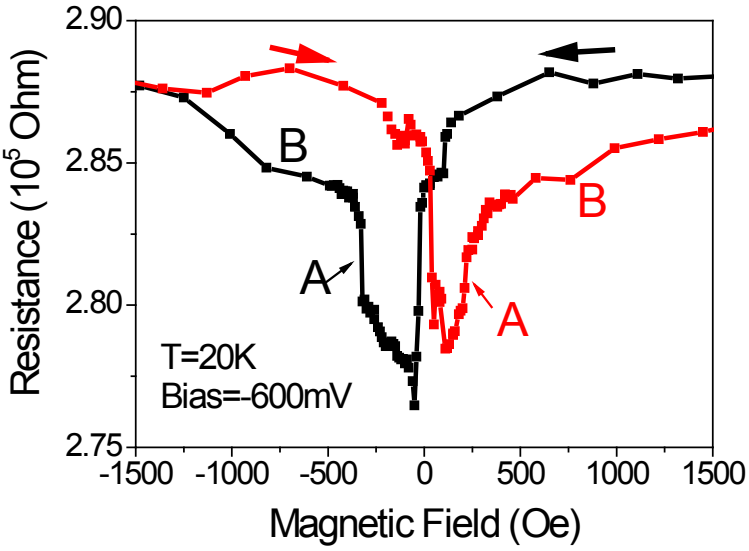

Fig 7.4 Negative TMR found for a 5×10 μm^2-sized Fe/MgO(2.4 nm)/LSMO magnetic tunnel junction.

Minor cycles are taken at 100 K for various applied biases (in Fig 7.5a we represent the results for V =-20, -200 and -400 mV). These minor loops, taken by sweeping the magnetic field from positive H to negative H and back to positive H as soon as the AP state has been reached, confirm the possibility of reversing the magnetization of only one of the ferromagnetic layers, thus confirming the phenomenon is indeed TMR –even if the values are quite low and do not exceed 4%. They also show the possibility of two

different resistance states at H=0. These states are stable, so that after switching to the AP configuration, the sweep can be stopped and the resistance remains at this value. In Fig 7.5b, the minor loop for -20 mV is plotted up to 4 kOe.

The dependence with bias of the resistances for P and AP configuration is exponential, in accordance with impurity-assisted tunnelling [11]. The dependence of TMR on voltage (represented in Fig 7.5c) is calculated in two independent ways: on one hand, from the subtraction of I-V curves taken at the parallel state (H=4 kOe) and antiparallel state (H~-300 Oe, after switching the resistance), depicted in red; on the other hand, from the subtraction of the resistances at the P and AP states (taken from the minor loops), depicted in blue dots. Although the tendency coincides for both cases, a certain overestimation of the TMR may come from the fact that the P state is taken at different H values (I-V for P state is taken at 4 kOe, whilst the resistance for P state taken from the minor cycle is measured close to H=0), so the I-V curves subtraction include the MR contribution at high magnetic fields.

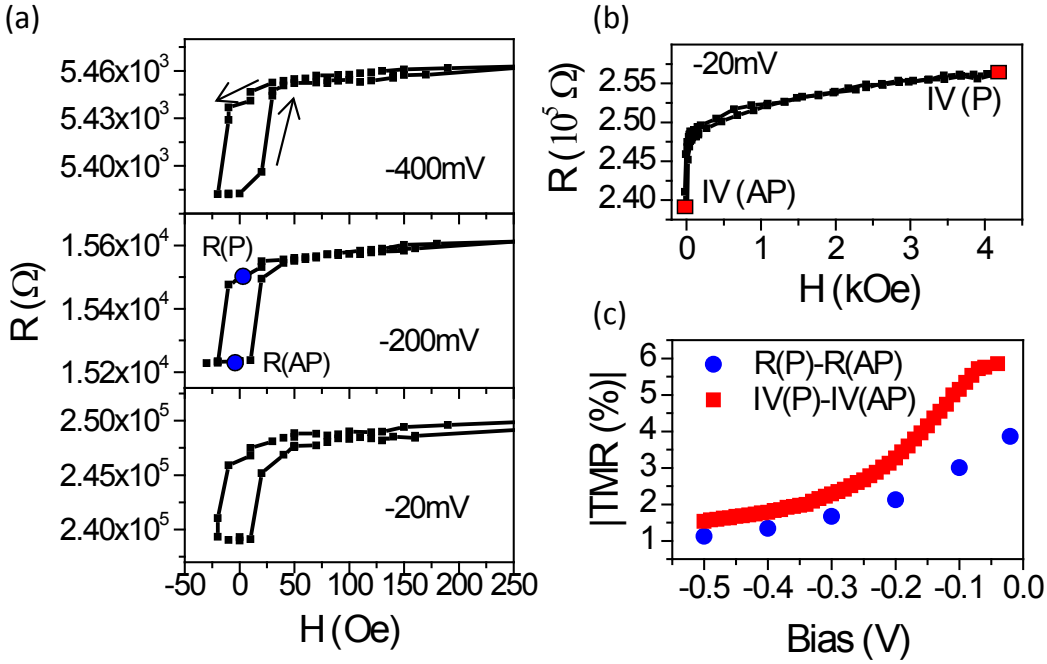

Fig 7.5 Voltage dependence of TMR for a 10×5 μm^2-junction from a stack with 2.4 nm of MgO at T=100 K. (a) Minor cycles taken at -400, -200 and -20 mV, for low fields, arrows show the direction of the sweep; (b) Minor cycle taken at -20 mV up to 4 kOe; (c) TMR(V) resulting from the subtraction between resistances at the parallel and antiparallel configuration (blue dots, also represented in the -200 mV measurement in (a)) and extracted from the subtraction of the I(V) curves in the parallel (H=4 kOe) and antiparallel configuration (red squares, also represented in (b)).

The TMR dependence on temperature is plotted in Fig 7.6. Above a certain temperature (around 100 K), TMR decreases monotonically. Around 200 K, TMR is no longer measurable (TMR~0). At low temperatures, there is no clear tendency and it depends on the different studied junctions.

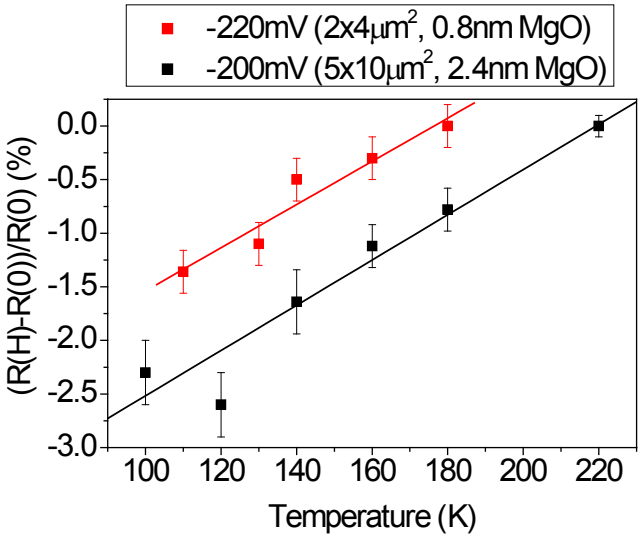

Fig 7.6 Temperature dependence of the TMR for two different junctions. Lines are guide to the eyes.

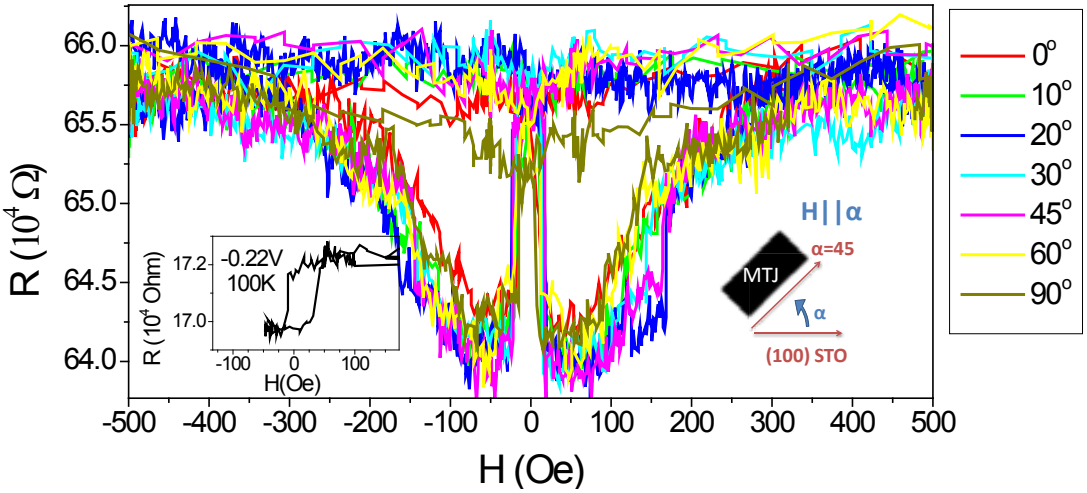

Fig 7.7 In-plane anisotropy of TMR for a junction of area 2×4 μm^2 from a stack with MgO barrier thickness of 0.8 nm, at 70 K and applied bias of -220 mV. Different angles are tested, being 45º the orientation at which H is applied along the patterned rectangle and the Fe(100). Inset shows a minor loop taken at 100 K.

The in-plane anisotropy is tested for a smaller junction with thinner barrier (2×4 μm^2, 0.8 nm MgO), as depicted in Fig 7.7. The sample is rotated an angle α with respect to the STO(100) direction. As the patterning of the samples and the easy axis of Fe both lie along the (110) direction of STO, we expect maximum TMR for H aligned at 45º. The reduction of TMR for angles away from that value, however, is not dramatic, and TMR is clearly visible for all orientations. For 0º and 90º, the difference between R(P) and R(AP) is not as pronounced as in the case of angles 20º to 60º. Besides a certain experimental misorientation in the determination of the exact 45º, this fact confirms a certain anisotropy due to the easy axis of Fe or the rectangular shape of the junction,

although its effect is very small. For 0º and 90º, in the parallel configuration (high R), for small H the electrodes must not be perfectly aligned (their magnetization may not be completely saturated in the direction of H due to anisotropy) and the same case applies for the AP configuration. The inset shows a minor loop to confirm the independent switching of both electrodes.

On the other hand, there is an important difference when applying the magnetic field perpendicular to the sample: the out-of-plane anisotropy was measured in a sample of area 5×10 μm^2 and MgO thickness of 1.2 nm, and compared with the in-plane MR. The results, plotted in Fig 7.8 in different scales for a clearer view, show TMR for both orientations of H but with different coercive fields.

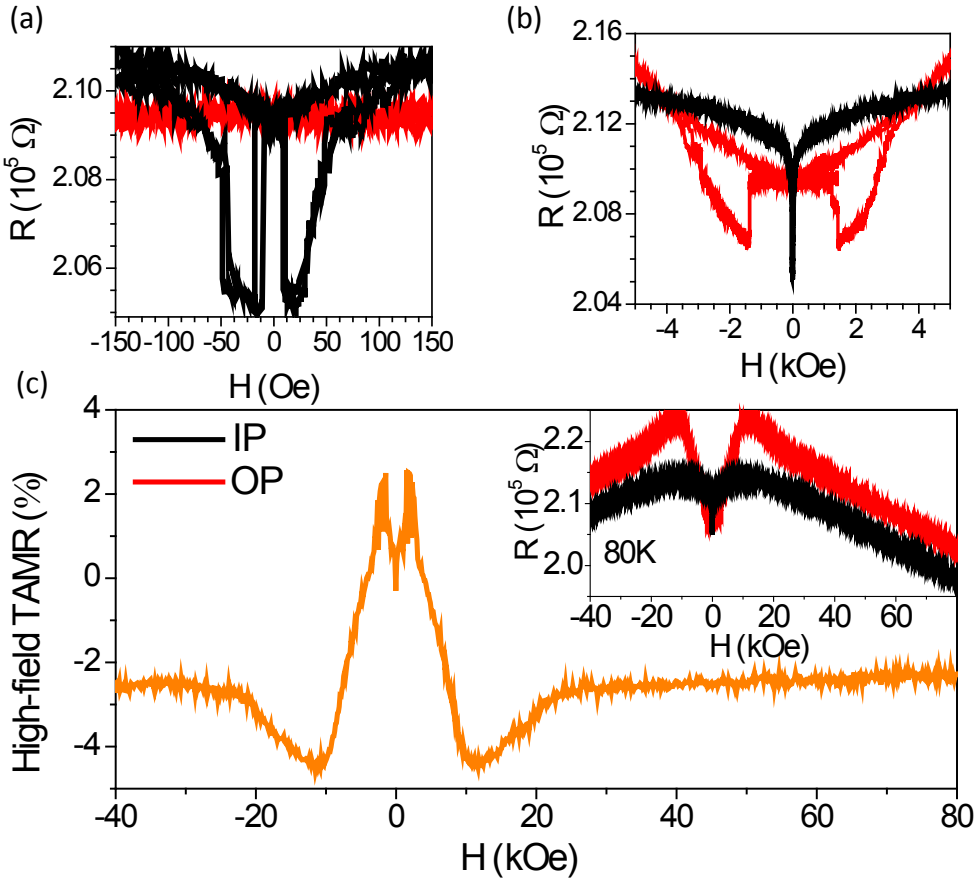

Fig 7.8. TMR for a junction of area 5×10 μm^2 from a stack with MgO barrier thickness of 1.2 nm, measured at 80 K with H applied in different orientations: in-plane (IP, in red) and out-of-plane (OP, in black). (a), (b) and inset in (c) show different scales of R(H). Two consecutive measurements are shown to probe reproducibility; (c) TAMR at high fields (up to 80 kOe).

For H below 150 Oe, the negative TMR for H-in-plane (see Fig 7.8a) comes from the in-plane AP alignment of the magnetization of the electrodes. The unexpected negative TMR for out-of-plane measurements (in Fig 7.8b) may be due to a certain misalignment of the H with respect to the out-of-plane direction or an indication that the easy axis alignment of the magnetizations is not fully in-plane, but also has an out-of-plane component. This is suggested by the also unexpected hysteretic M(H) loops for out-of-

plane applied H in unpatterned Fe/MgO/LSMO stacks, with larger H_C than the in-plane hysteresis loop (see Fig 7.9).

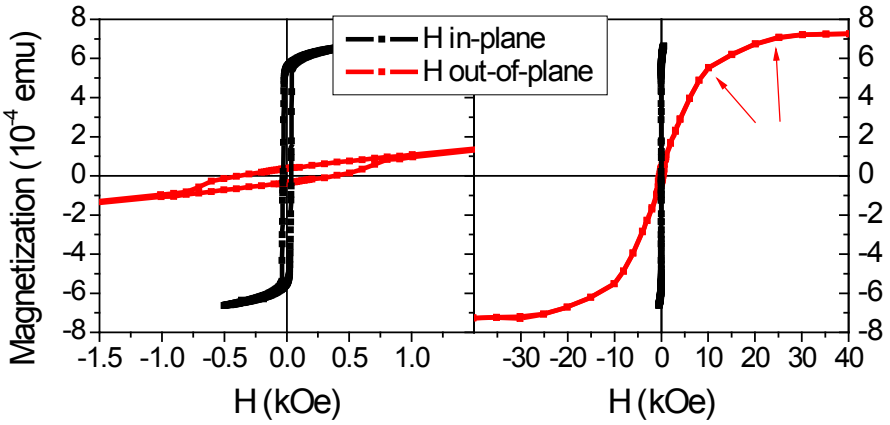

Fig 7.9. Hysteresis loops for H oriented in-plane (black) and out-of-plane (red) in a non-annealed Fe/MgO/LSMO stack before junction patterning, taken at 10 K, in different scales for clarity.

However, at high magnetic fields (see Fig 7.8c and inset) the different resistances for H applied in-plane and out-of-plane cannot be explained just as the relative direction of magnetizations (P and AP) between magnetic moments of both electrodes. This difference can only be explained as TAMR, a dependence of the magnetoresistance of the magnetic tunnel junction on the orientation of the magnetization of the electrodes with respect to the crystallographic and current flow direction. Originated from the spin-orbit coupling, this effect has already been reported in other tunnel junction systems, with a single or two magnetic layers [15–17], and we have studied it in detail for a LAO/LSMO system in Chapter 6.

The changes of slope of R(H||(001)STO) in Fig 7.8c (inset) at ~10 and ~25 kOe may be correlated to the out-of-plane magnetization saturation of the LSMO and Fe layers, respectively, as well as to the two different inflection points (around 10 and 25 kOe) in the M(H||(001)STO) in Fig 7.9.

The possible reasons for the modest values of TMR obtained (-4% for junctions Neg) are diverse:

1. The presence of FeO_x at the interface (also detected by TEM and consistent with the *in-situ* prepared samples of Fe/MgO/LSMO) is the most important factor to consider, as the quality of the interface is crucial towards the coupling between MgO and Fe Δ_1 Bloch states (as explained in Chapter 2). If the MgO/Fe symmetry filtering effect is lost, a dramatic decrease in TMR is predicted, although a more moderate decrease has been reported experimentally in some cases for 1 or 2 oxygen monolayers at the Fe/MgO interface [18,19]. It is important to note, however, that in such cases, the oxidation was performed in a

controlled manner and the interfaces remain relatively flat and ordered. In our case, the iron oxide layer is much thicker and the interface much rougher.

2. Also, the misalignment of 2-4º between LSMO and MgO, seen by TEM and the power spectra (Fig 3.19), may cause the absence of coupling between Δ_1-symmetry electrons.
3. Another reason could be the degradation of the LSMO magnetic properties, as indicated by the reduction of T_C (see Fig 3.16b), which could entail a loss of spin polarization. In fact, oxygen deficiency in LSMO films has already been reported to produce the loss of half-metallic character [20], in which we rely upon to act as efficient spin injector.

From these three factors, the presence of FeO_x is considered to be responsible for the small negative TMR discussed above, as well as the large increase of resistance as temperature is lowered (accessible states may cause the impurity-assisted tunnelling mentioned earlier, and if the extra FeO_x layer is insulating, it increases the effective barrier thickness). Furthermore, if the FeO_x formed at the Fe/MgO interface is continuous and magnetically ordered, filtering effects may arise and yield positive TMR, as observed for junctions Pos discussed in the following section.

7.5 MAGNETORESISTIVE MEASUREMENTS FOR JUNCTIONS POS (POSITIVE TMR)

A few junctions patterned from the same samples display positive TMR at low T and their behaviour is discussed in this section.

Magnetotransport measurements are performed on a junction of area $9\times18\mu m^2$ from a stack with MgO thickness of 2.4 nm. Positive TMR is found for temperatures below 110 K. In Fig 7.10, we show the resistance vs. H measurements performed for a fixed applied bias of 100 mV. At 70 K, as shown in the upper panel (a), the resistance is high and experiences an abrupt switch to even larger resistance values in the antiparallel electrode configuration, for magnetic fields between ~80 Oe and 300 Oe. For higher temperatures (140-180 K), the TMR curves evidence a negative magnetoresistance contribution. As can be seen from Fig 7.10c, this consists in an abrupt switch to lower resistance values at low H (~50-60 Oe), and a relatively gradual change back to the high-field resistance, similar to that found in junctions Neg. For a certain range in between these two regimes, particularly around 120K (as in Fig 7.10b), TMR curves evidence the superposition of positive and negative contributions. Around 200 K, all TMR contributions are lost and only the CMR response coming from the bottom LSMO electrode remains (Fig 7.10d).

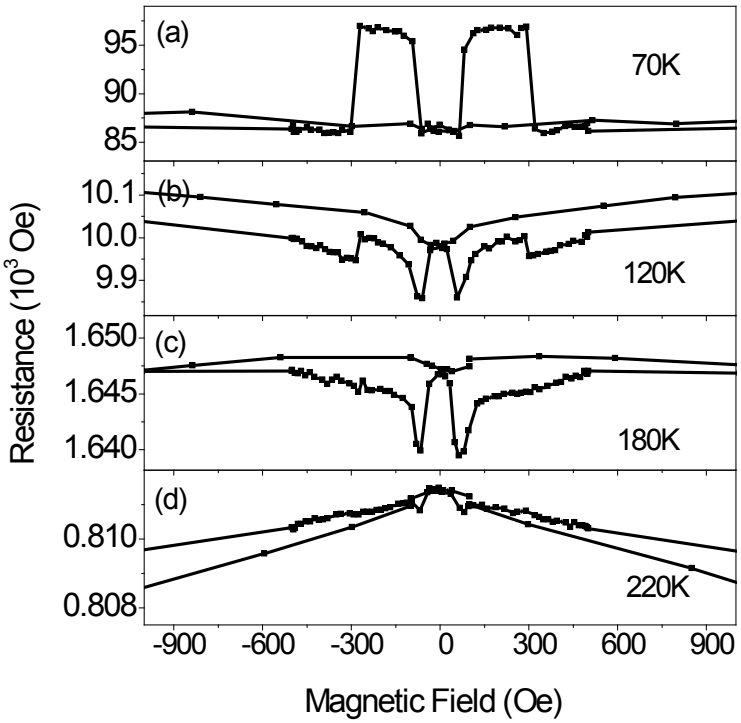

Fig 7.10 Temperature dependence of the R(H) curves for a junction of area 9×18μm^2 and MgO thickness of 2.4 nm. The voltage bias was fixed to 100 mV. (a) At 70 K, a positive TMR with well-defined antiparallel magnetizations of both LSMO and Fe electrodes is observed; (b) at 120 K, the TMR is mainly negative but a visible positive contribution persists. (c) at 180 K only the negative contribution remains; (d) above 200 K, only the CMR response coming from the bottom electrode can be distinguished.

The positive TMR obtained at low T is highly anomalous in view of the nominal negative and positive spin polarization of bulk Fe and LSMO, respectively. However, as mentioned in section 2.5.3, recent reports have shown that an inversion of the spin polarization occurs at oxidized interfaces due to 3*d*-2*p* hybridization. It has been theoretically demonstrated that the larger population of majority antibonding orbitals (as compared to the minority ones) has a spin filtering effect causing a positive spin polarization of the tunnelling current [2,21].

In our case, we detect FeO_x at the interface between Fe/MgO (as can be seen by TEM in Fig 3.19a and by XPS in similar samples grown *in-situ* (Fig 3.22)). So, interfacial effects are expected to play a relevant role on the behaviour displayed by our samples. The complex temperature dependence of the TMR results can thus be explained by considering the effect of this FeO_x layer at the Fe/MgO interface, if it is ordered. The change of sign of the TMR may come from the competing negative contribution of the (bulk) electrodes and the temperature dependent spin filtering effect of the interfacial Fe oxide, suggesting that the ordering temperature of the Fe-oxide interface is around 120 K. At low temperatures, the interfacial oxide induces the depolarization of the tunnelling current, besides the spin filtering, yielding the modest positive TMR. The switching fields for the positive TMR therefore correspond to the LSMO coercive field and to that of the FeO_x layer (perhaps exchange-coupled with the Fe electrode), so

considerably large (~300 Oe from Fig 7.10a). At high temperatures, however, the interfacial oxide no longer filters and the MR takes negative values.

The temperature dependence of the various magnetoresistance contributions is plotted in Fig 7.11a. The positive TMR has an important dependence on temperature, its maximum value found for 70 K (for 10 mV), around 25 %, as seen in Fig 7.11b. As shown in the inset, further lowering the temperature results in much larger R and measurements are noisier. The positive TMR is detectable until roughly 120 K. At higher temperatures the TMR becomes negative and takes values around 1 %.

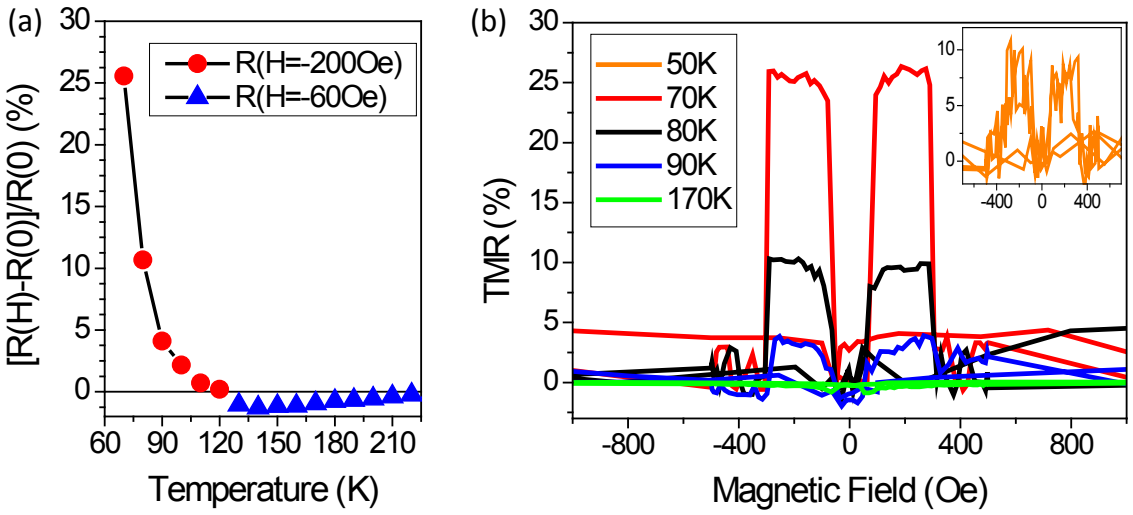

Fig 7.11. Temperature dependence for a junction of area 9×18 μm^2 and MgO barrier thickness of 2.4 nm, for a fixed bias of 10 mV. (a) Dependence of the MR as a function of temperature, for the different contributions: positive switch at -200 Oe (in red dots) and negative switch at -60 Oe (in blue triangles); (b) TMR *vs.*H at low temperatures, where positive TMR is shown to decrease as T increases.

Fig 7.12a shows the magnetoresistance loops, at 70 K, under various bias voltages. Positive TMR decreases with voltage. In our case, it reaches values of +25 % at 10 mV and its value is practically halved for 100 mV. This is common behaviour in magnetic tunnel junctions as discussed by Tsymbal *et al*. [22], but the limited tested voltage range does not allow to confirm or refute the typical voltage dependence of spin filters [23]. On the other hand, negative magnetoresistance, represented in Fig 7.12b for 150 K, turns out to have very small bias voltage dependence. However, some dependence at much higher voltage bias cannot be fully excluded, although in this case the spin filtering does not take place.

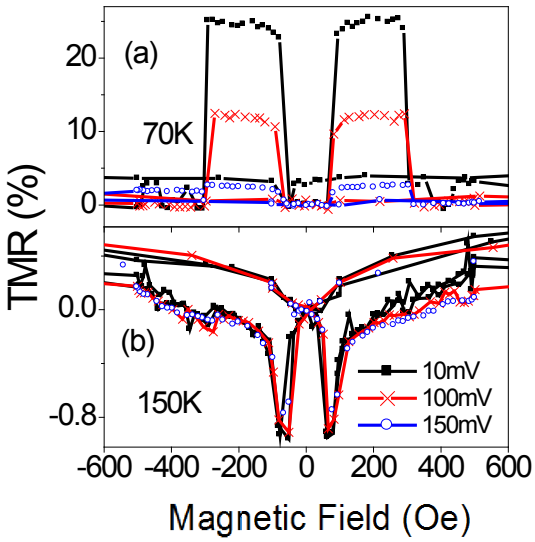

Fig 7.12. Bias voltage dependence of a junction of area 9×18μm^2 and MgO barrier thickness of 2.4 nm (a) At 70 K, the positive TMR notably decreases when increasing voltage bias. (b) At 150 K, the negative contribution is rather insensitive to changes of the voltage bias.

It is worth mentioning that the voltage dependence of junctions varies with the robustness of the barrier. Whilst in the latter case the decay of TMR with voltage is very important, much smaller voltage dependence (as shown in Fig 7.13) was found in a 5×15μm^2 junction with a 1.2 nm-thick MgO barrier. In addition, no difference was found for positive and negative applied biases. In this junction, the thinner MgO barrier yielded lower resistances which enabled less noisy data at low T, but the maximum TMR obtained was hardly above 10%. These smaller TMR values would be coherent with the loss of spin-filtering effect due to the reduction of MgO barrier thicknesses [1]. However, in our case, as we also have FeO_x, we cannot attribute this lower TMR to the Fe/MgO spin-filtering. Instead, we suggest that thinner MgO barrier favours the formation of FeO_x (either larger thickness of FeO_x or perhaps even different oxidation degree or quality). This explanation is coherent with the observation from Chapter 3 that the oxidation of Fe is driven by the oxygen transfer from LSMO to Fe layer through the MgO barrier. In such a scenario, a tunnel barrier with slimmer MgO could explain the larger robustness (for example, by a thicker FeO_x layer), or the reduced TMR (less spin-filtering due to FeO_x layer quality).

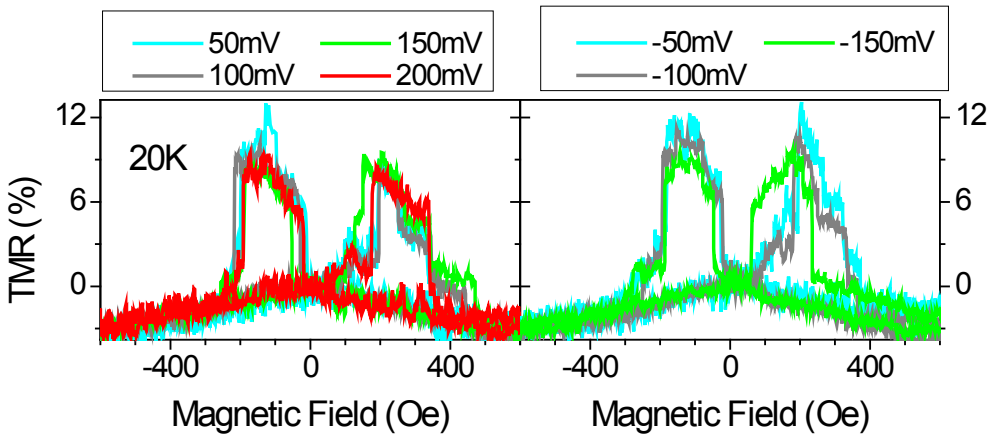

Fig 7.13. Voltage dependence of the TMR at 20 K for a 5×15μm^2 junction from a Fe/MgO(1.2nm)/LSMO stack. Only minute differences were found for the probed biases (from ±50 to ±200 mV, regardless of the sign).

In this last junction, positive TMR is also found for T<140 K. TMR *vs.* H cycles are plotted in Fig 7.14 for various voltages and temperatures, and the decrease of TMR with increasing temperature is visible. However, it is worth noting that the reproducibility of the switching fields (Fig 7.14) is clearly much worse than in the junction with 2.4 nm of MgO barrier (Fig 7.12a). We suggest that this is due to the larger aspect ratio *r* of the junction (5×15μm^2 instead of 9×18μm^2) which is known to favour the formation of different magnetic domains (as explained in Chapter 5). Different voltages, temperatures or even magnetic history (maximum magnetic field reached) may influence the switching of the latter, thus giving the different switching H.

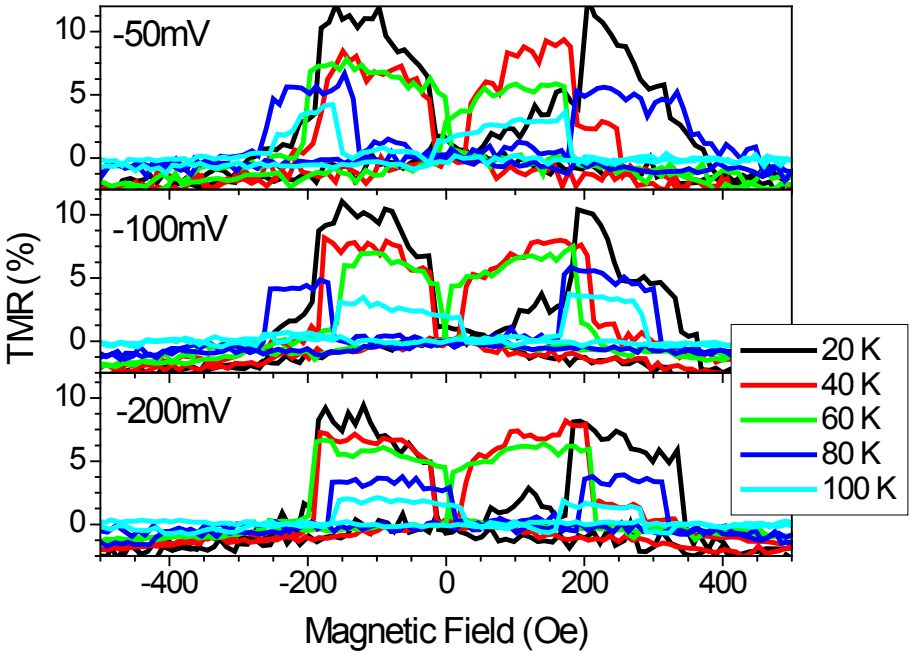

Fig 7.14. Temperature dependence of the MTR at different applied voltages (-50, -100 and -200 mV) for a 5×15μm^2 junction from a Fe/MgO(1.2nm)/LSMO stack.

Furthermore, the switching to the AP configuration (both for the sweeps with increasing and decreasing H) sometimes takes place even before zero magnetic field is reached. This fact, which cannot be attributed to the aspect ratio, can be explained through the existence of AF coupling between the LSMO electrode and the filtering FeO_x for this sample of 1.2 nm of MgO barrier thickness (and will be discussed further on). This effect competes with the coercive field of the electrodes, as illustrated in Fig 7.15 from two examples of minor loops taken at a fixed applied bias of -100 mV.

The measurement of a minor loop, (a) from Fig 7.15, centered at H=0 Oe and with relatively low T_C, follows the expected behaviour for uncoupled electrodes, so that the coercive field of the softer electrode dominates the measurement. On the other hand, measurement (b) presents clear signs of AF coupling of the electrodes: the switch from P to AP configuration takes place before crossing H=0, but also the switch back to P configuration takes place at larger H than expected (~400 Oe) because the system needs more energy to overcome the AF coupling. This effect has not been seen to be linked to temperature or voltage in the measured ranges (from 20 to 100 K and from -200 to 200 mV), but mostly to magnetic history.

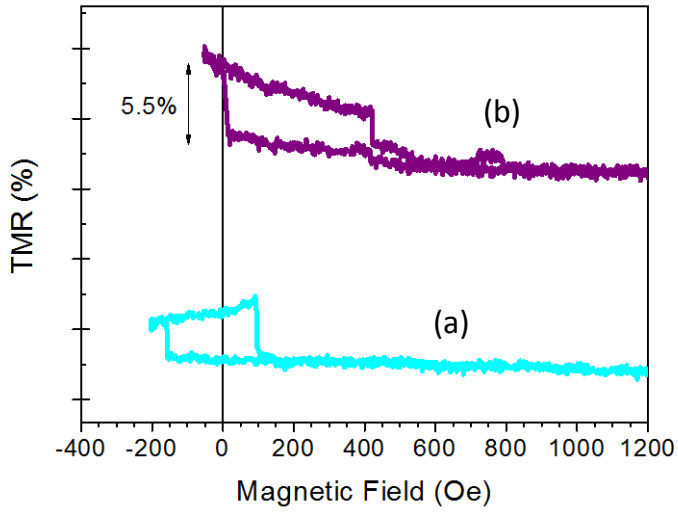

Fig 7.15. Minor loops measured fixing the applied bias at -100 mV, for a 5×15μm^2 junction from a Fe/MgO(1.2nm)/LSMO stack.

The existence of such AF coupling in this junction (5×15μm^2 junction from a Fe/MgO(1.2nm)/LSMO stack) is further confirmed by the magnetoresistance measurements performed with H applied out-of-plane, shown in Fig 7.16. For large applied H, the low resistance measured coincides for both in-plane (black line) and out-of-plane (red line) configurations: the magnetizations of both electrodes are parallel to each other and to the applied magnetic field, as represented by the small parallel arrows around ±6 kOe. Therefore, this resistance is the corresponding to the parallel configuration of the magnetization of the electrodes, R_P. However, as shown in the inset, the resistance obtained at low fields for the H-out-of-plane configuration coincides with the resistance measured for the antiparallel alignment of magnetizations

in the H-in-plane configuration (R_{AP}). This suggests that a rotation of the electrodes takes place to favour antiparallel alignment at H=0.

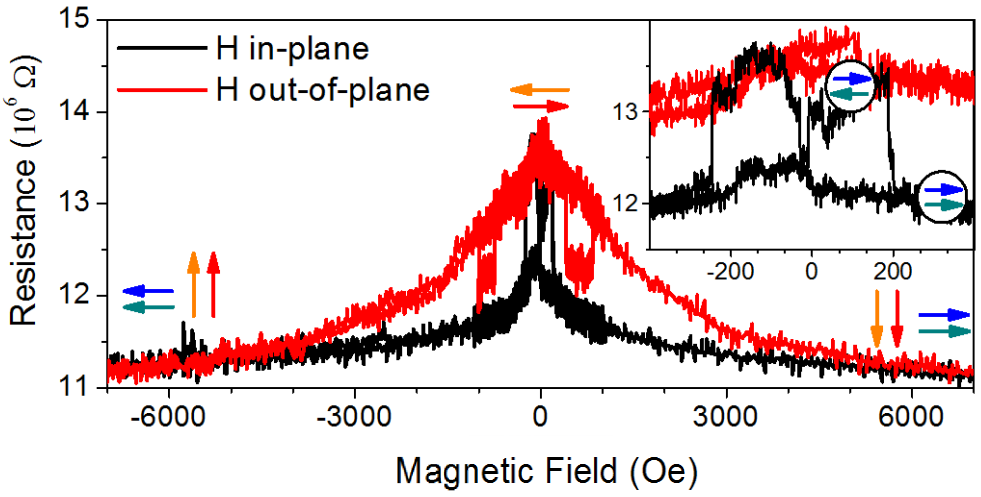

Fig 7.16. Dependence of the magnetoresistance on the direction of the applied magnetic field for a fixed applied voltage bias of -50 mV at T= 10 K. The magnetic field was applied parallel to the surface, along the [100] Fe easy axis (H in-plane) and perpendicular to the film (H out-of-plane).

Surprisingly, for the out-of-plane configuration, a switching towards lower resistance (which takes an intermediate value between the R_{AP} and R_P) occurs at fields above 400 Oe. We surmise that this negative TMR is a 90º configuration between magnetizations, which may result from the competition between the alignment of the magnetization of the electrodes along the externally applied H, the in-plane anisotropy of thin films and the AF coupling. It is worth mentioning here that strong perpendicular magnetic anisotropy has been reported, both theoretically and experimentally, in Fe/MgO system [24]. However, this perpendicular magnetic anisotropy has evidenced to be strongly dependent on the oxidation degree of interfaces [25,26].

Low-field magnetoresistance for the in-plane configuration (before switching) also suggests AF coupling (or at least some misalignment between the magnetization easy-axis) of both electrodes, not visible in the junction with MgO thickness of 2.4 nm.

Antiferromagnetic coupling due to interlayer exchange coupling has already been found for systems containing Fe/MgO, showing an important dependence on the MgO barrier thickness. In the case of Fe/MgO/Fe, AF interaction is reported for MgO thicknesses below 1 nm [27,28]. Furthermore, a theoretical study from Zhuravlev et al. [29,30] correlates the presence of impurities such as oxygen vacancies in the MgO barrier with AF coupling for MgO thicknesses of 3 monolayers (1.2 nm), although thicker barriers (5 monolayers of MgO, so ~ 2 nm) couple ferromagnetically. Wu et al. [31] experimentally find AF coupling for Fe_3O_4 electrodes separated by an MgO spacer thinner than 1.5 nm, and their *ab-initio* calculations reveal the importance of partial oxidation of the FM electrodes in the coupling. As our results fall within the thickness range for which the literature predicts AF coupling (~1.2 nm) and the presence of

oxygen vacancies is confirmed by the temperature dependence of resistance, AF coupling in these junctions is not surprising.

7.6 SUGGESTIONS FOR IMPROVEMENT

Solutions towards the preparation of a clean Fe/MgO interface (i.e. free from FeO_x), that is expected to significantly improve the TMR response, generally include thermal annealings and the incorporation of a thin ~5 Å Mg layer into the barrier/electrode interface. The effectiveness of thermal annealing in improving TMR response in MgO-based devices is well established in the literature for similar systems. However, thermal annealings after the deposition of Fe have already been explored in Chapter 3 for our LSMO/MgO/Fe system, revealing that annealing enhances the oxidation of the Fe at the interface, so we discard this possibility. On the other hand, the reasons why the Mg interlayer is effective are still unclear and either improvement of (001) texture in the MgO layer or improvement of interface sharpness and reduction of interfacial oxides are routinely suggested [32]. The incorporation of such a layer could be attempted for our system.

Smooth variations of the LSMO doping rate (La/Sr ratio) can also affect the properties of our tunnel junctions. For instance, strain-induced changes of local symmetry at the LSMO/barrier interface may promote weak changes on the local Mn valence [6,33], that could further degrade the TMR response. Therefore, improvements in the performance of these spin-tunnel junctions are expected by modulating the interface doping profile in a similar way to the approach reported by Yamada and co-workers [34].

Finally, it is also worth commenting here that the fabrication process used for junction patterning plays an important role on the uniformity and reproducibility of junctions' properties in these materials. Therefore, there is still significant room for improvement in the nanofabrication process and ensuring the total elimination of the resist from the lithographic process is crucial.

7.7 SUMMARY

Tunnel magnetoresistive measurements for Fe/MgO/LSMO magnetic junctions exhibit two different phenomenologies, depending on their quality: negative TMR found throughout all the temperature range (junctions Neg), and positive TMR at low temperatures (junctions Pos). We explain these results from the difference in oxidation state and quality of the Fe/MgO interface: for continuous and ordered FeO_x, we suggest that a spin-filtering effect takes place, which results in positive TMR at low T.

Junctions Neg display a negative TMR of around 3% at low T, coherent with the negative and positive spin polarization of Fe and LSMO, respectively. These low TMR values are ascribed to the imperfections of the stack properties (their origin discussed in Chapter 3): the rough and oxidized Fe/MgO interface, considered the main responsible,

as well as the misalignment between LSMO and MgO and the degradation of the LSMO properties (visible from its low T_C).

Junctions Pos display a positive TMR of 25% at 70 K indicative of an inversion of the spin polarization of the interface layer resulting from the formation of an ordered Fe oxide layer. In any case, these TMR values are similar to those previously reported in magnetic tunnel junctions combining LSMO and Co or Fe electrodes [35] and most likely result from modified bonding at the interface between the transition metal electrode and the oxide barrier. In our case, oxidation is originated from the transfer of oxygen coming from the LSMO, as seen from the *in-situ* grown samples of Fe/MgO/LSMO (section 3.9).

The reduction of the MgO barrier thickness to 1.2 nm is seen to yield antiferromagnetic coupling between the ferromagnetic electrodes. This fact gives rise to interesting magnetoresistance measurements probed for H out-of-plane, exhibiting a change of sign of the TMR with respect to the H in-plane results. Further interpretation is required for a full understanding of this effect.

7.8 BIBLIOGRAPHY

[1] Yuasa S., Nagahama T., Fukushima A., Suzuki Y., Ando K.; "Giant room-temperature magnetoresistance in single-crystal Fe/MgO/Fe magnetic tunnel junctions". *Nat. Mater.* 3; **2004**: 868–71. doi:10.1038/nmat1257.

[2] Belashchenko K.D., Tsymbal E.Y., van Schilfgaarde M., Stewart D.A., Oleynik I.I., Jaswal S.S.; "Effect of interface bonding on spin-dependent tunneling from the oxidized Co surface". *Phys. Rev. B* 69; **2004**: 7. doi:10.1103/PhysRevB.69.174408.

[3] Pesquera D., Herranz G., Barla A., Pellegrin E., Bondino F., Magnano E., et al.; "Surface symmetry-breaking and strain effects on orbital occupancy in transition metal perovskite epitaxial films". *Nat. Commun.* 3; **2012**. doi:10.1038/ncomms2189.

[4] Tebano A., Aruta C., Sanna S., Medaglia P.G., Balestrino G., Sidorenko A.A., et al.; "Evidence of orbital reconstruction at interfaces in ultrathin La0.67Sr0.33MnO3 films.". *Phys. Rev. Lett.* 100; **2008**: 137401.

[5] Huijben M., Martin L.W., Chu Y.H., Holcomb M.B., Yu P., Rijnders G., et al.; "Critical thickness and orbital ordering in ultrathin La(0.7)Sr(0.3)MnO(3) films". *Phys. Rev. B* 78; **2008**. doi:094413 10.1103/PhysRevB.78.094413.

[6] Valencia S., Peña L., Konstantinovic Z., Balcells L., Galceran R., Schmitz D., et al.; "Intrinsic antiferromagnetic/insulating phase at manganite surfaces and interfaces.". *J. Phys. Condens. Matter* 26; **2014**: 166001. doi:10.1088/0953-8984/26/16/166001.

[7] Wu X., Zhang Z., Meng J.; "Breakdown by magnetic field in a La0.7Sr0.3MnO3/MgO/Fe spin valve". *Appl. Phys. Lett.* 100; **2012**. doi:10.1063/1.3696670.

[8] Balcells L., Fontcuberta J., Martínez B., Obradors X.; "High-field magnetoresistance at interfaces in manganese perovskites". *Phys. Rev. B* 58; **1998**: R14697–700. doi:10.1103/PhysRevB.58.R14697.

[9] Jönsson-Åkerman B.J., Escudero R., Leighton C., Kim S., Schuller I.K., Rabson D.A.; "Reliability of normal-state current–voltage characteristics as an indicator of tunnel-junction barrier quality". *Appl. Phys. Lett.* 77; **2000**: 1870. doi:10.1063/1.1310633.

[10] Ma Q.L., Wang S.G., Zhang J., Wang Y., Ward R.C.C., Wang C., et al.; "Temperature dependence of resistance in epitaxial Fe/MgO/Fe magnetic tunnel junctions". *Appl. Phys. Lett.* 95; **2009**: 052506. doi:10.1063/1.3194150.

[11] Txoperena O., Song Y., Qing L., Gobbi M., Hueso L.E., Dery H., et al.; "Impurity-Assisted Tunneling Magnetoresistance under a Weak Magnetic Field". *Phys. Rev. Lett.* 113; **2014**: 146601. doi:10.1103/PhysRevLett.113.146601.

[12] Simmons J.G.; "Generalized formula for electric tunnel effect between similar electrodes separated by a thin insulating film". *J. Appl. Phys.* 34; **1963**: 1793 – &. doi:10.1063/1.1702682.

[13] Brinkman W.F.; "Tunneling Conductance of Asymmetrical Barriers". *J. Appl. Phys.* 41; **1970**: 1915. doi:10.1063/1.1659141.

[14] Gloos K., Poikolainen R.S., Pekola J.P.; "Wide-range thermometer based on the temperature-dependent conductance of planar tunnel junctions". *Appl. Phys. Lett.* 77; **2000**: 2915. doi:10.1063/1.1320861.

[15] Moser J., Matos-Abiague A., Schuh D., Wegscheider W., Fabian J., Weiss D.; "Tunneling Anisotropic Magnetoresistance and Spin-Orbit Coupling in Fe/GaAs/Au Tunnel Junctions". *Phys. Rev. Lett.* 99; **2007**: 056601. doi:10.1103/PhysRevLett.99.056601.

[16] Gould C., Rüster C., Jungwirth T., Girgis E., Schott G., Giraud R., et al.; "Tunneling Anisotropic Magnetoresistance: A Spin-Valve-Like Tunnel Magnetoresistance Using a Single Magnetic Layer". *Phys. Rev. Lett.* 93; **2004**: 117203. doi:10.1103/PhysRevLett.93.117203.

[17] Matos-Abiague A., Fabian J.; "Anisotropic tunneling magnetoresistance and tunneling anisotropic magnetoresistance: Spin-orbit coupling in magnetic tunnel junctions". *Phys. Rev. B* 79; **2009**: 155303. doi:10.1103/PhysRevB.79.155303.

[18] Zermatten P.-J., Bonell F., Andrieu S., Chshiev M., Tiusan C., Schuhl A., et al.; "Influence of Oxygen Monolayer at Fe/MgO Interface on Transport Properties in Fe/MgO/Fe(001) Magnetic Tunnel Junctions". *Appl. Phys. Express* 5; **2012**: 023001. doi:10.1143/APEX.5.023001.

[19] Bonell F., Andrieu S., Bataille A., Tiusan C., Lengaigne G.; "Consequences of interfacial Fe-O bonding and disorder in epitaxial Fe/MgO/Fe(001) magnetic tunnel junctions". *Phys. Rev. B* 79; **2009**: 224405. doi:10.1103/PhysRevB.79.224405.

[20] Picozzi S., Ma C., Yang Z., Bertacco R., Cantoni M., Cattoni A., et al.; "Oxygen vacancies and induced changes in the electronic and magnetic structures of La0.66Sr0.33MnO3: A combined ab initio and photoemission study". *Phys. Rev. B* 75; **2007**: 094418. doi:10.1103/PhysRevB.75.094418.

[21] Tsymbal E.Y., Oleinik I.I., Pettifor D.G.; "Oxygen-induced positive spin polarization from Fe into the vacuum barrier". *J. Appl. Phys.* 87; **2000**: 5230–2. doi:10.1063/1.373304.

[22] Tsymbal E.Y., Mryasov O.N., LeClair P.R.; "Spin-dependent tunnelling in magnetic tunnel junctions". *J. Phys. Condens. Matter* 15; **2003**: R109–42. doi:10.1088/0953-8984/15/4/201.

[23] Tiffany S.S., Jagadeesh S.M.; Spin-Filter Tunneling. Handb. Spin Transp. Magn., Chapman and Hall/CRC; **2011**, p. 251–66. doi:10.1201/b11086-17 10.1201/b11086-17.

[24] Koo J.W., Mitani S., Sasaki T.T., Sukegawa H., Wen Z.C., Ohkubo T., et al.; "Large perpendicular magnetic anisotropy at Fe/MgO interface". *Appl. Phys. Lett.* 103; **2013**: 192401. doi:10.1063/1.4828658.

[25] Yang H.X., Chshiev M., Dieny B., Lee J.H., Manchon A., Shin K.H.; "First-principles investigation of the very large perpendicular magnetic anisotropy at Fe|MgO and Co|MgO interfaces". *Phys. Rev. B* 84; **2011**: 054401. doi:10.1103/PhysRevB.84.054401.

[26] Rodmacq B., Auffret S., Dieny B., Monso S., Boyer P.; "Crossovers from in-plane to perpendicular anisotropy in magnetic tunnel junctions as a function of the barrier degree of oxidation". *J. Appl. Phys.* 93; **2003**: 7513. doi:10.1063/1.1555292.

[27] Faure-Vincent J., Tiusan C., Bellouard C., Popova E., Hehn M., Montaigne F., et al.; "Antiferromagnetic coupling by spin polarized tunneling". *J. Appl. Phys.* 93; **2003**: 7519. doi:10.1063/1.1540175.

[28] Faure-Vincent J., Tiusan C., Bellouard C., Popova E., Hehn M., Montaigne F., et al.; "Interlayer Magnetic Coupling Interactions of Two Ferromagnetic Layers by Spin Polarized Tunneling". *Phys. Rev. Lett.* 89; **2002**: 107206. doi:10.1103/PhysRevLett.89.107206.

[29] Zhuravlev M., Tsymbal E., Vedyayev A.; "Impurity-Assisted Interlayer Exchange Coupling across a Tunnel Barrier". *Phys. Rev. Lett.* 94; **2005**: 026806. doi:10.1103/PhysRevLett.94.026806.

[30] Zhuravlev M.Y., Velev J., Vedyayev A.V., Tsymbal E.Y.; "Effect of oxygen vacancies on interlayer exchange coupling in Fe/MgO/Fe tunnel junctions". *J. Magn. Magn. Mater.* 300; **2006**: e277–80. doi:10.1016/j.jmmm.2005.10.099.

[31] Wu H.-C., Arora S.K., Mryasov O.N., Shvets I. V.; "Antiferromagnetic interlayer exchange coupling between Fe[sub 3]O[sub 4] layers across a nonmagnetic MgO dielectric layer". *Appl. Phys. Lett.* 92; **2008**: 182502. doi:10.1063/1.2919081.

[32] Hindmarch A.T., Harnchana V., Ciudad D., Negusse E., Arena D.A., Brown A.P., et al.; "Magnetostructural influences of thin Mg insert layers in crystalline CoFe(B)/MgO/CoFe(B) magnetic tunnel junctions". *Appl. Phys. Lett.* 97; **2010**. doi:10.1063/1.3527939.

[33] Valencia S., Konstantinovic Z., Schmitz D., Gaupp A., Balcells L., Martinez B.; "Interfacial effects in manganite thin films with different capping layers of interest for spintronic applications". *Phys. Rev. B* 84; **2011**: 024413. doi:024413 10.1103/PhysRevB.84.024413.

[34] Yamada H., Ogawa Y., Ishii Y., Sato H., Kawasaki M., Akoh H., et al.; "Engineered interface of magnetic oxides". *Science (80-.).* 305; **2004**: 646–8. doi:10.1126/science.1098867.

[35] Fert A., Barthélémy A., Youssef J.B., Contour J.-P., Cros V., De Teresa J.M., et al.; "Review of recent results on spin polarized tunneling and magnetic switching by spin injection". *Mater. Sci. Eng. B* 84; **2001**: 1–9. doi:10.1016/S0921-5107(01)00548-7.

PART V:

CONCLUSIONS

CHAPTER 8. MAIN RESULTS AND CONCLUSIONS

1. The study of the interfacial quality of heterostructures towards the implementation of tunnel junctions with LSMO bottom electrodes has yielded two main results:
   - LSMO/MgO structures grown *in-situ* exhibit a decrease in T_C with respect to optimized LSMO, concomitant with the increase of its cell parameter, which suggests that oxygen is irreversibly removed from the LSMO through the MgO layer. These changes do not take place for *in-situ*-grown LSMO/MgO/Pt heterostructures, indicating that Pt acts as a barrier to the extraction of oxygen from the LSMO.
   - LSMO/MgO/Fe heterostructures have been grown *in-situ* and *ex-situ*: oxidation of Fe at the Fe/MgO interface is observed in both cases. This oxidation –enhanced when an annealing is performed after Fe deposition- is concomitant to the reduction of the LSMO, visible through a decrease in its T_C and the increase of its *c*-lattice parameter. Again, we ascribe this effect to oxygen transfer from the LSMO to the Fe through the MgO layer.
   - The effect of air exposure of an MgO thin layer grown on LSMO leads to brucite formation. But even after an annealing to remove brucite, good surface properties are not recovered, thus leading to larger interface roughness for *ex-situ* grown LSMO/MgO/Fe heterostructures, as well as a surprising 2-4º out-of-plane misalignment between LSMO and MgO.

2. The suitability of LCMO thin films as possible spin filter insulating barriers has been proposed after an optimization of the growth and characterization of such films:
   - Growth of LCMO thin films by sputtering has been optimized to achieve high T_C (~230 K). Epitaxial, insulating and ferromagnetic films with T_C above 200 K have been obtained for a thickness range from 20 to 5 nm. Their surface is flat and follows the steps and terraces of the substrate.
   - The oxygen content in the LCMO thin films correlates with the value of the T_C and the crystallographic orientation of the material on the STO substrate: low oxygen contents results in low-T_C samples with predominant *c*-in plane orientation, whilst high oxygen contents yields high-T_C samples with a unique *c*-out-of-plane orientation.
   - Both for high and low-T_C samples and for all the probed thicknesses (5-20 nm), perpendicular magnetic anisotropy is observed, whose origin remains yet to be determined. High T_C films reach magnetization saturation values of 6 μ_B/f.u., thus indicating full cationic ordering. The saturation magnetization of 5 μ_B/f.u. obtained for low-T_C samples is suggested to come from lower oxygen contents and change of the Co spin state.

- LCMO/LSMO heterostructures are grown using low and high-oxygenation conditions for the LCMO growth. Only for low-oxygenation conditions does the structure yield two distinct T_C at ~310 K and ~180 K corresponding to those of LSMO and LCMO, respectively. Characterization by TEM of such system reveals high epitaxiallity of the oxide layers while energy-filtered-TEM images rule out interdiffusion of Co.

3. Tunnel junction configurations which take advantage of the insulating properties of the resist to reduce the number of steps in the fabrication process are tested:
   - The use of PMMA resist for patterning with electron beam lithography is optimized to achieve dots of 100 nm in diameter, but such a resist may suffer contraction below ~ 120 K, so that its use as insulator for the measured device (tested in Pt/LAO/LSMO junctions) prevents proper transport measurements below this temperature.
   - The use of positive photoresist during the fabrication process and in the final measured configuration allows probing down to 10 K without any loss of the good contact properties. However, greater effort must be devoted to ensure that no resist remains at interfaces.

4. Tunnelling transport for Pt/LAO/LSMO junctions examined as a function of temperature and magnetic field allows the characterization of the LAO barrier and the LAO/LSMO interface:
   - LAO barrier maintains its insulating properties down to 1-2 nm, thus qualifying as an appropriate candidate for efficient spin injection. Scaling of the room temperature resistance as a function of junction area and direct tunnelling transport down to 200 K for a 0.8 μm^2-sized junction reflects the good quality of the LAO layer.
   - The temperature dependence of resistance shows a maximum at ~170 K, also reported for LSMO-based MTJ in the literature. Although the origin of such a peak remains to be clarified, the absence of shift in the peak when an external magnetic field is applied suggests that it is not linked to an oxygen-deficient layer at the LAO/LSMO interface.
   - A 16 μm^2-sized junction of this heterostructure yields a MR of 17 % at 10 K and 3 T, which is ascribed to a change in the DOS due to the application of a magnetic field and/or to magnetic disorder at the interface. Tunnelling anisotropic magnetoresistance of 4 % is found for magnetic fields above 5 kOe, reflecting uniaxial anisotropy, and a spin-valve-like TAMR signal is measured at lower magnetic fields, indicative of magnetic domains switching.

5. Magnetoresistive studies in Fe/MgO/LSMO magnetic tunnel junctions point towards the importance of interfacial effects:

- The measured TMR is either negative or positive, depending on the junction. We ascribe this effect to the formation of FeO_x, which may possess different oxidation states and quality for the different junctions. We suggest that magnetically ordered FeO_x produces a spin-filtering effect which results in 25% of positive TMR at 70 K, whilst non-ordered FeO_x yields negative TMR of 3% at low temperatures. These modest TMR values are discussed in terms of the quality of the magnetic tunnel junction stack.
- Antiferromagnetic coupling between the LSMO and the magnetically ordered FeO_x is found for a Fe/MgO/LSMO magnetic tunnel junction with 1.2 nm-thick MgO barrier, indirectly measured through the magnetoresistance curves, in the configurations with magnetic field applied in-plane and out-of-plane.

PART VI:

APPENDIX

A. EXPERIMENTAL TECHNIQUES

A.1 INTRODUCTION

This appendix is meant as a brief introduction to the most relevant experimental techniques used during this thesis. The correct understanding of the physical mechanisms involved in the measurements is of fundamental importance when analyzing the data and extracting what we can and cannot conclude from the results.

The experimental techniques described here will be divided into five sections depending on their purpose: the growth of the samples, characterization techniques (structural, magnetic and electrical) and patterning techniques.

A.2 THIN FILM GROWTH

The samples used in this work have been mostly grown at the ICMAB laboratory by radio frequency (RF) magnetron sputtering (see Fig A.2), so we will explain the technique in detail in this section.

Together with pulsed laser deposition (PLD), sputtering –using sintered ceramic as targets- is one of the most popular techniques to produce thin films of manganites. Other methods like metal-organic chemical vapour deposition (MOCVD), molecular-beam epitaxy (MBE), electrochemistry or spray pyrolysis and sol-gel dip coating may also provide good quality manganite films, as reviewed in reference [1], but are beyond the scope of this thesis.

A.3 MAGNETRON SPUTTERING

The sputtering technique consists in the bombardment of a target material in order to eject (neutral) particles from it by momentum transfer. We start by creating a plasma of a certain gas (usually Ar –because it does not react- or oxygen) around a target of the material we want to deposit. Plasma is the state of the matter in which neutral atoms, ions, electrons, and photons coexist. The photons come from the "reabsorption" of an electron by an ion, which gives rise to a neutral atom and emits a photon. When applying an electrical potential, the ions from the plasma are accelerated towards the target and as a result of the collisions, neutral target atoms are ejected and deposited on the substrate.

The electrons from the plasma are confined close to the target by a magnetron, which consists of two concentric magnets that create a magnetic field whose lines close in on the target. By the Lorentz force, the electrons are forced to a helicoidal trajectory around the magnetic field lines, causing higher electron density close to the target. This results in more ionizations of the gas atoms and more collisions with the target, thus enhancing

the sputtering deposition process and offering higher sputter rates, around nm/min. Cold water flows inside the magnetron to prevent magnetron damage due to excessive heating. Another advantage of the magnetron is that less electrons reach the substrate (less heating and less substrate damage).

If the applied voltage difference between the cathode (where the target is) and the rest of the chamber is constant (DC), we have a net flow of ions towards the target and atomic ablation occurs. But if the target is an insulator, positive charge accumulation prevents the growth of insulating materials. To overcome this setback, a radio frequency (RF) AC signal is added to the DC voltage; with the effective negative bias voltage produced, the number of electrons that arrive at the target while it is positive compensates the number of ions that arrive while it is negative (see Fig A.1). In this way, RF-sputtering enables the use of insulating targets [2].

This technique provides high quality thin films, presenting good stoichiometry and good adherence to the substrate, its main advantage with respect to PLD being its suitability for making large-area thin films and multilayer structures [1].

A good calibration of the sputtering conditions is vital, because the use of different parameters can result in different growth modes and therefore film quality, as we comment in detail in Chapter 3. The main parameters to take into account are the chamber pressure and RF power, which affect the growth rate, substrate temperature during deposition and cooling rate, which affect the crystallinity and roughness of the surface, besides others. The steps to grow LSMO thin films are the following:

1. We introduce the substrate on a heater inside the sputtering chamber, and set it to high vacuum (around 1×10^{-6} Torr) by means of a rotatory and a turbomolecular pump –to minimize the sample contamination.
2. We heat the substrate to 900 ºC, introduce gas flow (oxygen) in the chamber and reduce the speed of the turbomolecular pump to stabilize to the work pressure (around 0.1- 0.2 Torr).
3. We switch on the DC and RF generator, so the plasma is created and sputtering starts to take place (what we call "pre-sputtering", to clean the surface of the target from any possible contamination). After a few minutes, we place the heater a few cm beneath the magnetron so the film starts to grow on the substrate.
4. After sputtering the desired time (see calibration method at section A.4.2), the DC and RF generator is switched off, the pumps and the gas flow are turned off.
5. Before opening the chamber and collecting the sample, the sample is kept inside the chamber for an hour at 900 ºC and at a constant oxygen pressure of around 350 Torr. This process is known as "annealing" and it can lead to important modification of the oxygen stoichiometry and profound impact on the magnetic and electronic transport properties of the film [1].

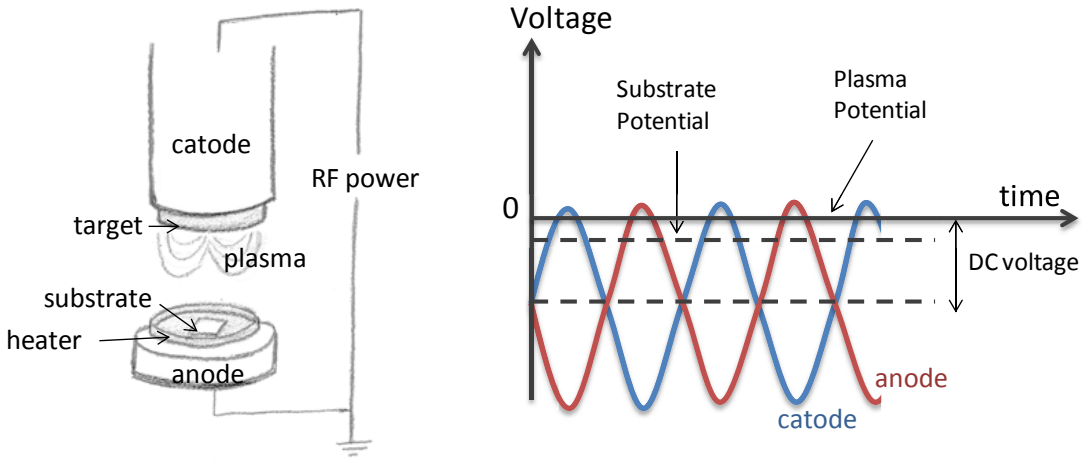

Fig A.1. Sketch of sputtering system and voltage *vs*. time graph to show how the radio-frequency magnetron sputtering process works.

In order to further reduce the base pressure during the deposition of materials which we grow in Ar atmosphere instead of oxygen, we introduce a cold finger, filled with liquid Nitrogen, in contact with the gas inside the chamber. The oxygen particles, besides others, condense above the liquid Nitrogen temperature, so they are attached to the cold finger and the base pressure is notably reduced. The Argon particles, however, condense below the Nitrogen liquid temperature, and are therefore not affected by the cold finger. This is an important improvement when growing Fe in our chamber, where oxidation must be avoided.

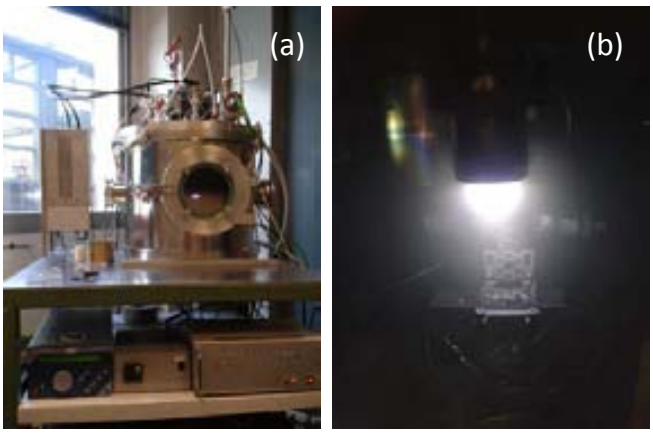

Fig A.2. Photos of the sputtering system (home-made) from the Institut de Ciència de Materials de Barcelona (ICMAB); (a) general view of all the system, (b) magnetron with Ar plasma while depositing Pt.

A.4 Structural characterization techniques

In order to determine the film quality and its physical properties, a wide variety of techniques are available. X-ray measurements provide a structural characterization of the film: we can probe the thickness of the film (X-ray reflectivity) and its crystallinity, its lattice parameters and the orientation of the film with respect to the substrate (X-ray

diffraction). We use atomic force microscopy (AFM) to characterize the film surface: topography (roughness, steps, etc) and differences in composition. The X-ray photoelectron spectroscopy (XPS) enables us to probe the composition of the materials (and the oxidation state), and the electron microscopy (SEM and TEM) provide images with very high resolution.

A.4.1 X-RAY DIFFRACTION

X-ray measurements have become an indispensable technique in thin-film analysis. As interatomic distances of crystals and molecules are around 10-40 Å, constructive and destructive interferences can be observed when exposing them to X-rays, whose wavelengths are in the range of 0.5 to 100 Å, obtaining information on the periodicity of the structures.

Crystalline materials disperse X-rays elastically in certain directions (due to constructive interferences), creating a diffraction pattern. This diffracted signal depends on the number of electrons of the atoms (Z) and the incident angle of the X-rays with respect to the crystallographic orientation of the sample.

In a crystal structure, atoms are located on imaginary parallel (*hkl*) planes, each plane separated a distance d_{hkl} from the next. For incident X-rays forming an angle θ with a certain plane, the diffracted beam emerges forming an angle of 2θ with respect to the incident beam. This is due to constructive interference between beams that follow different paths, and takes place only when the distance between planes fulfills Bragg's law:

$$2d_{hkl}sin\theta = n\lambda$$

where λ is the wavelength of the incident radiation and n is the diffraction peak order. We use a monochromator to select only the CuK_α radiation: $\lambda(CuK_{\alpha 1}) = 1.54056$Å.

The X-ray diffraction pattern intensities are proportional to the quantity of material the X-rays diffract with: for very small films, the peak intensity can be largely reduced, which can be a problem.

At the ICMAB, we have used a Rigaku Rotaflex RU-200B diffractometer to obtain the Θ/2Θ scans and the X-ray reflectivity spectra. This system is composed of an X-ray tube, a sample holder (whose surface is at an angle ω with respect to the incident beam) and a point detector (at an angle 2Θ with respect to the incident beam).

A.4.1.1 Θ/2Θ SCAN

The Θ/2Θ scan receives its name from the geometry of the system used to perform the measurement: the sample surface and the point detector are positioned at angles of Θ and 2Θ, respectively, from the incident X-ray beam (as in Fig A.3a). The diffraction pattern (shown in Fig A.3(b)) plots the scattered intensity as a function of the angle Θ,

collected by rotating the sample holder and the point detector while conserving the Θ/2Θ relationship at all times.

Our substrates are STO single crystals with (001) orientation, so the out-of-plane direction is perpendicular to the sample surface, and manganite thin films grow epitaxially on top of the substrate. This implies that in the Θ/2Θ scan diffractogram, only peaks corresponding to the (00l) reflections will appear, and only the out-of-plane cell parameter (c) will be determined from the angular position of the peaks –no information regarding the in-plane parameters (a,b) will be extracted from the Θ/2Θ scan. To determine the correct angle Θ experimentally, we use the known positions of the intense substrate peaks reflections as reference (they can be found in databases).

Apart from the peak positions, the broadening of the peaks can also provide information. Single crystals show intense and narrow peaks, but the width of the peaks obtained for thin films depends largely on instrumental parameters and crystallinity. By comparing the integral width of a certain peak in different samples –if measured with the same instrument- we can determine which sample has grown more crystalline.

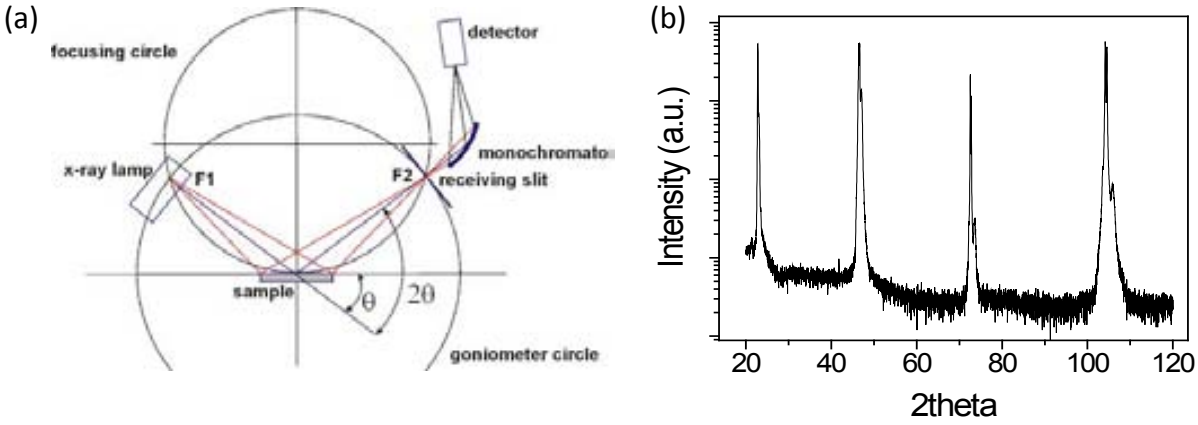

Fig A.3. (a) Θ/2Θ configuration for X-ray diffraction scans and X-ray reflectivity measurements; (b) Θ/2Θ scan of an LSMO sample grown on STO substrate.

A.4.1.2 Reciprocal space maps (Q-plots) and pole figures

The Fourier transform of the crystalline lattice is called the reciprocal lattice, and it is a mathematical construction to visualize the relationship between the real space (that is, the ordering of the atoms in the solid, forming a structure of imaginary planes) with the signal obtained from diffraction. The reciprocal space is represented on top of the real space, and its coordinates are Q_x, Q_y and Q_z, in units proportional to the inverse of real space units. The diffraction peaks are represented in the reciprocal space, in what is called "reciprocal space map", an example of which is illustrated in Fig 3.8.

At the ICMAB, we use a Bruker-AXS General Detector Diffraction System (GADDS) model D8 Advance, with a 2D detector, to carry out reciprocal space mappings. In order to do so, some angles from the goniometer must be fixed (see Fig A.4), and a scan is performed along another angle. The angle ϕ describes a rotation around the normal to

the sample surface, the angle Ψ is the deviation from the normal to the surface, the angle ω is the angle of incidence with respect to the sample surface (in the Θ/2Θ scan, ω= Θ). The detector is always set to 2Θ. Also, we define the angle $\chi=90^{O}-\psi$.

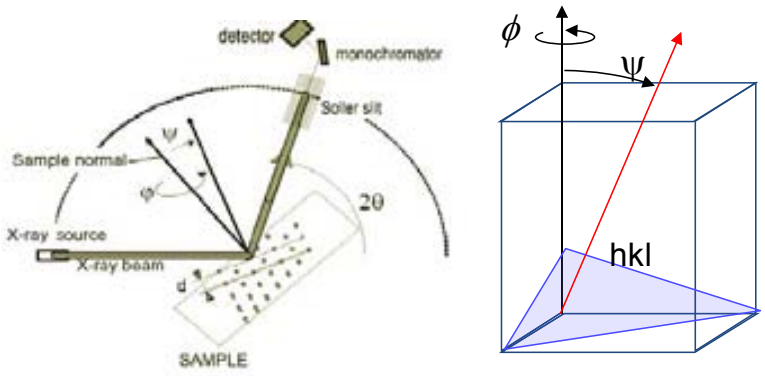

Fig A.4. Schematic representation of the Goniometer angles used to perform X-ray diffraction measurements.

The conversion from the reciprocal lattice coordinates (q_x, q_z) expressed in reciprocal lattice units (r.l.u.) (r.l.u. $= 2/\lambda$) to the measured angles is the following:

$$q_x[\text{r.l.u.}] = \frac{1}{2}(\cos\omega - \cos(2\theta - \omega))$$

$$q_z[\text{r.l.u.}] = \frac{1}{2}(\sin\omega + \sin(2\theta - \omega))$$

To extract the in-plane ($a_{\text{in-plane}}$) and out-of-plane (c) lattice parameters from the reciprocal space maps of a certain measured reflection $[h0l]$ or $[0hl]$:

$$a_{\text{in-plane}} = \frac{h}{q_{\text{in-plane}}} \text{ and } c = \frac{l}{q_z}$$

A pole figure is a representation (stereographic projection) of a ϕ scan, for a certain range of Ψ (as shown in Fig A.5). For a cubic system, the symmetry of the plane we are probing is extracted. The interest of a pole figure for different films grown on top of each other (or on top of a substrate) is to see whether the in-plane parameters of both structures follow the same crystallographic orientations or one is in-plane rotated with respect to the other.

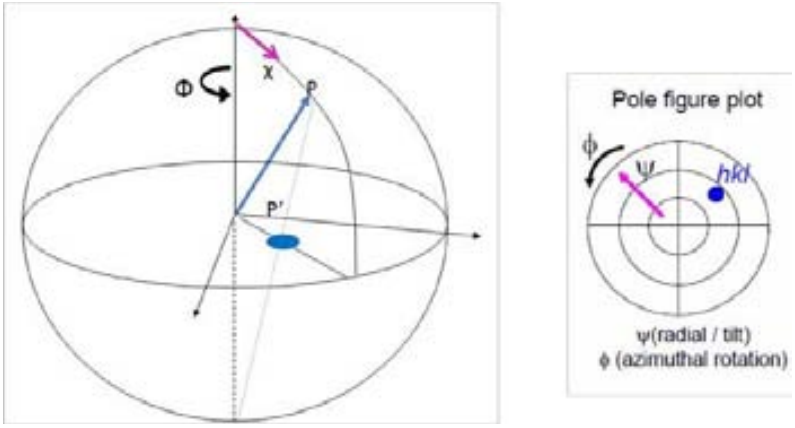

Fig A.5. Sketch of what a pole figure represents: the projection of the diffraction peak [*hkl*] is plotted.

A.4.2 X-RAY REFLECTIVITY (XRR)

The X-ray reflectivity pattern is measured in the same geometry as the Θ/2Θ scan (from section A.4.1.1) but with a much smaller angle of incidence Θ, often from 0.5 to 5°. The reflected X-ray beam at the different interfaces generates interferences due to the difference in electronic densities for each material, so oscillations in the reflectivity appear. The measurement system requires a divergence slit (parallel optics) and a beam attenuator, because when the angle is minimum the beam is practically impinging directly in to the detector. This results in a region of the reflectivity curve with a relatively constant large number of counts ("plateau", for smaller angles) and another region of steeply decreasing intensity and oscillations [3].

From an XRR curve we can extract information about the density, the roughness and the thickness of the layer (see Fig A.6). In our diffractometer Rigaku "Rotaflex" RU-200B, the information from the plateau and the critical angle (which provide the film density) are not reliable due to inevitable inaccurate positioning of the sample. We can, however, calculate its thickness from the periodicity of the oscillations.

i. CALCULATION OF FILM THICKNESS

For most films, the thickness d can be calculated through the periodicity of the oscillations:

$$\sin^2\theta_n = \sin^2\theta_P + n^2\left(\frac{\lambda}{2d}\right)^2$$

Where θ_n corresponds to the maxima of the reflected intensity, θ_P is the lowest angle for which there is detection, n is the order of the peak and λ is the wavelength of the incident radiation.

For ultrathin films or films with extremely rough surfaces, the intensity may decrease so fast that we are unable to calculate the periodicity of the oscillations or to distinguish the signal from the backgrown.

For heterostructures of more than one film, determining the thickness of each film can be an extremely difficult task and simulation methods may be required.

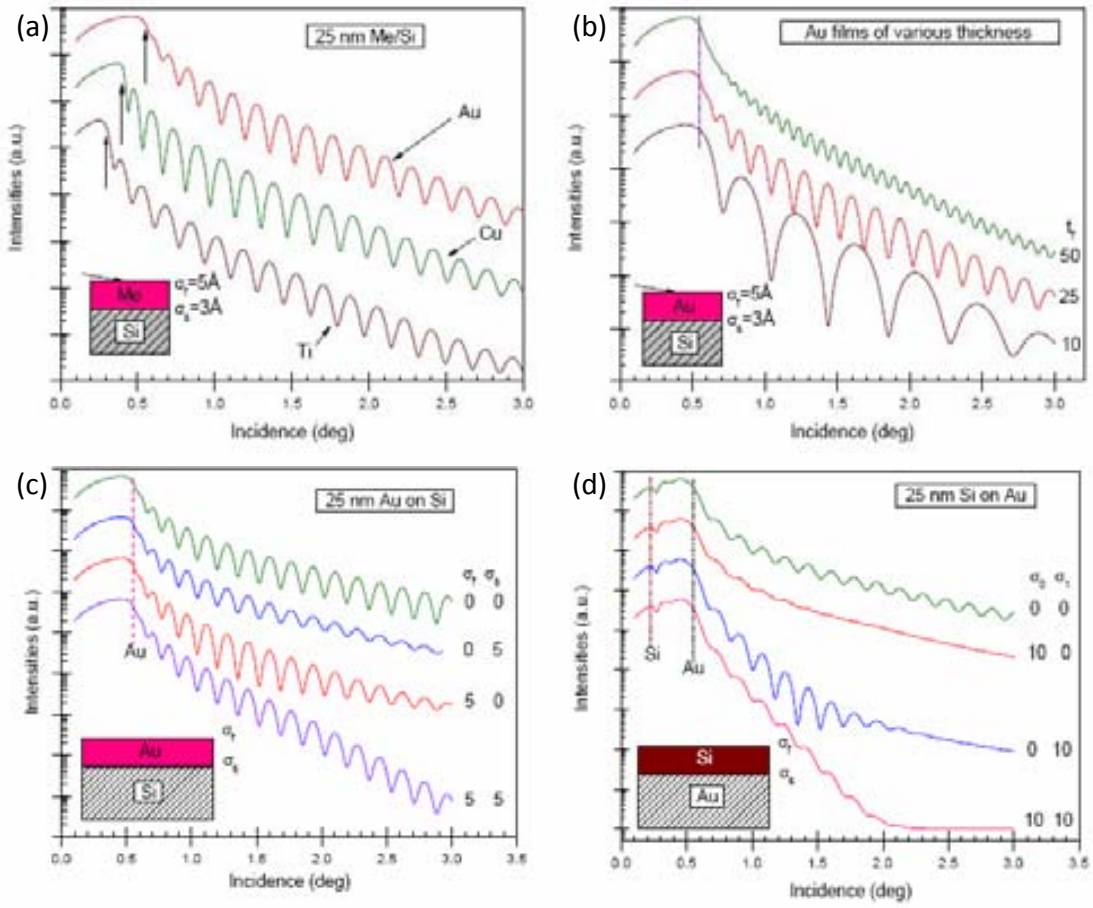

Fig A.6. Reflectivity curves for (a) different metals grown on Si, each metal having different density; (b) different thicknesses of Au grown on Si; (c) Au grown on Si, for different surface roughness for the substrate and film (σ_s and σ_f).; (d) Si grown on Au, for different surface roughness for the substrate and film (σ_s and σ_f). Images taken from [4].

A.4.3 X-RAY PHOTOELECTRON SPECTROSCOPY (XPS)

X-ray photoelectron spectroscopy, also known as XPS, relies on the photoelectric effect to extract information about the composition of a sample. A highly energetic photon interacts with matter, removing an electron from an atomic orbital or from a band and giving it enough energy to reach the vacuum level. The excitation energy ($h\nu$) must be large enough for the electrons to overcome the work function of the solid (W_f), so the following energy conservation equation must be obeyed:

$$h\nu = E_B + W_f + E_{kin}$$

where E_B is the binding energy (BE) relative to the Fermi level and E_{kin} is the kinetic energy of the photoelectron. A sketch of the process can be seen in Fig A.7.

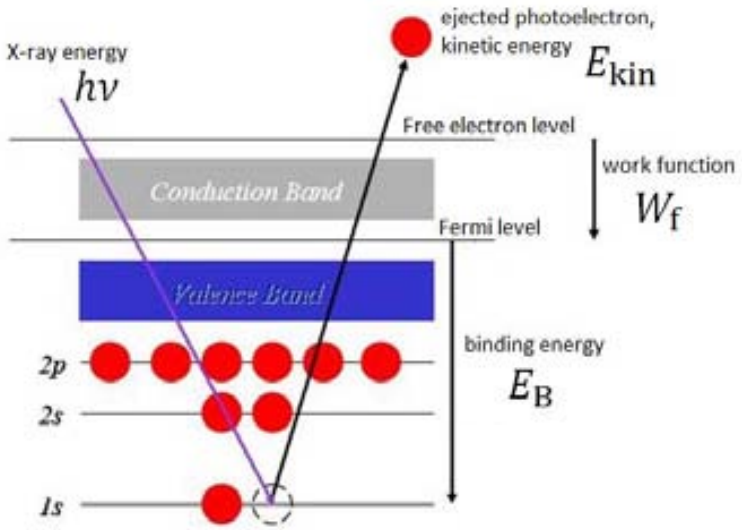

Fig A.7. Sketch of the photoelectron emission process. Image taken from [5].

At the XPS from the *Serveis Científicotècnics* at the *Universitat de Barcelona* and from *Institut Català de Nanociència i Nanotecnologia (ICN2)*, X-rays are generated either with an Al or an Ag anode source, giving energies of 1486 eV and 2984.2 eV, respectively. The photons go through a monochromator and interact with the sample, ejecting photoelectrons which are collected as a function of their kinetic energy.

Photoemission spectroscopy is suitable for surface analysis, because most of the detected photoelectrons originate from the first 2-10 nm of the sample (electrons of kinetic energies around 50-100 eV have mean free paths of a few Å). It is also sensitive to the chemical enviroment (the type of bonding, the oxidation state or the possible presence of adsorbates), resulting in peak-shifts or peak-shape changes [6].

Using angular-resolved XPS, impinging on the sample from different angles with respect to the normal to its surface, can probe different compositions for different penetration depths. We can even sputter in-situ with noble gas ions (such as Ar^+), to clean the sample or even remove some layers, thereby probing more deeply into the sample.

An XPS spectrum plots the amount of detected electrons (intensity) as a function of their binding energy (BE). What we really measure is the kinetic energy of the electrons, but the conversion is done with the simple formula from Fig A.7. W_f is not directly the workfunction of the solid, but depends also on the equipment used, and is calibrated by setting the Fermi level step of an Ag sample to zero. As can be seen in Fig A.8, an XPS spectrum can provide information about different origins of the electrons [7]:

a) Core levels emission
b) Auger processes
c) Valence band emission

d) Secondary electron excitation, or electrons that have lost energy by inelastic scattering before escaping the surface.

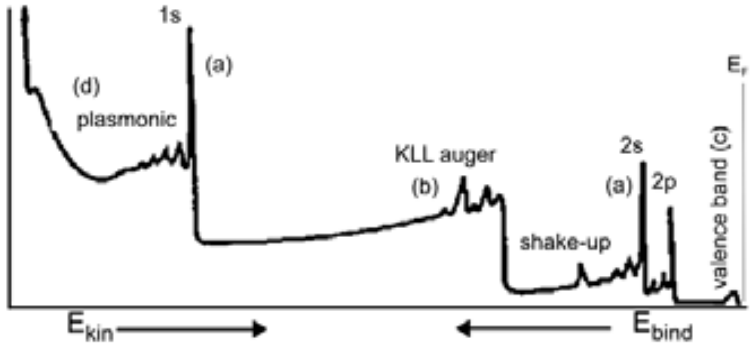

Fig A.8. Sketch of an XPS overview spectrum, with the different origins of the detected electrons. Image taken from [7].

A.4.4 ATOMIC FORCE MICROSCOPY (AFM)

Atomic Force Microscopy is also a powerful technique to characterize sample surfaces (surface topography, phase, resistivity,…) with atomic and molecular resolution, whether they are conductive or not, with a surface resolution from 1-100 μm (depending on the surface roughness or the material hardness) and a sub-nanometer resolution for z axis.

It consists in an extremely sharp tip (less than 10 nm in diameter) held at the end of a cantilever. Fig A.9a shows a sketch of the process. The tip is approached to a sample -until it is in contact or extremely close to its surface- and scans it to obtain information about its surface. As the name suggests, the physical mechanism involved is the interacting forces between the sample and the tip. The main one is the interatomic "van der Waals force" (see Fig A.9b), dependent on the distance between the atoms. When the tip is sufficiently far from the sample, it has a certain free oscillation amplitude and resonance frequency; when we engage the tip to the sample, the oscillation amplitude, phase and resonance frequency are modified due to the interactions between the sample and the tip. Other forces are also present besides de Van der Waals force: capillary force caused by build-up of water on the tip and force caused by the cantilever itself (like a compressed spring).

The tip is installed at the end of a cantilever that deflects (bends positive or negatively) according to the forces exerted on the tip. We use the laser reflection on the back side of the cantilever and a photodiode to detect and analyze the cantilever deflections. The cantilever is moved closer or further from the sample with a piezoelectric actuator.

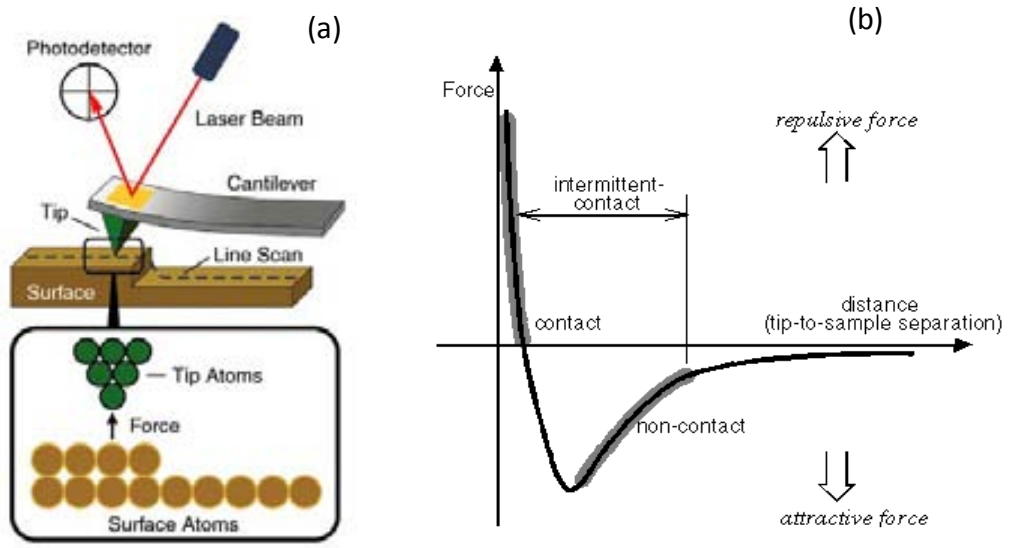

Fig A.9. (a) Sketch of working principle of Atomic Force Microscopy, taken from [8]; (b) sketch of van der Waals Force dependence on tip-to-sample separation distance.

Depending on the distance between the tip and the sample, AFM can be used in three different modes: the contact mode, the non-contact mode and the intermitent contact mode, each of which offers different advantages and drawbacks [8]; depending on the sample, different modes are recommended.

Contact mode (sample and tip are very close together, so that the exerted force between both is repulsive): the tip makes soft "physical contact" with the surface. The force acting on the tip is given by Hook's law: $F = -k \times \Delta x$, where Δx is the deflection of the cantilever. Constant-height mode (fixed height of the tip) or constant-force mode (fixed cantilever deflection) can also be used, and atomic resolution may be achieved. In order to avoid problems caused by capillary forces, the sample and the tip can be immersed in a liquid.

Non-contact mode: the tip is oscillating, but not touching the sample, in the attractive force regime. The forces are small, but changes in the resonant frequency and amplitude of the cantilever can be measured.

Tapping or "intermitent contact" mode: the tip oscillates (near its resonance frequency) between the attractive and the repulsive regime. Very stiff cantilevers ($30 - 50$ N/m) are used to avoid the tip getting stuck in the water contamination layer. Its main advantage is an improved lateral resolution for soft samples because dragging forces –present in the contact mode- are completely eliminated.

This last (tapping) mode has been the most used during this thesis. The amplitude of the oscillation is fixed to a "setpoint" (the lower the setpoint, the more the tip presses the sample). As the tip scans the sample, this amplitude is slightly altered. From a feedback loop, whose sensitivity is determined by the "proportional or integral gain", the system

is continuously moving the piezo to adjust the height z so that the amplitude can be maintained constant.

The same system may probe the twist of the cantilever, or the phase shift of the cantilever relative to the driving signal, to provide qualitative information about the changes in friction, adhesion and viscoelasticity of the sample surface. Quantitative measurements that can be extracted from AFM images comprise distance measurements, surface roughness and peak-to-valley measurements. As we are scanning in a certain pendulum-like manner, a second-order correction of the raw image becomes necessary. A good knowledge of the AFM system and the sample is certainly helpful to avoid artifacts or misrepresentations in an AFM image:

- Parameters such as gain, set point and scan speed must also be optimized, as they can greatly influence the quality of the image or may even damage the sample! For exemple, insufficient pressure exerted on the surface may result in blurred images caused by the tip not following the surface; on the other hand, too much pressure may alter the surface properties of the sample.
- Broken or worn down tips tend to give convolution of the tip contact surface with the real motifs, therefore displaying unreal patterns. Unclean samples also give a lot of problems due to the dragging of dirt by the tip, for example.
- Some AFM equippments are extremely sensitive to ambient noise (acoustic and electric), which can be discriminated as it gives rise to random placed peaks or lines of peaks on one scan but not the other.

At the ICMAB and during this thesis, images have been taken with various AFM equipments: 5100 SPM system from Agilent Technologies, Cervantes SPM system from Nanotec Electronica and Asylum MFP3D from Oxford Instruments.

A.4.5 ELECTRON MICROSCOPY

Visible-light microscopy has a limited resolution of a few hundred nm imposed by the wavelength of light (corresponding to a useful magnification of 1000-2000). As any particle possessing a moment p has an associated wavelength, far shorter wavelength than that of visible light can be achieved by accelerating electrons into a high energy beam. From a 20 kV gun, for example, we achieve a wavelength of 0.6 Å, therefore (theoretically) providing a resolution limit of 0.3 Å. The magnification is up to 2 million times! As the atoms have sizes around 2-3 Å, electron microscopy is an interesting tool to resolve structures at the atomic level.

There are two different electron microscopes, the Scanning Electron Microscope (SEM) and the Transmission Electron Microscope (TEM). Both the SEM and the TEM are equipped with an electron beam gun, electromagnetic lenses (which must be corrected for aberrations such as stigmatism) and detectors. As electrons interact with matter and we are interested in detecting the interactions with the sample, electron microscopy generally requires a certain degree of vacuum environment.

A.4.5.1 SCANNING ELECTRON MICROSCOPY (SEM)

Scanning Electron Microscope images the sample surface by scanning it with a high-energy beam of electrons (up to 30 kV). From the interaction of the electrons from the beam with the atoms that make up the sample, we collect information about the sample's surface topography and composition, among others.

Different detectors inserted in the SEM chamber probe different types of interactions [9], their signal providing different information depending on their origin (a schematic representation of the probing depth of each signal can be found in Fig A.10). Here we introduce the three most important for our purposes:

- **secondary electrons (SE):** electrons from the direct beam scatter inelastically with electrons from the sample surface. We detect these electrons ejected from the sample; they possess low energy (<50 eV) and receive the name of "secondary electrons". Their signal provides information about topography. As the electron beam is very narrow, it provides large depth of field, resulting in a 3-D image of the surface structure.
- **backscattered electrons (BSE):** beam electrons are reflected from the sample by elastic scattering. The intensity of the BSE signal is strongly related to the atomic number (Z) of the specimen, thus providing information about the distribution of different elements in the sample (atomic contrast), besides topography. If there is no important chemical or topographical contrast, the signal we collect may provide information about crystallographic structure (for example, twinning in the film [10]), through a process called channelling.
- **characteristic X-rays** (their detection is called Energy Dispersive X-ray analysis or EDAX): characteristic X-rays are emitted when the electron beam removes an inner shell electron from the sample, causing a higher energy electron to fill the shell and release energy. Therefore, it can be used to identify the composition and to measure the abundance of elements in the sample.

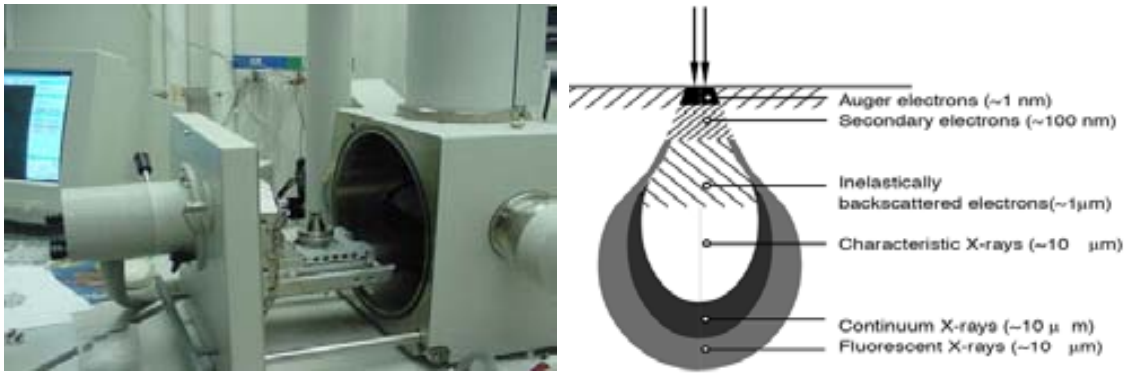

Fig A.10. Scanning electron microscope (SEM) image, together with a schematic representation of the electron-sample interaction, where we can see the depth of the origin of the detected signals. Image taken from [11].

At the ICMAB, we have a FEI Quanta 200 FEG scanning electron microscope, equipped with an EDAX microanalysis system and also a lithography system Elphy

Plus 3.2 (Raith) with a b eam b lanker. T he be am bl anker may d eflect t he b eam o f electrons in order not to expose a certain part of the sample to the electron beam, which will enable us to use the SEM to do electron beam lithography (process explained in section A.7.1).

A.4.5.2 TRANSMISSON ELECTRON MICROSCOPY (TEM)

Transmission E lectron Microscopy uses a b eam o f el ectrons accelerated t ypically t o 200 kV in order to image an extremely thin sample by transmission. The electrons go through t he s ample a nd a tomic r esolution is a chieved. The ma in limi tation is th e complexity of t he sample preparation procedure, to t hin dow n t o l ower t hat 100 nm (below 20 nm f or hi gh r esolution imaging), and th e f act th at it is d estructive. It is important to note that artifacts are inherent to any preparation method. Generally, there are two different types of specimen configurations for imaging heterostructures or thin films by TEM: the cross-section and the planar view, depending if we want to image perpendicular or parallel to the out-of-plane direction.

A **plan-view** is cut parallel to the sample surface (perpendicular to the *00l* planes), the thickness is reduced and a hole with non vertical walls is etched in order to create a wedge (see left hand sketch in Fig A.11). The thinnest part of the wedge is the one that can be imaged by TEM.

A **cross-section** consists in an extremely thin slice of the sample cut in the direction perpendicular to the substrate plane. The most common preparation consists in cutting two slices of the sample and joining them by the surface. After that, the joint slice's thickness is reduced as much as possible (see right hand sketch in Fig A.11). The substrate and different layers of the sample are resolved, and information is extracted about the quality of the interfaces, the in-plane and out-of-plane crystallographic /lattice parameters, the defects in the film, etc.

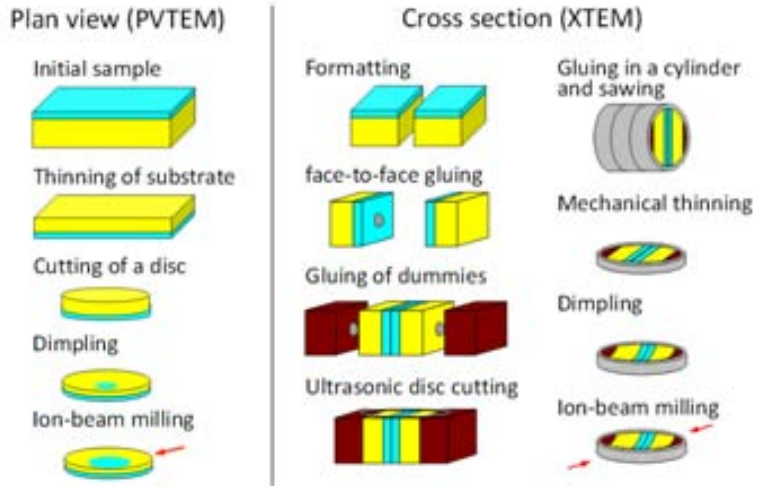

Fig A.11. Sketch of the preparation process of a plan view and cross section to be imaged by TEM. Figure taken from [12].

If we need to probe a very small, specific region of the sample, a focused ion beam (FIB) is used to cut the very small cross-section slice of sample directly, without distroying the rest of the sample. The advantage is that it is equipped with an electron gun (like in a SEM), so that we can image in-situ the part we are cutting with the ion beam. However, the ion beam used is of Ga ions and a common problem is Ga ions are often implantated on the sample, so modifying the original properties.

Depending on the physical process we are detecting, there exist two different TEM imaging modes (depending on the detector used): **Bright Field** (the collected intensity comes from the transmitted beam), and **Dark Field** (the intensity comes from the diffracted beam).

In this work, HAADF-STEM nanocharacterization of heterostructures was carried out in a probe-corrected FEI Titan 60-300 operated at 300 kV with a probe size below 1 Å. STEM, which stands for Scanning Transmission Electron Microscopy, consists in scanning a beam of electrons, focalized in a small spot on the sample, and the transmitted beam is collected. The used mode was High Angle Annular Dark field (HAADF), which means that the beam diffracted at high angle is collected.

We also used "Energy filtered transmission electron microscopy" (EFTEM), in which only electrons with a particular kinetic energy are used to form the image, which is therefore element-sensitive.

A.5 MAGNETIC CHARACTERIZATION

The magnetic measurements performed using the Superconducting Quantum Interference Device (or SQUID) provide information about the magnetic properties of the whole sample. More localized techniques exist for studying magnetic domains or specific regions of the sample, such as MO KE –MagnetoOptical Kerr Effect- or synchrotron radiation spectroscopy, such as X-ray Linear Magnetic Dichroism (XLD) and X-ray Circular Magnetic Dichroism (XCMD).

A.5.1 SUPERCONDUCTING QUANTUM INTERFERENCE DEVICE (SQUID)

The MPMS (or Magnetic Property Measurement System) is a magnetometer whose detection system is based on a superconducting quantum interference device allowing the magnetic characterization of small samples, at variable temperature (from 2 K to 400 K) and magnetic fields up to 7 T. It consists of a set of superconducting detection coils wound clockwise and anti-clockwise as indicated in Fig A.12(a) integrated in a flux transformer inductively coupled with a superconducting ring with two Josephson junctions. The sample is made to oscillate inside the detection coils thus modifying the magnetic flux through the coils, generating currents. This small change in current is detected through the superconducting ring and then is amplified and converted into a measurable voltage signal proportional to the magnetic signal of the sample.

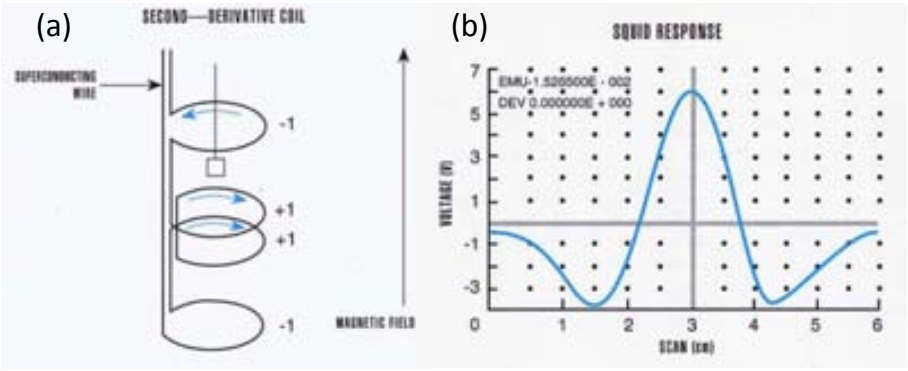

Fig A.12. (a) Squematic representation of the superconducting coils that detect the flux variation, the sample is made to vibrate inside the coils, following the magnetic field direction; (b) Squid response as the sample goes through the first coil (first voltage minima), the double coil (voltage maxima) and the last coil (the other voltage minima).

In Fig A.12(b) the typical SQUID voltage response is shown, it is used to center the sample before starting the measurements. The noise contribution is reduced and the sensitivity of the measurements can reach 5×10^{-7} emu. For a more complete explanation of the physical origin of this effect, we refer the reader to [13].

An interesting fact is that the magnetic flux produced by a sample is typically of the order of 100-1000 flux quanta, whilst the Earth magnetic field on a square cm is around 2 million flux quanta! It is therefore necessary to isolate the magnetic field created inside the MPMS and to stabilize the magnetic field present at the laboratory. The big cryostat in which the SQUID resides is therefore also used as magnetic shield [14].

At the ICMAB, we have used a Quantum Design MPMS-XL, and the most common measurements are the magnetization vs temperature, M(T), and the hysteresis cycle, M(H).

A.5.1.1 M(T) AND ZFC-FC

The M(T) is the measurement of the magnetic moment as a function of temperature, for a fixed applied magnetic field. From the $M(T)$ curve, like the one in Fig A.13(a), we obtain the saturation magnetization (M_{sat}, usually expressed in emu) and the Curie Temperature (T_C), which we take to be the interpolation of the final slope as it crosses the zero magnetization. The instrinsic property of the material is the magnetic moment, typically measured in emu/gr or emu/cm^3.

Another kind of M(T) measurement is the zero-field-cooled field-cooled (ZFC-FC) process. The process consist on cooling the sample down to low temperature in zero applied field and once the low temperature value is stable, the desired magnetic field is applied and the ZFC branch is measured while increasing temperature. After reaching the high temperature value, the sample is cooled down once more keeping the same magnetic field. After reaching the low temperature value again the FC branch is measured while increasing temperature.

A.5.1.2 MAGNETIZATION CURVE M(H):

M(H) is the measurement of the magnetization of the sample while sweeping the magnetic field from positive high magnetic field to high negative magnetic field and back to positive fields, for a fixed temperature. Ferromagnetic samples display hysteretic behavior, so the curve receives the name of "hysteresis cycle". In Fig A.13(b) we show an example of the hysteresis cycle of LSMO at 10 K and 300 K, where we see that the coercive field (H_C) and the saturation magnetization (M_{sat}) depend on temperature. The diamagnetic contribution of substrates (like in the case of $SrTiO_3$) must also be taken into account.

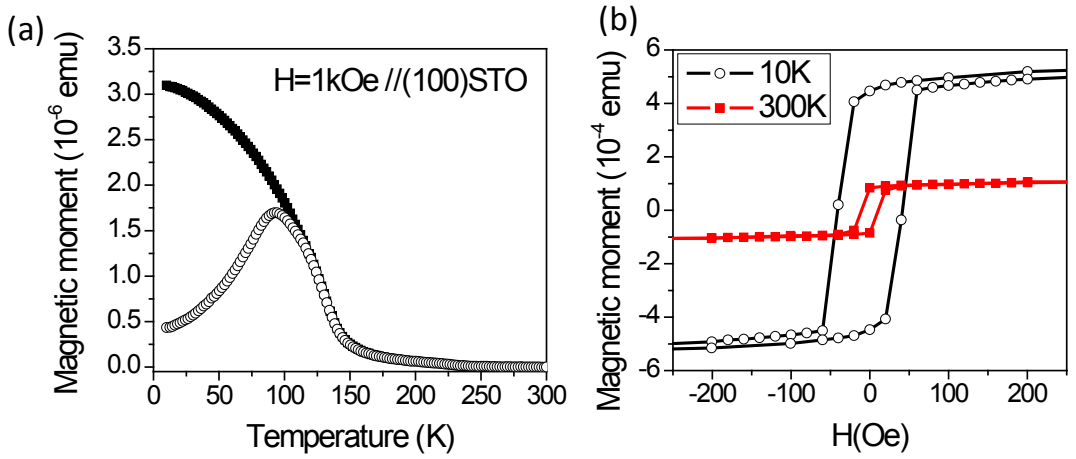

Fig A.13. (a) Magnetization *vs.* temperature curve (zero-field cooled curve in open round symbols and field cooled curve in black squares) for a low-T_C sample of La_2CoMnO_6. We determine that the Curie Temperature is slightly around 150 K by interpolating the steep slope when the magnetization decays; (b) Hysteresis cycle for an LSMO/MgO/Pt heterostructure. Only LSMO contributes to the magnetization, and we can see that the magnetization and coercive field are importantly reduced at room temperature, because the Curie temperature is not far above 300 K.

A.6 ELECTRICAL CHARACTERIZATION

To probe the transport properties, electrical characterization has been done using Keithley multimeters. We used a 4-point probe station for room temperature measurements with no applied magnetic field, and a Physical Properties Measurement System (PPMS) from Quantum Design to lower the temperature and apply a magnetic field, using the external operation mode and a Keithley multimeter also for the measurements.

The Keithley multimeter enables the control either by voltage or by current. We generally use the voltage control, and read the outcoming current. An excessive density of current flowing through a sample (or a nanostructure) may damage the sample, because of Joule heating; the sample gets burnt when the power is too large. As power is the product of current and voltage, we limit the current as a safety measure. We set a maximum value of current (called "compliance"), that the multimeter will not exceed. If the voltage we want to apply to a certain sample is such that the current needed is larger

than the compliance, the multimeter will automatically adjust the voltage so that the current does not exceed the compliance limit.

For extremely sensitive devices, such as magnetic tunnel junctions, an extra precaution is needed: we use an antistatic bracelet from the moment when we connect the sample to the moment when we finish our measurements, to avoid discharging possible static electricity to the sample.

We can use two basic measurement configurations: 2-point measurements or 4-point measurements. In the case of the 2-point measurement, current goes from one contact to a second one, and the voltage drop between the same two contacts is measured. In the case of the 4-point measurement, four contacts are involved: current flows between contacts 1 and 2, and the voltage drop between contacts 3 and 4 is measured, so the measured resistance has no contribution from the cables and contact resistances.

A.6.1 4-POINT PROBE STATION

The fastest and most flexible way to perform transport measurements is by using the Keithley multimeter in a 4-point probe station. This consists in the positioning of direct tips (needles) on the sample contacts, with the help of a magnifying glass, so that no wiring to an external sample holder is required. These needles are connected to the Keithley so that current vs voltage $-I(V)$- curves can be easily carried out. The main drawback, however, is that the tests are limited to room temperature and no applied magnetic field.

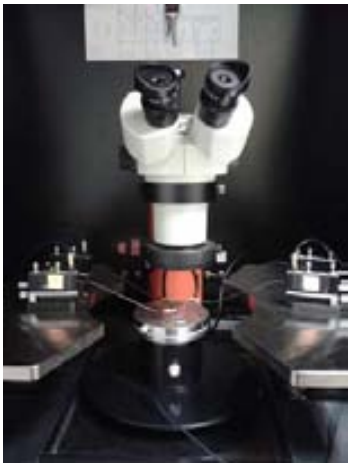

Fig A.14. Photo of the 4-probe station. Four needles are used to contact the sample and perform transport measurements.

A.6.2 PHYSICAL PROPERTIES MEASUREMENT SYSTEM (PPMS)

The PPMS is a variable temperature-magnetic field system designed to perform different automated measurements. The sample is mounted on a sample holder, called "puck", and introduced inside a chamber which incorporates a magnet, the temperature control and the sample puck connector. The whole system is mounted inside a liquid He

cryostat that in some cases may incorporate an insulating liquid N chamber to reduce He consumption.

The system incorporates a superconducting coil allowing the application of magnetic fields as high as ± 90 kOe in the center of the sample chamber and a variable temperature system that allows a precise control of the temperature of the sample between 1.9 K and 350 K. A thermometer set close to the sample reads the system temperature. The temperature can be swept very fast, but we use a maximum cooling or heating rate of 5 K/min in order not to damage the contacts done with silver paint.

Fig A.15. Photo of the Physical Properties Measurement System (PPMS) at the ICMAB, configured to use the external Keithley as source.

The most interesting part of the PPMS is the mounting of the sample. Contacts must be made from the sample to the sample holder or puck (as in Fig A.16(right)). The puck is mounted onto a 12-pin connector inside the PPMS chamber, pre-wired to the system electronics (Fig A.16(left)). Then, the sample is ready to be measured, and can be rotated to change the magnetic field orientation with respect to the sample surface (from an in-plane configuration to an out-of-field configuration). The great advantage is that the puck can be removed easily or mounted back again without manipulation of contacts on the sample.

Fig A.16. Sketch of the mounting of the sample puck inside the Physical Properties measurement system and photo of a 5x5mm^2 sample with hand-made contacts mounted on a puck.

At the ICMAB, we have a Quantum Design PPMS, which is specially configured to measure electro-transport applications (to measure in "AC transport" and "resistivity" modes). This means that each pin of the puck has a specific function.

However, for most of our transport measurements, to have more flexibility, we use an external Keithley as source and only the temperature and magnetic field control of the PPMS. Of course, we also take advantage of the mounting of the sample in a puck. This enables us to probe more devices just by modifying the external connections.

A.6.2.1 PPMS LIMITATIONS: MAGNETIC FIELD SWEEPING RATE AND REMANENCE OF THE SUPERCONDUCTING RING

The rate of the magnetic field sweeping must be controlled, as fast sweeping can lead to non-reliable switching field values. Fig A.17a shows magnetoresistance measurements of the same junction performed at different H-sweeping rates. The combination of two different sweeping rates was also tested: fast sweeping for high H and slow sweeping for low H. This causes a "jump" to be seen in the MR data (close to ± 100 Oe in Fig A.17a, where the resistance at a fixed applied magnetic field appears multivalued) but does not alter the switching field values (see that the low-field MR is the same for rate 20 Oe/s and that of 20 Oe/s+200 Oe/s).

Hall probe measurements, depicted in Fig A.17b, confirm the inadequacy of the fast sweeping rates in the determination of precise H values. The hall probe resistance – whose value is proportional to the magnetic field, so acts as a sensor- is plotted as a function of the magnetic field value estabished by the PPMS equipment. The multivaluation of the hall probe resistance for a same nominal H value at high sweeping rates (for example, 200 Oe) indicates a certain delay in the PPMS H determination, which introduces an error of 60 Oe in the magnetic field value given by the PPMS. However, for low sweeping rates, the Hall probe resistance is found to be proportional to the nominal H given by the PPMS, so H values are reliable for such sweeping rates (10 Oe/s). The optimal configuration has been established as a combination of sweeping rates of ±200 Oe/s for large H and ±10 Oe/s for small H.

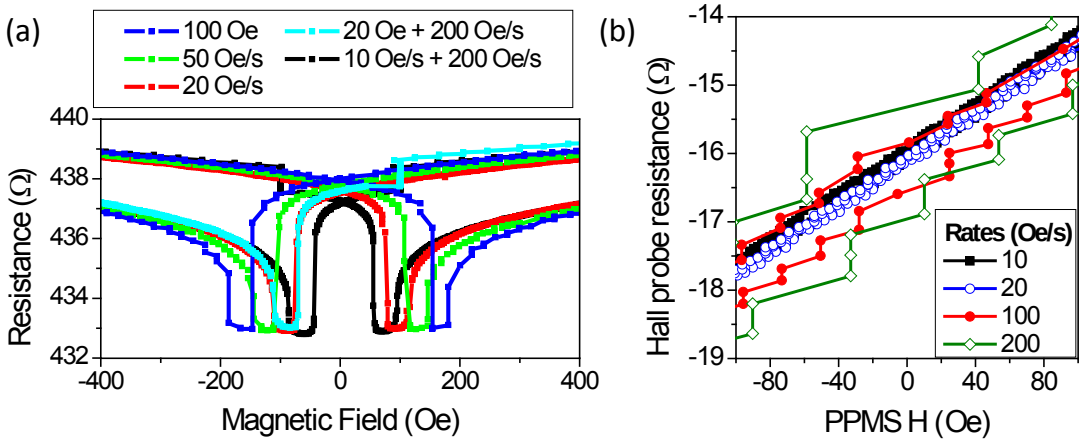

Fig A.17. Effect of the H sweeping rate: (a) R(H) measured at different magnetic field sweeping rates for an Fe/MgO(2.4 nm)/LSMO MTJ (V=150 mV, T=120 K); (b) Hall probe resistance measured at different sweeping rates (from 10 to 200 Oe/s).

Another aspect that we must take into account is that as the PPMS uses a superconducting coil, after application of a high magnetic field, vortices may remain inside the coil, yielding slightly shifted magnetic field values. The value of this shift depends on the magnetic history of the superconducting coil, so the maximum magnetic field applied is relevant. For small magnetic fields, the remanent magnetic field is practically zero, but this is not the case for large magnetic fields, where the remanent H may reach ±50 Oe. In the R(H) measurements, this may be reflected in an off-centering of the switching with respect to H=0. In some cases, large magnetic fields may be required to saturate the sample and favour the switching of all domains.

A.6.2.2 Electrical contacts

In order to make the electrical contacts directly on the sample, either wirebonding or handmade silver paint contacts are made, depending on the sensitivity of the device.

A.6.2.2.1 Wirebonding

Fast and clean, the wirebonding method is extremely useful when the sizes of the contacts are small. For the wedge bonding process, we approach an aluminum wire to the surface of the first contact and use ultrasounds to melt the wire and weld it on the surface. The process is repeated for the second contact and the wire is cut.

An important limitation of this method arises when the structures are too sensitive: the ultrasonic process may perforate a very thin layer of material, for example. In the case of magnetic tunnel junctions, as they are quite sensitive, we will avoid this method in order to prevent its being damaged.

A.6.2.2.2 Handmade

The contacts are done by carefully manually applying a silver paint droplet on top of the contact and the wire. If the sizes are very small, as is often the case, this task becomes very complicated and requires a lot of manual precision, because silver paint either dries

relatively quickly or, if it is too liquid, may extend too much and create too big a contact.

The main disadvantage of handmade contacts is the technical difficulty of the procedure but also the fact that if the quality of the contact is not very good, a change of temperature may result in the detaching of the wire from the contact.

A.7 PATTERNING TECHNIQUES

Micro or nanostructures can be created using the top down approach by combining the use of UV and e-beam lithography with deposition and etchings. Patterns can also be created by depositing through a physical mask (to that effect, a shadow mask was fabricated in section 5.2.2 to facilitate the deposition of contacts). In this section, we describe the lithographic process and some etching techniques used for this work.

A.7.1 LITHOGRAPHIC PROCESS

A lithographic process consists in transfering a pattern onto a resist on top of the sample. There are three basic steps in order to do that: (1) First, the deposition of a thin film of resist on top of the sample surface by spinning; (2) next, the exposure of the resist (with electrons or light) to modify the properties of the resist at certain locations according to a desired pattern; (3) finally, developing the resist, which means that the exposed resist dissolves (in the case of positive resists), and the pattern that had been exposed has been transferred to the resist.

If the exposure is done with photons (UV light), the process is called "photolithography", whilst if it is done with electrons, it is "electron beam lithography" (EBL).

In this section we will comment on the three different steps of the lithographic process, for photolithography and electron beam lithography, mentioning the relevant parameters for a good transfer of the pattern.

(1) Resist and its deposition by spin coating:

The word photoresist comes from "photo-sensitive" and "acid-resistant", two properties that resin used for photolithography must have to be patterned and to stand acid etch for patterned etching. In the case of EBL, the only difference is that the chosen resist must be sensitive to electrons instead of light. Other requirements for both processes such as thermal stability, easy removal, resolution or adhesion must also be met [15].

There are two types of resists, with regards to the effect the exposure has on them. For positive resists, the exposed regions are the ones that disolve faster during the developing step, while for negative resists it is the contrary, and the developed regions are less soluble in the developer solution. The most used resists are positive:

the most popular electron-sensitive ones are PMMA (Polymethyl methacrylate) and MMA (methyl me thacrylate), which b asically differ in th e h igher s ensitivity o f MMA (see section 5.2.1 for an example of their combined use). The photoresist we use is Microposit S1813 photoresist from Shipley.

The deposition of the resist is done by spin coating: a drop of the resin is deposited on a f lat s ample, w hich i s r otated i n or der t o s pread t he de posited f luid b y centrifugal force. With this, we obtain a thin coating on t he sample. The machine used i n t his pr ocess i s c alled s pinner (see Fig A.18(a)) and de pending on t he parameters involved i n t he pr ocess (spin ve locity, acceleration a nd t ime) a nd t he deposited substance, the thickness of the coating film can be controlled [16].

The equipment used in this thesis was mostly a spinner SMA AC 6000 from SMA (Suministro de Materiales y Asistencia) at ICMAB clean room facilities.

Fig A.18. (a) Photo of the machine used for spin coating (called “spinner”); (b) Sketch of the spin coating procedure used as a first step in the lithographic process.

The parameters used for spinning the resist are indicated in Table A.1. The soft bake is us ed t o r educe t he r emaining s olvent c oncentration (which i mproves adhesion, avoids mask contamination and prevents the dissolution of the first resist layer in a multiple coating process, among other desirable effects).

Table A.1. Wet etching recipe and parameters for Si etch using KOH solution at 60 ºC.

Resist	Spin speed (rpm)	Spin acceleration (rpm/s)	Soft bake
Photoresist	5	7500	1’ at 95 ºC
Electron-beam-sensitive resist (PMMA)	3.5	1500	1’ at 180 ºC

(2) Exposure of the photoresist

The resist-coated sample is then exposed with light (photolithography) or electrons (EBL) forming a certain pattern.

In t he case o f E BL, a b eam o f el ectrons i s r aster-scanned on t op of t he s ample, deflected in the regions we do not want exposed. The parameters we can control are the dot size of the electron beam and the dose (the amount of electrons reaching the sample). T he m ain a dvantage of t his m ethod i s t he e xtremely hi gh r esolution w e achieve and t he m ain ch allenge arises if we ne ed to a lign t he de sired p attern w ith other m otifs o r r egions t hat m ay already exist i n t he s ample, b ecause we can not

visualize the sample in the SEM without at least slightly exposing the resist. For precise alignment, some marks must be carefully designed.

In the case of photolithography, the resolution is around 1 μm and two methods are available; using either a UV-lamp and an optical mask or using a microwriter.

- **UV-lamp method**: we must align a Cromium mask with the sample and then expose with a UV-lamp during a certain amount of time, which will determine the dose. The main advantage of this method is that the whole sample is exposed at once, so it is really fast (less than one minute) once the alignment has been done. However, an optical mask for each different pattern is required.
- **Microwriter method:** focused lasers are raster-scanned on top of the sample, exposing the desired regions. The main advantage is the versatility of the method (we can quickly design a different pattern each time using the corresponding software) but, on the other hand, the exposure is extremely time-consuming. To align the pattern to an already existing pattern on the sample we use a laser of different wavelength (not UV) that does not expose the photoresist. In this thesis, a MicroWriter of LOT-Oriel Group Company located in the ICMAB clean room has been used. The exposure can be done with two different-sized lasers: one with spot 1 μm and the other with spot 5 μm, depending on the resolution of the pattern we need. We can even combine the use of both to optimize time and resolution of the pattern.

The main parameters we have to control during the exposure of a lithographic process are the dose, and in the case of EBL and MicroWriter, also the spot size.

Dose:

The required dose depends on the material underneath the resist, the thickness of the resist (which may be inhomogeneous, specially for a square sample) and the size of the patterned element. The resin profile depends on the dose and the developing (see Fig A.19). The correct dose and correct developing time leads to a vertical wall profile.

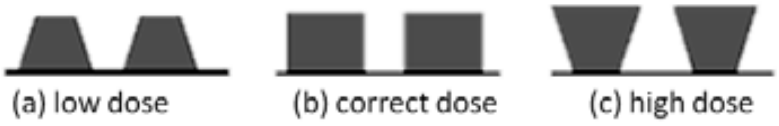

Fig A.19. Sketch of resin profiles after different exposition doses and developing.

The necessary dose also depends on the size of the element we want to lithographiate. For smaller details, the required dose is less than for larger ones. The proximity effect is also worth taking into account. This effect limits the minimum spacing between small features in the lithography, because electrons from the exposure of an adjacent region unavoidably come into contact with the already exposed region, reducing the contrast and enlarging the feature. Secondary electrons

leaving the surface and penetrating the resist from below also contribute to the proximity effect.

(3) Developing

The developing solution is used to remove the exposed resina (for positive resists), thereby completing the process of transfering the pattern to the resist on the sample surface.

The used developer solution is Microproposit MF-319 from Shipley for the photoresist and the sample is soaked in the solution for 45 s, as specified by the manufacturer. For the PMMA and MMA resists, we develop with a solution of MIBK:IPA 1:3 for 50 s and rinse for 30 s in a stopper solution (IPA) [17].

A.7.2 ETCHING TECHNIQUES

Different etching techniques have been carried out during this work: Reactive Ion Etching (RIE) and Ion Beam Etching (IBE), which include a physical process, and Wet Etching, which is an exclusively chemical process.

A.7.2.1 REACTIVE ION ETCHING (RIE)

This technique is used to etch straight-walled and flat-bottomed holes in substrates. The sample is introduced inside a chamber and plasma of a certain gas is created on top. The gas is ionized and its ions are accelerated by an electric field towards the substrate surface. When the ions collide with the sample they react chemically, and due to the fact that the electric field is perpendicular to the sample, the etch profiles are highly anisotropic (see Fig A.20).

The etch conditions in RIE systems depend on the set parameters: pressure, gas flows and RF power. Due to the fact that it is a chemical reaction, the etch rate is also dependent on the substrate material. In some of our samples we used Ar ions, so in those cases the etching was produced only by bombarding and there was no chemical reaction.

In this work, we used the RIE Oxford 80Plus from the clean room at UAB to carry out the etching during the creation of a shadow mask, and the RIE 2000 CE from South Bay Technology inc. from the clean room at the ICMAB.

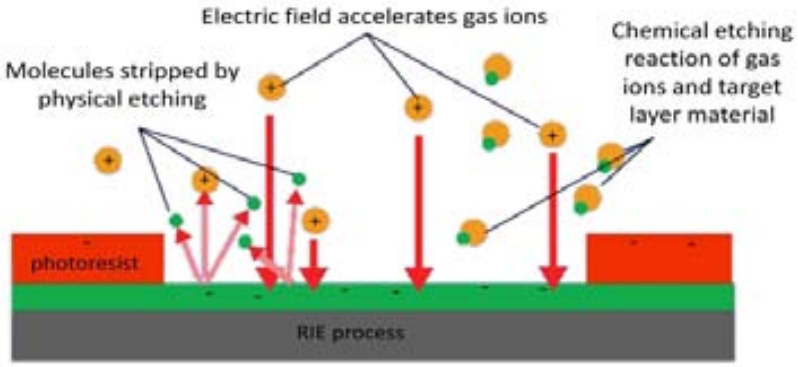

Fig A.20. Reactive Ion Etching process.

A.7.2.2 ION BEAM ETCHING (IBE)

Ion beam etching means physically milling a sample using an energetic (300-1000 eV) ion source with a broad, collimated and highly directional beam. The ions used for the process are inert, usually Ar, so they do not react specifically with the sample material. The sample may be tilted and rotated (to enable tailored sidewall profiles and prevent sputtered redeposition), and is etched uniformly and anisotropically (on the direction of the ion beam). To prevent charging of the sample, an independent electron source is available to neutralize the bombarding. A sketch of the Ion Beam Etching system is shown in Fig A.21.

In this thesis, we have used a 4Wave Ion beam Etch System from NanoGUNE laboratory.

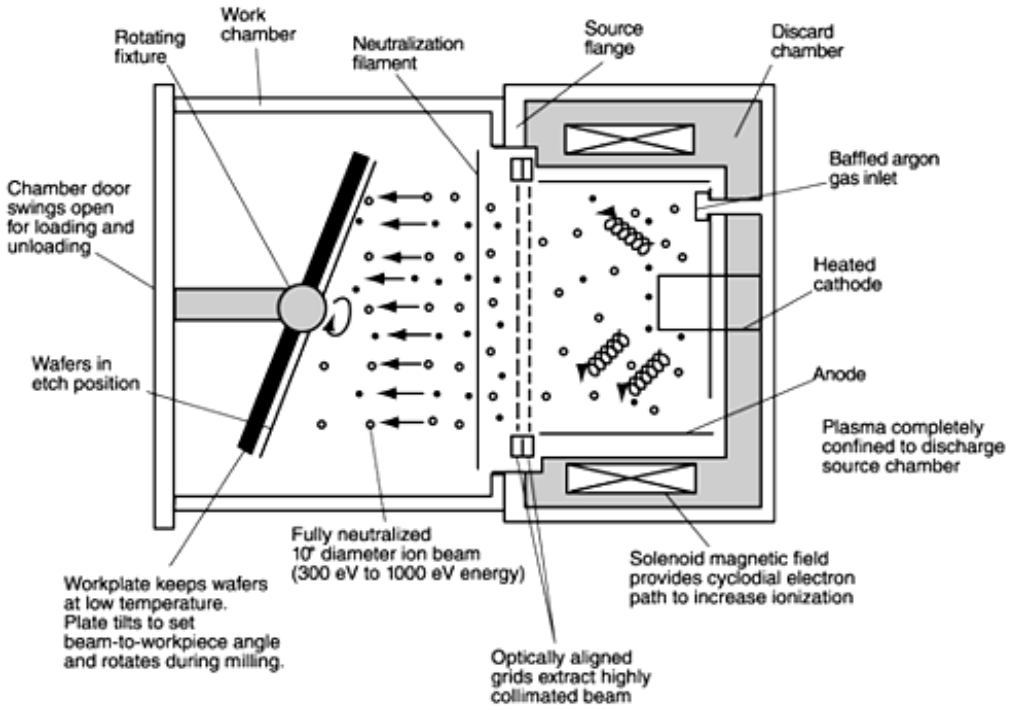

Fig A.21. Sketch of the Ion Beam Etching process. Image taken from [18].

A.7.2.3 WET ETCHING

Wet etching is a process by which a sample is left inside a bath of chemical solution which dissolves unprotected metal. The mask that protects the metal (to create a pattern) must dissolve at a slower rate than the unprotected metal, so that the wet etching process is finished before having dissolved the masking material. The main drawback of most etching chemical processes is its isotropic character; the sides of the pattern are exposed to the etching solution, the problem of "undercut", resulting in less control of the etch (smaller or less defined motifs).

Materials such as silicon, for instance, are etched in certain chemicals (in our case, a KOH solution) that exhibit different etch rates depending on the crystallographic direction, so that the walls of the carved hole are not vertical, but follow the <111> direction. Also, the etch rates are dependent on the bath temperature [19,20].

A.8 REFERENCES

[1] Coey J.M.D., Viret M., von Molnar S.; "Mixed-valence manganites". *Adv. Phys.* 48; **1999**: 167–293. doi:10.1080/000187399243455.

[2] Aufderheide B.E.; Sputtered Thin Film Coatings. In: Tracton AA, editor. COATINGS Technol. Handb. Third Edit, Taylor and Francis Group, LLC, CRC Press; **2006**.

[3] Birkholz M.; "Thin Film Analysis by X-Ray Scattering". Wiley-VCH Verlag GmbH & Co. KGaA; **2006**. doi:10.1002/3527607595.

[4] Lamas; "Difracción de rayos X con incidencia rasante y reflectometría de rayos X" online. http://www.tandar.cnea.gov.ar/eventos/Nano2010/Lamas.pdf.

[5] Dresden L.-I. für F.W.; "X-Ray Photoelectron Spectroscopy (XPS)" 2014; online. http://www.ifw-dresden.de/de/institute/institut-fuer-komplexe-materialien/abteilungen/mikro-und-nanostrukturen/methodenuebersicht/x-ray-photoelectron-spectroscopy-xps/.

[6] lightsources E., FERMI; "X-ray Photoelectron Spectroscopy" 2014; online. http://www.elettra.trieste.it/lightsources/labs-and-services/surface-lab/x-ray-photoelectron-spectroscopy.html.

[7] "Ma4: X-ray photoelectron spectroscopy (XPS)" online. http://www.physik.fu-berlin.de/studium/praktika-forward/fp_master_SoSe2011/doc/Ma4_XPS1.pdf?1359123007.

[8] Vilalta-Clemente A., Gloystein K.; "Principles of Atomic Principles Force Microscopy(AFM), based on lecture by Prof. Nikos Frangis". **2008**.

[9] Eastman M.; "Scanning Electron Microscopy". *Univ. Texas El Paso* **2010**. http://materialsworld.utep.edu/Background/SCANNING ELECTRON MICROSCOPY/SccaningElectronMicroscopy.htm.

[10] Sandiumenge F., Santiso J., Balcells L., Konstantinovic Z., Roqueta J., Pomar A., et al.; "Competing Misfit Relaxation Mechanisms in Epitaxial Correlated Oxides". *Phys. Rev. Lett.* 110; **2013**. doi:10.1103/PhysRevLett.110.107206.

[11] "Microscopy". *Can. Cent. Weld. Join.* **2012**. http://www.ualberta.ca/~ccwj/teaching/microscopy/.

[12] Kirmse H. (Humboldt U. of B.; "Sample Preparation for Transmission Electron Microscopy" **2013**. http://crysta.physik.hu-berlin.de/~kirmse/pdf/VL_TEM_Probenpraeparation_v2013_WS.pdf (accessed August 02, 2014).

[13] Fagaly R.L.; "Superconducting quantum interference device instruments and applications". *Rev. Sci. Instrum.* 77; **2006**: 101101. doi:10.1063/1.2354545.

[14] McElfresh M.; "Fundamentals of Magnetism and Magnetic Measurements" **1994**. http://www.qdusa.com/sitedocs/appNotes/mpms/FundPrimer.pdf.

[15] Jones S.W.; "Photolithography" **2008**. http://diyhpl.us/~bryan/papers2/photolithography/Photolithography chapter by Scotten W. Jones.pdf.

[16] "Shipley microposit® S1800® series photo resists" online. http://nanofab.ece.cmu.edu/resources/s1800seriesDataSheet.pdf (accessed April 01, 2011).

[17] Peña Guédez L., Martínez Perea B.; Sistemas Nanoestructurados y Propiedades de Transporte en Capas Delgadas de Manganita. Universitat de Barcelona, **2014**.

[18] "About the Ion Milling Process". *Ion Beam Milling, Inc.* online. http://www.ionbeammilling.com/about_the_ion_milling_process (accessed July 02, 2014).

[19] Collins S.D.; "Semiconductor Micromachining: Vol. II. Techniques and Industrial Applications". Wiley; **1998**.

[20] Madou M.J.; "Fundamentals of Microfabrication: the Science of Miniaturization". Second Edi. CRC Press LLC; **2000**.

B. COMPLEMENTARY ANALYSIS OF La_2CoMnO_6 CHARACTERIZATION

B.1 SUBTRACTION OF THE DIAMAGNETIC CONTRIBUTION

The diamagnetic contribution of STO is done by subtracting the corresponding M(H) loops measured at 350 K. This approximation considers no paramagnetic contribution of the LCMO at this temperature $\left[\chi\left(T=350\mathrm{K}\right)=\chi_{diam}+\chi_{PM}\left(350\mathrm{K}\right)\approx\chi_{diam}\right]$, so this section aims at providing an estimate of the error that this may introduce. To do so, we calculate the theoretical paramagnetic susceptibility for LCMO at 350 K $\left(\chi_{PM}\left(350\mathrm{K}\right)\right)$ considering the T_C value we have found, and compare it with a typical value of the susceptibility of an entire $5\times5\ \mathrm{mm}^2$ sample of STO, $\chi_{STO}=6\times10^{-9}$ emu / Oe.

The susceptibility for a ferromagnetic material follows the Curie-Weiss Law:

$$\chi_{molar}=\frac{\mathrm{C}}{T-T_{\mathrm{C}}} \qquad [B.1]$$

Where C is the Curie constant, T_C is the Curie Temperature and χ_{molar} is the molar susceptibility. The effective magnetic moment is related to the Curie constant through the following equation:

$$\left[\mu_{eff}\left(\mu_{\mathrm{B}}\right)\right]^2=g_s^2\cdot S\left(S+1\right);\mu_{eff}\left(\mu_{\mathrm{B}}\right)=\sqrt{\frac{3k\chi T}{N}}=\sqrt{8\mathrm{C}} \qquad [B.2]$$

For a sample with Co^{2+} and Mn^{4+}, both possessing $S=\frac{3}{2}$, and g_s=2, we calculate the Curie constant (using equation B.2):

$$\left[\mu_{eff}\left(\mu_{\mathrm{B}}\right)\right]^2=\left[\mu_{eff}\left(\mu_{\mathrm{B}}\right)\right]^2_{Co^{2+}}+\left[\mu_{eff}\left(\mu_{\mathrm{B}}\right)\right]^2_{Mn^{4+}}=30=8C=\frac{30}{8}\frac{emu\cdot K}{mol} \qquad [B.3]$$

and extract the molar susceptibility at T=350 K for a sample with T_C=225 K:

$$\chi_{molar}\left(T=350\mathrm{K}\right)=\frac{\mathrm{C}}{T-T_{\mathrm{C}}}=0.03\frac{emu}{mol\cdot Oe} \qquad [B.4]$$

The susceptibility in a 20 nm-thick film is calculated by the product: $\chi=\chi_{molar}\times N_{mol}$, where N_{mol} is the number of moles: $N_{mol}=\frac{1}{\mathrm{N_A}}\times N_{f.u.}=\frac{1}{\mathrm{N_A}}\times\frac{V_{film}}{V_{f.u.}}$, $N_{f.u.}$ being the number of formula units of LCMO. Taking into account that the formula unit volume for this material is $V_{f.u.}=120.47\text{Å}$ and that the volume of our sample is 5×10^{-7} cm^3, $\chi=\chi_{molar}\times N^{o}mols=0.207\times10^{-9}\ emu/Oe$.

Therefore, in considering the paramagnetic susceptibility of LCMO films at 350 K as negligible, we are accepting an error of

$$\text{Error}(\%) = \frac{\chi_{PM}(350\text{K})}{\chi_{STO}} = \frac{0.207\times10^{-9}}{6\times10^{-9}} = 3.4\ \% \qquad [B.5]$$

If for the low T_C sample (T_C=125 K) we were to suppose that the sample contained Co^{3+} and Mn^{3+} ($S = 2$, and g_s=2), we would have $C = \frac{48}{8}\frac{emu\cdot K}{mol}$, $\chi_{molar}(T = 350\text{K}) = 0.0267\frac{emu}{mol\cdot Oe}$, the error would be:

$$\text{Error}(\%) = \frac{\chi_{PM}(350\text{K})}{\chi_{STO}} = \frac{0.184\times10^{-9}}{6\times10^{-9}} = 3.1\ \% \qquad [B.6]$$

As the error does not exceed 4 %, we will consider this method as valid to perform the subtraction of the diamagnetic contribution of the STO substrate.

B.2 JUSTIFICATION OF DIFFRACTION PEAKS

From sketch on top of Fig 4.4, we can obtain the relationship between crystallographic directions (100), (010) and (001) for STO and LCMO in real space, for both possible configurations (LCMO c parameter in-plane or out of plane with respect to STO) –the correspondence is detailed in the "real space" columns in Table B.1. The conversion to reciprocal space is also shown, to help determine which peaks exist for each orientation.

For LCMO oriented with *c*-out of plane, peak $(0\ \bar{3}\ \frac{5}{2})$ indexed with respect to STO corresponds to the $(\bar{3}\ 3\ 5)$ peak of LCMO, whilst $(0\ \frac{\bar{5}}{2}\ 3)$ does not exist (it would correspond to $(\frac{\bar{5}}{2}\ \frac{5}{2}\ 6)$, but Miller indices must be integer). Following the same arguments, for LCMO oriented with *c*-in plane, peak $(0\ \bar{3}\ \frac{5}{2})$ indexed with respect to STO does not exist, but diffraction peak $\left(0\ \frac{\bar{5}}{2}\ 3\right)$corresponds to $(3\ \bar{3}\ \bar{5})$ peak of LCMO. These calculations (taking table Table B.1 as reference) consider that the c parameter of LCMO is in-plane and parallel to (010)STO instead of parallel to (100)STO. However, for the same reasoning as before, $(0\ \frac{\bar{5}}{2}\ 3)$ peak –indexed with respect to STO- will only exist when c (LCMO)//(100)STO and peak $(\frac{\bar{5}}{2}\ 0\ 3)$ will only exist for c(LCMO)//(010)STO. As we do not expect a preferential orientation between these two c-in plane configurations, we expect both measurements to be equivalent. But in order to be certain that in sample E there is no c-in plane-oriented LCMO, (Fig 4.4e), we perform two measurements of the peak, rotating the sample 90 ºC to probe both configurations with c-in plane, that with c (LCMO)//(100)STO and that with c(LCMO)//(010)STO.

Table B.1. Relationship between crystallographic orientations of LCMO and STO for LCMO//STO (for *c*-out of plane and *c*-in plane configurations, as depicted in sketch in Fig 4.4) in real space and its correspondence in reciprocal space.

***c*-out of plane**			
	Real space	**Reciprocal space**	
STO	**LCMO**	**STO**	**LCMO**
(100)	½(110)	(100)	(110)
(010)	½(-110)	(010)	(-110)
(001)	½(001)	(001)	(002)

***c*-in plane**			
	Real space	**Reciprocal space**	
STO	**LCMO**	**STO**	**LCMO**
(100)	½(110)	(100)	(110)
(010)	½(001)	(010)	(002)
(001)	½(-110)	(001)	(1-10)

B.3 Origin of the biloop feature in the hysteresis loops

The measured biloops were found not to be reproducible. Due to the large perpendicular anisotropy of the films, hysteresis cycles are strongly affected by the crystal orientation in the SQUID magnetometer. This has been the origin of large discussion during the thesis, to determine the origin of the observed biloop feature, observed both for H applied in-plane and out-of-plane.

To clarify whether the biloop might be related to different crystallographic phases, sample F (which possesses a unique crystallographic phase oriented with c-out of plane) was measured with an intentional misalignment. Fig B.1a and Fig B.1b show the comparison between perfect alignment of the sample or a misalignment of 5-10º, in the in-plane and out-of-plane configuration, respectively. When the sample is misaligned with respect to the applied magnetic field, a biloop contribution is measured. With this test, we have ruled out the contribution of the different phases (c-out-of-plane and c-in-plane) as the origin of the biloop.

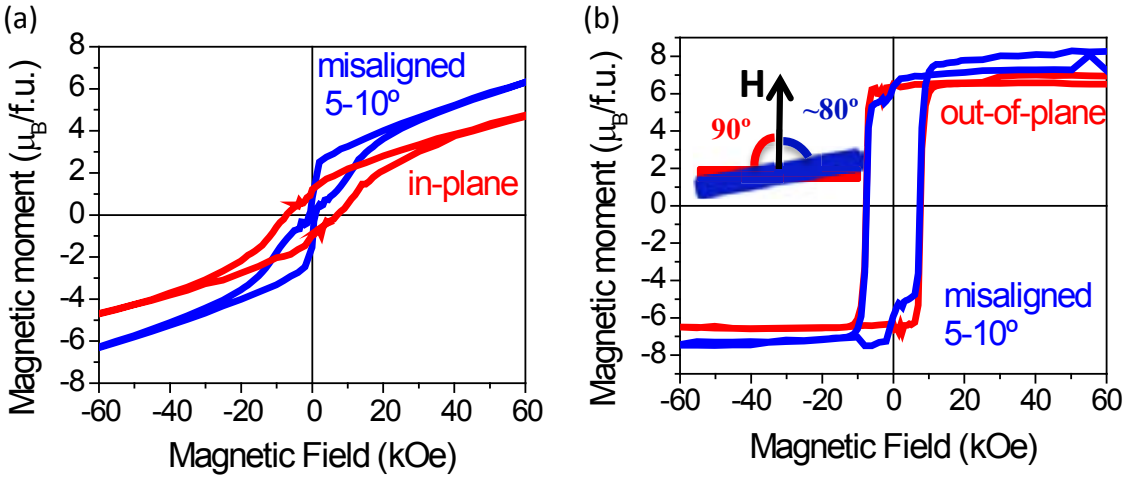

Fig B.1. Effect of a 5-10º misalignment of the sample orientation during the measurement on the biloop features; (a) for in-plane configuration and (b) out-of-plane configuration.